

Structural Characteristics of InGaAs/GaP Quantum Dots and Related Materials on the Atomic Scale

vorgelegt von
Diplom-Physiker

Christopher Prohl

Von der Fakultät II – Mathematik und Naturwissenschaften
der Technischen Universität Berlin
zur Erlangung des akademischen Grades

Doktor der Naturwissenschaften
- Dr. rer. nat. -
genehmigte Dissertation

Promotionsausschuss:

Vorsitzende: Prof. Dr. Kathy Lüdge
Gutachter: Prof. Dr. Mario Dähne
Gutachter: Prof. Dr. Holger Eisele
Gutachter: Priv.-Doz. Dr. Philipp Ebert

Tag der wissenschaftlichen Aussprache: 17. Juni 2019

Berlin 2019

Abstract

Self-assembled (In,Ga)As quantum dots (QDs) embedded in a GaP matrix are a promising semiconductor material for possible applications in optoelectronics and nanomemory cells. Even more, GaP with its particular low lattice mismatch to silicon offers the possibility to monolithically integrate III-V semiconductor nanotechnology into silicon.

In this thesis, cross-sectional scanning tunneling microscopy (XSTM) was intensely used to analyze the structural characteristics of differently grown (In,Ga)As/GaP QDs and related materials on the atomic scale, investigating both samples grown by metal-organic vapor-phase epitaxy (MOVPE) and by molecular beam epitaxy (MBE). The XSTM data have been evaluated via the image contrast in combination with a stoichiometry analysis based on the local lattice parameter.

A GaAs interlayer before the $\text{In}_{0.25}\text{Ga}_{0.75}\text{As}$ deposition on GaP by using MOVPE enables the Stranski-Krastanow growth mode leading to the formation of QDs by an intense material redistribution. The QDs have a truncated pyramidal shape, consist of phosphorus-free (In,Ga)As, and contain the total amount of deposited indium distributed in a reversed-cone stoichiometric profile. The surrounding wetting layer consists of inhomogeneously distributed indium-free Ga(As,P).

The duration of the growth interruption (GRI) after the growth of $\text{In}_{0.5}\text{Ga}_{0.5}\text{As}$ /GaAs QDs in GaP has an influence on the photoluminescence intensity. A structural redistribution of the QD layer occurs during the GRI, which is characterized by an intermixing of the locally concentrated indium within the layer, transforming the truncated pyramidal shaped QDs into a more homogeneous quaternary (In,Ga)(As,P) layer.

MBE-grown $\text{In}_{0.25}\text{Ga}_{0.75}\text{As}$ /GaAs/GaP QD layers show comparable structural properties as their MOVPE-grown equivalents with phosphorus-free (In,Ga)As QDs and an indium-free Ga(As,P) wetting layer. $\text{In}_{0.5}\text{Ga}_{0.5}\text{As}$ layers grown directly on GaP by MBE have an inhomogeneous material distribution. Small agglomerations, which get more pronounced with increasing deposited material, presumably consist of quaternary (In,Ga)(As,P), while the surrounding layer consists of indium-reduced (In,Ga)(As,P).

Investigations on thin GaAs and (Al,Ga)P layers in GaP show that the total deposited material amount is located within the layers and only slight segregation occurs.

Computational calculations on $\text{In}_{0.25}\text{Ga}_{0.75}\text{As}$ /GaAs/GaP QDs give a brief insight into the electronic structure.

Initial XSTM experiments on promising MOVPE-grown $\text{In}_{0.5}\text{Ga}_{0.5}\text{Sb}$ /GaAs QD layers on GaP show the formation of nanostructures with inner agglomerations, where the material distribution depends on the duration of an additional Sb-flush before the $\text{In}_{0.5}\text{Ga}_{0.5}\text{Sb}$ deposition. Within the nanostructures the material seems to arrange in a quaternary or even quinary way, which desires a detailed investigation in the future.

Zusammenfassung

Selbstorganisierte (In,Ga)As-Quantenpunkte (QDs), eingebettet in eine GaP-Matrix, sind ein vielversprechendes Halbleitermaterial für mögliche Anwendungen in der Optoelektronik und für Nanospeicher-Zellen, insbesondere da GaP mit seiner besonders geringen Gitterfehlpassung zu Silizium die Möglichkeit zur monolithischen Integration der III-V-Halbleiter-Nanotechnologie in Silizium bietet.

In dieser Arbeit wurde die Querschnitts-Rastertunnelmikroskopie (XSTM) intensiv verwendet, um die Strukturmerkmale unterschiedlich gewachsener (In,Ga)As/GaP-QDs und verwandter Materialien auf atomarer Skala zu untersuchen, wobei die Proben sowohl mit metallorganischer Gasphasenepitaxie (MOVPE) als auch mit Molekularstrahlepitaxie (MBE) gewachsen wurden. Die XSTM-Daten wurden über den Bildkontrast in Kombination mit einer Stöchiometrie-Analyse basierend auf dem lokalen Gitterparameter ausgewertet.

Eine GaAs-Zwischenschicht vor der $\text{In}_{0.25}\text{Ga}_{0.75}\text{As}$ -Abscheidung auf GaP mittels MOVPE ermöglicht den Stranski-Krastanow-Wachstumsmodus, der durch eine intensive Materialumverteilung zur Bildung von QDs führt. Die QDs haben die Form einer abgestumpften Pyramide, bestehen aus Phosphor-freiem (In,Ga)As und enthalten die Gesamtmenge an abgeschiedenem Indium, das in einem stöchiometrischen Profil in Form eines umgekehrtem Kegels verteilt ist. Die umgebende Benetzungsschicht besteht aus inhomogen verteiltem Indium-freiem Ga(As,P).

Die Dauer der Wachstumsunterbrechung (GRI) nach dem Wachstum von $\text{In}_{0.5}\text{Ga}_{0.5}\text{As}/\text{GaAs}$ -QDs in GaP beeinflusst die Intensität der Photolumineszenz. Eine strukturelle Umverteilung der QD-Schicht tritt während der GRI auf. Diese ist durch eine Durchmischung des lokal konzentrierten Indiums innerhalb der Schicht gekennzeichnet, welche die pyramidenstumpfartigen QDs in eine homogenere quaternäre (In,Ga)(As,P)-Schicht überführt.

MBE-gewachsene $\text{In}_{0.25}\text{Ga}_{0.75}\text{As}/\text{GaAs}/\text{GaP}$ -QD-Schichten zeigen vergleichbare strukturelle Eigenschaften wie ihre mit MOVPE gewachsenen Äquivalente, mit Phosphor-freien (In,Ga)As-QDs und einer Indium-freien Ga(As,P)-Benetzungsschicht. $\text{In}_{0.5}\text{Ga}_{0.5}\text{As}$ -Schichten, die mittels MBE direkt auf GaP gewachsen wurden, besitzen eine inhomogene Materialverteilung. Kleine Agglomerationen, die mit zunehmendem abgeschiedenem Material ausgeprägter werden, bestehen vermutlich aus quaternärem (In,Ga)(As,P), während die umgebende Schicht mehr aus Indium-reduziertem (In,Ga)(As,P) besteht.

Untersuchungen an dünnen GaAs- und (Al,Ga)P-Schichten in GaP zeigen, dass sich die gesamte abgeschiedene Materialmenge innerhalb der Schichten befindet und nur eine geringe Segregation auftritt.

Computergestützte Berechnungen zu $\text{In}_{0.25}\text{Ga}_{0.75}\text{As}/\text{GaAs}/\text{GaP}$ -QDs geben einen kurzen Einblick in die elektronische Struktur.

Erste XSTM-Experimente zu vielversprechenden mittels MOVPE gewachsenen $\text{In}_{0.5}\text{Ga}_{0.5}\text{Sb}/\text{GaAs}$ -QD-Schichten auf GaP zeigen die Ausbildung von Nanostrukturen mit inneren Agglomerationen, wobei die Materialverteilung von der Dauer eines zusätzlichen Sb-Flushes vor der $\text{In}_{0.5}\text{Ga}_{0.5}\text{Sb}$ -Abscheidung abhängt. Innerhalb der Nanostrukturen scheint sich das Material in einer quaternären oder sogar quinären Weise anzuordnen, was eine detaillierte Untersuchung in der Zukunft verlangt.

Publications

Parts of this work have been published in:

Growth of $In_{0.25}Ga_{0.75}As$ quantum dots on GaP utilizing a GaAs interlayer,

G. Stracke, A. Glacki, T. Nowozin, L. Bonato, S. Rodt, C. Prohl, A. Lenz, H. Eisele, A. Schliwa, A. Strittmatter, U. W. Pohl, and D. Bimberg, Applied Physics Letters **101**, 223110 (2012).

Spatial structure of $In_{0.25}Ga_{0.75}As/GaAs/GaP$ quantum dots on the atomic scale,

C. Prohl, A. Lenz, D. Roy, J. Schuppang, G. Stracke, A. Strittmatter, U. W. Pohl, D. Bimberg, H. Eisele, and M. Dähne, Applied Physics Letters **102**, 123102 (2013).

Further publications:

Energy surfaces of rare-earth silicide films on Si(111),

M. Wanke, M. Franz, M. Vetterlein, G. Pruskil, B. Höpfner, C. Prohl, I. Engelhardt, P. Stojanov, E. Huwald, J. D. Riley, and M. Dähne, Surface Science **603**, 2808-2814 (2009).

Evolution of the InAs wetting layer on GaAs(001)-c(4×4) on the atomic scale,

J. Grabowski, C. Prohl, B. Höpfner, M. Dähne, and H. Eisele, Applied Physics Letters **95**, 233118 (2009).

Atomic structure of the (4×3) reconstructed InGaAs monolayer on GaAs(001),

H. Eisele, B. Höpfner, C. Prohl, J. Grabowski, and M. Dähne, Surface Science **604**, 283-289 (2010).

Atomic structure and strain of the InAs wetting layer growing on GaAs(001)-c(4×4),
C. Prohl, B. Höpfner, J. Grabowski, M. Dähne, and H. Eisele,
Journal of Vacuum Science & Technology B **28**, C5E13 (2010).

Electronic properties of dysprosium silicide nanowires on Si(557),
M. Wanke, M. Franz, M. Vetterlein, G. Pruskil, C. Prohl, B. Höpfner, P. Stojanov,
E. Huwald, J.D. Riley, and M. Dähne,
Journal of Applied Physics **108**, 064304 (2010).

*Atomic structure and stoichiometry of In(Ga)As/GaAs quantum dots grown on an
exactoriented GaP/Si(001) substrate,*
C. S. Schulze, X. Huang, C. Prohl, V. Füllert, S. Rybank, S. J. Maddox, S. D. March,
S. R. Bank, M. L. Lee and A. Lenz,
Applied Physics Letters **108**, 143101 (2016).

*Cross-sectional scanning tunneling microscopy of antiphase boundaries in epitaxially
grown GaP layers on Si(001),*
C. Prohl, H. Döscher, P. Kleinschmidt, T. Hannappel, and A. Lenz,
Journal of Vacuum Science & Technology A **34**, 031102 (2016).

Growth and electronic properties of Tb silicide layers on Si(111),
M. Franz, S. Appelfeller, C. Prohl, J. Große, H.-F. Jirschik, V. Füllert, C. Hassenstein,
Z. Diemer, and M. Dähne,
Journal of Vacuum Science & Technology A **34**, 061503 (2016).

Instruction of students

The following student theses were performed under my guidance:

Strukturelle Untersuchungen der GaP(001)-Oberfläche,

Milan Gajewski, Bachelorarbeit,

Institut für Festkörperphysik, Technische Universität Berlin, February 2010.

Atomare Struktur von InGaAs-Quantenpunkten in GaP,

Dominik Roy, Bachelorarbeit,

Institut für Festkörperphysik, Technische Universität Berlin, February 2013.

Guidance in cooperation with Andrea Lenz.

Cross-sectional scanning tunneling microscopy investigations of InGaSb/GaAs/GaP(001) nanostructures,

Stavros Rybank, Master thesis,

Royal Institute of Technology (KTH) /

Institut für Festkörperphysik, Technische Universität Berlin, October 2015.

Guidance in cooperation with Andrea Lenz.

Contents

Abstract	iii
Zusammenfassung	v
Publications	vii
Instruction of students	ix
1 Introduction	1
2 Experimental methods and setup	5
2.1 Epitaxial growth of semiconductor Quantum Dots	5
2.1.1 Growth mechanisms for semiconductor heteroepitaxy	5
2.1.2 Metal-organic vapor phase epitaxy	7
2.1.3 Molecular beam epitaxy	7
2.2 Cross-sectional scanning tunneling microscopy	10
2.2.1 Principle of scanning tunneling microscopy	10
2.2.2 XSTM at III-V semiconductor cleavage surfaces	12
2.2.3 Experimental setup	18
2.2.4 XSTM data evaluation	24
3 (In,Ga)As/GaP Quantum Dots grown by MOVPE	31
3.1 First XSTM investigations on (In,Ga)As Quantum Dots in a GaP matrix	31
3.1.1 Sample structure	31
3.1.2 XSTM results	32
3.2 In _{0.25} Ga _{0.75} As/GaAs Quantum Dots in GaP	36
3.2.1 Sample structure	36
3.2.2 XSTM results: image contrast analysis	36
3.2.3 XSTM results: stoichiometry analysis	42
3.3 In _{0.5} Ga _{0.5} As/GaAs Quantum Dots in GaP	51

3.3.1	Sample structure	52
3.3.2	XSTM results: image contrast analysis	54
3.3.3	XSTM results: stoichiometry analysis	64
3.3.4	Quantum Dot layer transformation with longer GRI	73
4	(In,Ga)As/GaP Quantum Dots grown by MBE	75
4.1	Sample overview	75
4.1.1	Sample structure	75
4.1.2	XSTM results: overview	76
4.2	In _{0.25} Ga _{0.75} As/GaAs Quantum Dots in GaP	80
4.2.1	XSTM results: image contrast analysis	80
4.2.2	XSTM results: stoichiometry analysis	83
4.2.3	Comparison between MBE and MOVPE Quantum Dots	87
4.3	In _{0.5} Ga _{0.5} As Quantum Dots in GaP	89
4.3.1	XSTM results: image contrast analysis	89
4.3.2	XSTM results: stoichiometry analysis	101
4.3.3	Quantum Dot layer evolution with increasing material amount	108
5	Thin GaAs and (Al,Ga)P layers in GaP	109
5.1	GaAs/GaP layers grown by MOVPE	109
5.1.1	10-fold superlattices of GaAs/GaP	109
5.1.2	3-fold layers of GaAs/GaP with varying material amount	115
5.2	GaAs/GaP layers grown by MBE	125
5.3	(Al,Ga)P/GaP layers grown by MOVPE	129
5.4	(Al,Ga)P/GaP layers grown by MBE	132
5.5	Growth behavior of thin GaAs and (Al,Ga)P layers in GaP	134
6	Excursus: Calculations on the electronic structure	135
6.1	The Quantum-Dot model	135
6.2	Performed calculations and results	138
6.3	Results and discussion about the electronic properties	139
7	Outlook: (In,Ga)Sb/GaAs Quantum Dots in GaP	145
8	Conclusions	151
	Bibliography	157
	Acknowledgments	167

Chapter 1

Introduction

Over the last century semiconductor materials more and more infiltrated our every day life, since they are the basis for every technology in our computerized multimedia society and for the ongoing development of semiconductor based devices. Having started with the invention of the first transistor in 1947 [1] this led to today's high-end consumer electronics like multifunctional smartphones and others (already predicted by G.E. Moore in 1965 [2]), which continuously change the way we live.

The basic material for common semiconductor technology is of course silicon. Although naturally only present in compounds, silicon is the second most abundant element present in the earth's crust [3] and simply therefore has become an economically promising, i.e. low-cost, material for industrial processes. Wafers of silicon single crystals, which are produced via the Czochralski process out of a melt of amorphous elemental silicon gained by the reduction of naturally present silicon dioxide, are the fundament for any silicon semiconductor application [4]. Concerning its physical properties, silicon crystallizes in the cubic diamond structure with a lattice constant of 5.431 Å [5]. Unfortunately, crystalline silicon behaves electronically as an indirect semiconductor, which makes it a bad candidate for using it as an active medium in an optoelectronic device [4].

Besides silicon, on the other hand a variety of compound semiconductors has been investigated throughout the last 60 years [6, 7]. Especially the III-V compound semiconductors provide a highly investigated research field including applications for optoelectronics since they show (in many cases) direct band gaps related to wavelengths in the range from the mid infrared over visible light to the ultraviolet [5, 8].

Especially semiconductor nanostructures like quantum wells, quantum wires, and, in particular, quantum dots came into focus. Thereby, a (III-V compound) semiconductor material is embedded into a surrounding matrix of another one. For quantum dots the dimensionality of the active material is reduced in all of the three directions of

space, so that its extension is below the exciton Bohr radius of the host material. This leads to a quantum confinement of the charge carriers within the quantum dot and a change of the root-like electronic density of states with quasi-continuous band states for the bulk material to a delta-function like density of states with discrete state energies. This zero-dimensional electronic structure is comparable to the one of a single atom, which is the reason quantum dots are called "artificial atoms", although quantum dots consist of about hundreds to ten-thousands atoms and still have typically dimensions of several nanometers. But in contrast to single atoms, the electronic properties of the quantum dots, which are determined by their atomic structure like size, shape, and material composition, can be controlled, offering a variety of possible applications for multiple kinds of devices [9–11].

The most intensively studied III-V compound semiconductor material for quantum dots is (In,Ga)As, which is epitaxially grown on GaAs substrates. Thus, the (In,Ga)As/GaAs material system is the model system for III-V semiconductor quantum dots with a broad knowledge in various fields, including studies of growth mechanisms from self-assembly [12–16] to site-controlled quantum dot positioning [17–21], characterization of electronic and optical properties [22–26], and finally applications in optoelectronics from light emitting diodes (LEDs) [27, 28] over quantum dot lasers [29–32] and optical amplifiers [33, 34] to single photon emitters for quantum cryptography applications [35–37]. Regarding the fundamental research also the investigation of the structural properties within this material system has led to revealing results, including studies of the (In,Ga)As wetting layer evolution from the pure GaAs surface up to quantum dot formation [38–41], high resolution microscopy of free standing InAs/GaAs quantum dots [42, 43], and also structural characterization of overgrown (In,Ga)As/GaAs quantum dots [44–47] and submonolayer quantum dot layers [48–50].

Apart from other III-V materials, recently (In,Ga)As embedded in a GaP matrix was selected as a further promising material system due to several possible applications, although the exploration of suitable growth conditions in this highly strained (In,Ga)As/GaP system proved to be very challenging [51–57].

As already demonstrated, III-V semiconductor quantum dots can serve as a basis for a newly developed memory application, which combines benefits of both common dynamic random-access memories (DRAM) and flash memories. These nano-memory cells, also called *QD-Flash memory*, can be realized with various III-V materials [58], but they also initially contained (In,Ga)As/GaAs quantum dots, resulting in storage times (for holes) of 0.5 ns [59]. A change of the matrix material from GaAs to GaP was predicted to exceed these values due to expected higher hole localization energies [60].

First experiments with $\text{In}_{0.25}\text{Ga}_{0.75}\text{As}/\text{GaAs}/\text{GaP}$ quantum dots already showed longer storage times of $3 \mu\text{s}$ [55].

Further applications lie in the development of new optoelectronic devices, especially in aspects of the direct integration into silicon technology. As GaP crystallizes in the zincblende crystal structure with a lattice constant of 5.451 \AA [5], it has only a slight lattice mismatch of 0.4% to silicon which makes it an ideal candidate for combining III-V optoelectronic technology with silicon substrates [61]. During the progress of this thesis, already a first LED consisting of $(\text{In,Ga})\text{As}$ grown on a GaP/Si template has been successfully demonstrated by Song et al. [62].

These ideas and proposed (and partly already demonstrated) applications open the field of a new spectrum of fundamental research activities. As for the structural analysis on the one hand the detailed characterization of the GaP/Si interface with its appearing aspects of antiphase boundaries and domains is for itself a challenging task [61, 63–68] on the other hand the development and characterization of newly created $(\text{In,Ga})\text{As}$ nanostructures in a GaP matrix is as much important and indispensable.

In this work, fundamental structural investigations of $(\text{In,Ga})\text{As}$ quantum dots grown within a GaP matrix were performed on an atomic scale by using the instrument of cross-sectional scanning tunneling microscopy (XSTM) to reveal a detailed structural insight into this new material system [55, 69].

This thesis is structured as follows: **Chapter 2** gives an overview on the growth mechanisms and techniques used for the provided samples that were investigated. Further, an introduction on all important aspects of cross-sectional scanning tunneling microscopy is given including the basic principle of XSTM, specialties on XSTM at III-V cleavage surface, details on the used experimental setup, and the necessary evaluation techniques for the data analysis.

In **Chapters 3 and 4** XSTM investigations of $(\text{In,Ga})\text{As}$ quantum dot layers grown on GaP by metal-organic vapor phase epitaxy (MOVPE) and molecular beam epitaxy (MBE) are presented with a special concern on image contrast but also on stoichiometry analysis. **Chapter 5** gives analogous insight into thin GaAs/GaP and $(\text{Al,Ga})\text{P}/\text{GaP}$ layers.

An excursus in **Chapter 6** has a view on calculations on the electronic structure of a specific type on $(\text{In,Ga})\text{As}/\text{GaP}$ quantum dots. A short outlook on Sb-containing $(\text{In,Ga})\text{Sb}/\text{GaAs}$ quantum dots in GaP is given in **Chapter 7**, before the thesis finally concludes the major results in **Chapter 8**.

Chapter 2

Experimental methods and setup

2.1 Epitaxial growth of semiconductor Quantum Dots

Within the last 50 years epitaxial growth methods have become the ideal tool for the fabrication of crystalline semiconductor layers and nanostructures [70]. Originating from the Greek language the term epitaxy, consisting of "epi - upon" and "taxis - order", describes the ordered crystal growth of a material on a crystalline substrate. While for the growth of layers on a substrate of the same material the term homoepitaxy is used, the growth of differing materials for layer and substrate is called heteroepitaxy.

Several epitaxial techniques have been developed and continuously improved. For the growth of semiconductor layers and nanostructures and especially quantum dots in particular the metal-organic vapor phase epitaxy and the molecular beam epitaxy became essential techniques not only for research but also for the industrial fabrication of semiconductor devices.

While in the following only some necessary basics of epitaxy are discussed, for details on epitaxy fundamentals and experimental techniques several textbooks were published, which are referred to (Refs. [16, 70, 71]).

2.1.1 Growth mechanisms for semiconductor heteroepitaxy

The difficulty in heteroepitaxy is that the different crystalline materials have different physical properties like their vapor pressure, their decomposition temperature, their thermal expansion coefficient, and their bulk crystal structure, including the lattice constant. Even for two materials with similar thermal expansion coefficients and the same crystal structure, e.g. zinc blende, a difference in their lattice constant leads to a pseudomorphic strained layer which is either tensile strained, when growing a material with smaller lattice constant on a substrate with a larger lattice constant, or

compressively strained in the vice versa case. This strain then has a significant impact on the fundamental growth mode.

During heteroepitaxy three fundamental growth modes can occur [72], which are illustrated in Fig. 2.1: In the Frank-van der Merve mode the growth occurs layer by layer meaning a new monolayer begins to form after the previous one is completed [73]. In the Volmer-Weber mode the deposited material forms islands on the surface, which then go on growing three-dimensionally (3D) [74]. In the Stranski-Krastanow mode the material first forms a so-called wetting layer, which continues growing up to a critical thickness, where the three-dimensional island growth starts [75].

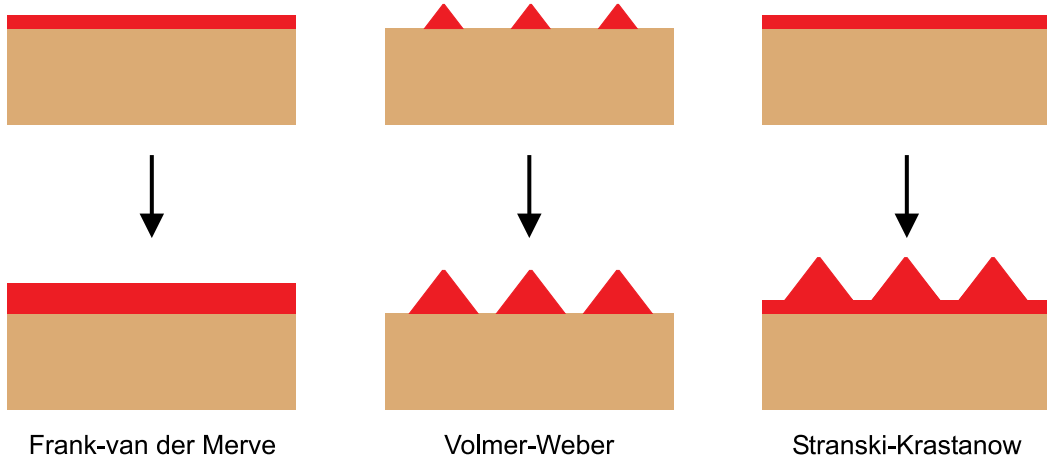


Figure 2.1: Schematic diagram of the fundamental growth modes.

The kind of occurring growth mode is determined by the lattice mismatch and the energetic situation at the interface where a state of minimized energy is favored [16, 70, 76]: For the Frank-van der Merve mode the sum of the film (epilayer) surface energy γ_f and the interface energy γ_i is lower than the substrate surface energy γ_s , $\gamma_s > \gamma_f + \gamma_i$, while in the Volmer-Weber mode $\gamma_s < \gamma_f + \gamma_i$, which leads to the 3D island growth in order to keep as much of the substrate surfaces uncovered as possible. In the Stranski-Krastanow mode there is a switch in the energetic behavior at the critical thickness, where a further energetic minimization is realized by a two-dimensional (2D) to 3D transition in order to reduce the increasing strain energy at the interface. This energetically driven island formation process in the Volmer-Weber and Stranski-Krastanow mode is called self organization.

For the InAs/GaAs material system with a lattice mismatch of 7% the growth occurs in the Stranski-Krastanow mode beginning with a wetting layer formation of (In,Ga)As, followed by a 2D to 3D transition at a critical thickness of about 1.4 monolayers (ML), which leads to the formation of quantum dots [39, 40, 77, 78].

For the growth of (In,Ga)As on a GaP substrate (with a lattice mismatch of 11%

between InAs and GaP) the Volmer-Weber mode for direct island formation was observed in early experiments [51, 79], but later also the Stranski-Krastanow mode was found to appear for certain growth conditions [53, 57, 80], which will also be confirmed in the experimental data presented in Chapters 3 and 4.

2.1.2 Metal-organic vapor phase epitaxy

Metal-organic vapor phase epitaxy (MOVPE), also called metal-organic chemical vapor deposition (MOCVD) is one of the favored techniques for the growth of semiconductor layers and nanostructures. The principle, illustrated in Fig. 2.2, can be summarized shortly as follows [16, 70, 71]: Within a reactor a gas mixture consisting of a carrier gas, which is usually hydrogen (H_2), and metal-organic compounds, which inhibit e.g. the III-V materials, is carried over a heated and usually rotating substrate, where these so-called precursors decompose. The resulting elemental materials then can interact with the substrate via surface mechanisms like adsorption, diffusion, and finally lattice incorporation, which leads to the crystal growth, while the remaining reaction products desorb from the surface and get transported out of the reactor by the carrier gas. The precursor materials, usually in liquid or rarely in solid phase, are separately stored in so-called bubblers, through which the carrier gas flows carrying a defined material flux into the reactor.

The growth parameters in this epitaxial technique are the substrate temperature and the choice of the partial pressures (and thereby also the V/III ratio) of the different gases which get mixed just when they enter the reactor, both influencing growth rate and composition of the growing layers. To be able to decompose the precursor materials within the reactor the substrate temperature usually is in the range of 500–800 °C [70].

Metal-organic materials which are used as precursors for the samples investigated within this thesis (see Chapter 3) are phosphine (PH_3), tertiarybutylphosphine (TBP), tertiarybutylarsine (TBAs), trimethylgallium (TMGa), triethylgallium (TEGa), and trimethylindium (TMIn). For further details Ref. [57] is referred to.

2.1.3 Molecular beam epitaxy

As much important as MOVPE and also competitive for semiconductor growth in research is the technique of molecular beam epitaxy (MBE). The principle, illustrated in Fig. 2.3, is as follows [16, 70, 71, 81]: In solid/liquid source MBE the elemental materials, which are of high purity, are evaporated from effusion cells, and the generated molecular/atomic beams are directed onto the heated and often rotated substrate, where they interact with the surface resulting in crystal growth. In opposite to MOVPE, for MBE

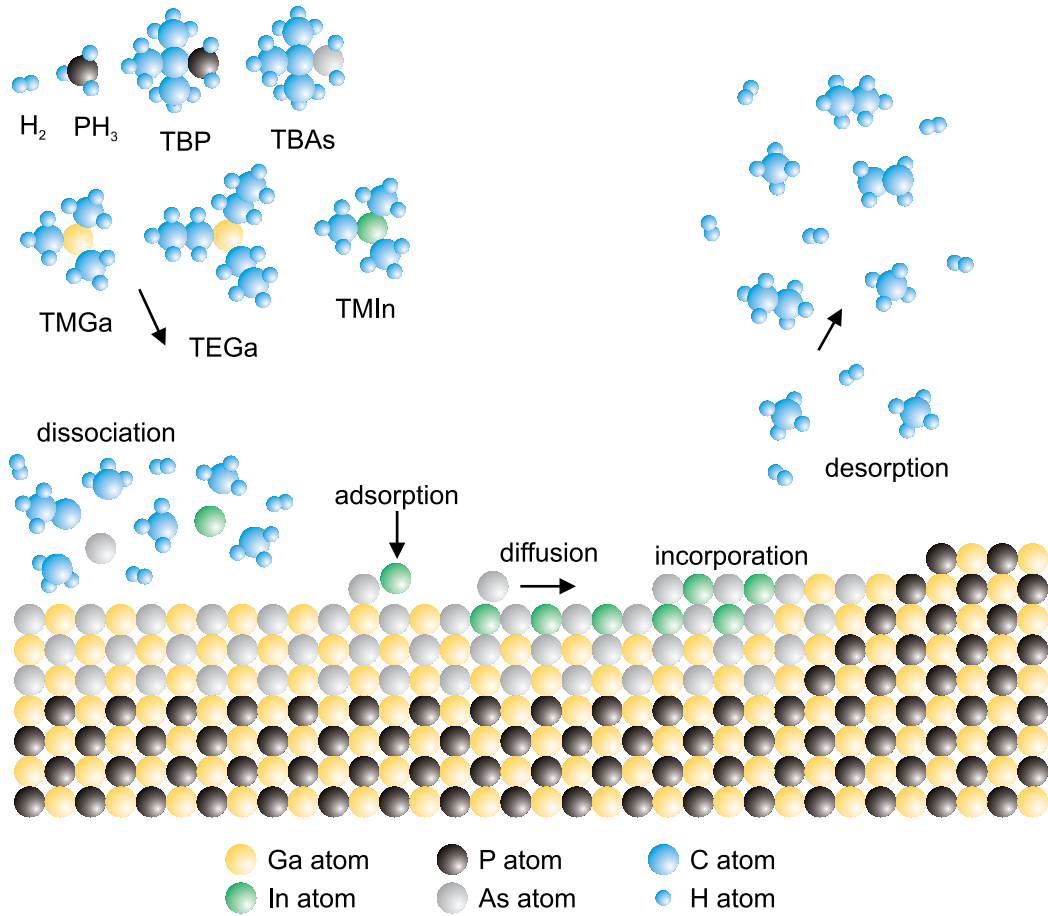


Figure 2.2: Schematic principle of the processes in metal-organic vapor phase epitaxy.

ultra high vacuum conditions (base pressure below $1 \cdot 10^{-9}$ mbar = $1 \cdot 10^{-7}$ Pa) are applied to ensure the purity of the molecular beams and to prevent collision interactions of the beam molecules with the environment. For III-V semiconductors the materials are mostly evaporated from so-called Knudsen-cells. While the group-III metals evaporate as atoms, the group-V materials like phosphorus and arsenic mainly evaporate as molecular tetramers (P_4 , As_4) but also as dimers (P_2 , As_2). As the dimer stage preferentially supports the crystal incorporation, the effusion cells for these group-V materials are often equipped with a cracker stage dissociating the tetramers into dimers.

The growth parameters that need to be chosen carefully are again the substrate temperature but also the beam equivalent pressures (BEPs) of the individual molecular/atomic beams. By choosing the BEPs also the V/III ratio can be adjusted, which is — apart from the substrate temperature — the critical parameter to influence the balance between adsorption, desorption, and incorporation processes at the substrate surface and thereby influencing growth rate and composition of the grown layers. MBE growth can in situ be monitored by reflection high energy electron diffraction (RHEED),

allowing to observe appearing changes in the surface reconstruction, as well as 2D-3D transitions, and also to determine the growth rate [71].

For details on the MBE growth for the samples investigated within this thesis (see Chapter 4) Ref. [56] is referred to.

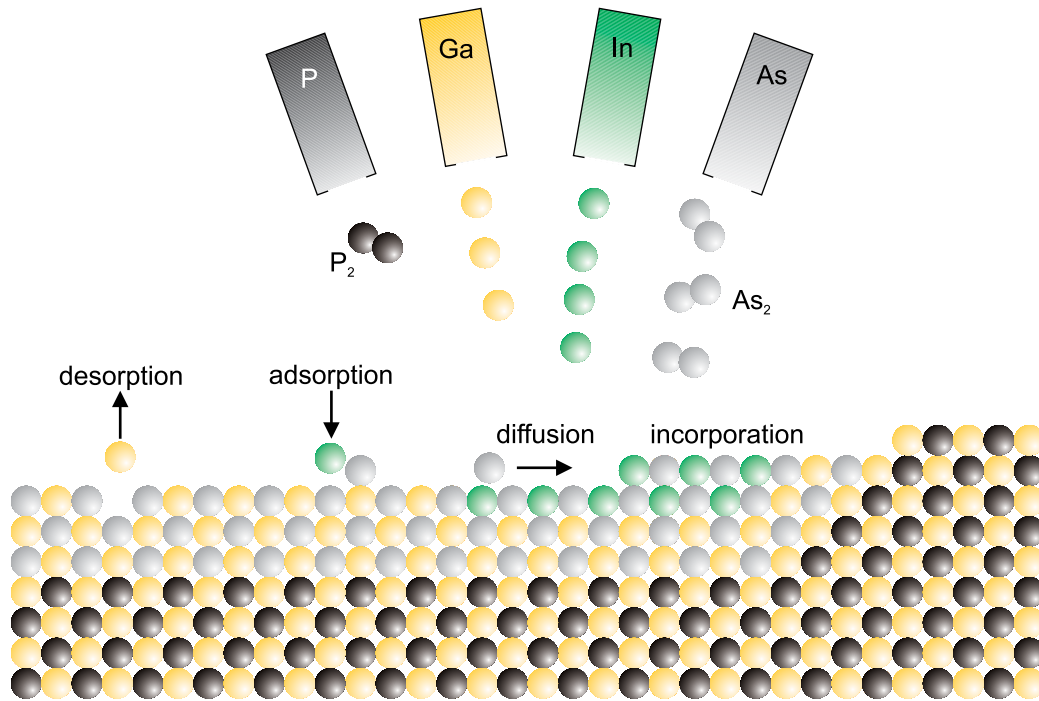


Figure 2.3: Schematic principle of the surface processes in molecular beam epitaxy.

2.2 Cross-sectional scanning tunneling microscopy

For the structural analysis of material surfaces on a scale going down to the nanoscopic or even to the atomic regime, several experimental techniques have been developed during the last century. Apart from electron microscopy techniques such as scanning electron microscopy (SEM) and transmission electron microscopy (TEM) and their further developments, scanning probe microscopy methods (SPM) evolved into essential methods in science and engineering. Especially for the analysis of semiconductor surfaces on the atomic scale, SPM methods like scanning tunneling microscopy (STM) and atomic force microscopy (AFM) became reliable allies.

2.2.1 Principle of scanning tunneling microscopy

The scanning tunneling microscope was invented by C. Binnig, H. Rohrer, Ch. Gerber, and E. Weibel at the IBM Zürich Research Laboratory, Switzerland, and presented in 1982 [82]. The principle of STM is that a very thin metallic tip is scanning over an electrically conductive sample without having a physical contact (as illustrated by Fig. 2.4 taken from Refs. [82,83]). The applied voltage between tip and sample results in a tunneling current, which is a measure for the electronic states at the surface and thereby the atomic structure.

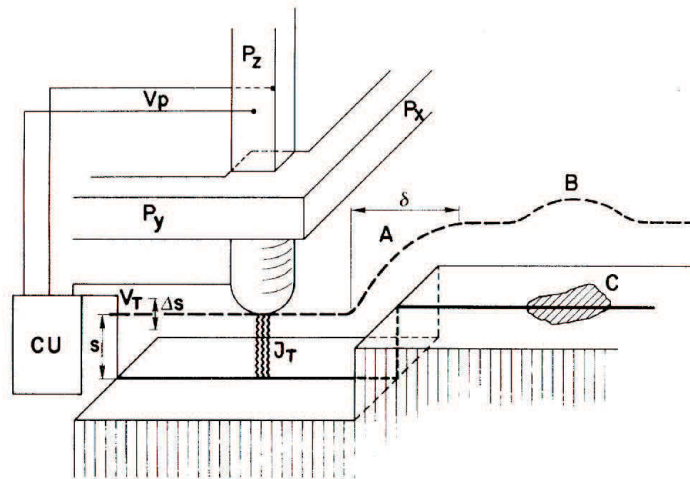


Figure 2.4: Schematic principle of STM, from [82,83].

The fundament, on which this behavior is based on, is the quantum-mechanical tunneling of an electron through a potential barrier. While according to classical physics an electron cannot penetrate through a potential barrier, from a quantum mechanically point of view the wavefunction describing the electron shows an exponential

decay. Hence, there is a finite probability for electron tunneling through the barrier. The tunneling current I_T in the STM operation depends on the applied voltage V_T and the distance s between tip and sample, and in a first approximation, can be expressed with

$$I_T \sim \frac{V_T}{s} \exp(-A s \sqrt{\Phi}), \quad (2.1)$$

where $A \approx 1.025 \text{ (eV)}^{-\frac{1}{2}} \text{ \AA}^{-1}$ for a vacuum gap and Φ is the average of the work functions of tip and sample [82–84].

The scanning unit, on which the tip is mounted, is moved across the sample in all three dimensions with piezo elements (P_x, P_y, P_z in Fig. 2.4). Applied voltages on the piezo elements lead to slight deformations, which enable the scanning of the sample (x,y) as well as the close approach (z). As for the original STM setup a simple tripod was used, nowadays the scanner in STM setups usually has a single piezo tube which is able to move in all three dimensions [85].

By adjusting the voltage V_z to the piezo P_z the local distance s between tip and sample during scanning and thereby the tunneling current I_T is held at a fixed value using a feedback control unit (CU). In this so-called *constant current mode* the varying height of the piezo P_z is the actually measured value. For each scanned position data values of the type $V_z(V_x, V_y)$ of the voltages at the piezos are measured and electronically converted into a topographic image of the scanned sample surface [83].

For further details on STM theory and STM applications in general several textbooks have been published which is referred to (Refs. [86–90]), while in the following the focus is on fundamentals, experimental details, and data analysis about XSTM on semiconductors, which was the main experimental tool performed during work on this thesis.

2.2.2 XSTM at III-V semiconductor cleavage surfaces

For the use of STM as a tool to investigate material surfaces, two setup geometries are possible. The classical arrangement, as already illustrated in Fig. 2.4, is to approach the tip directly onto the surface. Concerning epitaxial grown semiconductor surfaces and nanostructures this top-view arrangement is used to investigate the structural properties of growth surfaces and free-standing nanostructures like self-assembled quantum dots, as shown in the left part of Fig. 2.5. In the cross-sectional or XSTM arrangement the tip is approached to the side of the sample, which was cleaved before. Nanostructures like quantum dots need to be covered with a cap layer in order to use them within any device application. Furthermore, it is also already known that during overgrowth the structural and thereby also the electronic properties of quantum dots will change [47, 91]. Hence, the XSTM gives the chance to investigate these buried nanostructures, as shown in the right part of Fig. 2.5. One should note that the physical principle of STM is the same in both arrangements since only the scanned surface is different. Nevertheless, the XSTM setup and measurements are more complex and time-consuming than standard STM measurements at surfaces, since the approached cleavage surface is much smaller than the sample surface. Therewith also the interesting layers first need to be located, which is more difficult than in top-view STM where the surface can be approached at an arbitrary position.

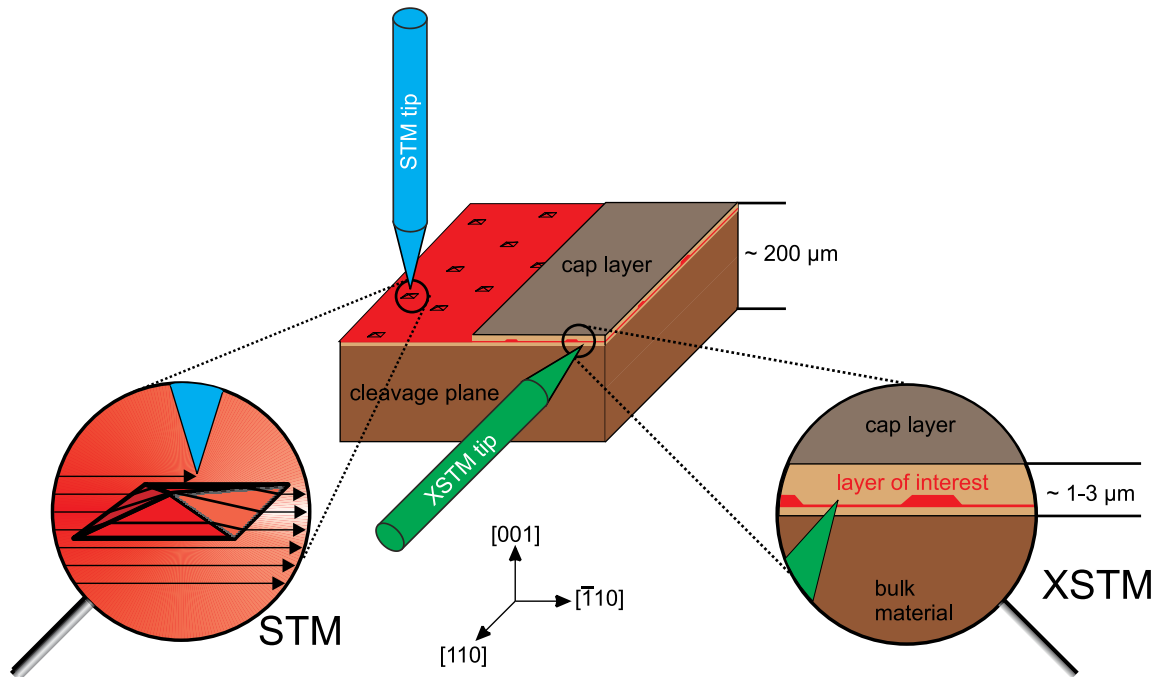


Figure 2.5: Schematic comparison of (top-view) STM at the growth surface and XSTM at the cleavage plane, adapted from [92].

The (110) cleavage surface

In the experiments discussed within this thesis only III-V semiconductors, which crystallize in the zincblende structure, were under investigation. Furthermore, the investigated samples were all epitaxially grown on (001)-oriented substrates where the common cleavage surfaces for XSTM are the $\{110\}$ surfaces. In Fig. 2.6 the structural model for the (110) surface is shown, exemplarily for GaP. In the side view of the surface in Fig. 2.6 (a) a buckling of the surface atoms is visible: In the cleaved (110) surface the top group-V atoms (e.g. P, As) are shifted outwards while the top group-III atoms (e.g. Ga, In) are shifted inwards in comparison to their bulk positions [93,94]. This surface relaxation is caused by an electron transfer: On the unrelaxed cleaved surface, each of the surface atoms has one dangling bond which contains one electron. But on the relaxed surface, each surface group-V atom has a dangling bond fully filled with two electrons while each top group-III atom has an empty dangling bond. In Fig. 2.6 (b) it is shown that the top surface atoms are arranged in zigzag chains of alternating group-III and group-V atoms along the $[1\bar{1}0]$ direction. A first XSTM image can be found in Fig. 2.6 (c) showing a GaP(110) surface. Corresponding to the structure model in Fig. 2.6 (b) the surface unit cell is highlighted. The surface is characterized by a rectangular pattern with chains along the $[1\bar{1}0]$ and along the $[001]$ direction. In this highly-resolved image each protrusion of bright contrast represents a single empty dangling bond of the corresponding Ga atom in the top layer. It should be noted that in XSTM experiments the tip can only reach the atoms in the topmost layer which leads to the fact that only every second monolayer of atoms (of each group) can be imaged. As indicated in Fig. 2.6 (a) the distance between neighboring chains (along the $[1\bar{1}0]$ direction) is 2 ML.

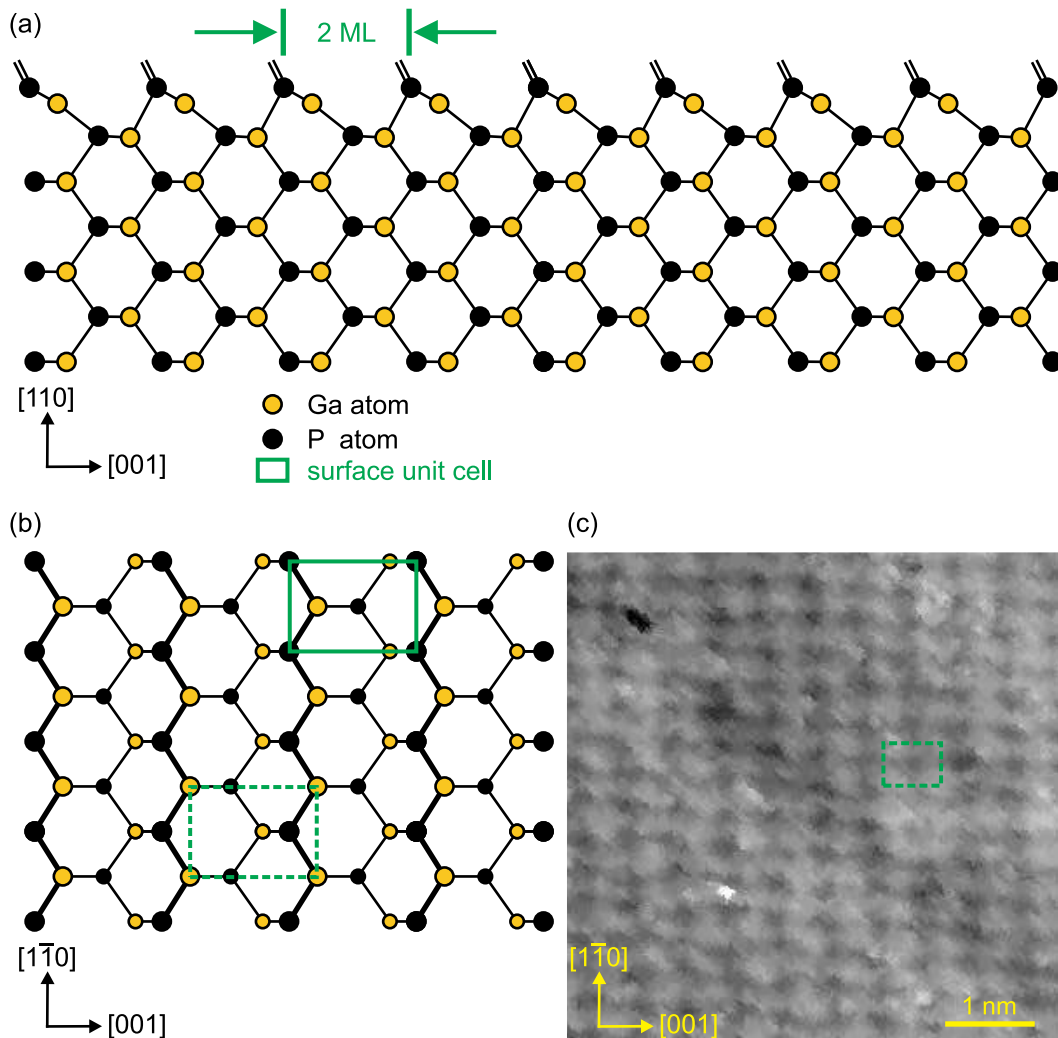


Figure 2.6: The relaxed GaP(110) surface: Schematics of (a) the side view and (b) the top view, both adapted from [95]. (c) Empty-state XSTM image of the GaP(110) surface. The image was taken at a sample voltage $V_T = +3.0$ V and a tunneling current $I_T = 50$ pA. The surface unit cell is marked by the green rectangle.

Image contrast mechanisms

In XSTM several mechanisms play a significant role concerning the image contrast, from which the important ones will be addressed briefly now.

As already implicitly mentioned in the paragraph above, only one kind of atoms can be imaged at a time, which is related to the occupation of the dangling bonds at the (110) surface. Depending on the polarity of the sample bias during scanning, the electrons either tunnel from the tip into the empty states of the group-III atoms (positive sample bias) or from the filled states of the group-V atoms into empty states of the tip (negative sample bias) [96,97]. As shown in Fig. 2.7 (a) in filled-state images a change in the group-V lattice (here from P to As) in the top layer leads to a significant contrast due to the different (here longer) bond lengths. The same effect appears for a change in the group-III surface lattice (here from Ga to In) in empty-state images, as shown in Fig. 2.7 (b). Although in filled-state images the XSTM at the (110) surface is only sensitive to the group-V atoms a change in the group-III also causes a contrast, as the bonded group-V surface atom also gets shifted, as indicated for the In atom in Fig. 2.7 (a).

The difference in bond length even more has an influence on the image contrast when whole layers of different material or nanostructures like quantum dots are grown into a crystal. As these materials have a different lattice constant than the substrate and the surrounding matrix material, the embedded layer or quantum dot material gets strained. E.g., the material of an (In,Ga)As layer or quantum dot within a GaP matrix gets compressively strained due to the larger lattice constant. As illustrated in Fig. 2.8 (a) a cleavage through such a quantum dot allows the material to relax outward. This so-called strain-induced outward relaxation then gives a significant contribution to the image contrast in XSTM, a topographic contrast.

Even more, the quantum dot layer material and the surrounding matrix do not only differ in their lattice constants but also in their electronic properties. This difference in the electronic band gaps leads to different tunneling probabilities for the same applied sample bias V_T , as illustrated in Fig. 2.8 (b), which results in a material dependent electronic contrast in the XSTM image.

Of course, in XSTM imaging the discussed contrast images do appear at the same time in combination. Due to their origin, the electronic contrast is more prominent at suitable low absolute bias voltages while the topographic contrast dominates at high bias voltages. Nevertheless, for the relevant III-V semiconductors, the materials with larger lattice constants usually have smaller band gaps, as shown in Tab. 2.1.

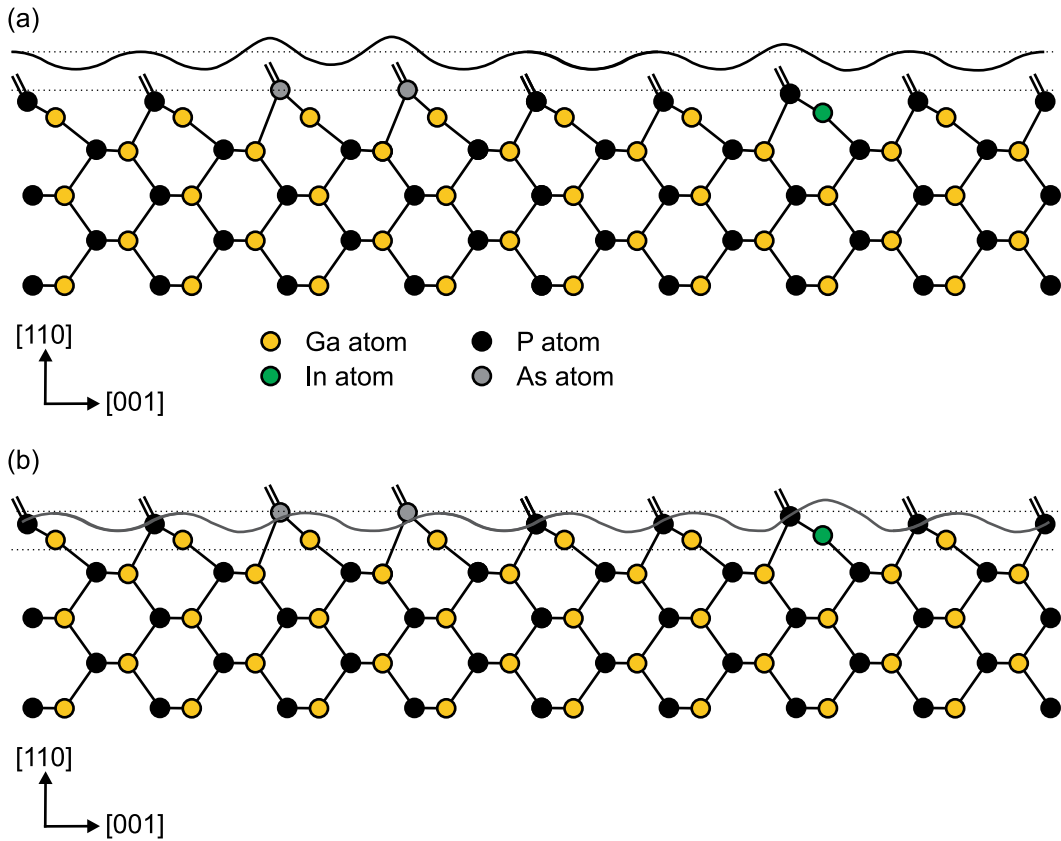


Figure 2.7: Schematic of the bias-dependent atom-selective contrast at the GaP(110) surface: (a) filled-state mode (negative sample bias); (b) empty-state mode (positive sample bias), adapted from [95].

So for the XSTM imaging, the topographic image contrast due to the strain-induced outward relaxation and the electronic contrast due to the varying band gaps at least have the same trend (adding each other up) in imaging the materials.

Table 2.1: Lattice constants and band gaps of relevant bulk semiconductors [98].

	GaP	GaAs	InAs	GaSb	InSb
lattice constant [\AA]	5.451	5.653	6.058	6.096	6.479
band gap ($T = 300\text{K}$) [eV]	2.26	1.43	0.36	0.72	0.17

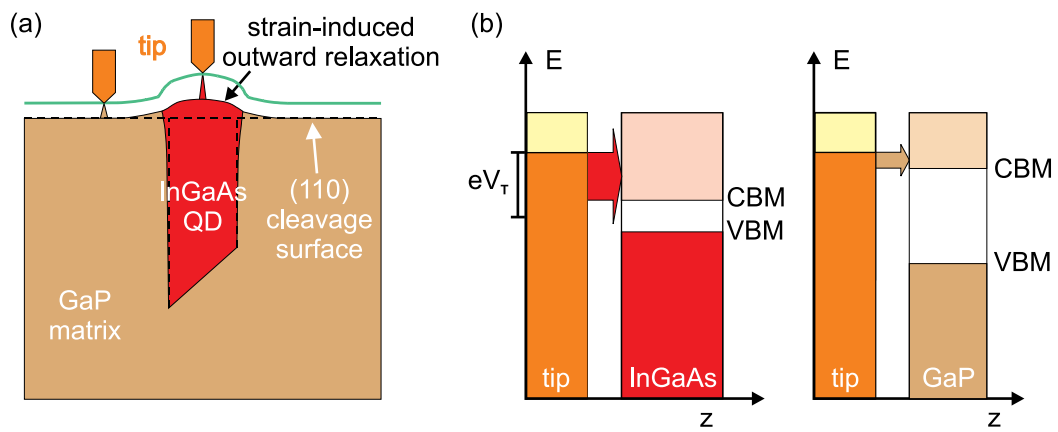


Figure 2.8: Schematics of image contrast mechanisms in XSTM: (a) topographic contrast (strain-induced outward relaxation for compressively strained quantum dots); (b) electronic contrast.

2.2.3 Experimental setup

XSTM-UHV chamber-system

The experimental setup used for the performed investigations is a multi-chamber UHV system, which was originally built up in 1999 and since then has been steadily enhanced and extended. As illustrated in Figs. 2.9 and 2.10, the main part consists of three chambers, which are separated by UHV valves. These are the fast entry (load lock) chamber, the preparation chamber, and the XSTM chamber.

The small fast entry chamber works as a load lock and enables to enter new samples and XSTM tips into the system without breaking the UHV within the other chambers. A magnetic UHV transfer connects the fast entry to the preparation chamber and can be loaded with up to two sample holders and six tips at a time.

The larger preparation chamber functions as location for tip and sample storage and also for in situ tip preparation (see also next paragraph). The tip storage shelf can hold up to 32 tip holders. The main magnetic transfer, which is located here and enables a quick transfer to the attached XSTM chamber, can further hold six tips at a time and also can store up to five sample holders. Within the preparation chamber the tip heating position gives space for a single tip holder to perform an in situ tip treatment by electron bombardment. Opposite to the tip a heating filament can supply electrons which then are accelerated onto the tip by applying an electrical field between tip and filament. The installed wobble stick within the preparation chamber serves as a tool to manipulate the positions of sample and tip holders inside the UHV chamber from the outside, i.e. between the storage positions on the magnetic transfer, the tip storage shelf, and the heating position.

The XSTM chamber has its own wobble stick for manipulating tip and sample holders between the transfer and the XSTM. The chamber also has a storage unit for up to sixteen spare tips and also one sample holder resting position. The XSTM itself is mounted on the upper vertical flange and is a home built and customized instrument, which is connected to and operated with an *RHK Technology SPM 1000 control unit*. The XSTM chamber is further equipped with several windows to enable tip and sample manipulation as well as the sample cleavage and the precise positioning of the tip and sample on the XSTM table. For the latter mirrors on the XSTM flange (in situ) and an optical microscope located at the front window (ex situ) are installed.

Within the first phase of this thesis the original XSTM flange unit has been replaced by an identical duplicate, which was constructed to have a second XSTM unit in spare in case of any kind of appearing future operating problems. The replacement was necessary because the aged piezo crystals in the original XSTM unit already showed

an asymmetric behavior, meaning that the imaging of the scanned surfaces showed a distortion due to asymmetric piezo shearing along the x - and y -scanning directions. For data evaluation, this required an additional distortion compensation of the measured images, which can be difficult, as therefore high-resolution along both the x - and y -scanning directions is needed. For further technological details on the customized XSTM and its duplicate, Refs. [95,99] are referred to.

The whole chamber system is equipped with several pump stages to initiate (diaphragm and turbomolecular pumps) and maintain (ion getter pumps) a stable UHV with a base pressure below $1 \cdot 10^{-10}$ mbar = $1 \cdot 10^{-8}$ Pa, as these conditions are necessary to preserve clean and non-oxidized cleavage surfaces and tips during XSTM measurements. After venting a chamber for maintenance reasons or sample/tip exchanges, the respective chambers are additionally baked out for several hours at a temperature of 120 °C to vaporize condensed water molecules, which are present due to air humidity, in order to reestablish suitable UHV conditions.

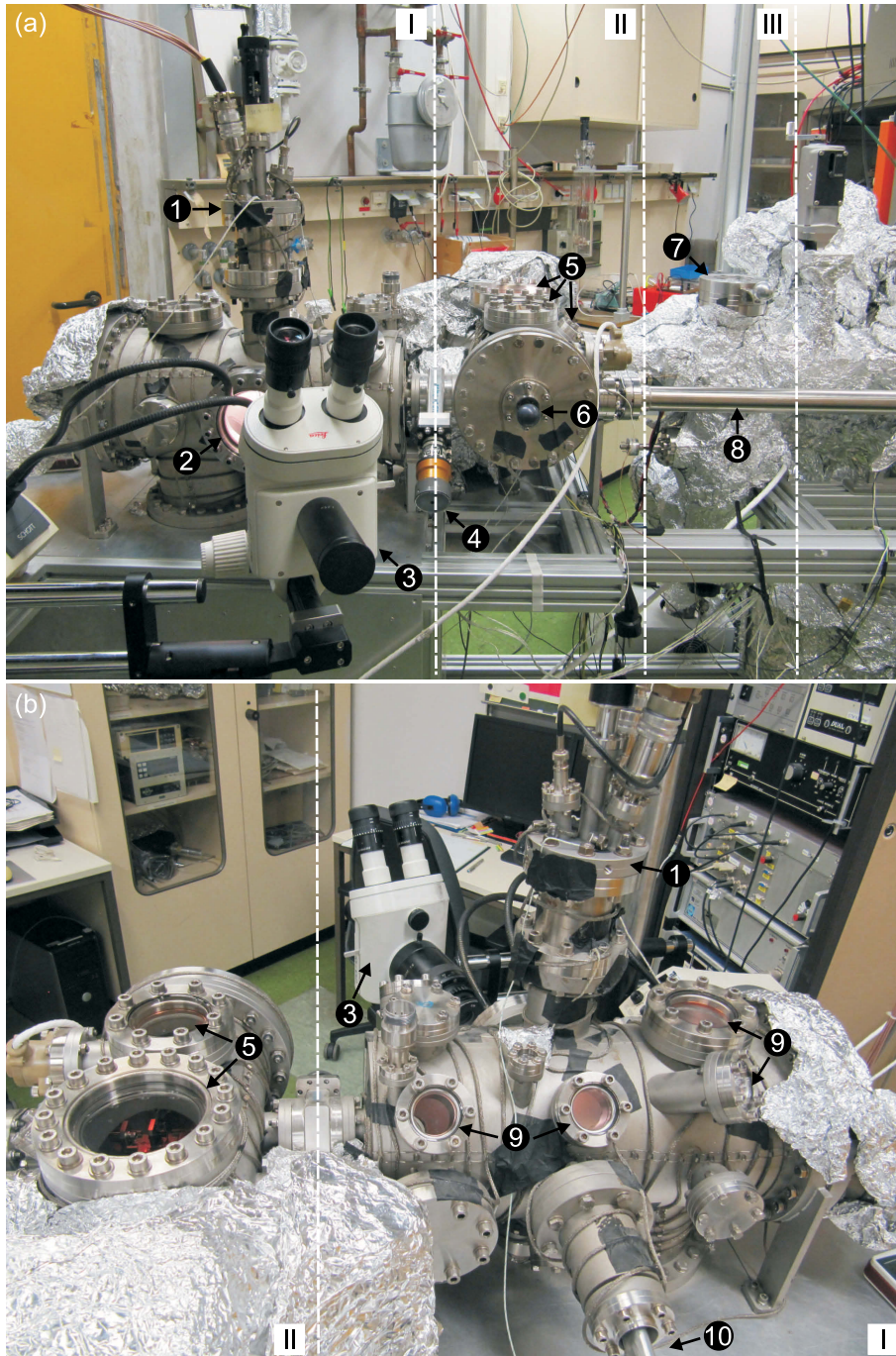


Figure 2.9: (a) Front and (b) back view on the XSTM-UHV chamber-system consisting of (I) the XSTM chamber, (II) the preparation chamber and (III) the fast entry chamber: (1) XSTM flange, (2) front window for optical tip-sample approach (3) light microscope, (4) UHV valve, (5) preparation chamber windows, (6) preparation chamber wobble stick, (7) fast-entry load-lock, (8) main magnetic transfer, (9) XSTM chamber windows, (10) XSTM chamber wobble stick.

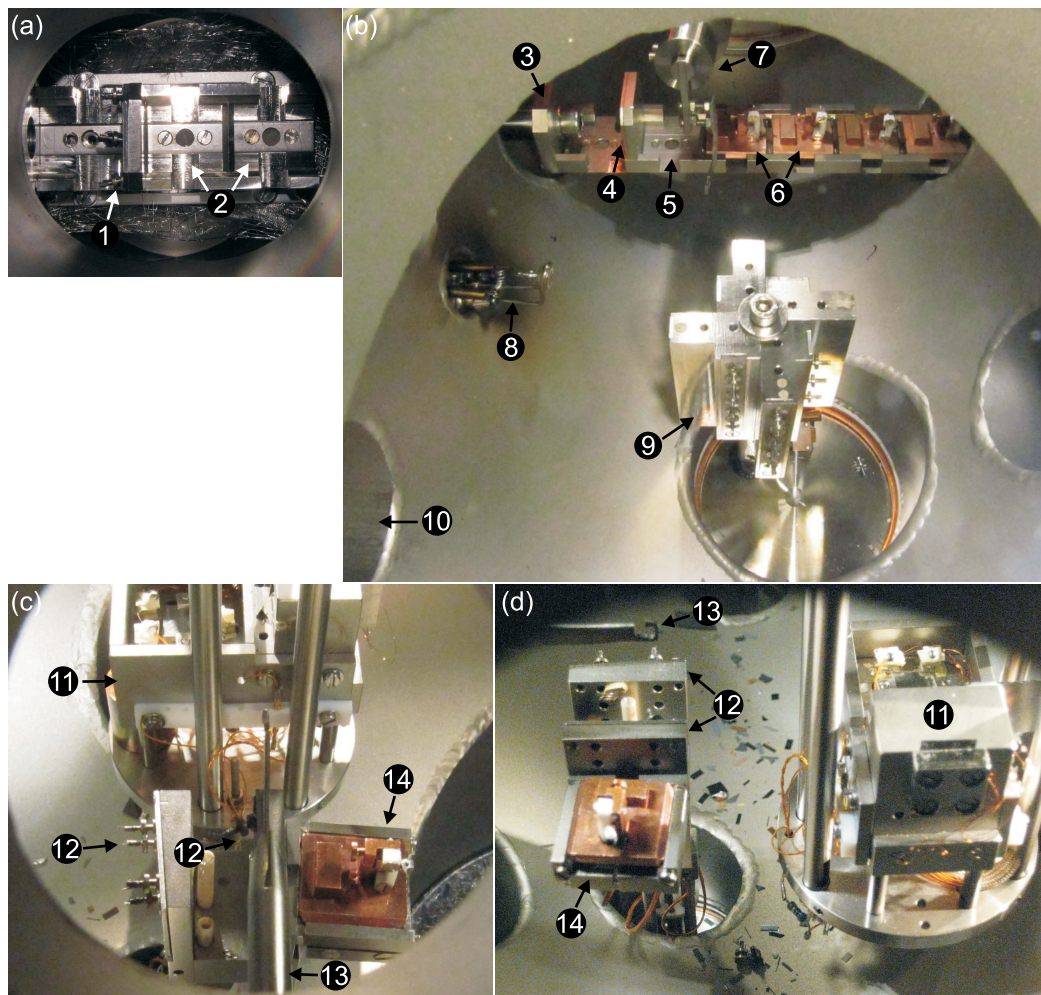


Figure 2.10: Views into the different UHV chambers. (a) Fast entry chamber with magnetic transfer: (1) tip holder in storage position, (2) two storage positions for sample holders; (b) Preparation chamber: (3) main magnetic transfer, (4) tip storage position, (5) sample holder storage position, (6) sample holders, (7) wobble stick, (8) tip heating facility, (9) tip storage shelf, (10) connection tube to fast entry chamber; (c) back and (d) side view into XSTM chamber: (11) XSTM, (12) tip storage unit, (13) wobble stick, (14) sample holder in resting position.

XSTM tip preparation

For the XSTM experiment the tips used were all self-manufactured, as illustrated in Fig. 2.11. In this procedure, tungsten wire was electrochemically etched within an NaOH solution [100]. The tips then were spot welded on a tip holder, which allows transfer inside the UHV chamber system from the fast-entry load lock via the preparation chamber to the XSTM chamber and vice versa. Before usage in the XSTM the tips were further cleaned in situ inside the preparation chamber by electron bombardment.

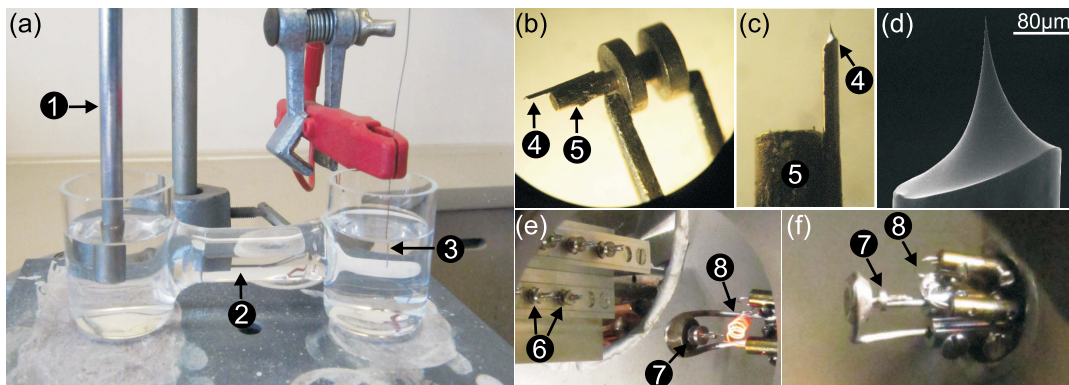


Figure 2.11: XSTM tip preparation: (a) electrochemical etching: (1) stainless steel cathode, (2) NaOH solution, (3) tungsten wire (anode); (b-c) (4) W tip on (5) tip holder, (d) scanning electron microscopy image of W tip; (e-f) view into the preparation chamber: (6) tip holders on tip storage shelf, (7) tip holder on heating (electron bombardment) position, (8) heating filament for electron supply.

XSTM sample preparation and cleavage

Before the epitaxially grown samples can be investigated with the XSTM, they carefully have to undergo a few but necessary preparation steps, as illustrated in Fig. 2.12. All of the provided samples that have been investigated throughout this thesis were epitaxially grown on 1/4 of a two inch GaP wafer. This wafer needs to be cut using a precision diamond scribe into rectangular pieces where the edges are nearly exactly aligned with the $\langle 110 \rangle$ directions and have dimensions of $(9 \times 10) \text{ mm}^2$, which is a good size for the available thinning stamp. Mounted on this stamp the sample piece gets thinned from the typical wafer thicknesses of $350\text{--}500 \text{ }\mu\text{m}$ down to thicknesses of about $150 \text{ }\mu\text{m}$, being optimal for a good and sharp cleavage. Each $(9 \times 10) \text{ mm}^2$ sample piece is then further cut into four smaller pieces, with typical dimensions of $(4.5 \times 5) \text{ mm}^2$, which is a proper size for the used sample holder technique. Each of these four samples is further prepared with a slight notch extending across about 1/3 of the sample, being aligned with the crystal direction where the sample cleavage should

occur. To get mounted onto the sample holder a sample has to be carefully glued on a small and thin copper plate. For the initial experiments the non-conductive *Torr Seal Low Vapor Pressure Resin Sealant* (by Varian), a two-component self-hardening epoxy resin, was used as glue which requires a further connection between the sample and the copper plate using indium to ensure the electrical contact. In all later experiments *EPO-TEK[®]H20E*, a two component, electrically conductive, 100% solids silver-filled epoxy system (by Epoxy Technology) was used, which turned out to provide a better electrical contact of the sample. The sample on the copper plate can now be mounted on the sample holder and entered into the UHV chamber system; where it can be easily transferred between the chambers, analogous to the tip holders.

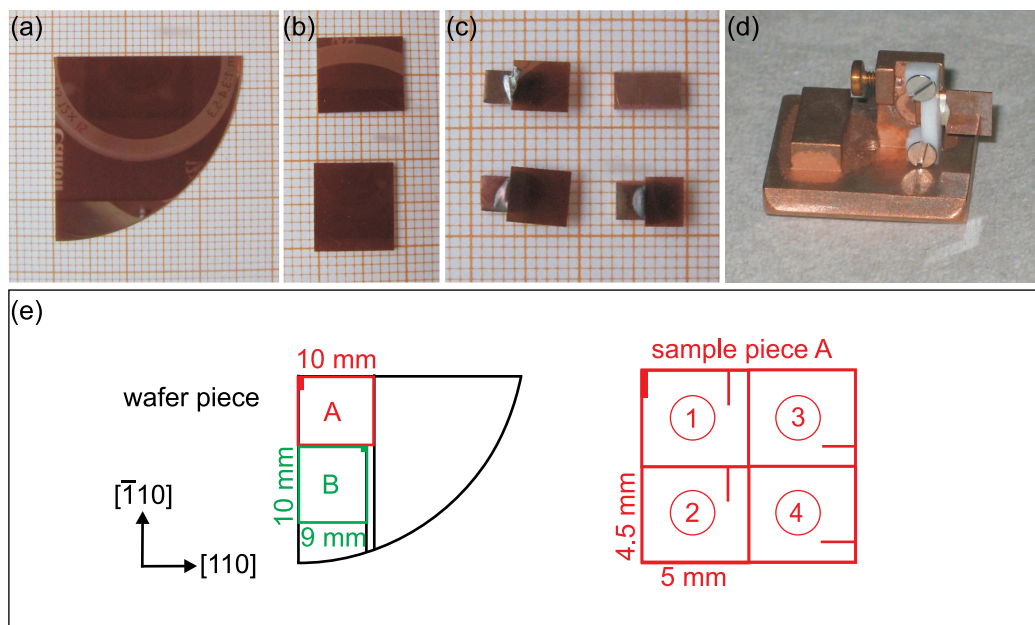


Figure 2.12: Stages of XSTM sample preparation: (a) epitaxially grown sample on 1/4 of a two inch GaP wafer; (b) cut sample pieces for thinning; (c) samples glued on copper plates with Torr Seal + indium (upper left) and with electrically conductive EPO-TEK[®]H20E (lower left) as well as a cleaved sample (lower right) and a copper plate without sample (upper right); (d) sample mounted on XSTM sample holder; (e) schematic of the wafer and sample dimensions and the location of the cuts and notches.

The cleavage of the sample itself takes place within the XSTM chamber, immediately before the measurement series starts. For a better visualization different perspectives into the XSTM chamber are shown in Fig. 2.13. The sample holder is taken by the wobble stick (not shown here) and for cleavage the sample is carefully controlled but resolutely rammed towards the XSTM table. Afterwards the sample holder with the nicely cleaved sample is released on the XSTM table and a tip is positioned opposite to the cleavage surface. The further adjustment of the sample cleavage surface towards

the tip is performed with the piezo motor drive under observation through the optical microscope and the mounted mirrors, before the automatic sample-tip approach can be initiated. After reaching tunneling contact, the measurements usually starts by locating the upper edge of the sample cleavage surface. This is because, although the sample is thinned down to about $150\ \mu\text{m}$, the epitaxial layers of interest are still located in the upper around $2\ \mu\text{m}$ of the sample. For localization of the upper edge the tip is retracted, the sample is electronically moved sideways and the tip is approached again up to tunneling. This procedure is repeated until the tip cannot approach to tunneling, indicating the position where the tip crossed the edge. From that point one can now start the search for the layers of interest.

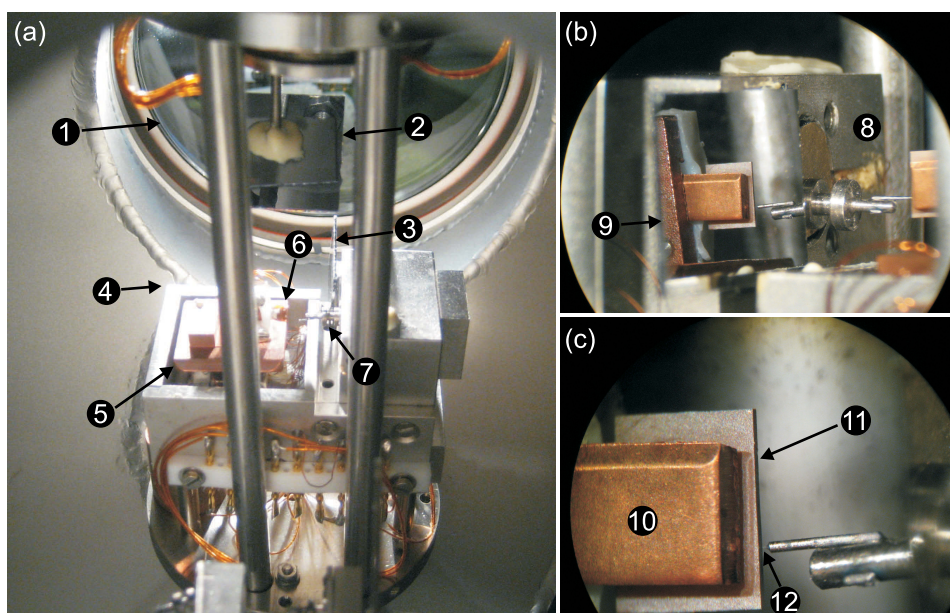


Figure 2.13: Different perspectives after XSTM sample cleavage: (a) View into the XSTM chamber through the backside window: (1) front window for optical microscope observation, (2) upper mirror, (3) side-view mirror, (4) XSTM table position for cleavage, (5) sample holder, (6) cleaved sample, (7) XSTM tip; (b) view through the light microscope onto the sample position: (8) real image, (9) mirror image, and (c) close-view on the side-view mirror image: (10) copper plate, (11) sample cleavage surface, (12) XSTM tip in tunneling contact.

2.2.4 XSTM data evaluation

In Chapters 3, 4, and 5 a lot of XSTM data will be presented. Although most of the data evaluation and interpretation will be understood on the ride, some necessary evaluation methods that will be used are so crucial that a more detailed explanation is needed at some point. For a better understanding these essentials are presented here:

Determination of the quantum dot density

For the analysis of nanostructures like quantum dots the areal density is an important value, both as a pure structural information as well as in terms of potential applications, as the quantum dot density also has an influence on the optoelectronic properties.

In general, one critical issue by analyzing XSTM data is to get 3D information out of data which seems at first glance to be 2D. For the determination of the quantum dot density ρ_{QD} out of the XSTM images, the following formula is used

$$\rho_{\text{QD}} = \frac{4}{5} \frac{N_{\text{QD}}}{L \cdot l_{\text{QD}}}, \quad (2.2)$$

where N_{QD} is the number of detected quantum dots on a total length L of the scanned range along the quantum dot layer direction and l_{QD} is the average quantum dot base length. Here, it is assumed that the quantum dots have a symmetric structure, meaning the base length l_{QD} is approximately equal along both the $[110]$ direction and the $[\bar{1}10]$ direction and that they are homogeneously and statistically distributed at the growth surface. The correction term $\frac{4}{5}$ comes into account as in XSTM images not only quantum dots at the surface are observable as bright contrast. Also those quantum dots which are buried by 25% of their lateral size underneath the cleavage surface can still be observed due to their strain field. So the probing depth of the (X)STM on (cleavage) surfaces for nanostructures or quantum dots is $\frac{5}{4}$ of the lateral size l_{QD} of the nanostructure which needs to be taken into account when calculating areal densities [92, 95].

Determination of the quantum dot growth surface coverage

Another important parameter in terms of a more detailed evaluation of the XSTM data also concerning the analysis of the material distribution within a quantum dot layer is the quantum dot growth surface coverage, which is the percentage of the growth surface area that is covered by the quantum dots.

This growth surface coverage can be derived from the lateral extension L_{QD} and the areal density ρ_{QD} of the quantum dots as follows

$$\text{growth surface coverage} = \rho_{\text{QD}} \cdot (L_{\text{QD}})^2 \quad (2.3)$$

It should be noted that the lateral extension used in this calculation is a slightly reduced quantum dot base length, which would occur when distributing the quantum dot material homogeneously over the whole quantum dot height, i.e. by assuming the quantum dot shape not as a typical truncated pyramid but as a square-based cuboid.

Analysis of the local stoichiometry within quantum dot layers

XSTM data not only enable to determining structural properties of nanostructures like size, shape, and density. Furthermore, also a detailed analysis and quantitative evaluation of the local stoichiometry can provide a deeper insight into the material distribution within epitaxially overgrown layers. Therefore, the so-called local lattice parameter in growth direction, as derived from the XSTM data, is the essential function.

For this purpose, the distance of neighboring atomic chains is determined within a selected area of a highly-resolved XSTM image. This is performed by the following procedure, as also illustrated in Fig. 2.14: (a,b) for the selected area an averaged overall height profile of the data is taken. As only the undulations of the curve are essential here, the background of the curve, which is related to the strain induced outward relaxation of the material, is fitted and subtracted to get the atomic corrugation profile. (c) The resulting difference curve then represents the atomic chain positions and can now be used to determine the chain-to-chain-distance, by fitting every positive peak of the curve with a Gaussian profile followed by subtracting neighboring peak center positions from each other. (d) The plot of these values for the local lattice parameter finally has to be calibrated by a linear fit to the known lattice parameter of the matrix material surrounding the strained layers, which in this work is GaP with a nominal value of 5.451 Å. (e) In the final graph the local lattice parameter is plotted versus the position along growth direction and can now be compared with calculated reference values for the stoichiometric composition (see next paragraph).

This procedure was originally used to analyze XSTM data of (In,Ga)As quantum dot layers in a GaAs matrix (e.g. Refs. [45, 101]). As such a powerful tool, this procedure was continuously improved and modified which also led to the Mathematica based data evaluation software tool, programmed and thankfully provided by Dr. Ernst Lenz, formerly TU Berlin, which was used for the XSTM data analysis during this work [102].

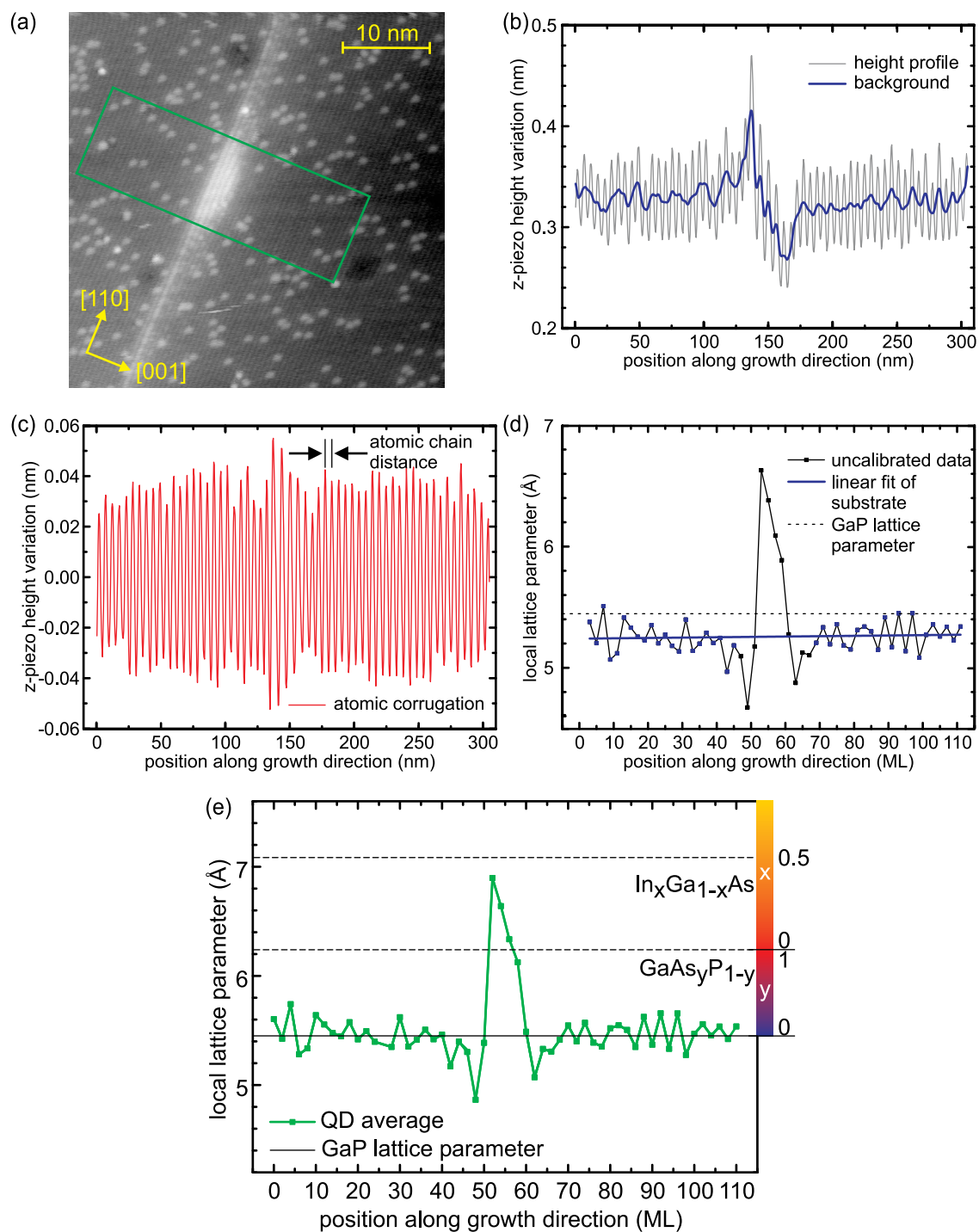


Figure 2.14: Illustration of the analysis of the local stoichiometry for an $(\text{In,Ga})\text{As}$ quantum dot in a GaP matrix (example taken from Section 3.3.3 Fig. 3.28). (a) Filled-state XSTM image of a quantum dot with the evaluated region highlighted by the colored box; (b) height profile of the evaluated region (grey) and smoothed background (blue), (c) atomic corrugation profile, (d) resulting uncalibrated profile for the atomic chain distance/local lattice parameter (black) with linear fit in the GaP substrate areas (blue), (e) final calibrated graph for the local lattice parameter and the related stoichiometric composition along growth direction.

The local lattice parameter for (In,Ga)(As,P)/GaP and (In,Ga)(Sb,As)/GaP

For a further quantitative analysis of the local stoichiometry within the quantum dot layers the values for the local lattice parameter determined from the XSTM data need to be compared with reference values. These reference values were calculated by Prof. Dr. Holger Eisele, TU Berlin, by using continuum-mechanical strain-relaxation calculations on a biaxially strained system for Ga(As,P), (In,Ga)P, (In,Ga)As, Ga(Sb,P), and (In,Ga)Sb layers of different composition within a GaP matrix [103], in analogy to former simulations for the (In,Ga)As/GaAs [45, 48, 49, 95, 101, 104] and the GaSb/GaAs systems [105–108] (and also later for the tensile-strained GaAs/GaSb system [109]). The resulting values are listed in Tab. 2.2.

Furthermore a two-dimensional color-coded contour plot, shown in Fig. 2.15, was created by E. Lenz and modified by the author using these calculations to map the local lattice parameter for different material compositions of (In,Ga)(As,P) and (In,Ga)(Sb,As) layers on a GaP substrate [110]. Therefore the deduced values as listed in Tab. 2.2 were used as corner values and starting points to, as an approximation, apply a two-dimensional linear fit of the local lattice parameter.

For the (In,Ga)(As,P)/GaP system only the lower half of the plot is relevant. Starting from the lower left corner with the GaP bulk lattice constant of 5.451 Å the x -axis represents the continuous change in the group-III component from gallium to indium, i.e. $\text{In}_x\text{Ga}_{1-x}\text{P}/\text{GaP}$ with x ranging from 0 to 1, while the y -axis represents the continuous change in the group-V component from phosphorus to arsenic, i.e. $\text{GaAs}_y\text{P}_{1-y}/\text{GaP}$ with y ranging from 0 to 1, changing the local lattice parameter to the calculated values of 6.241 Å for pure GaAs on GaP and 7.182 Å for pure InP on GaP. To complete the lower half of the map the axes for $\text{In}_x\text{Ga}_{1-x}\text{As}/\text{GaP}$ and $\text{InAs}_y\text{P}_{1-y}/\text{GaP}$, both ranging up to the value of pure InAs on GaP of 7.930 Å, were added. The resulting equidistant contour lines represent identical values for the local lattice parameter matching different compositions of quaternary $\text{In}_x\text{Ga}_{1-x}\text{As}_y\text{P}_{1-y}$ material on GaP.

The upper half of the plot is arranged analogously and attached by further changing the group-V component from arsenic to antimony, leading to a map of the local lattice parameter for quaternary $\text{In}_x\text{Ga}_{1-x}\text{Sb}_y\text{As}_{1-y}$ material on GaP.

These maps now give the chance to allocate experimentally determined evaluated local lattice parameters from XSTM data to possible matching material compositions of III-V layers on GaP.

Table 2.2: Calculated reference values for the local lattice parameter along the [001] direction for different III-V compound semiconductor layers on a GaP substrate [103] and deduced resulting values.

Calculated values for the local lattice parameter (in Å) from [103]										
GaP	GaAs/GaP		InP/GaP		InAs/GaP		GaSb/GaP		InSb/GaP	
	50%	100%	50%	100%	50%	100%	50%	100%	50%	100%
	1 ML	2 ML	1 ML	2 ML	1 ML	2 ML	1 ML	2 ML	1 ML	2 ML
5.451	5.846	6.241	6.316	7.182	6.693	7.930	6.712	7.974	7.557	9.664

Deduced resulting values for the local lattice parameter (in Å) as plotted in Fig. 2.15							
y	GaAs _y P _{1-y} /GaP			GaSb _y As _{1-y} /GaP			
	0.0	0.5	1.0	0.0	0.5	1.0	
	5.451	5.846	6.241	6.241	7.108	7.974	
y	InAs _y P _{1-y} /GaP			InSb _y As _{1-y} /GaP			
	0.0	0.5	1.0	0.0	0.5	1.0	
	7.182	7.556	7.930	7.930	8.797	9.664	

x	In _x Ga _{1-x} P/GaP			In _x Ga _{1-x} As/GaP		
	0.0	0.5	1.0	0.0	0.5	1.0
	5.451	6.316	7.182	6.241	7.085	7.930
x	In _x Ga _{1-x} Sb/GaP					
	0.0	0.5	1.0			
	7.974	8.819	9.664			

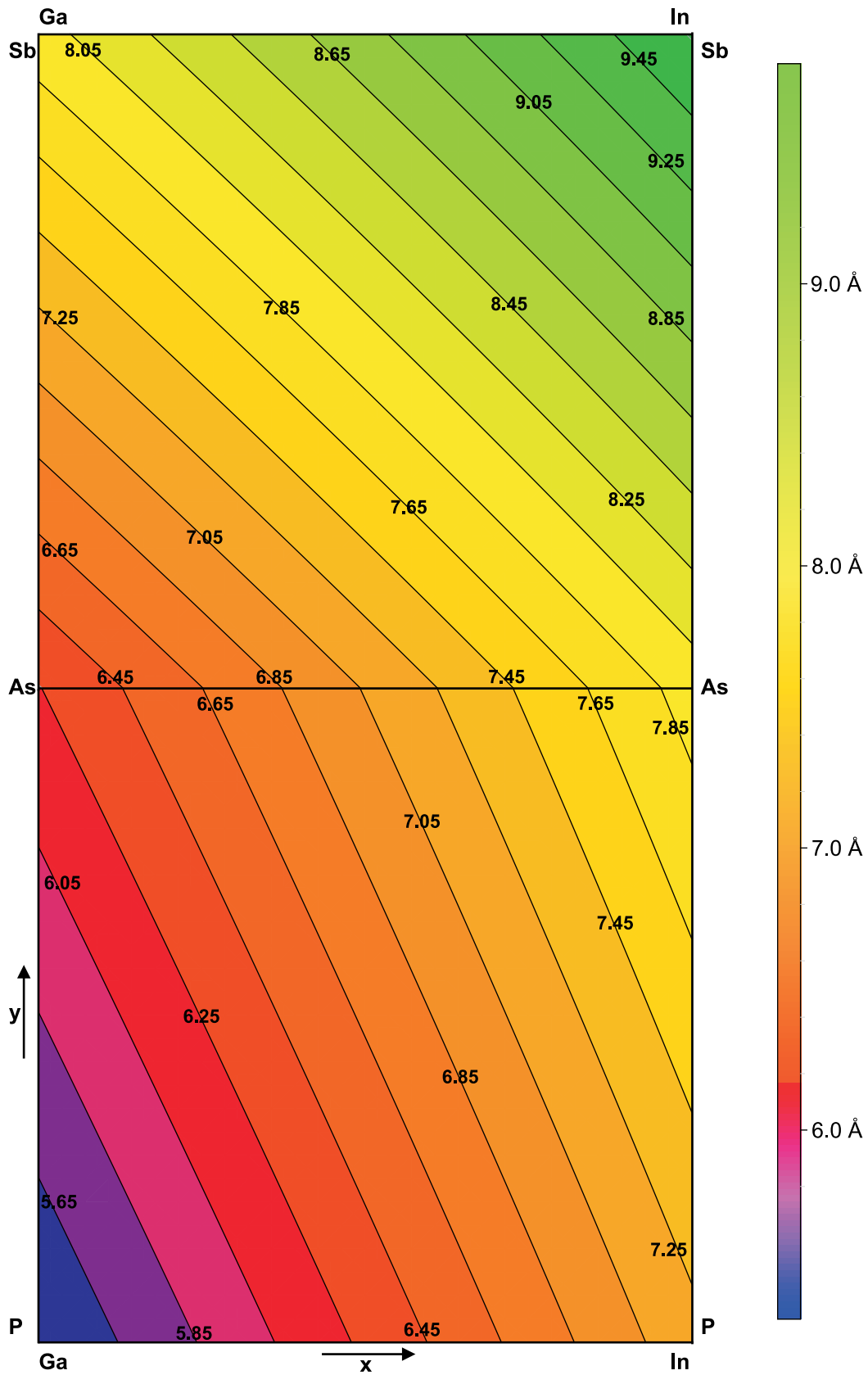


Figure 2.15: Two-dimensional color-coded plot of the local lattice parameter (in Å) for $\text{In}_x\text{Ga}_{1-x}\text{As}_y\text{P}_{1-y}$ and $\text{In}_x\text{Ga}_{1-x}\text{Sb}_y\text{As}_{1-y}$ layers on a GaP substrate, adapted from [110].

Chapter 3

(In,Ga)As/GaP Quantum Dots grown by MOVPE

The samples for the XSTM investigations presented in this chapter were all grown with metal-organic vapor-phase epitaxy (MOVPE) by Gernot Stracke in the workgroup of Prof. Dr. D. Bimberg at the TU Berlin.

3.1 First XSTM investigations on (In,Ga)As Quantum Dots in a GaP matrix

3.1.1 Sample structure

Based on the results of several growth experiments on (In,Ga)As/GaP by G. Stracke [55], the first sample containing (In,Ga)As quantum dots in a GaP matrix especially designed for XSTM investigations was fabricated. A schematic of the structure of this sample (TU9675) is shown in Fig. 3.1 (a). On a *p*-doped GaP(001) substrate a 500 nm thick buffer layer of *p*-doped GaP was grown at 750 °C to improve crystal quality and surface roughness, before a 50 nm thick undoped GaP layer was grown at 750 °C. The quantum dot layer starts with 3.0 ML GaAs followed by 2.5 ML of In_{0.25}Ga_{0.75}As and a growth interruption of 1 s, all at 490 °C. The GaAs interlayer deposited prior to the In_{0.25}Ga_{0.75}As layer was used to induce the Stranski-Krastanow growth mode, leading to quantum dot formation [55]. The quantum dots were capped with a 50 nm thick undoped GaP layer, with the initial 6 nm grown at 490 °C and the following 44 nm grown at 600 °C. A 10-fold superlattice of 2.0 ML GaAs and 10 nm GaP was grown on top at 600 °C. The latter serves primarily as marker layer in the XSTM experiment but also gives the opportunity to study the initial growth of pure GaAs layers in GaP

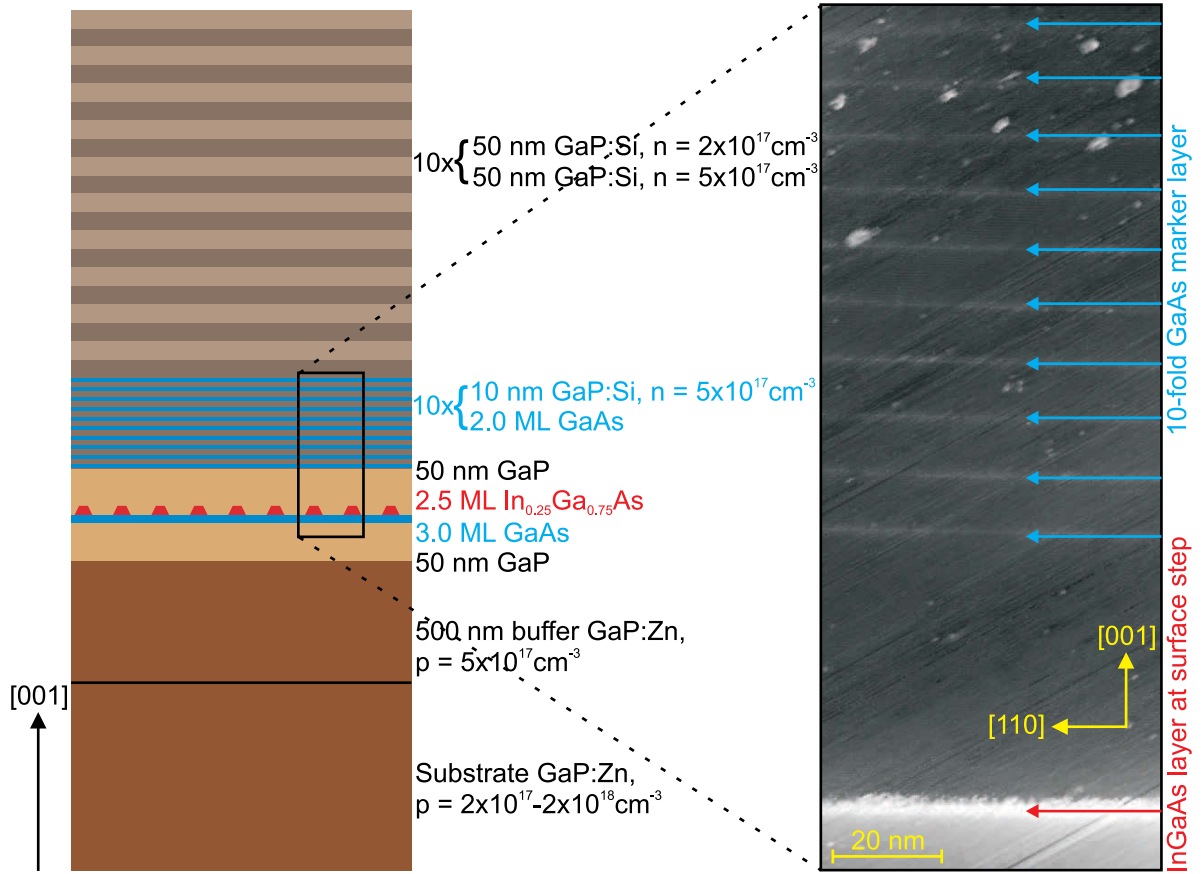


Figure 3.1: (a) Schematic of the structure of sample TU9675 and (b) corresponding filled-state XSTM overview image taken at a sample voltage $V_T = -3.2$ V and a tunneling current $I_T = 70$ pA.

separately without the influence of further (In,Ga)As deposition. The sample then got a final capping consisting of 20 alternately n -doped 50 nm thick GaP layers, each grown at 600 °C, resulting in a total GaP cap thickness of 1 μm .

3.1.2 XSTM results

A first filled-state XSTM overview image across the $(\bar{1}10)$ cleavage surface is shown in Fig. 3.2. Although this first image is characterized by scan artifacts and adatoms on the surface, one can already identify a 10-fold stack of parallel bright lines in the center of the image and an even brighter appearing surface step lying below this stack. Figure 3.1 (b) shows a closer view of this area. It is found that the thin bright lines of the 10-fold stack are equidistant along the $[001]$ direction with distances of around 10 nm, and therewith they have to be related to the GaAs marker layer. For details on the GaAs layers see Chapter 5.

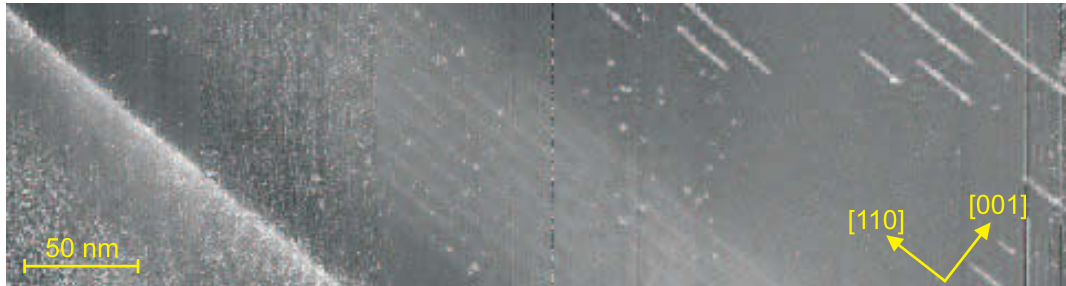


Figure 3.2: Filled-state XSTM overview image. The image was taken at a sample voltage $V_T = -3.3$ V and a tunneling current $I_T = 70$ pA.

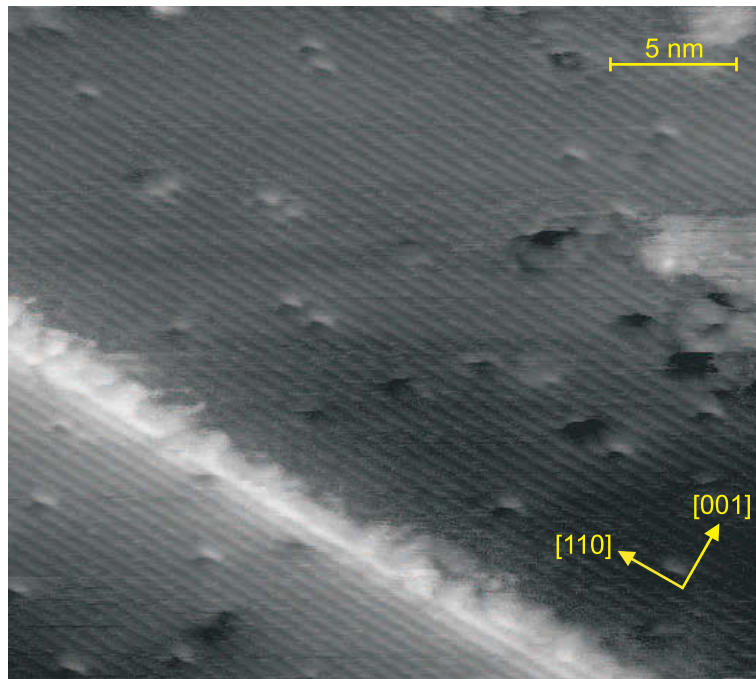


Figure 3.3: Filled-state XSTM image of the $\text{In}_{0.25}\text{Ga}_{0.75}\text{As}/\text{GaAs}$ layer located at a surface step. The image was taken at a sample voltage $V_T = -2.8$ V and a tunneling current $I_T = 70$ pA.

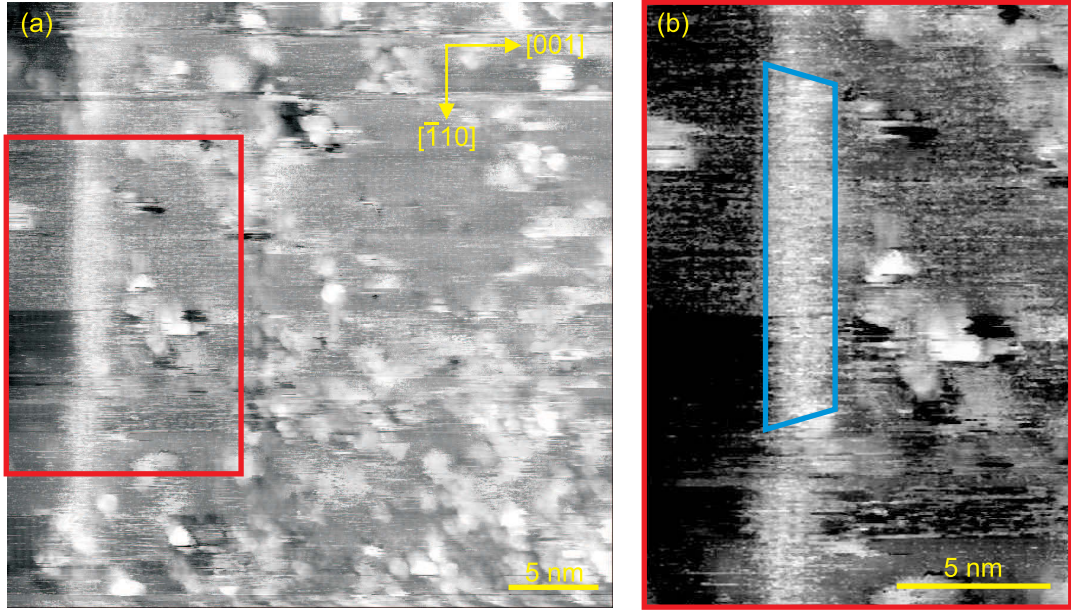


Figure 3.4: Filled-state XSTM image of the $\text{In}_{0.25}\text{Ga}_{0.75}\text{As}/\text{GaAs}$ layer, taken at a sample voltage $V_T = -3.5$ V and a tunneling current $I_T = 40$ pA. (a) shows the whole image with an intermediate contrast. (b) shows a close-up on the red box with the contrast being adjusted to the $\text{In}_{0.25}\text{Ga}_{0.75}\text{As}/\text{GaAs}$ layer to identify a quantum dot (highlighted by the blue trapezoid).

The bright appearance of the surface step and its distance to the GaAs layers of about 50 nm indicates that the $\text{In}_{0.25}\text{Ga}_{0.75}\text{As}/\text{GaAs}$ layer is located directly at this cleavage induced surface step. A closer high-resolved image of this area is shown in Fig. 3.3. The atomic chains are clearly visible along the $[110]$ direction. On the surface step 2–3 atomic chains show a bright contrast, which would refer to 4–6 ML of (In,Ga)As material being in accordance with the nominally distributed total material amount of 5.5 ML (3.0 ML GaAs + 2.5 ML $\text{In}_{0.25}\text{Ga}_{0.75}\text{As}$) inside the $\text{In}_{0.25}\text{Ga}_{0.75}\text{As}/\text{GaAs}$ layer. Since the surface step lies directly on the $\text{In}_{0.25}\text{Ga}_{0.75}\text{As}/\text{GaAs}$ layer across the whole scanned area and due to the fact that the step does not appear very sharp, the inner structure of the $\text{In}_{0.25}\text{Ga}_{0.75}\text{As}/\text{GaAs}$ layer could not be revealed at this first experiment. The GaP itself shows features like adatoms and holes, which will turn out to be typical for XSTM experiments on GaP material and are due to the scanning process itself.

Figure 3.4 (a) again shows a high-resolution image of the $\text{In}_{0.25}\text{Ga}_{0.75}\text{As}/\text{GaAs}$ layer, this time on the (110) cleavage surface and without a surface step. Although this image is characterized by several scanning artifacts, it shows that the $\text{In}_{0.25}\text{Ga}_{0.75}\text{As}/\text{GaAs}$ layer has an inhomogeneous structural behavior. The thickness of the layer varies so that agglomerations inside the layer can be identified. The marked area of Fig. 3.4 (a)

is magnified in Fig. 3.4 (b) to reveal that these agglomerations are related to the expected Stranski-Krastanow growth mode. The islands can be supposed to have the shape of a truncated pyramid (highlighted by the blue lines), which is typical for quantum dots in other III-V material systems like InAs/GaAs [45, 47, 91, 101, 111]. Despite the lacking image quality over the whole scanned area, a statistical analysis of the identified quantum dot-like islands was raised. A total number of 26 islands within different areas could be identified where the sum of the analyzed scanned range along the layers amounts to about 1650 nm. Here, the observed islands show dimensions of 11–18 nm in base length and 8–10 ML in height. Using Equation (2.2) the areal density of these quantum dots was determined to be about $7\text{--}8 \times 10^{10} \text{ cm}^{-2}$.

3.2 In_{0.25}Ga_{0.75}As/GaAs Quantum Dots in GaP

3.2.1 Sample structure

Based on the first experiences with XSTM on (In,Ga)As nanostructures in GaP and further improvements in the MOVPE growth of these structures, a new XSTM sample setup was designed, which is shown in Fig. 3.5. This sample (TU10350) was grown on a *n*-doped GaP(001) substrate starting with a 500 nm thick buffer layer of *n*-doped GaP and 50 nm of undoped GaP, with both layers grown at 750 °C. The following stack contains three (In,Ga)As/GaAs layers grown at 500 °C, each consisting of nominally 3.0 ML GaAs followed by 2.0 ML of In_{0.25}Ga_{0.75}As and a growth interruption of 10 s. The GaAs layer deposited prior to the In_{0.25}Ga_{0.75}As layer again was used to induce the Stranski-Krastanow growth mode, leading to quantum dot formation [55]. The three In_{0.25}Ga_{0.75}As/GaAs layers are separated from each other by 50 nm undoped GaP to prevent strain-induced alignment, where the initial 6 nm of GaP were grown at 490 °C and the following 44 nm at 600 °C. Finally, a marker layer consisting of a 10-fold superlattice of 2.0 ML GaAs and 10 nm *p*-doped GaP and a final cap of 1 μm of *p*-doped GaP with alternating doping concentration was grown on top at 600 °C.

3.2.2 XSTM results: image contrast analysis

Figure 3.6 shows a filled-state XSTM overview image across the (110) cleavage surface. In the right half of the image four bright stripes can be identified, which lie parallel to the (001) growth surface and are equidistantly separated by spacers of about 50 nm. The three lower and brighter stripes can be considered as the In_{0.25}Ga_{0.75}As/GaAs layers, while the slightly darker contrast of the fourth stripe refers to the first of the ten thin GaAs layers. As already observed in the previous sample (see Section 3.1) surface steps frequently form during the cleavage process at or near the (In,Ga)As layers due to the higher strain inside the layers. In this cleavage two monoatomic surface steps near the first of the three In_{0.25}Ga_{0.75}As/GaAs layers are present, one of them lying directly at the layer which makes a detailed investigation of this layer again difficult. Nevertheless, from Fig. 3.6 one can already observe that the contrast in each of the three In_{0.25}Ga_{0.75}As/GaAs layers is not homogeneous along the $[1\bar{1}0]$ direction. Instead, regions of brighter contrast are visible, which already indicates an island formation during growth.

In Fig. 3.7 a closer view of one of the In_{0.25}Ga_{0.75}As/GaAs layers in its GaP environment is shown. Due to the good resolution the atomic chains are visible along the $[1\bar{1}0]$ direction. Here, the GaP surface is again characterized by many bright spots,

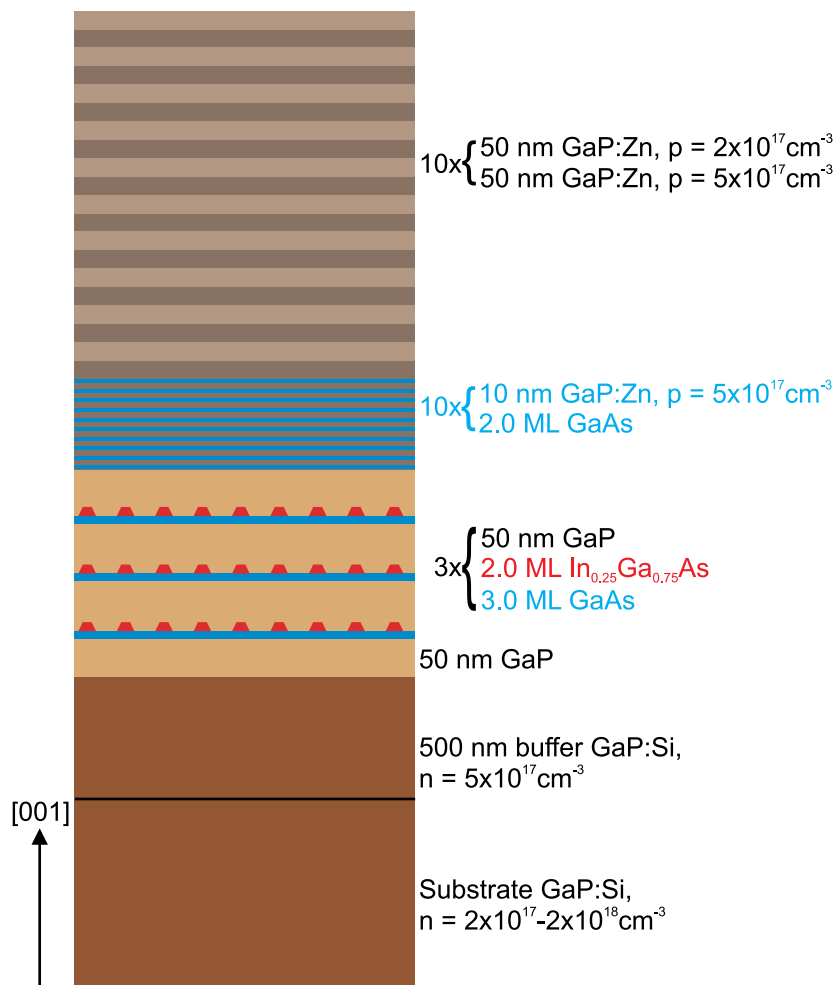


Figure 3.5: Schematic of the structure of sample TU10350.

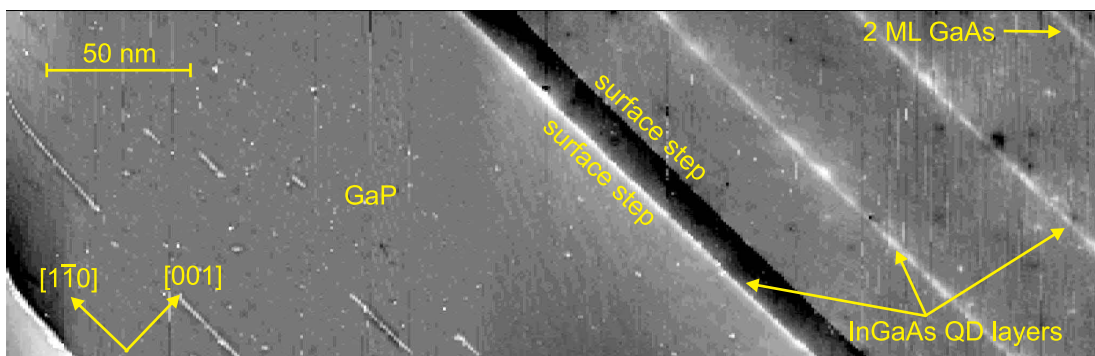


Figure 3.6: Filled-state XSTM overview image showing the three $\text{In}_{0.25}\text{Ga}_{0.75}\text{As}/\text{GaAs}$ layers as well as one of the GaAs layers in the GaP matrix. In addition two monoatomic surface steps are visible, one very close to the first (In,Ga)As QD layer. The image was taken at a sample voltage $V_T = -2.5 \text{ V}$ and a tunneling current $I_T = 50 \text{ pA}$.

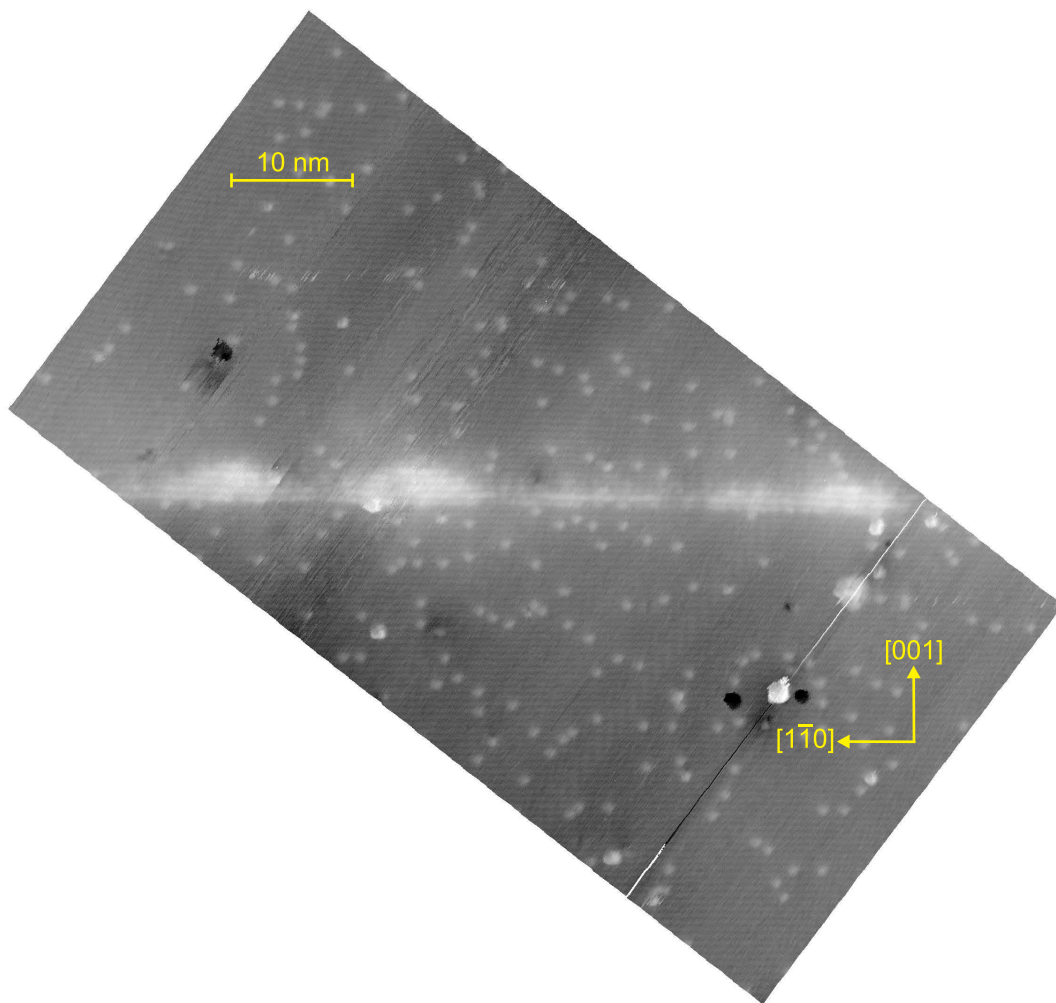


Figure 3.7: Filled-state XSTM images showing one of the three $\text{In}_{0.25}\text{Ga}_{0.75}\text{As}/\text{GaAs}$ layers (layer 2) and the surrounding GaP matrix. The images were taken at a sample voltage $V_T = -3.0$ V and a tunneling current $I_T = 30$ pA.

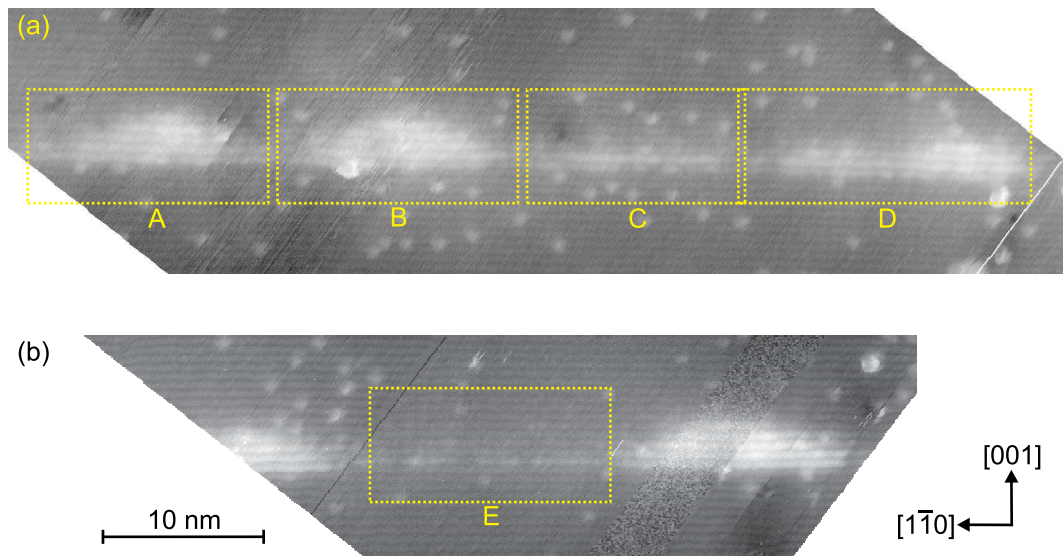


Figure 3.8: Filled-state XSTM image showing one of the three $\text{In}_{0.25}\text{Ga}_{0.75}\text{As}/\text{GaAs}$ layers (layer 2). The image was taken at a sample voltage $V_T = -3.0$ V and a tunneling current $I_T = 30$ pA.

which occur during scanning and whose number increases when repeating the scanning across the same area. They are supposed to be due to phosphorus adatoms pulled out of the cleavage surface during the scanning process [112]. The inhomogeneity of the contrast in the $\text{In}_{0.25}\text{Ga}_{0.75}\text{As}/\text{GaAs}$ layer clearly reveals the three-dimensional formation of nanostructures during growth, as pronounced islands of brighter contrast are visible.

In order to investigate the kind of growth mechanism, a closer investigation of this layer has to be performed. Figure 3.8 (a,b), again taken in filled-state mode, reveals several different kinds of appearances within the $\text{In}_{0.25}\text{Ga}_{0.75}\text{As}/\text{GaAs}$ layer. Trapezoidal-shape like islands of bright contrast (like in regions A and B), darker islands (C) and two closely neighboring/overlapping islands (D) can be observed. In between all of these kinds of nanostructures, regions with an intermediate contrast, as compared with the dark appearing GaP matrix and the bright islands, are found (E). This intermediate contrast is related to a thin wetting layer. Also rare empty-state images like in Fig. 3.9 show the same behavior of islands within a wetting layer. These structural findings again indicate a Stranski-Krastanow growth mode for the investigated $(\text{In,Ga})\text{As}/\text{GaAs}/\text{GaP}$ system.

For this sample a statistical analysis of the nanostructure occurrence across several XSTM overview images leads to a determined areal density of about $2.4 \times 10^{11} \text{ cm}^{-2}$ for the nanostructures. In total 15 highly-resolved nanostructures were analyzed on a scanned range along the layers direction of about 320 nm.

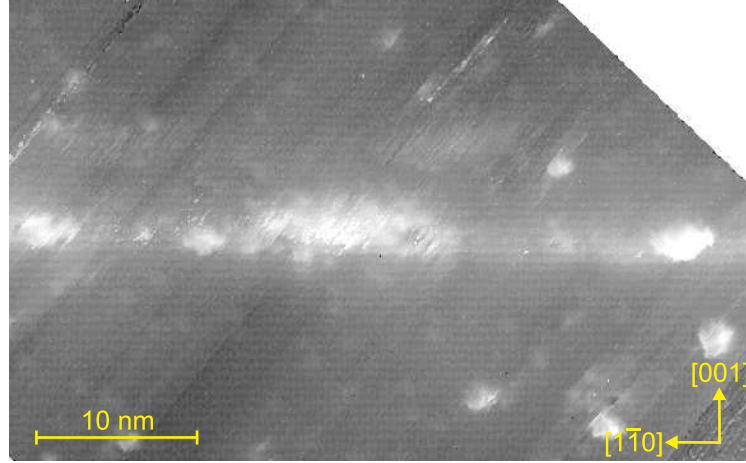


Figure 3.9: Empty-state XSTM image showing one of the three $\text{In}_{0.25}\text{Ga}_{0.75}\text{As}/\text{GaAs}$ layers (layer 2). As rarely observed this image shows atomic resolution along both the $[\bar{1}10]$ and the $[001]$ direction, at least on the GaP matrix material. The image was taken at a sample voltage $V_T = +3.0$ V and a tunneling current $I_T = 50$ pA.

In the following the occurring nanostructures are investigated in more detail: Figure 3.10 shows high-resolution filled-state XSTM images of two different single nanostructures. In Fig. 3.10 (a,c) a typical island with a trapezoidal cross section, as highlighted by the solid lines in Fig. 3.10 (c), is shown. Hence, these quantum dots are considered to have a truncated pyramidal shape. Such a truncated pyramidal shape is typical for capped quantum dots and was already found for other material systems like InAs/GaAs [45, 47, 91, 101, 111]. In the present case of the $\text{In}_{0.25}\text{Ga}_{0.75}\text{As}/\text{GaAs}/\text{GaP}$ material system the average quantum-dot base length is found to be 12 nm, while quantum-dot heights up to 10 ML are observed.

A closer look at Fig. 3.10 (a,c) also yields a non-uniform contrast within the quantum dots. The dot center is characterized by a significantly brighter contrast than the dot sides. Furthermore, the width of the region with bright contrast is narrowest at the quantum dot base and broader towards its top. Thus, the area of brighter contrast has the shape of a reversed truncated cone as highlighted by the dashed lines in Fig. 3.10 (c). This contrast is caused by a higher indium content at the center as compared with the outer parts of the quantum dot. Such a stoichiometry profile has already been observed for (In,Ga)As quantum dots in a GaAs matrix [45, 113].

Larger nanostructures as shown in Fig. 3.10 (b,d) are also observed for which two smaller trapezoidal cross sections appear very close to each other or even overlap. This kind of appearance was already occasionally observed in experiments growing (In,Ga)As on GaAs [45] but more frequently for GaSb on GaAs [107]. Such a cross-sectional shape is obtained by cleaving through so-called quantum rings [107]. Since the

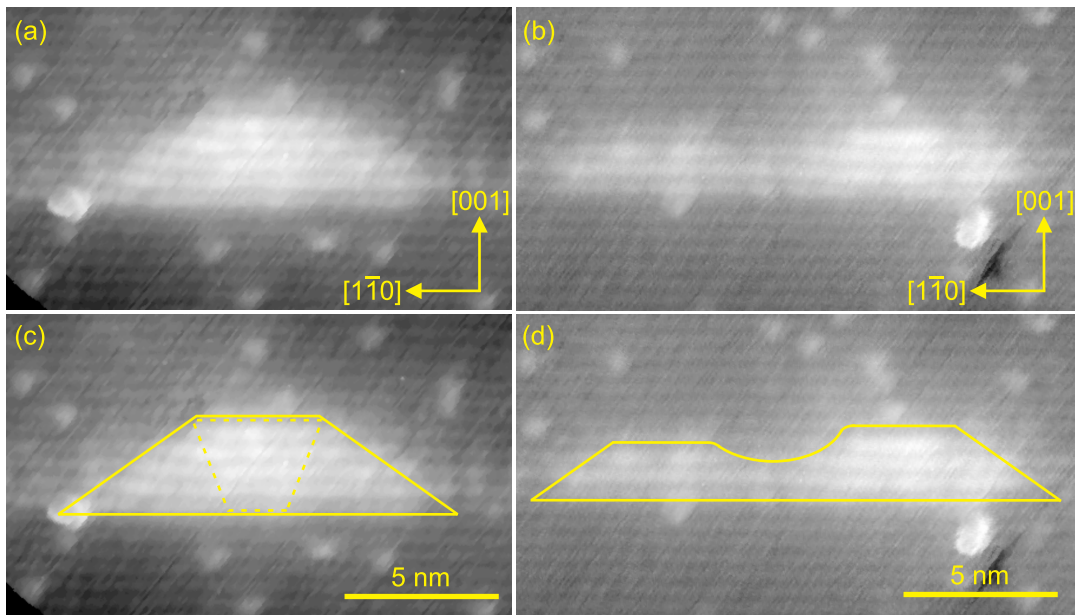


Figure 3.10: Filled-state XSTM images of (a,c) a quantum dot and (b,d) a quantum ring. The images were taken at a sample voltage $V_T = -3.0$ V and a tunneling current $I_T = 30$ pA. The contours of the nanostructures are marked by the solid lines. The dashed line in (c) marks the indium-rich area.

cleavage through the quantum rings occurs at an arbitrary position, their appearance in XSTM experiments may vary between a double structure for more central cleavages and a single structure—being equivalent to the cross-section of a quantum dot—for a cleavage near the side of the quantum ring. Here, the quantum rings show average total base lengths of 21 nm with heights up to 9 ML. Hence, the larger quantum dots transform into quantum rings during growth [107] or capping [45, 114]. The similar contrast of quantum dots and rings indicates a comparable chemical composition.

The object shown in Fig. 3.11 (a,c) is characterized by a darker contrast than the quantum dots and rings described before. Moreover, its extension along the [001] direction is much smaller, but still a trapezoidal shape can be assumed, as highlighted by the dashed lines in Fig. 3.11 (c). Hence, this object can be assumed also to be a quantum dot, which was cleaved very close to its side. Then, to be more precise, the quantum dot was either almost completely cut off during cleavage or it is almost completely buried under the cleavage surface. Here, the latter case is more likely when regarding the brightness of the quantum dot, indicating a considerable amount of strained material underneath the surface. A further proof that this indeed is a quantum dot will be given in Section 3.2.3 by analyzing the local lattice parameter in this region.

In Fig. 3.11 (b,d) an XSTM filled-state image of a wetting-layer region in between two quantum dots is shown. The wetting layer has heights between 2 and 6 ML and

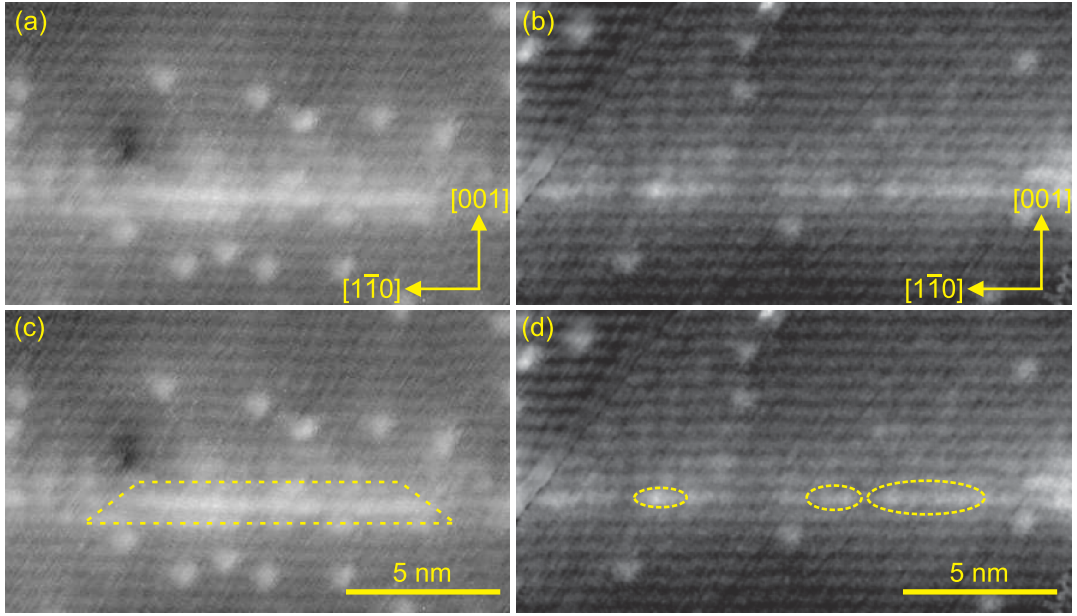


Figure 3.11: Filled-state XSTM images of (a,c) a quantum dot almost buried under the cleavage plane and (b,d) a wetting layer region. The images were taken at a sample voltage $V_T = -3.0$ V and a tunneling current $I_T = 30$ pA. The dashed line in (c) marks the position of the almost buried quantum dot. In (d) arsenic-rich regions with brighter contrast are marked by yellow ovals.

also shows an inhomogeneous contrast, but weaker than the one for the quantum dots. Since the image is measured in filled-state mode, corresponding to negative sample bias, the image contrast is mostly sensitive to the group-V sublattice with darker phosphorus and brighter arsenic atoms. The contrast is characterized by the appearance of regions with two different brightnesses allowing to distinguish between phosphorus-rich and arsenic-rich regions inside the wetting layer. The latter ones are marked exemplarily by ovals in Fig. 3.11 (d). The rather homogeneous brightness within these regions may also indicate the absence of indium within the wetting layer.

3.2.3 XSTM results: stoichiometry analysis

For a quantitative evaluation of the XSTM data the local stoichiometry, i.e. the local material composition and distribution, for different regions in the $\text{In}_{0.25}\text{Ga}_{0.75}\text{As}/\text{GaAs}$ layers is analyzed by evaluating the local lattice parameter (as described in Section 2.2.4).

Wetting layer Figure 3.12 shows data for a wetting-layer region of the $\text{In}_{0.25}\text{Ga}_{0.75}\text{As}/\text{GaAs}$ layer. In Fig. 3.12 (b) the local lattice parameter for the selected wetting-layer region is averaged perpendicular to the growth direction over about 5 nm, as high-

lighted by the green box in Fig. 3.12 (a). The local lattice parameter underneath and above the wetting layer is normalized to the value of the GaP bulk lattice constant of 5.451 Å. The slight variation is of statistical origin, e.g. due to scanning artifacts or adatoms at the surface. In the area of the wetting layer the local lattice parameter increases considerably due to the change in material composition. Moreover, the compressive strain originating from the lattice mismatch leads to a relaxation along growth direction (biaxial strain), further increasing the local lattice parameter. The small undershoot before the (In,Ga)As/GaAs deposition in the graph of Fig. 3.12 (b) is characteristic for an inhomogeneity of the wetting-layer composition, as already observed above in Fig. 3.11 (b,d). The local lattice parameter is found to be increased in a 2–3 ML wide region, in good agreement with the visual appearance of the wetting layer in the XSTM image showing local heights of 2–6 ML in growth direction.

For a quantitative analysis of the local stoichiometry, the reference values for the local lattice parameter for Ga(As,P) layers of different composition within a GaP matrix were taken into account (see Section 2.2.4). The resulting relation between the local lattice parameter and the arsenic content is shown by the scale bar on the right side in Fig. 3.12 (b). The measured local lattice parameter increases roughly up to the calculated value for pure GaAs embedded in GaP, again supporting the assumption that no indium is present within the wetting layer.

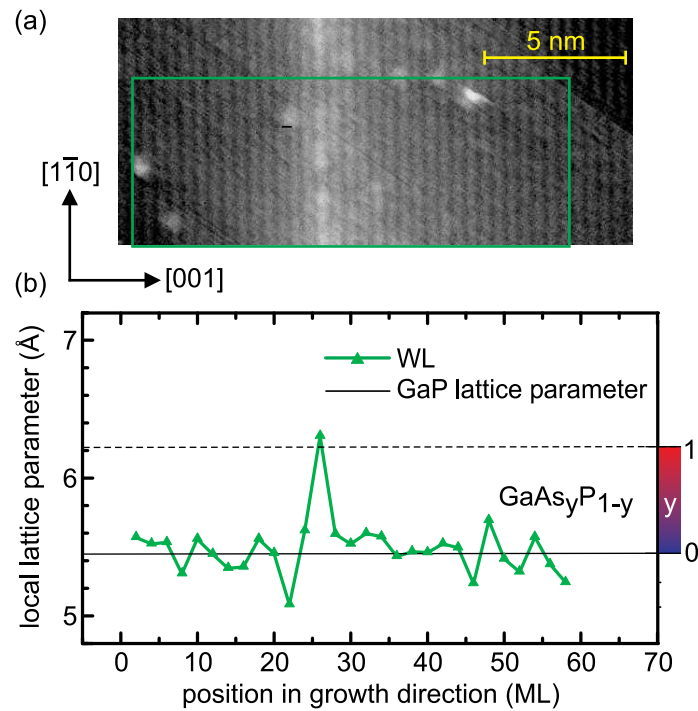


Figure 3.12: (a) Filled-state XSTM image of the wetting layer region, taken at $V_T = -3.0$ V and $I_T = 30$ pA. (b) Evaluation of the local lattice parameter along growth direction within the green box in (a). The local lattice parameter is related to the local arsenic concentration. The right scale bar and the dashed line in (b) indicate the calculated values for the local lattice parameter for strained $\text{GaAs}_y\text{P}_{1-y}$ layers in a GaP matrix.

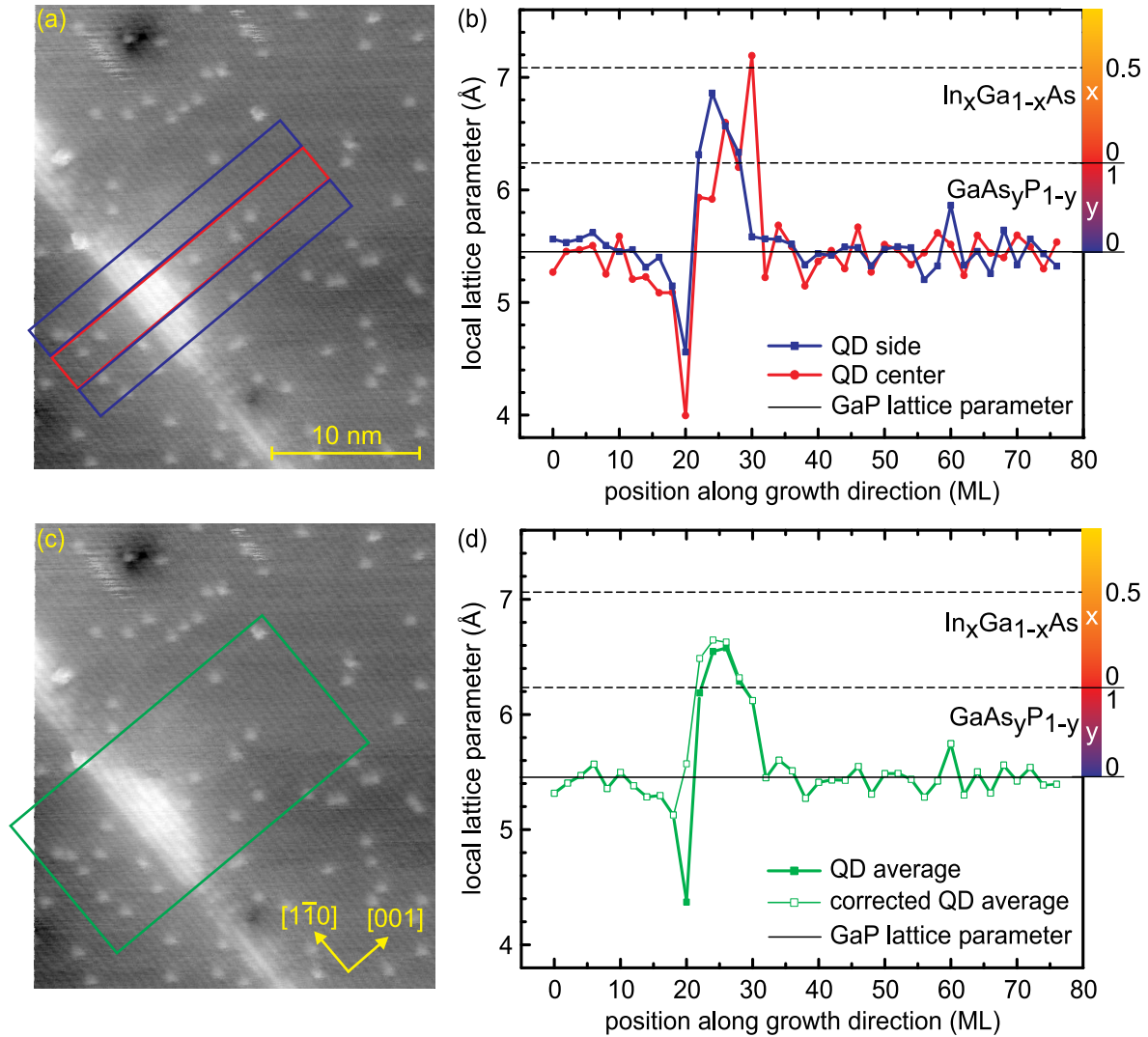


Figure 3.13: (a,c) Filled-state XSTM image of a representative quantum dot. The evaluated regions are highlighted by the colored boxes. The image was taken at $V_T = -3.0$ V and $I_T = 30$ pA. (b,d) Corresponding evaluation of the local lattice parameter and the related stoichiometric composition along growth direction. The graphs show the evaluated data (b) for the quantum-dot center in red dots and for the quantum-dot sides in blue squares and (d) averaged over the entire quantum dot region in filled green squares and the corrected data in open green squares. For the latter the compression around the quantum dot base is taken into account. The right scale bars and the dashed lines in the graphs indicate the calculated values for the local lattice parameter for strained $\text{GaAs}_y\text{P}_{1-y}$ and $\text{In}_x\text{Ga}_{1-x}\text{As}$ layers in a GaP matrix.

Quantum dots Figure 3.13 shows stoichiometry profiles for the well-resolved quantum dot, which was already discussed in Fig. 3.10 (a,c). This quantum dot has been analyzed in different parts: the quantum-dot center, sides, and also the entire dot. Figure 3.13 (b) shows the two graphs of the local lattice parameter corresponding to the data derived at the quantum-dot center and at the quantum-dot sides, as highlighted by the red and blue boxes in the XSTM image in Fig. 3.13 (a).

The local lattice parameter at the quantum-dot center is found to be much higher at the top of the quantum dot than at its base. This is in agreement with the already discussed reversed-cone stoichiometry profile of the quantum dot obtained by visual inspection of the XSTM image contrast in Fig. 3.10 (a,c). In Fig. 3.13 (d) the profile of the local lattice parameter averaged over the entire quantum dot area is shown as highlighted by the green box in Fig. 3.13 (c). The local lattice parameter is compressed underneath the quantum dot and rises to comparably high values within the quantum dot, exceeding the value of GaAs in GaP. This proves the incorporation of indium within the quantum dots during growth. Also the undershoot below the GaP lattice parameter is much larger as compared with the case of the wetting layer [Fig. 3.12 (b)], indicating a stronger compression of the material directly underneath the quantum dot as well as at the quantum dot base, as compared with the weak compression due to the stoichiometry fluctuations within the wetting layer. Taking this compression into account, the curve can be locally corrected as shown by the open green squares in Fig. 3.13 (d), in order to reflect the actual material content within the quantum dot.

As already discussed, the filled-state XSTM image contrast for the quantum dots is characterized by a much softer variation compared to the wetting layer. Therefore, one can assume that no phosphorus is present within the quantum dots, which then consist of pure (In,Ga)As. From the local lattice parameter now the indium content within the (In,Ga)As quantum dots can be derived, as illustrated by the upper scale bars on the right sides in Fig. 3.13 (b,d) and subsequent figures, where as an approximation the value for the local lattice parameter of $\text{In}_{0,0}\text{Ga}_{1,0}\text{As}$ (calculated for (In,Ga)As on GaP) is set as the value for $\text{GaAs}_{1,0}\text{P}_{0,0}$ (see also Section 2.2.4). For the quantum dot in Fig. 3.13 (a,c) it is found that the average indium content inside the quantum dot reaches up to almost 50%.

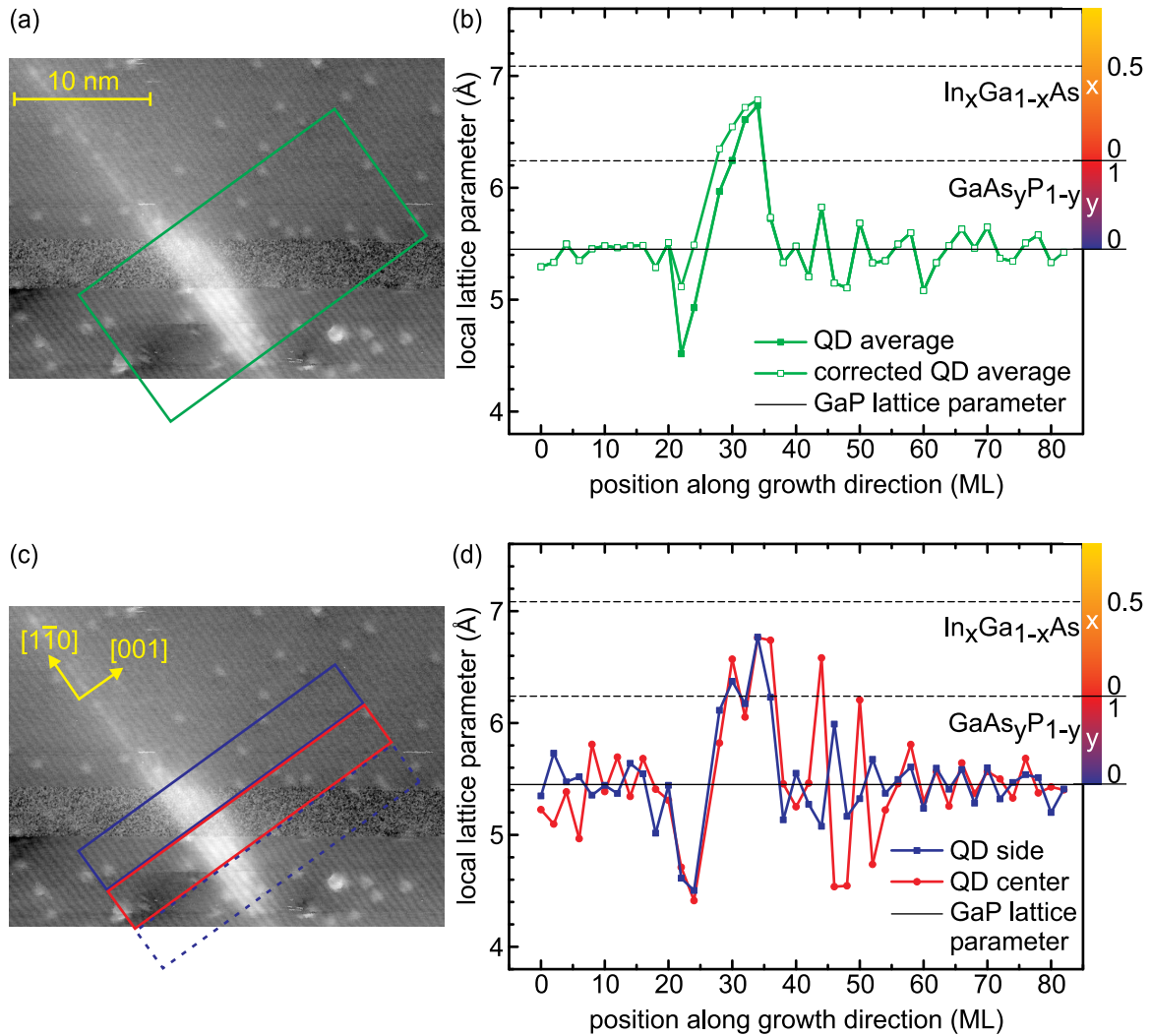


Figure 3.14: (a,c) Filled-state XSTM image of another representative quantum dot. The evaluated regions are highlighted by the colored boxes. The image was taken at $V_T = -3.0$ V and $I_T = 30$ pA. (b,d) Corresponding evaluation of the local lattice parameter and the related stoichiometric composition along growth direction. The graphs show the evaluated data (b) for the entire quantum dot region in green squares and (d) for separated profiles of the quantum-dot center in red dots and for the quantum-dot sides in blue squares. For the latter only one of the quantum-dot sides was taken into account, since for the region highlighted by the blue dotted box the substrate data underneath the dot were not sufficient for an evaluation.

Another highly-resolved quantum dot with its analogous data evaluation is shown in Fig. 3.14. The analysis of the local lattice parameter averaged over the entire quantum dot in Fig. 3.14 (b) is indicated by the green box in the XSTM image in Fig. 3.14 (a). It shows a similar behavior compared with the one in Fig. 3.13 (a,b), i.e. a clear peak in the local lattice parameter ranging over the whole quantum-dot position, a pronounced undershoot at the quantum dot base, and comparable values for the local average indium content. Figure 3.14 (c,d) even shows that the local lattice parameter at the quantum-dot center is again higher at its top than at its base indicating a higher indium concentration at the top.

Figure 3.15 (a) again shows the object already discussed in Fig. 3.11 (a,c) which was assumed to be a buried quantum dot. The analysis of the local lattice parameter in this region [Fig. 3.15 (b)] proves this assumption that this is indeed a quantum dot and not a wetting-layer region. Even at this position of the cleavage surface the presence of indium within this buried nanostructure leads to a significant increase in the local lattice parameter above the value for GaAs in GaP and also again to a compression of the material underneath the quantum dot, resulting in an undershoot that is more pronounced than in a wetting-layer region.

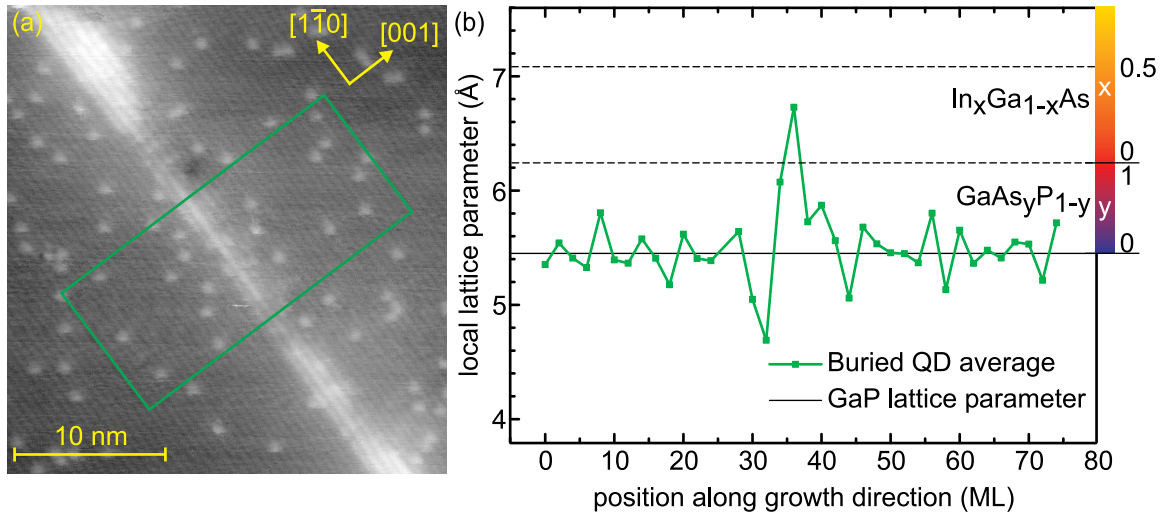


Figure 3.15: (a) Filled-state XSTM image of a buried quantum dot. The evaluated region is highlighted by the colored box. The image was taken at $V_T = -3.0$ V and $I_T = 30$ pA. (b) Corresponding evaluation of the local lattice parameter and the related stoichiometric composition along growth direction.

Material distribution The total material content in the wetting layer and in the quantum dots (including the quantum rings) can be derived from the stoichiometry profiles shown in Figs. 3.12 (b), 3.13 (d), and 3.14 (b) [48]. The results of the evaluation are summarized in Table 3.1. From an integration of the curves a local amount of 3.1 ML GaAs is found for the wetting layer. On the other hand the total indium content inside the quantum dots is calculated to be about 1.9 ML assuming that no phosphorus is present within the quantum dots. Since about 24% of the growth surface is covered with quantum dots or rings, as derived from their lateral extension and their density, it results that about 2.4 ML of the deposited arsenic is located inside the wetting layer, and a total amount of about 0.5 ML indium is located in the quantum dots. The latter value nicely agrees with the nominally deposited amount of 0.5 ML indium. As there is no amount of indium left for the wetting layer, this confirms the above assumption that the deposited amount of indium is only located inside the nanostructures.

These material compositions of the wetting layer and the quantum dots are further supported by the graphs in Figs. 3.13 (d) and 3.14 (b). If phosphorus was inside the quantum dots, the scale bar for the indium content would shift to lower lattice parameters, resulting in an indium content within the quantum dots even higher than the nominal amount of deposited indium material of 0.5 ML. These quantitative results additionally confirm that no phosphorus can be present within the quantum dots. The lack of indium material inside the wetting layer for this material system again shows the occurrence of an intense lateral material transport from the wetting layer into the quantum dots during Stranski-Krastanow growth, which is already well-known for the $(\text{In,Ga})\text{As}/\text{GaAs}$ [39, 45, 91] and also for the GaSb/GaAs material system [115].

Since the remaining group-III material in the quantum dots can only be gallium, the total GaAs material within the quantum dots is derived using average quantum dot heights of 9–10 ML, resulting in 7–8 ML GaAs inside the quantum dots and therewith a GaAs content corresponding to an area averaged amount of about 1.8 ML. Together with the area averaged GaAs amount within the wetting layer of 2.4 ML, a total GaAs incorporation of about 4.2 ML can be derived, which is in good agreement with the nominally deposited amount of 4.5 ML.

Table 3.1: Stoichiometry data of the $\text{In}_{0.25}\text{Ga}_{0.75}\text{As}/\text{GaAs}$ quantum dot layer.

	Wetting Layer	Quantum Dots
Local approximated arsenic content from stoichiometry profile	3.1 ML	-
Local approximated indium content from stoichiometry profile	-	1.9 ML
Remaining gallium content from quantum dot height	-	7–8 ML
Growth surface coverage	76%	24%
Area averaged arsenic amount	2.4 ML	-
Area averaged indium amount	-	0.5 ML
Area averaged gallium amount	-	1.8 ML
Total material amount	4.2 ML GaAs + 0.5 ML InAs	
Nominal material amount	4.5 ML GaAs + 0.5 ML InAs	

3.3 $\text{In}_{0.5}\text{Ga}_{0.5}\text{As}/\text{GaAs}$ Quantum Dots in GaP

A next step in the detailed analysis of the quantum dot growth behavior was to change the nominal deposited indium supply to a higher indium-to-gallium ratio, i.e. $\text{In}_{0.5}\text{Ga}_{0.5}$, which was reported the better ratio for light emitting quantum dots at least in MBE experiments (see Chapter 4 and Refs. [53, 56, 62]).

Preliminary MOVPE experiments were then performed with a nominally higher indium supply, also regarding the influence of further growth parameters [57, 116]. One aspect was the effect of the growth interruption (GRI) after the $\text{In}_{0.5}\text{Ga}_{0.5}\text{As}$ deposition and the resulting photoluminescence (PL) intensity. Figure 3.16 (a) shows room temperature PL spectra of buried quantum dot layers with varying GRI after $\text{In}_{0.5}\text{Ga}_{0.5}\text{As}$ deposition, while (b) shows the integrated PL intensity over the duration of the GRI. For low GRI up to 10 s no significant PL intensity is measurable, while at a GRI of 20 s a first PL signal could be detected. The PL intensity rises fast in the range up to a GRI of 30 s, while further on it increases less rapidly with its maximum at a GRI of 200 s before it decreases again. A change in the PL intensity for different GRI must be related to the structural properties of the quantum dot layers, which will be investigated in the following.

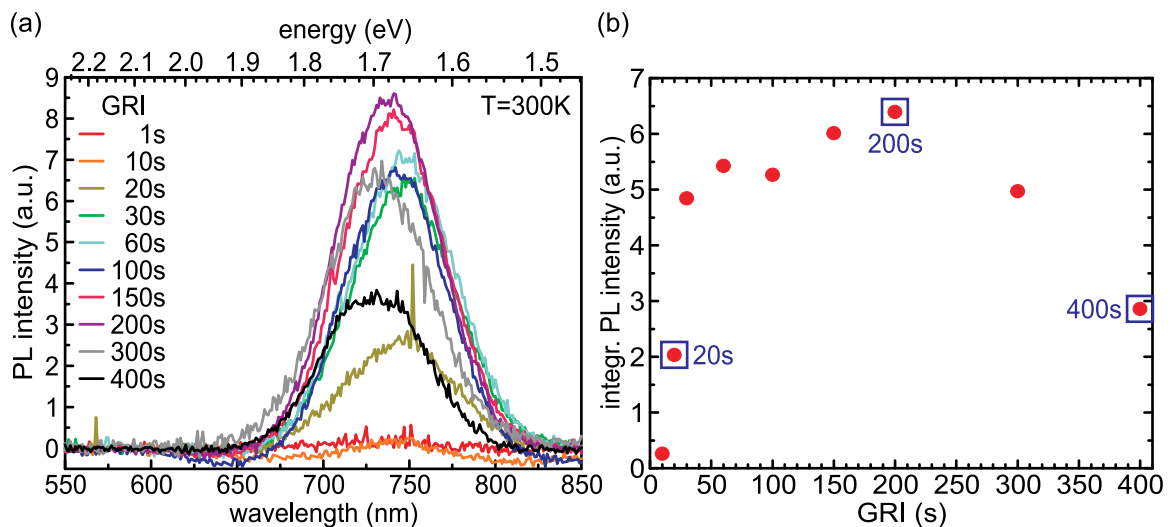


Figure 3.16: (a) Room temperature PL spectra of buried $\text{In}_{0.5}\text{Ga}_{0.5}\text{As}/\text{GaAs}$ QDs on GaP(001) with varying GRI after the $\text{In}_{0.5}\text{Ga}_{0.5}\text{As}$ deposition. (b) Integrated PL intensity versus the duration of the GRI [116, 117]. The blue boxes in (b) highlight the chosen GRI values for the layers in the sample TU10815 for XSTM investigations.

3.3.1 Sample structure

Concerning the preliminary growth experiments and the PL results mentioned above, the resulting design for the corresponding XSTM sample setup is shown in Fig. 3.17. This sample (TU10815) was grown on a *p*-doped GaP(001) substrate starting with a 500 nm thick buffer layer of *p*-doped GaP and 50 nm of undoped GaP, both layers grown at 750 °C. In the following, several layers with different materials were deposited: First, a primary GaAs marker layer was grown consisting of a 3-fold superlattice of 1.0 ML GaAs and 6 nm undoped GaP grown at 500 °C and a spacer of 50 nm GaP grown at 620 °C. The following stack contains six (In,Ga)As/GaAs layers grown at 500 °C, each consisting of nominally 2.2 ML GaAs followed by 0.8 ML of In_{0.5}Ga_{0.5}As and a growth interruption, covered by 56 nm undoped GaP with the initial 6 nm of GaP grown at 500 °C and the following 50 nm at 620 °C. The growth interruption (without any precursor supply) after the In_{0.5}Ga_{0.5}As growth was varied, being 20 s for the first two layers, 200 s for the following two and 400 s for the latter ones. The durations of the GRI were chosen to values which represent three significant phases in the effect of the GRI on the PL intensity, i.e. a first significant PL signal (20 s), the PL maximum (200 s) and the PL decrease (400 s) [as highlighted by the blue boxes in Fig. 3.16 (b)]. Then a secondary GaAs marker layer was grown on top consisting of a 3-fold superlattice of 2.0 ML GaAs and 6 nm undoped GaP and a 3-fold superlattice of 3.0 ML GaAs and 6 nm undoped GaP, all grown at 500 °C. After a spacer of 100 nm of GaP an additional marker layer was inserted, consisting of a 3-fold superlattice of 2 nm Al_{0.23}Ga_{0.77}P and 2 nm undoped GaP, all grown at 620 °C. The final capping includes a spacer of 50 nm undoped GaP, 600 nm of *n*-doped GaP, an *n*-doped Al_{0.23}Ga_{0.77}P barrier of 200 nm, and finally again 200 nm of *n*-doped GaP, again all grown at 620 °C. The aluminium-containing barrier was introduced for attracting migrating surface adatoms and therewith getting a cleaner cleavage surface around the relevant layers for the XSTM experiments.

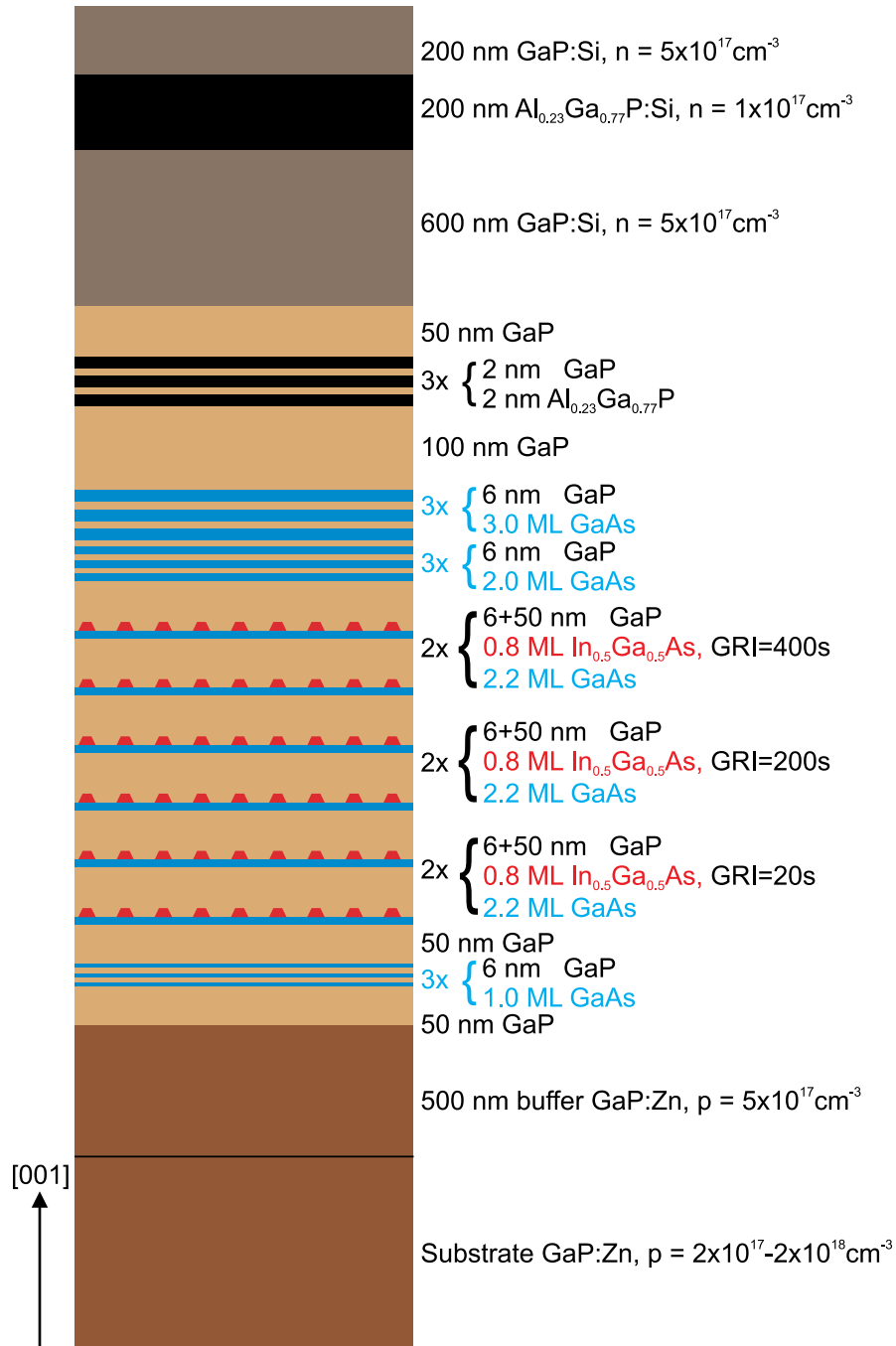


Figure 3.17: Schematic of the structure of sample TU10815.

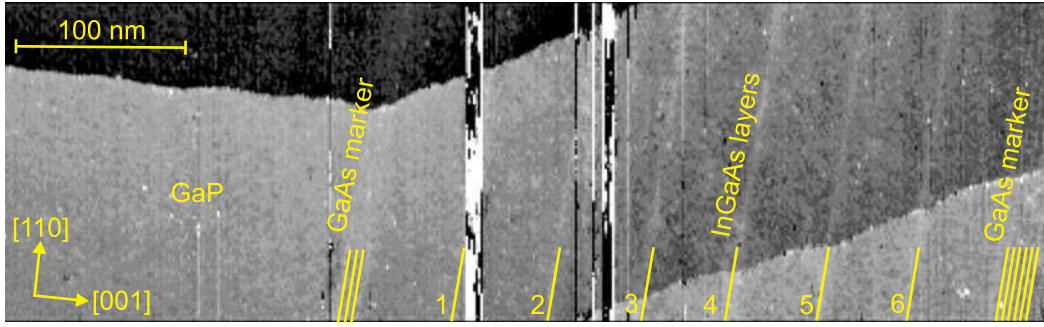


Figure 3.18: Filled-state XSTM overview image showing all six $\text{In}_{0.5}\text{Ga}_{0.5}\text{As}/\text{GaAs}$ layers (indicated with 1–6) as well as the GaAs marker layers above and below. The image was taken at a sample voltage $V_T = -6.0$ V and a tunneling current $I_T = 30$ pA.

3.3.2 XSTM results: image contrast analysis

Figure 3.18 shows a filled-state XSTM overview image across the $(\bar{1}10)$ cleavage surface. The surface in this image is characterized by large terraces divided by monoatomic surface steps. The bright stripes of weak contrast that appear perpendicular to the growth direction can again be identified due to their number and their equal distance of about 50 nm to each other. The six $\text{In}_{0.5}\text{Ga}_{0.5}\text{As}/\text{GaAs}$ layers as well as the GaAs marker layers below and above are indicated by the yellow lines in Fig. 3.18. Although the layers can be identified, the weakness of the contrast in this overview image does not give closer information on their structural properties, such as their similarities or differences or a confirmation of the expected Stranski-Krastanow growth mode.

Therefore, a detailed analysis of the different $\text{In}_{0.5}\text{Ga}_{0.5}\text{As}/\text{GaAs}$ layers will be given in the following.

Layers 1 and 2: GRI of 20 s

Figure 3.19 shows a closer overview of layers 1 and 2 and the surrounding GaP matrix. The XSTM image of the surface is well resolved as the atomic chains parallel to the $[110]$ direction are again clearly visible. Scan-induced adatoms, which, as mentioned before, are typical for XSTM on $\text{GaP}\{110\}$ cleavage surfaces, are again present as well as surface steps. Being nominally identically grown, both of the $\text{In}_{0.5}\text{Ga}_{0.5}\text{As}/\text{GaAs}$ layers with a GRI of 20 s also exhibit a similar appearance in the XSTM measurements. Both layers show an inhomogeneous contrast along the $[110]$ direction. Thus, pronounced islands of brighter contrast are clearly visible, indicating the formation of three-dimensional nanostructures during growth.

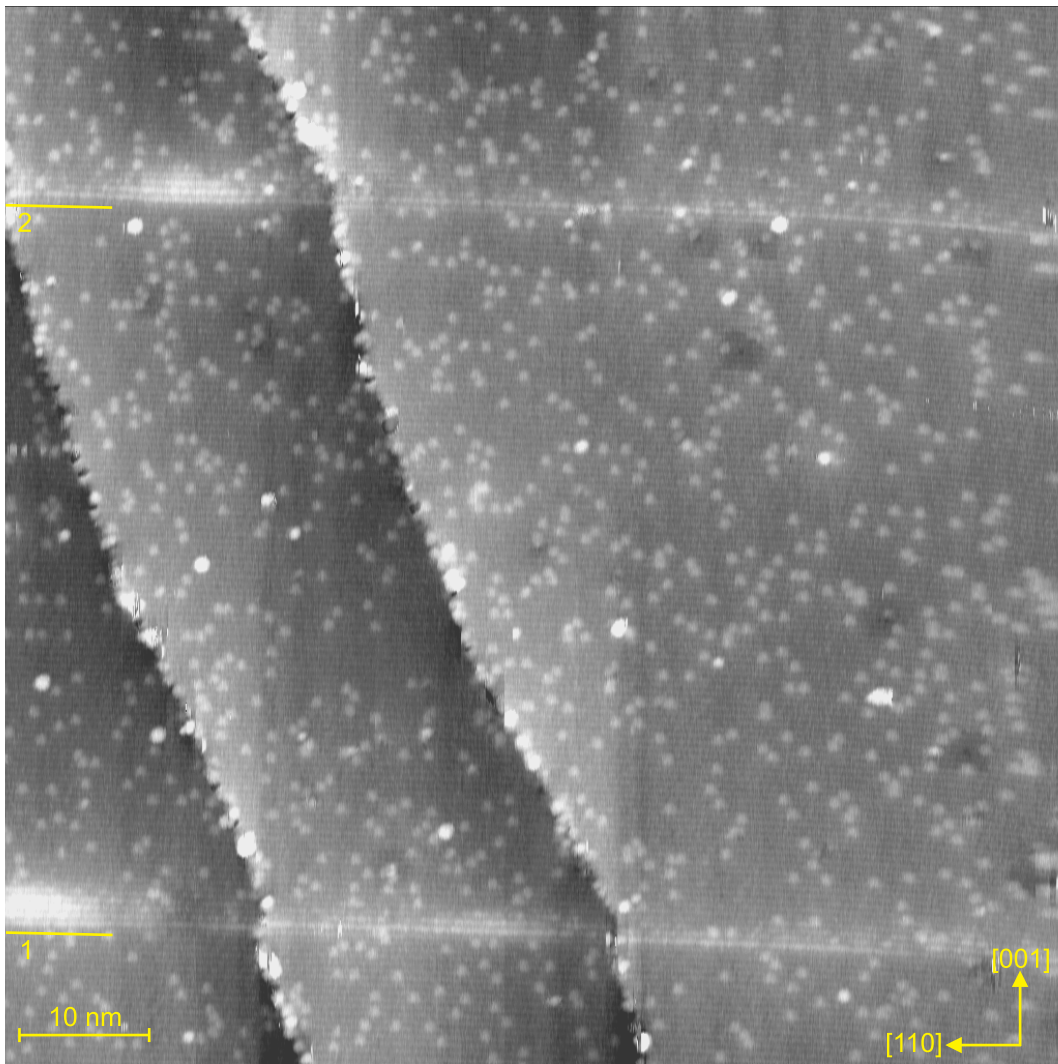


Figure 3.19: Filled-state XSTM overview image showing layers 1 and 2 (GRI 20 s). The image was taken at a sample voltage $V_T = -7.5$ V and a tunneling current $I_T = 20$ pA.

A closer view on layer 2, again taken in filled-state imaging mode, can be found in Fig. 3.20, which highlights the different appearances within the layer. This layer again features, similar to the sample discussed in Section 3.2, trapezoidal-shape like islands of bright contrast (like in regions A, B, D, and E). Also darker islands (C) can be observed as well as regions in between these nanostructures with an intermediate contrast (F). This intermediate contrast in comparison to the dark GaP matrix and the bright islands is again related to a thin wetting layer. Thus, these findings again indicate a Stranski-Krastanow growth mode for this material system.

In the following a more detailed investigation of the appearing nanostructures and the wetting layer will be given. Therefore, high-resolution XSTM filled-state images are shown in Figs. 3.21 and 3.22.

As an example, in Fig. 3.21 (a,c) a typical single nanostructure is shown, which exhibits the trapezoidal cross-section, as highlighted by the yellow lines in Fig. 3.21 (c). Such a shape appears for all nanostructures in these layers 1 and 2. Hence, also these quantum dots are considered to have a truncated pyramidal shape. In Fig. 3.21 (b,d) a smaller nanostructure with darker contrast is shown, which refers to an almost completely buried quantum dot which was cleaved very closely to its side. Again a trapezoidal shape can be assumed, as highlighted by the dashed lines in Fig. 3.21 (d).

For these two layers, a statistical analysis of 24 identified quantum dots on a scanned range of about 1280 nm along the layers reveals values of 10.1 nm for the average base length and 8.0 ML for the average quantum dot height, while the observed maximum height is 11 ML. The areal density for the quantum dots can be determined to about $1.5 \times 10^{11} \text{ cm}^{-2}$ in these layers.

Despite the good image quality no inner structure like a reversed-cone like stoichiometry distribution of the quantum-dot center is visible, in contrast to the formerly investigated $\text{In}_{0.25}\text{Ga}_{0.75}\text{As}/\text{GaAs}/\text{GaP}$ quantum dots discussed in Section 3.2.

And even though the scanned range is larger, there is no clear observation regarding the formation of quantum rings. The base length of the quantum dots lies in the range of 7.0–12.4 nm and there is not a single position within the scanned two layers with two smaller structures neighboring or even *overlapping*. In XSTM experiments the cleavage of the nanostructures always occurs at random positions. So, if quantum rings had formed here, all of them would have been cleaved through their center as a more side-like cleave would have led to overlapping objects or objects with wider base lengths, which was not observed here. Although the experimental observations make the formation of quantum rings in these layers rather improbable, it cannot be fully excluded.

In Fig. 3.22 a filled-state XSTM image of a wetting-layer region between quantum dots is shown. These regions have different thicknesses throughout the layer, which vary in the range between 2 and 8 ML. The wetting layer looks inhomogeneous along the [110] direction and thereby has a similar appearing contrast as compared with the one discussed in Section 3.2. Different brightnesses appear where the brightest contrast is connected to the scan-induced adatoms which are randomly present on the surface both besides and at the wetting layer, as indicated by the green arrows in Fig. 3.22 (b). Apart from these adatoms two different brightnesses are present within the wetting layer in filled-state images, where the image contrast is mostly sensitive to the group-V sublattice. As shown in Fig. 3.22 one may distinguish between brighter arsenic-rich regions, as marked by ovals in Fig. 3.22 (b), and darker phosphorus-rich regions inside the wetting layer. These observations and their similarity to those for

the wetting layer discussed in Section 3.2 may again indicate the absence of indium within the wetting layer regions here.

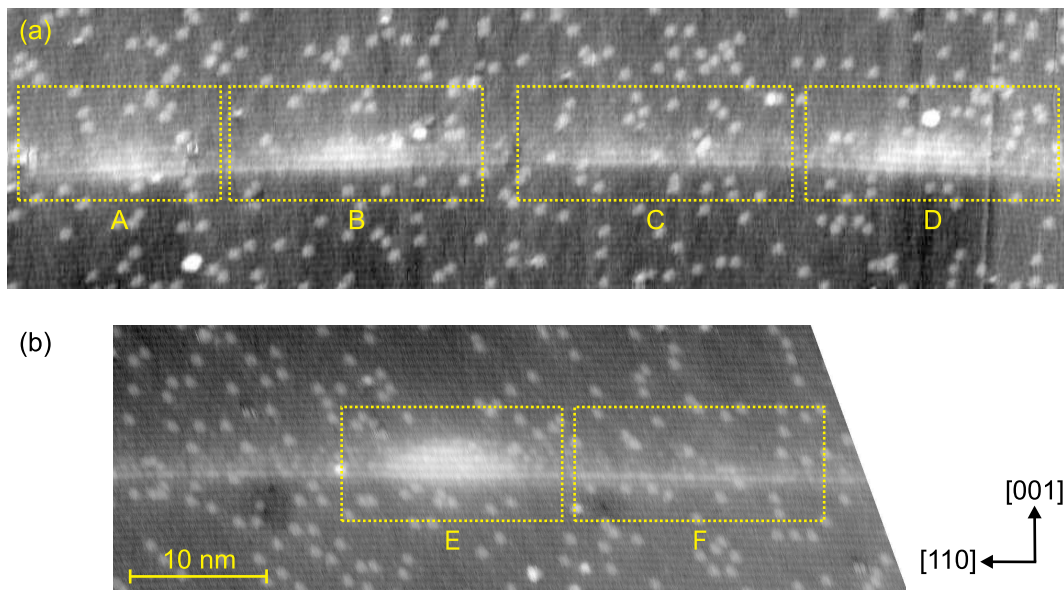


Figure 3.20: Filled-state XSTM images showing layer 2 (GRI 20 s). The images were taken at a sample voltage $V_T = -7.5$ V and a tunneling current $I_T = 20$ pA.

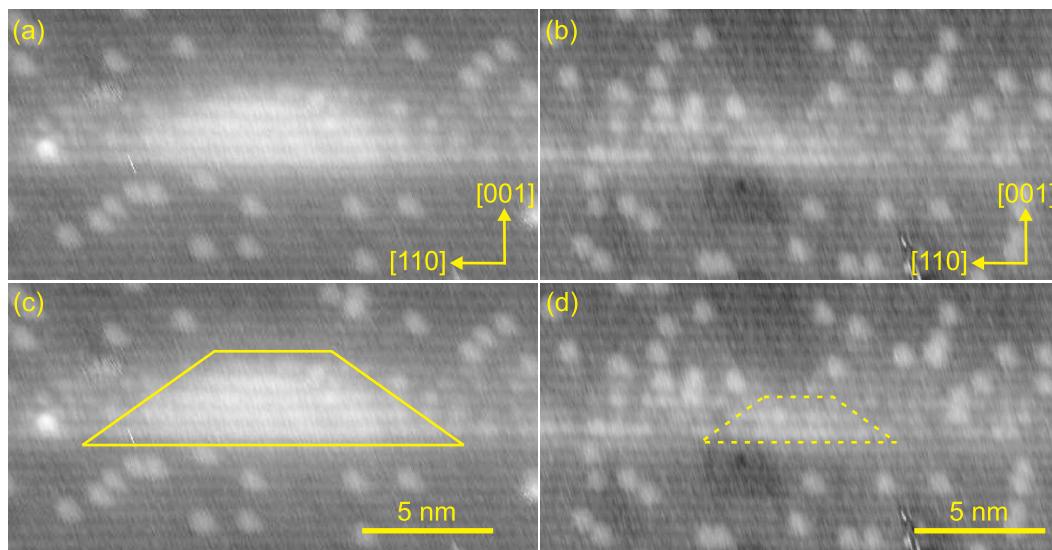


Figure 3.21: Filled-state XSTM images of (a,c) a centrally cleaved quantum dot and (b,d) an almost completely buried quantum dot, both within layer 2 (GRI 20 s). The images were taken at a sample voltage $V_T = -7.5$ V and a tunneling current $I_T = 20$ pA. The contour of the quantum dot is marked by the solid line in (c), while the dashed line in (d) marks the position of the buried quantum dot.

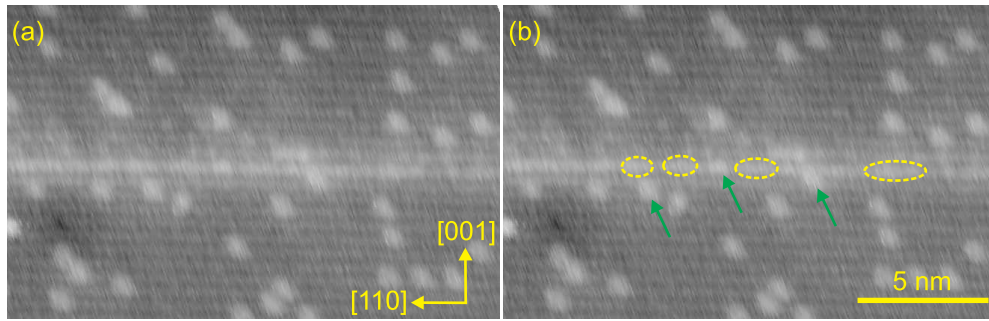


Figure 3.22: Filled-state XSTM image of a wetting layer region within layer 2 (GRI 20 s). The image was taken at a sample voltage $V_T = -7.5$ V and a tunneling current $I_T = 20$ pA. In (b) arsenic-rich regions with brighter contrast are marked by yellow ovals, while adatoms on the surface are indicated by green arrows.

Layers 3 and 4: GRI of 200 s

Figure 3.23 shows an overview image comparing layers 2 and 3. At first sight layer 3 with a GRI of 200 s is structurally clearly different from layer 2 (GRI 20 s). It is characterized by a much darker contrast, which already shows a remarkable influence of the duration of the growth interruption after the $\text{In}_{0.5}\text{Ga}_{0.5}\text{As}$ deposition regarding the structural properties of the layer and the material distribution. In comparison to layer 2, no pronounced (bright) islands can be detected in layer 3, which may indicate the absence of indium-rich quantum dots, but definitely shows a material redistribution during the longer growth interruption.

A closer look at layer 3 is shown in Fig. 3.24 (a,b). In general, the layer appears to be inhomogeneous along the [110] direction. While the layer shows a sharp borderline at its bottom, the thickness along the [001] direction varies between values of 2 and 10 ML. Because of the weak contrast in the image of this layer, there is no clear hint of remaining 3D islands or quantum dots after the growth interruption and the following overgrowth. In the best case, one may consider the presence of small indium-rich material agglomerations within the layer, as indicated by the dashed line in Fig. 3.24 (a). But the weak contrast and disturbing adatoms on the surface (as indicated exemplarily by the green arrows) prevent clear statements at this point.

Typical regions of layer 4 are shown in Fig. 3.25 (a,b). As expected from the identical growth parameters compared with layer 3, the image contrast indicates identical structural properties for both layers.

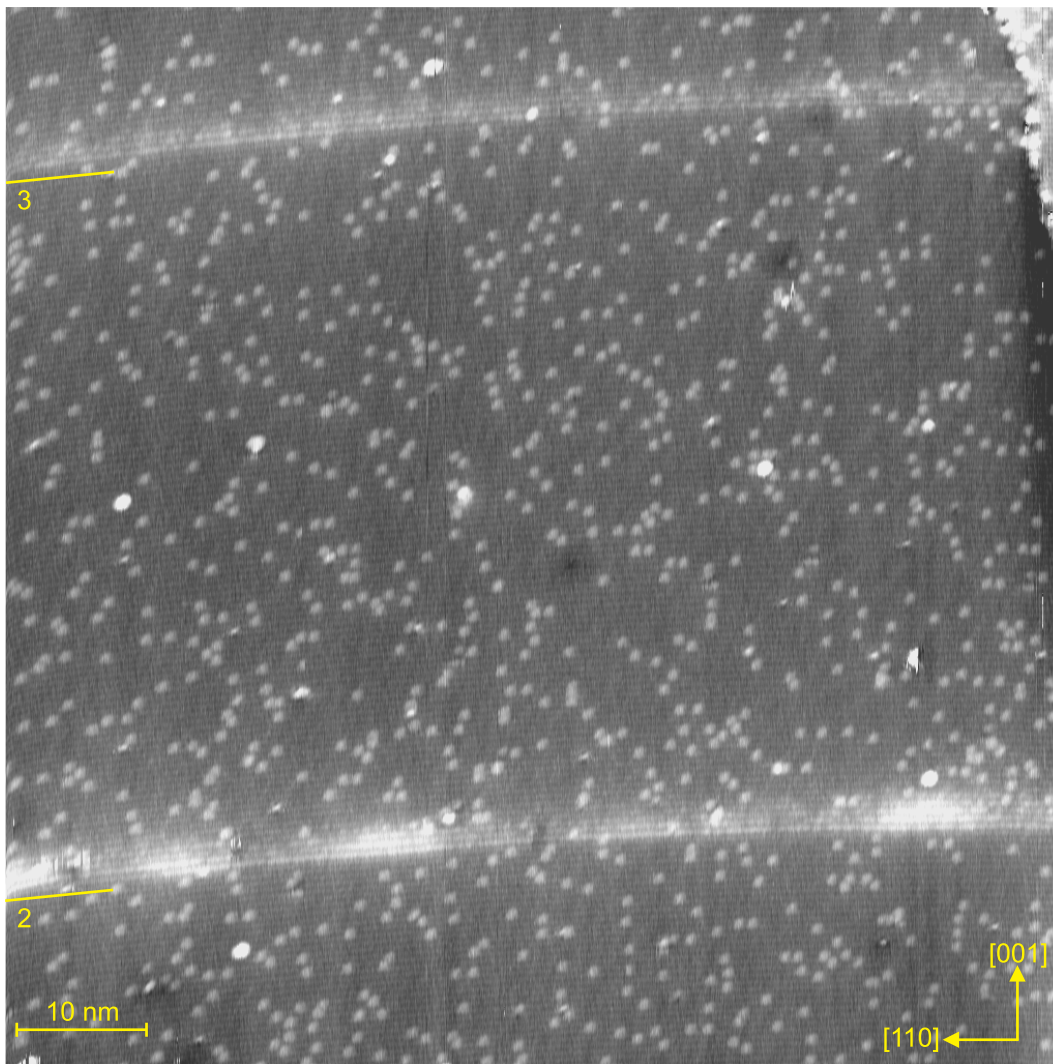


Figure 3.23: Filled-state XSTM overview image showing layer 2 (GRI 20 s) and layer 3 (GRI 200 s). The image was taken at a sample voltage $V_T = -7.5$ V and a tunneling current $I_T = 20$ pA.

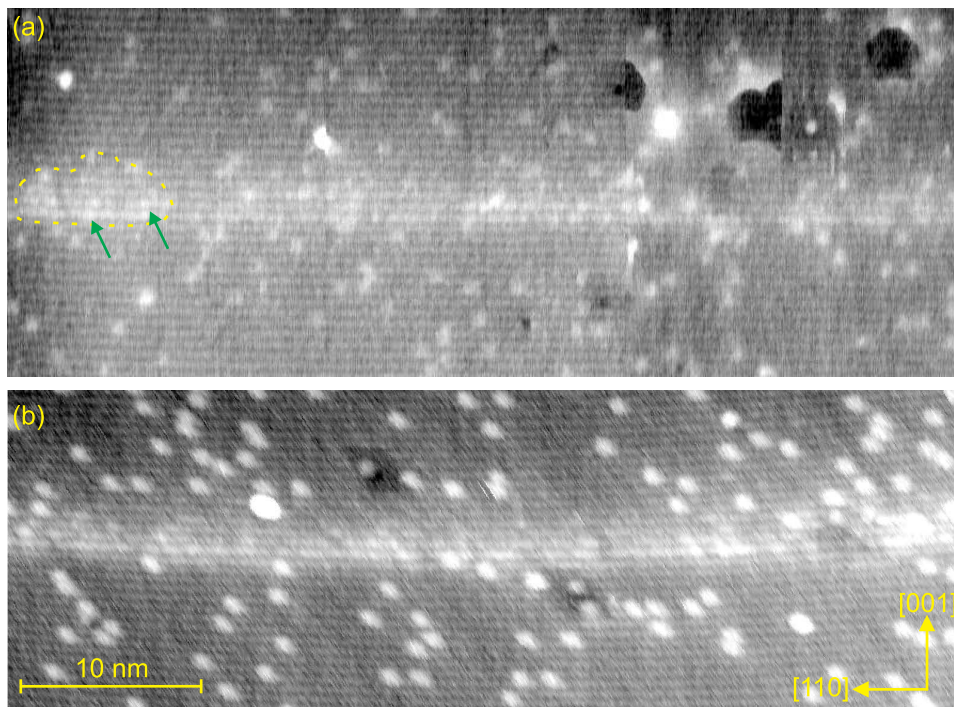


Figure 3.24: Filled-state XSTM images of layer 3 (GRI 200 s). The images were taken at a sample voltage $V_T = -7.8$ V and a tunneling current $I_T = 20$ pA. In (a) a possible agglomeration indicated by a slightly brighter contrast is marked by a yellow dashed line, while adatoms on the surface are indicated by green arrows.

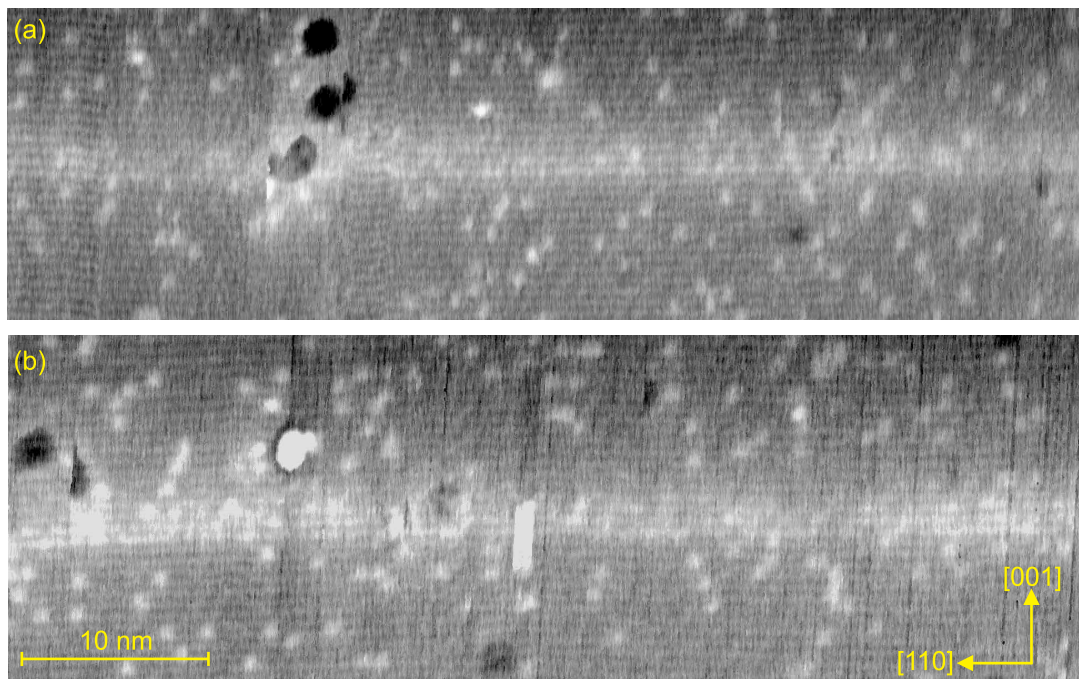


Figure 3.25: Filled-state XSTM images of layer 4 (GRI 200 s). The images were taken at a sample voltage $V_T = -7.8$ V and a tunneling current $I_T = 20$ pA.

Layers 5 and 6: GRI of 400 s

Figure 3.26 shows an overview image of layers 4–6. Although this image is characterized by many scan artifacts and scan-induced adatoms and holes, a difference regarding the contrast between layer 4 on the one hand and layers 5 and 6 on the other hand is still observable. With the contrast in this image being adapted to the layers, here, the layers 5 and 6 (GRI 400 s) still appear much darker than layer 4 (GRI 200 s). Also indium-rich material agglomerations, which again may be guessed in layer 4, as indicated by the dashed lines in Fig. 3.26, seem to be at least less or even not existent in layers 5 and 6. Thus, an effect of the growth interruption on the layers' structure becomes evident again.

A closer image of layer 5 can be found in Fig. 3.27. The layer also appears inhomogeneous along the $[110]$ and along the $[001]$ direction, again with a sharp borderline at its bottom. From the few data with high resolution it seems that the layer is even thinner than the ones with shorter growth interruptions. Observed thicknesses here are 2–8 ML. A closer discussion about indium-rich material agglomerations in this layer seems very difficult. Although a general statement is hard to make, the image data give the visual impression that layer 5 (GRI 400 s) is even less ordered or, in other words, laterally more intermixed than layers 3 and 4 (GRI 200 s).

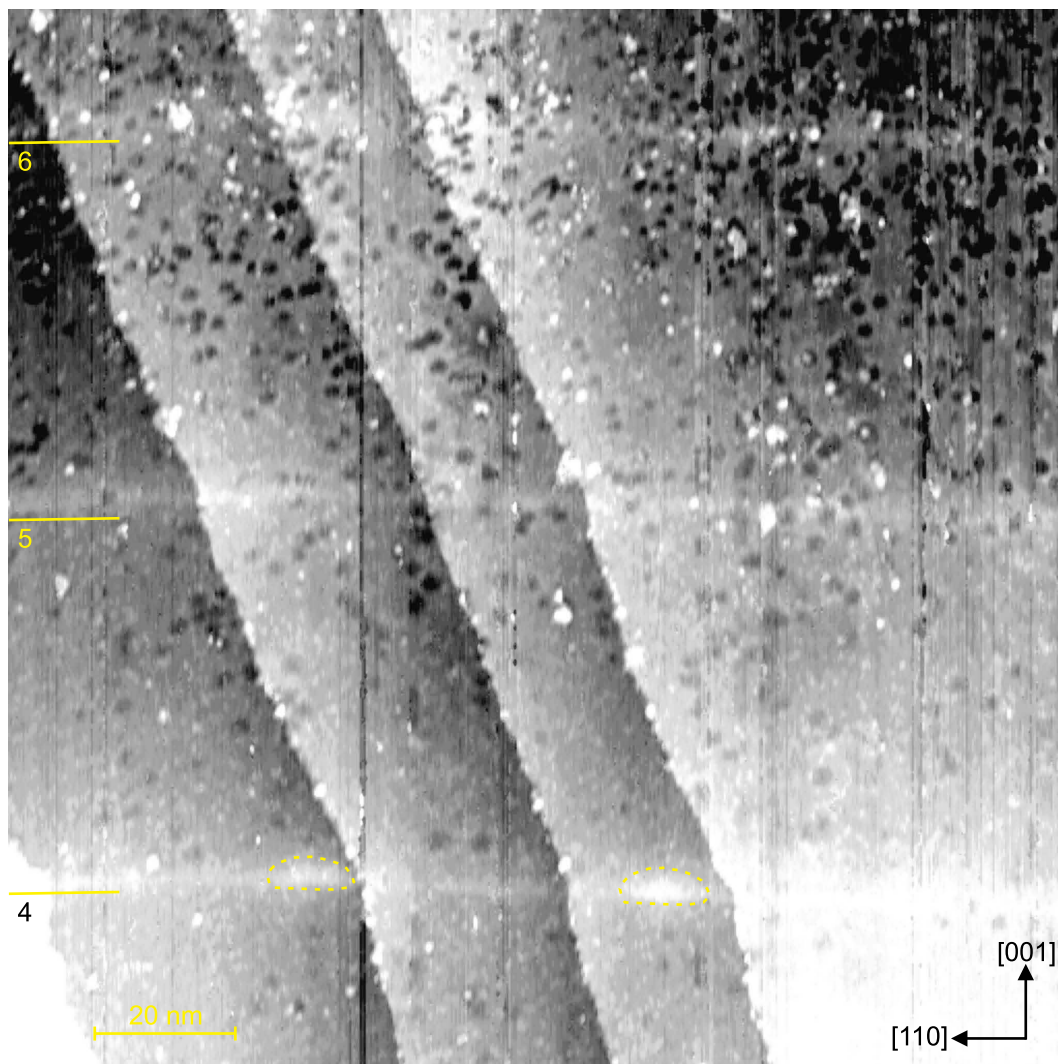


Figure 3.26: Filled-state XSTM overview image showing layer 4 (GRI 200 s) and layers 5 and 6 (GRI 400 s). Possible agglomerations within layer 4 are marked by yellow dashed lines. The image was taken at a sample voltage $V_T = -7.8$ V and a tunneling current $I_T = 20$ pA.

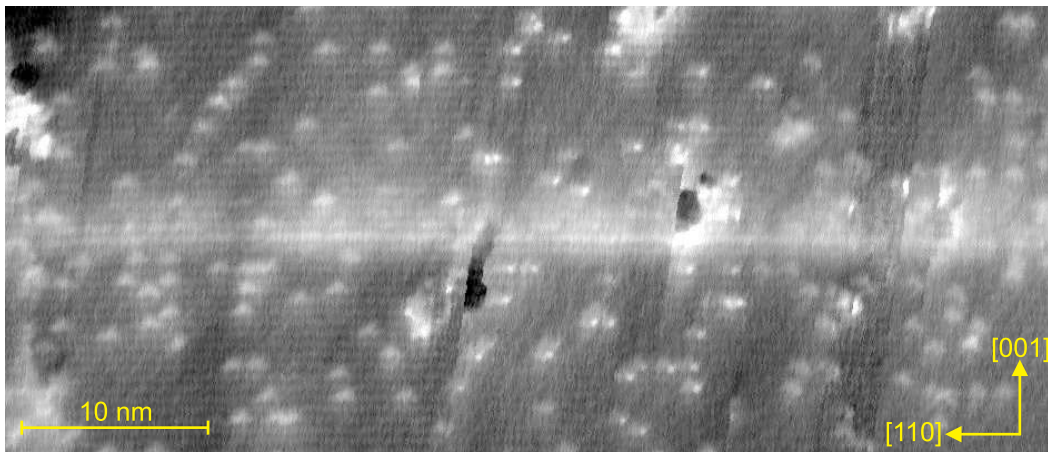


Figure 3.27: Filled-state XSTM image of layer 5 (GRI 400 s). The image was taken at a sample voltage $V_T = -5.4$ V and a tunneling current $I_T = 20$ pA.

3.3.3 XSTM results: stoichiometry analysis

For a quantitative evaluation of the XSTM data, again the local stoichiometry is analyzed by evaluating the local lattice parameter (analogous to Section 3.2.3). In this Section various regions of the $\text{In}_{0.5}\text{Ga}_{0.5}\text{As}/\text{GaAs}$ layers with differing growth interruptions were under investigation.

Layers 1 and 2: GRI of 20 s

Quantum dots Figure 3.28 shows stoichiometry profiles of a well-resolved quantum dot within layer 2. The quantum dot has been analyzed in different parts: the entire quantum dot region, the quantum-dot sides, and the quantum-dot center. In Fig. 3.28 (b) the profile of the local lattice parameter averaged over the entire quantum dot area is shown, as highlighted by the green box in in Fig. 3.28 (a). From the graphs in both figures it results that a change in the local lattice parameter is observed at the position of the quantum dot, which occurs for about 4 data points. This is in accordance with the average quantum dot height of 8 ML determined from the image contrast. Here, the local lattice parameter reaches values, which are higher than the value for pure GaAs in GaP. This again proves the incorporation of indium within these quantum dots. Regarding the different parts of the quantum dot, a higher indium content at the quantum dot base decreasing to the top can be observed, similarly for the quantum-dot center and sides. The typical small undershoot at the base, indicating a strong but significant compression of the material underneath the quantum dot, is again present as well as a not so typical undershoot at the top of the quantum-dot center [red curve in Fig. 3.28 (d)], also indicating a material compression at this position. Following the scale bars on the right side of Fig. 3.28 (b,d), which are based on the assumption of phosphorus free quantum dots, as found in Section 3.2, here again local indium contents of up to 50% are present. One should keep in mind that a change in the group-V element from arsenic to phosphorus would lower the local lattice parameter. So for the same value of the local lattice parameter an intermixing within the group-V lattice between arsenic and phosphorus would even shift this value to higher indium contents.

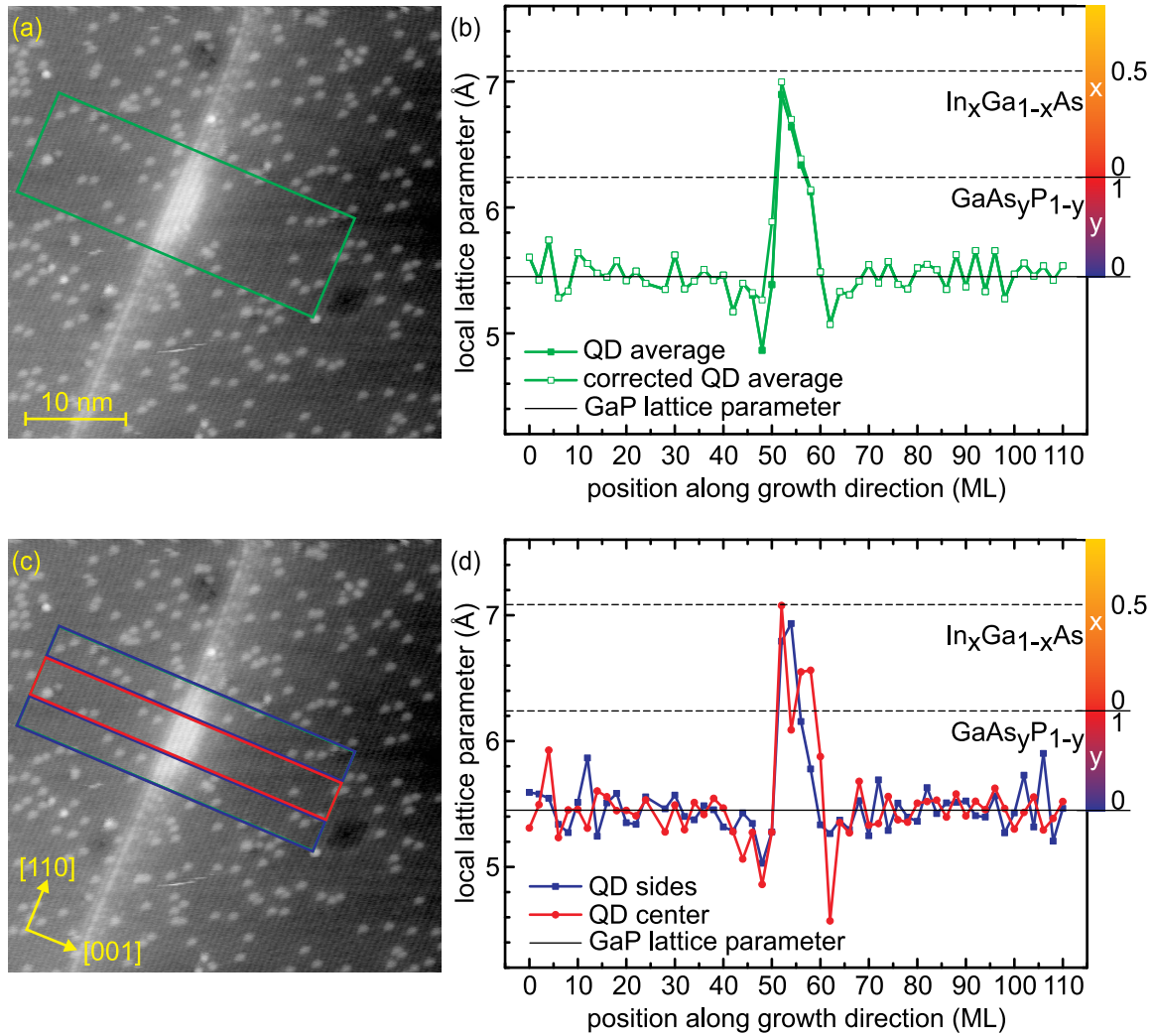


Figure 3.28: (a,c) Filled-state XSTM image of a quantum dot within layer 2. The evaluated regions are highlighted by the colored boxes. The image was taken at $V_T = -7.5$ V and $I_T = 20$ pA. (b,d) Corresponding evaluation of the local lattice parameter and the related stoichiometric composition along growth direction. The graphs show the evaluated data (b) for the entire quantum dot region in green squares and (d) for separated profiles of the quantum-dot center in red dots and for the quantum-dot sides in blue squares.

Wetting layer Figure 3.29 shows the evaluation of the local lattice parameter of the wetting layer in regions directly surrounding a quantum dot (the same one as in Fig. 3.28). Here, the local lattice parameter is found to increase in a 4 ML wide region, which is in good agreement with the visual appearance of the wetting layer. Surprisingly, in these regions the local lattice parameter rises to values higher than for pure GaAs in GaP, implying that indium must be definitely present here. From the curves in Fig. 3.29 (b) local indium contents of 25-50% can be approximated in the case that no phosphorus is present here (otherwise the indium content would be even higher).

Figure 3.30 shows data for wetting layer regions located further away from such pronounced quantum dots. In these cases again the local lattice parameter is found to increase in a 4 ML wide region in accordance with the visual layer height. However, here the local lattice parameter reaches only values in the range of the ones for pure GaAs on GaP (considering the higher noise level for the green curve WL1), which indicates the absence of indium here, in agreement with the assumptions made on basis of the image contrast where rather homogenous bright regions are observed that can be attributed to pure GaAs.

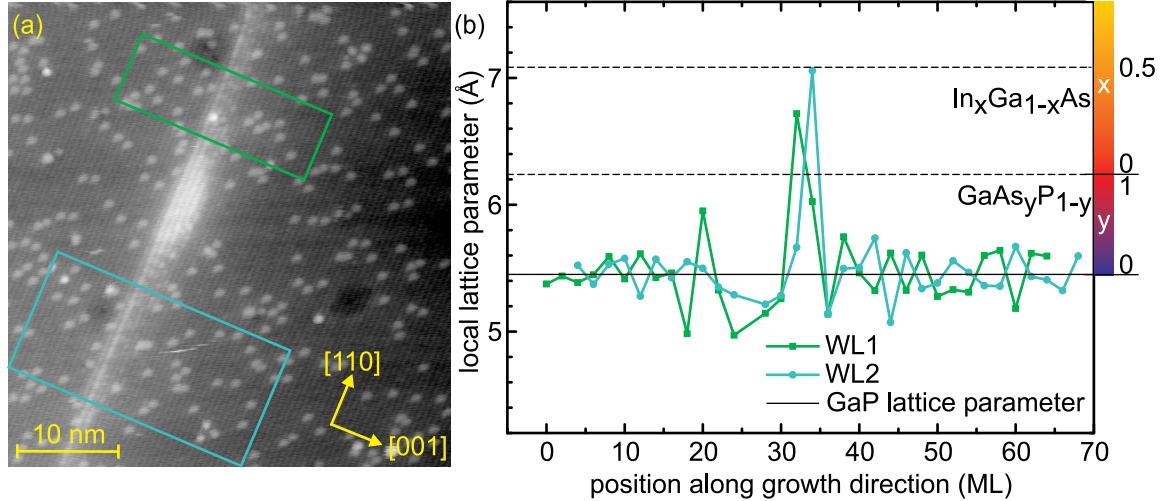


Figure 3.29: (a) Filled-state XSTM image of a quantum dot and the surrounding wetting layer within layer 2. The evaluated regions are highlighted by the colored boxes. The image was taken at $V_T = -7.5$ V and $I_T = 20$ pA. (b) Corresponding evaluation of the local lattice parameter and the related stoichiometric composition along growth direction. The graphs show the evaluated data for two wetting layer regions in separated profiles for region one (WL1) in green squares and for region two (WL2) in light blue dots.

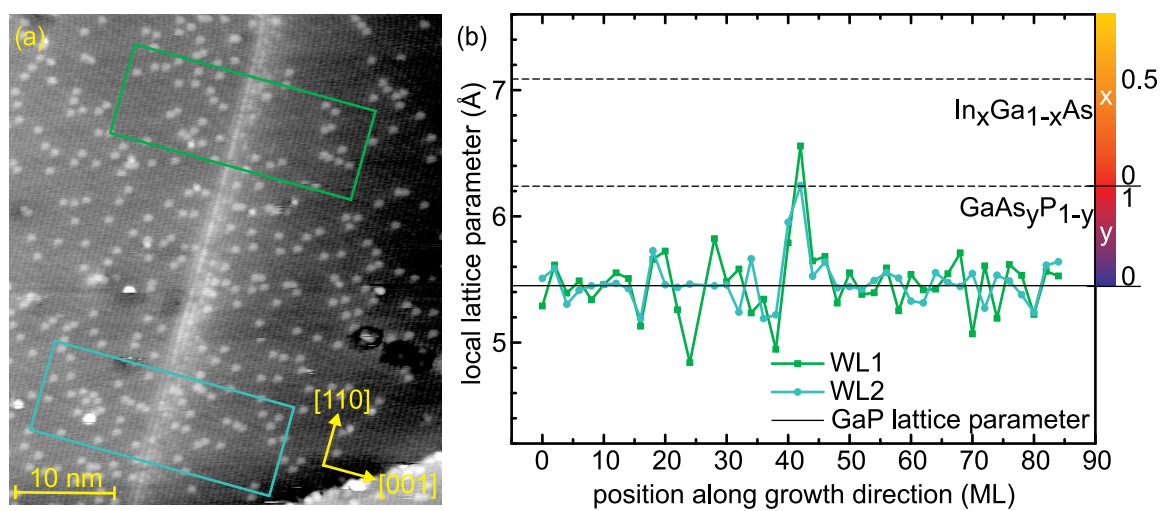


Figure 3.30: (a) Filled-state XSTM image of the wetting layer away from the quantum dots within layer 2. The evaluated regions are highlighted by the colored boxes. The image was taken at $V_T = -7.5$ V and $I_T = 20$ pA. (b) Corresponding evaluation of the local lattice parameter and the related stoichiometric composition along growth direction. The graphs show the evaluated data for two wetting layer regions in separated profiles for region one (WL1) in green squares and for region two (WL2) in light blue dots.

Table 3.2: Stoichiometry data of layers 1 and 2 (GRI 20 s).

	Quantum Dots	Wetting Layer around QDs	Wetting Layer away from QDs
Local approx. indium content from stoichiometry profile	1.6 ML	0.8 ML	-
Growth surface coverage	7%	42%	51%
Area averaged indium amount	0.1 ML	0.3 ML	-
Total indium amount	0.4 ML		
Nominal indium amount	0.4 ML		

Material content The results of the quantitative evaluation of the stoichiometry profiles are summarized in Table 3.2. The total indium content inside the quantum dots is calculated to be about 1.6 ML. Since about 7% of the growth surface is covered with quantum dots, as derived from their lateral extension and their density (the latter being slightly smaller than in the quantum dots discussed in Section 3.2), it results that a total amount of only about 0.1 ML indium is located within the quantum dots, which is a lower value than the nominally deposited amount of 0.4 ML indium, supporting the above conclusion of a presence of indium within the wetting layer.

The calculated indium content within the wetting layer around the quantum dots (Fig. 3.29) amounts to about 0.8 ML. Considering that each region covers an area being about 6 times larger than the surrounded quantum dot leads to an estimated coverage of 42% of the growth surface and therewith a laterally averaged amount of about 0.3 ML indium within these regions. As the calculated amount of indium within the quantum dots is 0.1 ML, the total indium amount (quantum dots + surrounding wetting layer) is 0.4 ML, which is in accordance with the nominal deposited value of 0.4 ML. This shows that within the remaining 51% of the layer, i.e. within the rest of the wetting layer, no significant amounts of indium can be present, since this would exceed the nominal deposited amount.

As the previous discussion is only valid under the assumption that no phosphorus is present within quantum dots and the surrounding wetting layer, this even more proves the absence of indium within the rest of the wetting layer because phosphorus within quantum dots and the surrounding wetting layer would shift the values of the local lattice parameter. In other words, in the case of phosphorus within quantum dots and the surrounding wetting layer, the amount of indium in these regions would be even higher than discussed above, which would contradict the nominally available amount of indium during growth. Therefore one may conclude that the quantum dots

Table 3.3: Approximation of arsenic content within layers 1 and 2 (GRI 20 s).

	Quantum Dots	Wetting Layer around QDs	Wetting Layer away from QDs
Height	8 ML	4 ML	4 ML
Growth surface coverage	7%	42%	51%
Local arsenic concentration	100%	$\leq 100\%$	$\approx 82\%$
Area averaged arsenic amount	0.6 ML	≤ 1.7 ML	≈ 1.7 ML
Total arsenic amount		≤ 3.9 ML	
Nominal arsenic amount		3.0 ML	

and the surrounding wetting layer consist of (In,Ga)As (without phosphorus) while the remaining wetting layer regions consist of Ga(As,P) (without indium).

Finally, with these finding one can try to estimate the local arsenic amount in the different areas of the layer, as summarized in Table 3.3. For the phosphorus-free quantum dots with their average height of 8 ML it results that they contain about 0.6 ML of arsenic. According to the stoichiometry profiles of the wetting layer, a height of 4 ML is assumed for further considerations. The wetting layer parts surrounding the quantum dots (assumed to be almost phosphorus-free) hence contain up to 1.7 ML of arsenic. For the wetting layer away from the quantum dots a local arsenic concentration of 82 % can be approximated by averaging the light blue curve (with low noise (WL2)) in Fig. 3.30 (b) in the 4 ML wide region of the wetting layer (to a value of about 6.1 Å), which leads to an area averaged arsenic amount of about 1.7 ML. Thus, the total arsenic amount can be estimated to less than 3.9 ML. Compared to the nominal value of 3.0 ML this at least indicates that the total deposited amount of arsenic is found within the quantum dot layer and no further segregation effects occur during growth or the following GRI.

Layers 3 and 4: GRI of 200 s

Figure 3.31 shows evaluated data for layer 3. The evaluated regions as highlighted by the colored boxes have been selected because of their relatively bright contrast within the layer and the larger height. A change in the local lattice parameter is indeed visible at the position of the layer in a range of up to 6 ML. Nevertheless, the local lattice parameter lies below the value for pure GaAs on GaP which could indicate the absence of indium within this layer. According to the visual observation it is also possible and probably more likely due to the longer GRI that a material intermixing occurs so that an alloy of quaternary (In,Ga)(As,P) forms within the layer. In any case, because the local lattice parameter stays below the value for pure GaAs on GaP there must be both phosphorus and arsenic present within the layer.

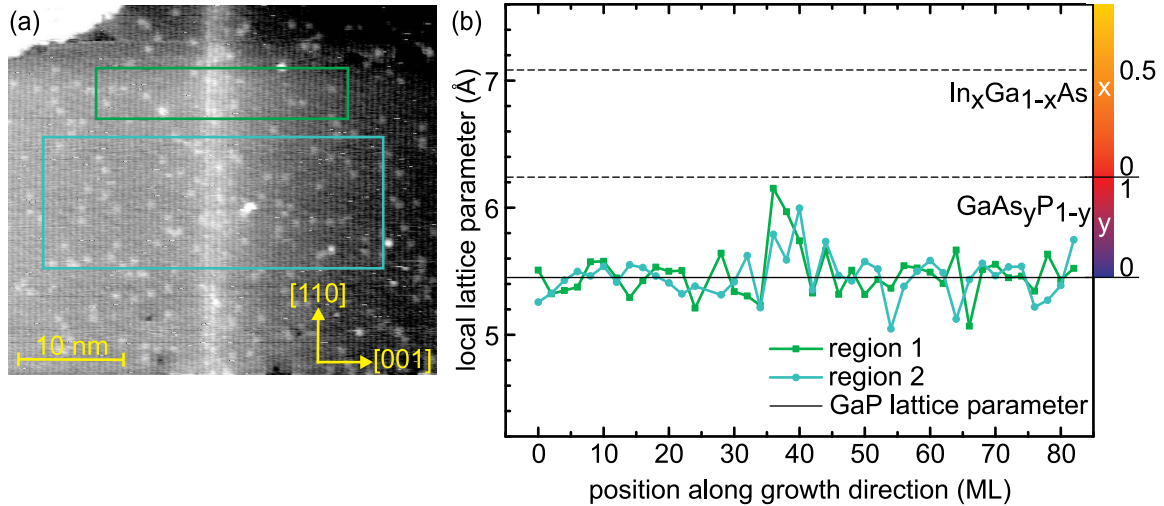


Figure 3.31: (a) Filled-state XSTM image of layer 3. The evaluated regions are highlighted by the colored boxes. The image was taken at $V_T = -7.8$ V and $I_T = 20$ pA. (b) Corresponding evaluation of the local lattice parameter and the related stoichiometric composition along growth direction. The graphs show the evaluated data for two regions in separated profiles for region 1 in green squares and for region 2 in light blue dots.

Considering a layer with a quaternary (In,Ga)(As,P) alloy one can try to approximate the material composition within. Starting with the deposited material amount of 2.2 ML GaAs and 0.8 ML $\text{In}_{0.5}\text{Ga}_{0.5}\text{As}$ this would equal 3.0 ML $\text{In}_{0.13}\text{Ga}_{0.87}\text{As}$. By distributing this material homogeneously over a layer thickness of 6.0 ML this would correspond to 6.0 ML of quaternary $\text{In}_{0.07}\text{Ga}_{0.93}\text{As}_{0.5}\text{P}_{0.5}$. According to Fig. 2.15, the local lattice parameter for these layers on GaP can be extrapolated to about 5.96 Å. Now for layer 3 the local lattice parameter for both curves in Fig. 3.31 (b) in the 6 ML

wide region of the layer can be averaged to a value of about 5.9 \AA . This match gives a further indication of a quaternary arrangement of the material within the layer.

The evaluation of analyzable data for layer 4, which has the same growth conditions as layer 3, is shown in Fig. 3.32. As expected, it provides similar results, while the higher noise level in the data almost hides the local increase of the local lattice parameter. Hence, no definite signs of indium are found but leaving again the possibility of a rather quaternary intermixing of $(\text{In,Ga})(\text{As,P})$.

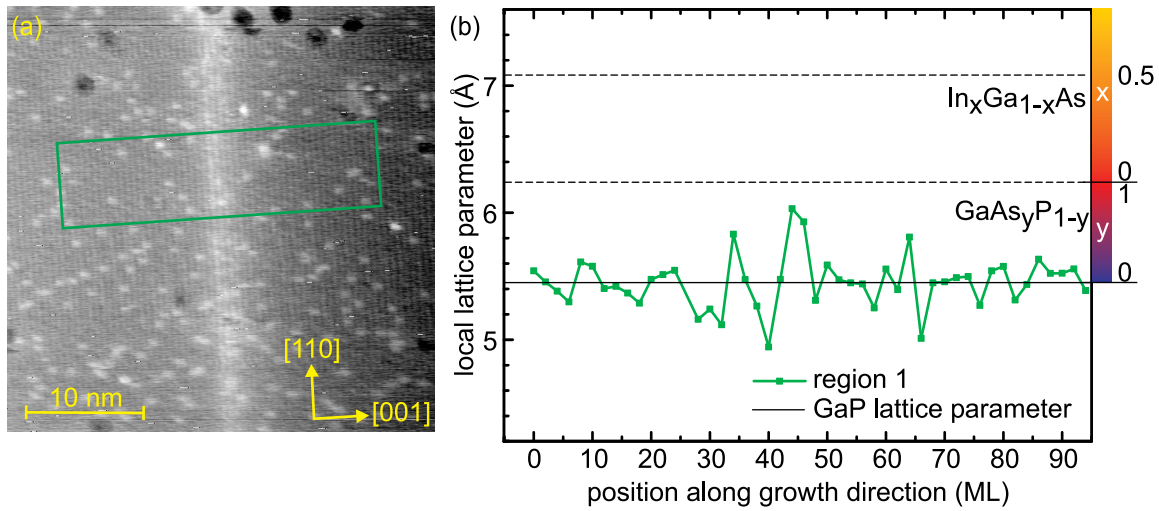


Figure 3.32: (a) Filled-state XSTM image of layer 4. The evaluated region is highlighted by the colored box. The image was taken at $V_T = -7.8 \text{ V}$ and $I_T = 20 \text{ pA}$. (b) Corresponding evaluation of the local lattice parameter and the related stoichiometric composition along growth direction. The graph shows the evaluated data in green squares.

Layers 5 and 6: GRI of 400 s

Figure 3.33 shows the evaluation of one of the few analyzable images of layer 5. In a range of more than 4 ML a notable rise in the local lattice parameter compared with the GaP lattice constant can be observed in the analyzable region, which is comparable with the visual impression of the layer height. Unfortunately, due to the lack of image quality the noise level for the local lattice parameter is even higher than before. Thus, the one data point above the $\text{GaAs}_{1.0}\text{P}_{0.0}$ line in Fig. 3.33 (b) is not a sufficiently strong evidence for a local indium concentration within the layer. A clear interpretation of the data cannot easily be made but a further quaternary intermixing of the layer to $(\text{In,Ga})(\text{As,P})$ alloy or even a further dissolution may be possible. Nevertheless, in the quaternary case the local lattice parameter for a homogeneous $(\text{In,Ga})(\text{As,P})$ layer in GaP containing all deposited InAs material would be in the range between 5.96 \AA (extrapolated value for 6.0 ML $\text{In}_{0.07}\text{Ga}_{0.93}\text{As}_{0.5}\text{P}_{0.5}$) and 6.21 \AA (extrapolated value for 4.0 ML $\text{In}_{0.1}\text{Ga}_{0.9}\text{As}_{0.75}\text{P}_{0.25}$). In Fig. 3.33 (b) the local lattice parameter in the region of the layer can be averaged to 6.1 \AA for a layer thickness of 6 ML or to 6.3 \AA for a thickness of 4 ML, being in rough agreement with the theoretical values, considering the high noise level of the data here. This match to the predicted values at least gives the possibility of a quaternary arrangement within this layer.

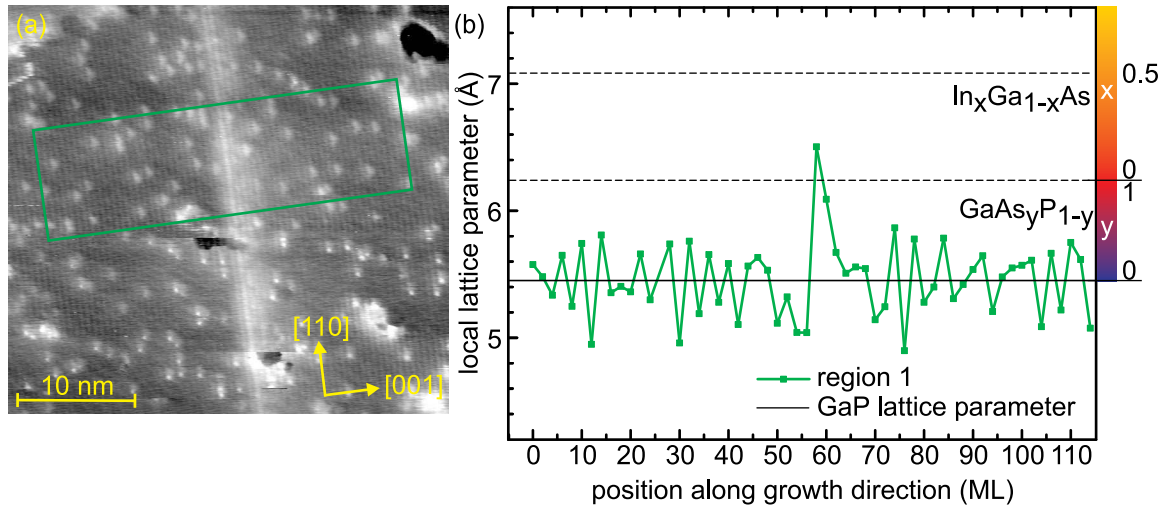


Figure 3.33: (a) Filled-state XSTM image of layer 5. The evaluated region is highlighted by the colored box. The image was taken at $V_T = -5.4 \text{ V}$ and $I_T = 20 \text{ pA}$. (b) Corresponding evaluation of the local lattice parameter and the related stoichiometric composition along growth direction. The graph shows the evaluated data (region 1) in green squares.

3.3.4 Quantum Dot layer transformation with longer GRI

The previous results confirmed that the duration of the GRI after the (In,Ga)As deposition has a significant effect on the structural properties of the quantum dot layer. The deposited amount of nominally 2.2 ML GaAs followed by 0.8 ML of $\text{In}_{0.5}\text{Ga}_{0.5}\text{As}$ leads to indium-rich quantum dots with a supposed pyramidal shape. For short GRI durations the overgrown layer then consists of indium-rich truncated-pyramidal shaped quantum dots with a small indium containing wetting layer environment and an indium-free Ga(As,P) wetting layer. Higher GRI durations before the capping with GaP then lead to a transfer of the indium material into the wetting layer. Thereby, a dissolution of the quantum dots into agglomerations and a further intermixing of the quantum dot with the wetting layer material occurs. With longer duration of the GRI the ongoing material intermixing seems to form a more homogeneous quaternary (In,Ga)(As,P) layer.

Chapter 4

(In,Ga)As/GaP Quantum Dots grown by MBE

The sample for the XSTM investigations presented in this chapter was grown using molecular beam epitaxy (MBE) by Yuncheng Song in the workgroup of Prof. M.L. Lee, formerly at Yale University.

4.1 Sample overview

4.1.1 Sample structure

The setup of the sample was designed to combine several aspects also to be able to investigate many of them during one experimental session. This sample (Yale20130725) was grown on a *p*-doped GaP(001) substrate starting with a 200 nm thick buffer layer of *p*-doped GaP and 100 nm of undoped GaP, both layers grown at 620 °C. The following stack contains six (In,Ga)As or (In,Ga)As/GaAs layers grown at 480 °C, each followed by 50 nm undoped GaP, where the initial 10 nm of GaP were grown at 480 °C and the following 40 nm at 580 °C. The first (In,Ga)As layers were chosen in accordance with the ones for the previously studied LED structure [62]. They contain 2.0 ML (layer 1), 3.0 ML (layers 2 and 3), and 4.0 ML (layer 4) In_{0.5}Ga_{0.5}As. Layers 5 and 6 were grown using exactly the same nominal material amount which was used for the MOVPE-grown (In,Ga)As/GaAs quantum dot sample from TU Berlin (see Section 3.2), consisting of a 3.0 ML GaAs interlayer followed by 2.0 ML of In_{0.25}Ga_{0.75}As. Prior to each In_{0.5}Ga_{0.5}As or In_{0.25}Ga_{0.75}As/GaAs layer there is a growth interruption of 20 s followed by 4 s of arsenic flux while after each (In,Ga)As layer a growth interruption of 20 s is followed by 2 s of phosphorus flux. The final In_{0.25}Ga_{0.75}As/GaAs layer was followed by 50 nm undoped GaP grown at 480 °C and a marker layer consisting of a 5-fold superlattice of

2.0 ML GaAs and 6 nm GaP. After a spacer of 100 nm of GaP an additional marker layer was inserted, consisting of a 3-fold superlattice of 2 nm $\text{Al}_{0.25}\text{Ga}_{0.75}\text{P}$ and 2 nm undoped GaP, all grown at 580 °C. The final capping includes a spacer of 100 nm undoped GaP, 500 nm of *n*-doped GaP, an *n*-doped $\text{Al}_{0.25}\text{Ga}_{0.75}\text{P}$ barrier of 50 nm, and finally again 10 nm of *n*-doped GaP. The aluminium-containing barrier was again introduced for attracting migrating surface adatoms and therewith getting a cleaner cleavage surface around the relevant layers in the XSTM experiment.

4.1.2 XSTM results: overview

Figure 4.2 shows an empty-state XSTM overview image across the (110) cleavage surface. Although the image is characterized by weak resolution and scan artifacts, five stripes of bright contrast lying perpendicular to the growth direction and with a distance of about 50 nm between each other can be identified as the first five (In,Ga)As layers (indicated by the yellow lines). Despite the lack of image quality, all of the five layers already appear inhomogeneous along the $[\bar{1}\bar{1}0]$ direction.

Figure 4.3 (a-c) shows a series of empty-state XSTM overview images across the $(1\bar{1}0)$ cleavage surface. Again, some (In,Ga)As layers (indicated with 3–6) could be identified as well as the 5-fold GaAs marker layer (indicated with M1) and the 3-fold (Al,Ga)P marker layer (indicated with M2). From Fig. 4.3 (a) layers 3 and 4 appear with a darker contrast compared to layers 5 and 6. Especially those $\text{In}_{0.25}\text{Ga}_{0.75}\text{As}/\text{GaAs}$ layers 5 and 6 also already show an indication of the formation of islands during growth at these overview images sizes [Fig. 4.3 (a,b)].

A closer investigation of the different layers and their structural properties will be given in the following, while the marker layers will be discussed separately (see Chapter 5).

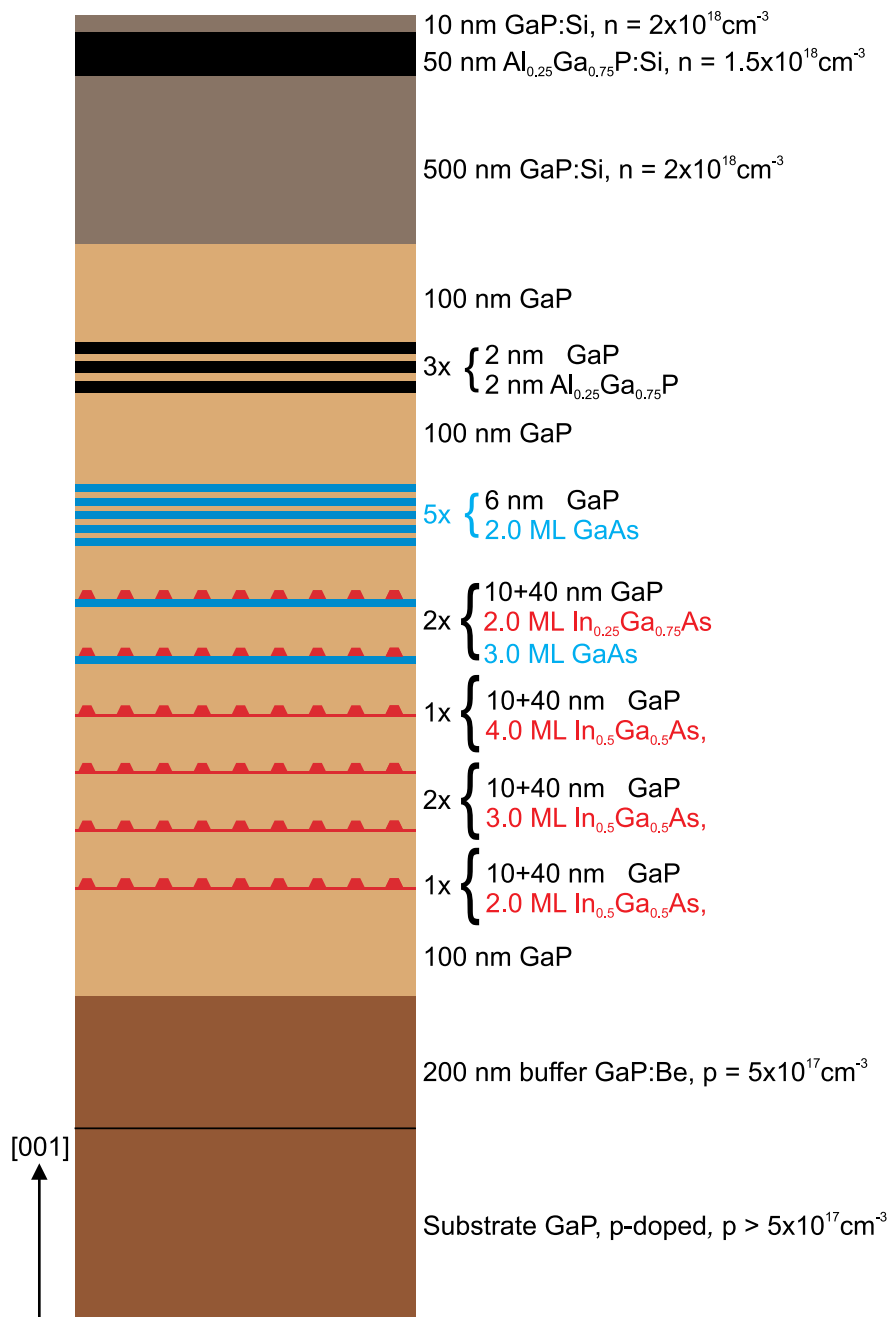


Figure 4.1: Schematic of the structure of sample Yale20130725.

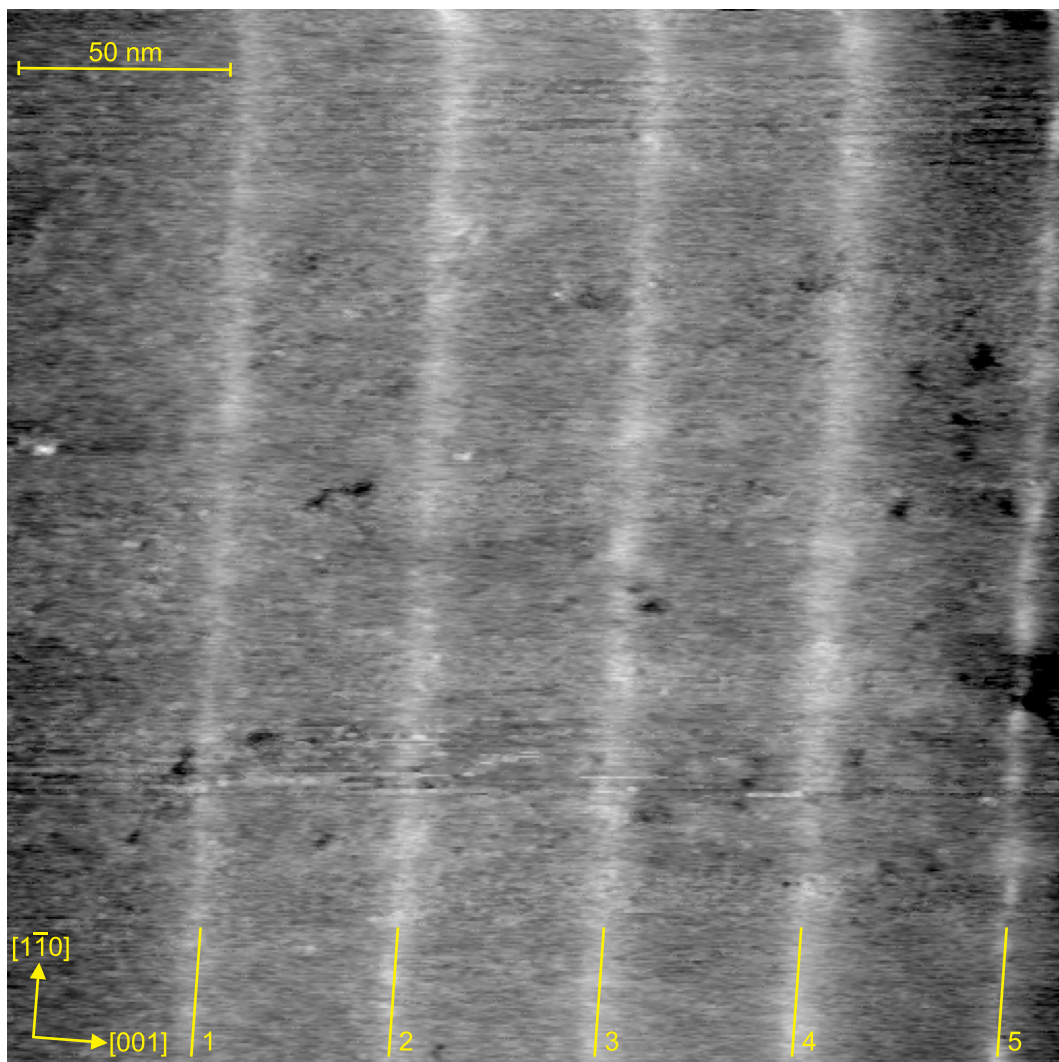


Figure 4.2: Empty-state XSTM overview image showing five of the (In,Ga)As layers (indicated with 1–5). The image was taken at a sample voltage $V_T = +4.3$ V and a tunneling current $I_T = 40$ pA.

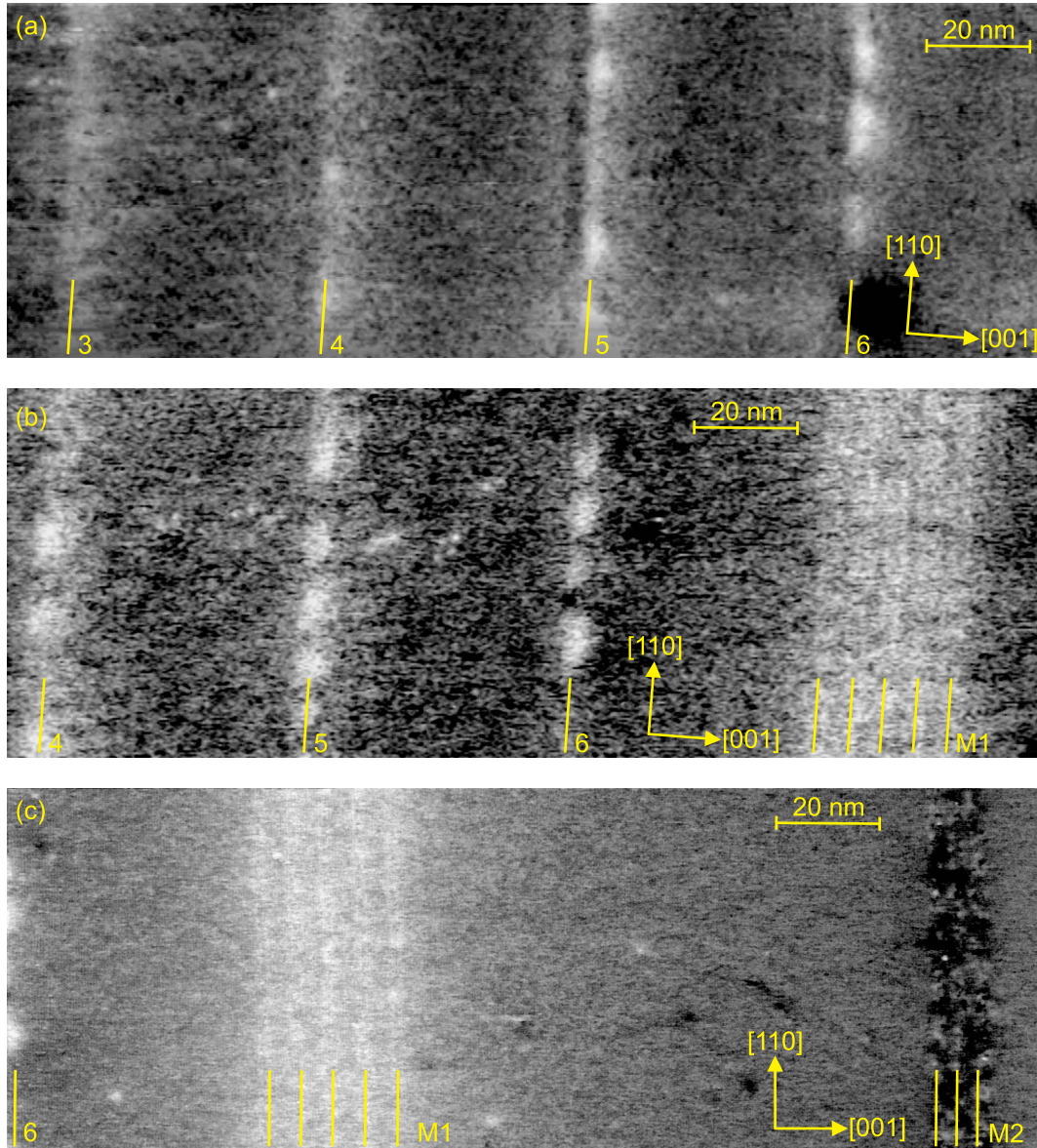


Figure 4.3: Empty-state XSTM overview images showing (a) (In,Ga)As layers 3–6, (b) layers 4–6 and the GaAs marker layer (M1) and (c) layer 6, marker M1, and the (Al,Ga)P marker layer (M2). The images were all taken at a sample voltage $V_T = +4.0$ V and a tunneling current $I_T = 40$ pA.

4.2 In_{0.25}Ga_{0.75}As/GaAs Quantum Dots in GaP

4.2.1 XSTM results: image contrast analysis

Figure 4.4 shows a closer overview of the In_{0.25}Ga_{0.75}As/GaAs layers (layers 5 and 6) in filled-state mode. The presence of islands within both layers is clearly visible, but due to the image quality in between those islands an intermediate contrast (compared to the bright islands and the dark GaP matrix) is only slightly observable, thus already indicating a wetting layer formation and therewith the expected Stranski-Krastanow growth mode. Figure 4.5 (a) shows an empty-state XSTM image of layer 6 where the region highlighted by the dotted lines is investigated in more detail in Fig. 4.5 (b). In both images of Fig. 4.5 the islands of bright contrast are again clearly visible, while in Fig. 4.5 (b) the image gives also atomic resolution along the [001] direction.

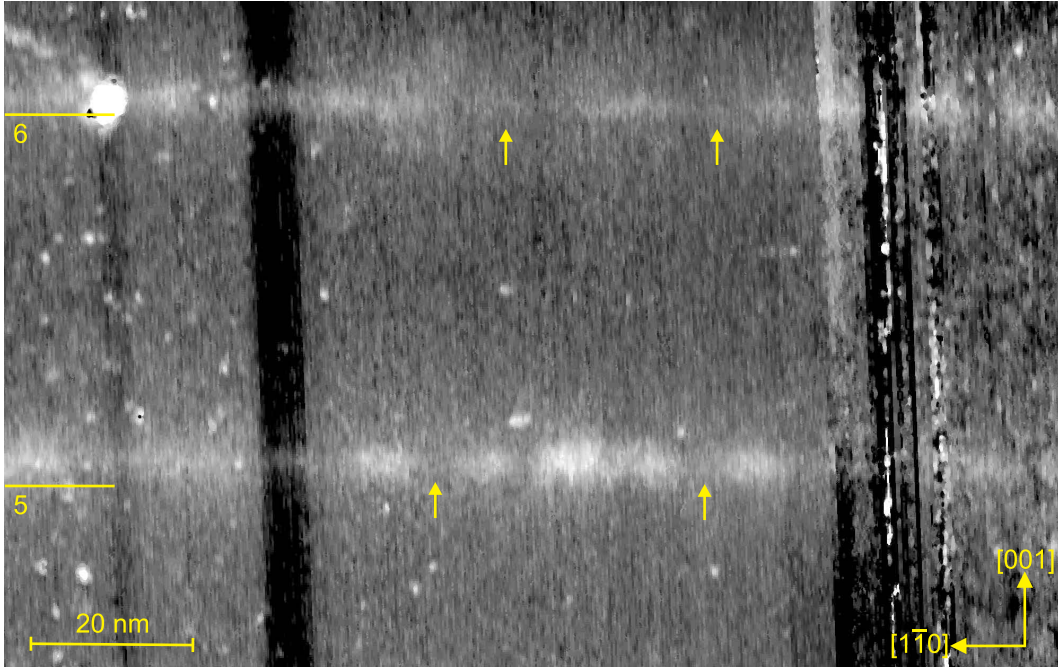


Figure 4.4: Filled-state XSTM image showing (In,Ga)As layers 5 and 6. The yellow arrows exemplarily point to the slightly visible wetting layer. The image was taken at a sample voltage $V_T = -3.9$ V and a tunneling current $I_T = 30$ pA.

For a closer investigation of these nanostructures and the regions in between, high-resolution XSTM empty-state images are shown in Figs. 4.6 and 4.7. As expected from the nominally identical growth parameters both layers (5 and 6) show the same growth behavior. In Fig. 4.6 (a,c) a typical single quantum dot within layer 6 is shown, which exhibits a trapezoidal cross-section, as highlighted by the yellow lines in Fig. 4.6 (c). These findings are also identical to the nanostructures within layer 5,

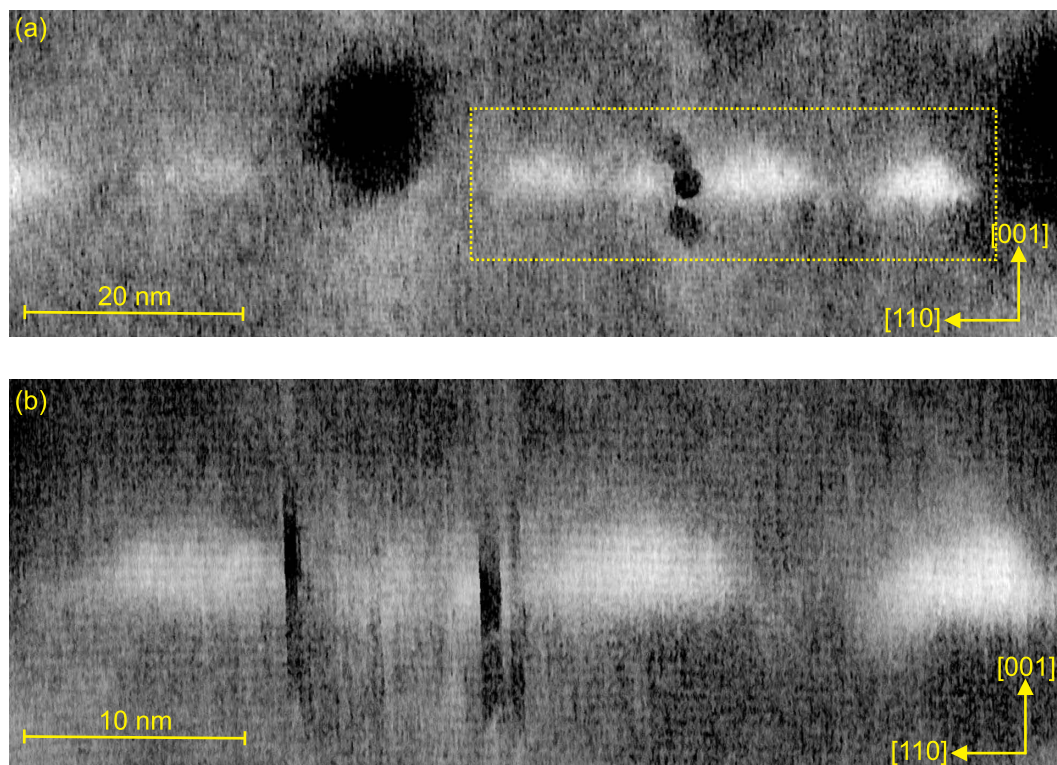


Figure 4.5: Empty-state XSTM images showing layer 6. The dotted lines in (a) highlight the region which has been further investigated with higher resolution in (b). Both images were taken at a sample voltage $V_T = +4.0$ V and a tunneling current $I_T = 40$ pA.

exemplarily shown by the two neighboring nanostructures in Fig. 4.6 (b,d). Hence, also these quantum dots are considered to have a truncated pyramidal shape.

For this sample (layers 5 and 6), a statistical analysis of 40 identified quantum dots on a total scanned range of about 870 nm along the layers results in values of 9.2 nm for the average base length and 13.6 ML for the average quantum dot height, while the observed maximum height is 20 ML. Using Equation (2.2), the areal density for the quantum dots can be determined to about $4.2 \times 10^{11} \text{ cm}^{-2}$ in these layers. Compared to the nominally identically $\text{In}_{0.25}\text{Ga}_{0.75}\text{As}/\text{GaAs}$ layers grown with MOVPE (see Section 3.2) the quantum dots show a similar areal density and sizes of the same magnitude. A further comparison will be given in Section 4.2.3. A structuring within the quantum dots like the observed reversed-cone geometry for the MOVPE quantum dots cannot be fully supported here, at least not from the visual impression of the presented images. A slightly brighter appearance within the quantum dot center in Fig. 4.6 (a,b) may only be guessed by the expert eye.

A conclusion about the formation of quantum rings is also difficult as there are no images with an *overlapping* of two neighboring small structures. But this might not

necessarily be due to the absence of quantum rings. Most of the images were taken in empty-state mode where the group-III atoms (indium, gallium) are directly imaged. Thus, such thin *overlapping* areas, which should be imaged when a quantum dot is cleaved close to its center may also appear with less contrast in the STM image due to a low indium content. Together with the moderate image quality as compared with the experiments on the MOVPE samples (see Sections 3.2 and 3.3.2), this could hinder the visual observation of quantum rings in the present case.

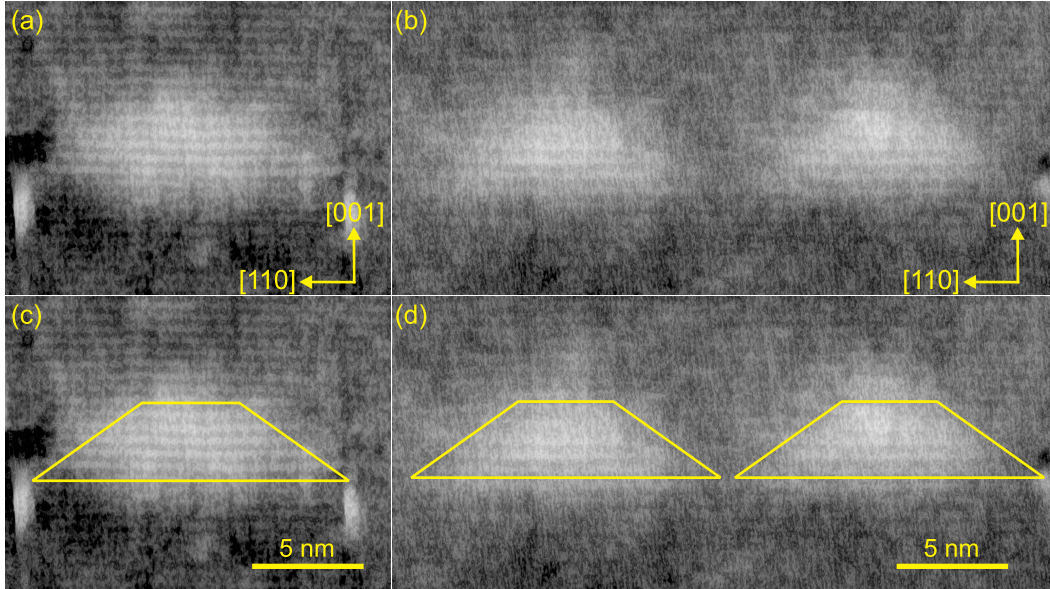


Figure 4.6: Empty-state XSTM images of (a,c) a quantum dot (layer 6) and (b,d) two neighboring quantum dots (layer 5). The images were taken at a sample voltage $V_T = +3.5$ V for (a,c) and at $V_T = +2.9$ V for (b,d), but both at a tunneling current $I_T = 40$ pA. The contours of the nanostructures are marked by the solid lines.

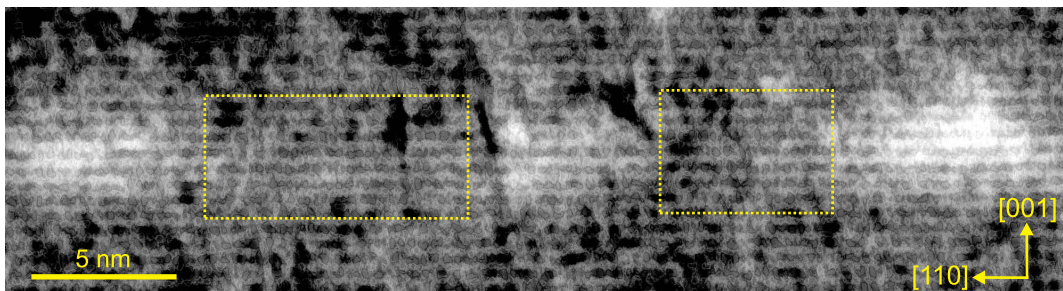


Figure 4.7: Empty-state XSTM image showing quantum dots in layer 5. The dotted lines highlight regions in between the quantum dots where a wetting layer is supposed to be located. The image was taken at a sample voltage $V_T = +3.4$ V and a tunneling current $I_T = 40$ pA.

Figure 4.7 shows an empty-state high-resolution XSTM image of a quantum dot region in layer 5. Here, the dotted lines highlight regions in between the quantum dots, where in a Stranski-Krastanow growth a wetting layer is supposed to be located. As already also visible in Fig. 4.5 (a,b), there is no direct observation of a wetting layer in empty-state images, where the group-III atoms (indium, gallium) are directly imaged, but a slight indication of a wetting layer is found in the rare filled-state images (as shown in Fig. 4.4), where the group-V atoms (arsenic, phosphorus) are imaged. These findings from the visual impression of the (In,Ga)As layer already give the hint that no indium is present within the wetting layer and it therefore would consist of Ga(As,P), which would be also in accordance to the comparable MOVPE-grown layers.

4.2.2 XSTM results: stoichiometry analysis

For a quantitative evaluation of the XSTM data, again the local stoichiometry is analyzed by evaluating the local lattice parameter (analogous to Section 3.2.3).

Quantum dots Figure 4.8 shows stoichiometry profiles of a well-resolved quantum dot within layer 6. The quantum dot has been analyzed in different parts: the entire quantum dot region, the quantum-dot sides, and the quantum-dot center. In Fig. 4.8 (b) the profile of the local lattice parameter averaged over the entire quantum dot area is shown, as highlighted by the green box in Fig. 4.8 (a). In accordance with the image contrast in Fig. 4.8 (a,c), where the quantum dot shows a maximum height of about 12 ML, the local lattice parameter in all the graphs in Fig. 4.8 (b,d) rises to higher values (as compared to the GaP lattice parameter) in the same extension. The local lattice parameter reaches values being higher than the one for pure GaAs in GaP, which again proves the incorporation of indium within the quantum dots. At the quantum-dot center, the local lattice parameter is found to be a little higher at the quantum dot top than at its base, which indicates a slight material concentration of indium at the top. But as such a behavior appears as well at the quantum-dot sides, this contradicts a reversed-cone stoichiometry profile, which was present in the comparable MOVPE quantum dots. Obviously, there is a significant undershoot of the local lattice parameter indicating a strong compression of the material underneath the quantum dot. Taking the scale bar for a complete group-V exchange to arsenic within the quantum dots into account, as discussed in Section 3.2, here the local indium content reaches up to 30% (even when not including the strong compression underneath, which shifts the indium content to even higher values).

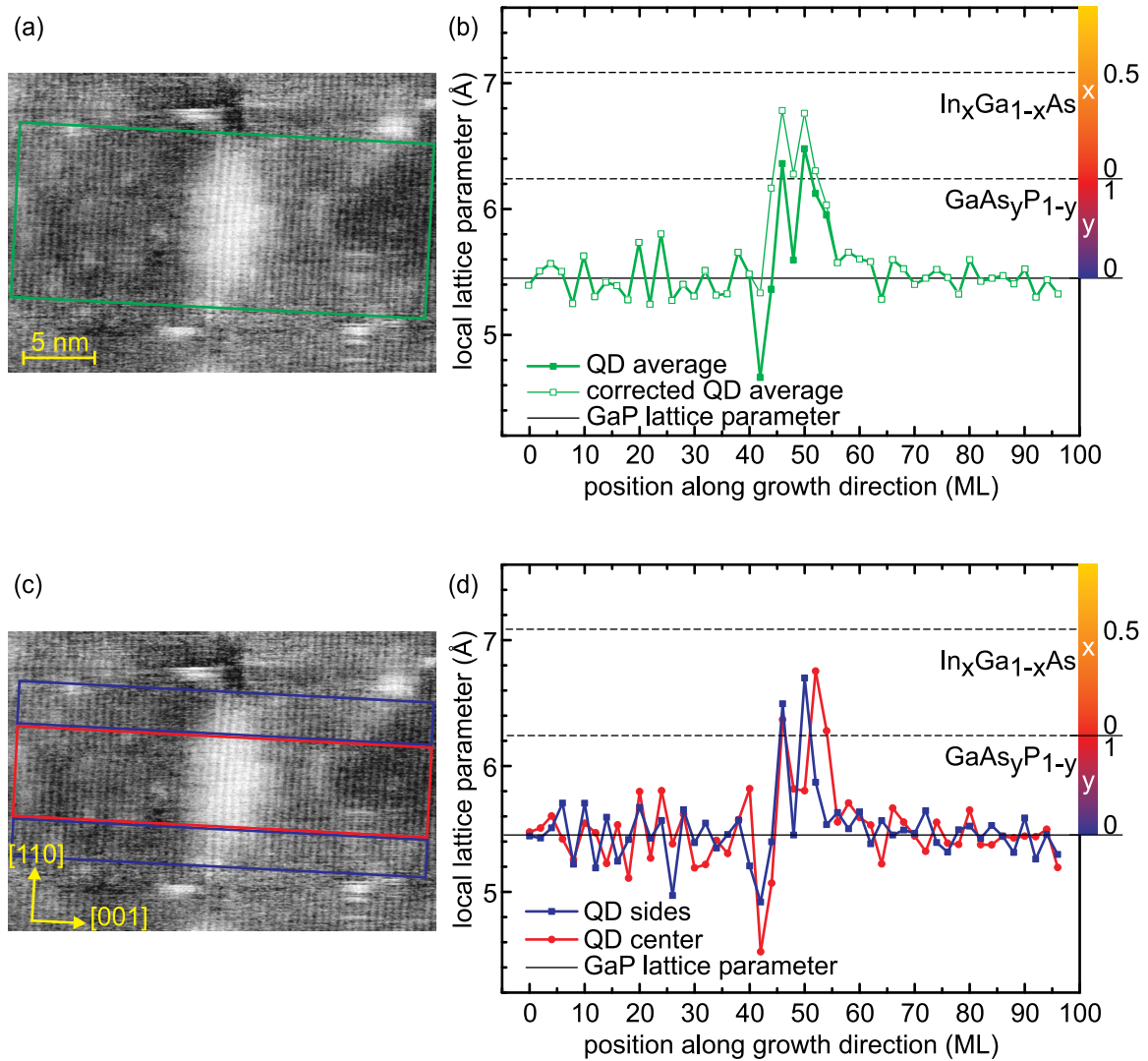


Figure 4.8: (a,c) Empty-state XSTM image of a quantum dot. The evaluated regions are highlighted by the colored boxes. The images were taken at $V_T = +3.5$ V and $I_T = 40$ pA. (b,d) Corresponding evaluation of the local lattice parameter and the related stoichiometric composition along growth direction. The graphs show the evaluated data (b) for the entire quantum dot region in green squares and (d) for separated profiles of the quantum-dot center in red dots and for the quantum-dot sides in blue squares. The corrected data for which the compression around the quantum dot base is taken into account is represented by the green open squares in (b).

Wetting layer Figure 4.9 (a) shows an image of a quantum dot region in layer 5. Here, the stoichiometry profile is taken for the region in between the two quantum dots as highlighted by the green box. Figure 4.9 (b) shows the resulting profile for the local lattice parameter. Although the noise level of these data is high, the graph shows that the local lattice parameter is increased in a 2–4 ML wide region located at the center of the green box. This indicates the formation of a wetting layer during growth, as expected for the Stranski-Krastanow growth mode. Within the wetting layer region the local lattice parameter rises to values below the one for pure GaAs on GaP. This further confirms the absence of indium here in accordance with the visual appearance in the XSTM images.

Material content The total indium content inside the quantum dots amounts to about 1.7 ML, as it can be approximated from the corrected curve for the quantum dot average in Fig. 4.8 (a) taking the undershoot into account. Since about 21% of the growth surface is covered with quantum dots, as derived from their lateral extension and their density, it results that a total amount of about 0.4 ML indium is located within the quantum dots, which is in the range of the nominally deposited amount of 0.5 ML indium. This also indicates that the total deposited amount of indium is only located within the quantum dots.

The material content within the (assumed indium free) wetting layer can only be carefully approximated due to the high noise level. The local GaAs amount extracted from the curve in Fig. 4.9 (b) should lie below 3.0 ML, which then would result in a laterally averaged value below 2.4 ML of GaAs within the wetting layer covering about 79% of the growth surface.

Considering the average quantum-dot height one can carefully approximate the gallium content within the quantum dots, as summarized in Table 4.1, to a laterally averaged value of about 2.5 ML. This would result in an overall material content of 4.9 ML GaAs and 0.4 ML InAs within the layer. Thus, the value for the found material amount of GaAs is slightly higher than the nominally deposited amount of 4.5 ML. This may originate from a too high approximated local material value for the GaAs within the wetting layer due to the high noise level.

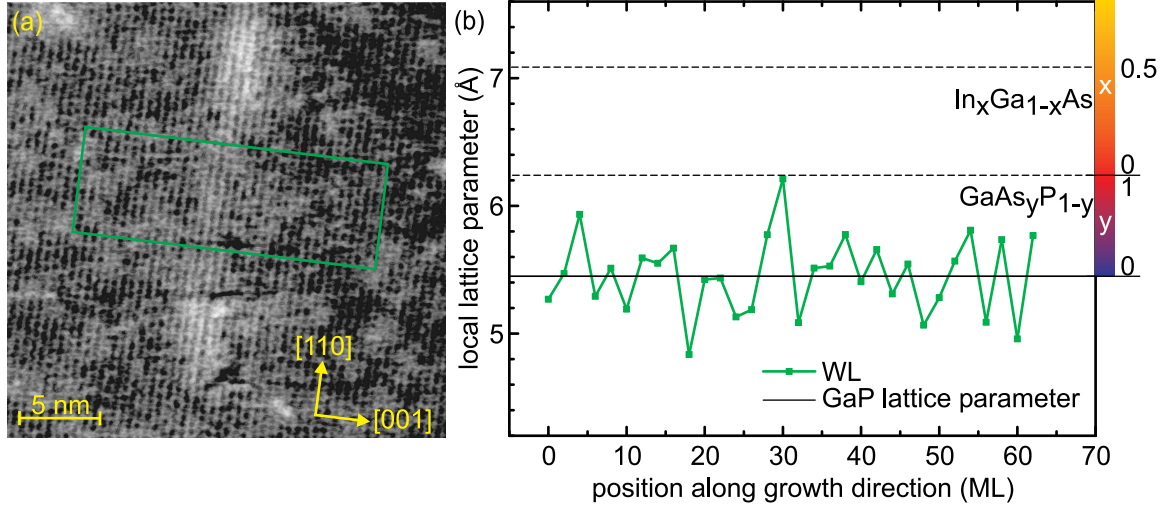


Figure 4.9: (a) Empty-state XSTM image of the wetting layer (layer 5). The evaluated region is highlighted by the colored box. The image was taken at $V_T = +3.4$ V and $I_T = 40$ pA. (b) Corresponding evaluation of the local lattice parameter and the related stoichiometric composition along growth direction. The graph shows the evaluated data in green squares.

Table 4.1: Stoichiometry data of the $\text{In}_{0.25}\text{Ga}_{0.75}\text{As}/\text{GaAs}$ quantum dot layer.

	Wetting Layer	Quantum Dots
Local approximated arsenic content from stoichiometry profile	≤ 3.0 ML	-
Local approximated indium content from stoichiometry profile	-	1.7 ML
Remaining gallium content from quantum dot height	-	11.9 ML
Growth surface coverage	79%	21%
Area averaged arsenic amount	≤ 2.4 ML	-
Area averaged indium amount	-	0.4 ML
Area averaged gallium amount	-	2.5 ML
Total material amount	4.9 ML GaAs + 0.4 ML InAs	
Nominal material amount	4.5 ML GaAs + 0.5 ML InAs	

4.2.3 Comparison between MBE and MOVPE Quantum Dots

In the following the results for the quantum dot layers prepared by the same nominally deposited material amount of 3.0 ML GaAs followed by 2.0 ML $\text{In}_{0.25}\text{Ga}_{0.75}\text{As}$, but being grown with different epitaxial methods, will be compared. Table 4.2 lists the XSTM results of the comparable quantum-dot layers grown with MOVPE (as presented in Section 3.2) and with MBE (as presented in Section 4.2).

Table 4.2: Results of comparable MOVPE and MBE quantum dots.

	MOVPE TU10350	MBE Yale20130725
Nominal material amount	3.0 ML GaAs + 2.0 ML $\text{In}_{0.25}\text{Ga}_{0.75}\text{As}$	
Results from XSTM image contrast		
Quantum dots		
shape	truncated pyramid	truncated pyramid
average base length	11.5 ML	9.2 nm
average height	≈ 9 ML	13.6 ML
areal density	$2.4 \times 10^{11} \text{ cm}^{-2}$	$4.2 \times 10^{11} \text{ cm}^{-2}$
Wetting layer		
height	2–5 ML	not observable
Results from XSTM data stoichiometry analysis		
Quantum dots		
material	(In,Ga)As	(In,Ga)As
indium localization	higher in QD center	higher in QD center
local indium content	up to 50%	up to 30%
	total indium	total indium
Wetting layer		
height	2–3 ML	2–4 ML
material	Ga(As,P)	Ga(As,P)
	no indium	no indium

From the visual inspection of the XSTM images the quantum dots show a similar appearance independent from the growth method. In both cases the quantum dots have the shape of a truncated pyramid. Also their average dimensions and their areal density are in the same range. In detail, in the MBE case the quantum dots are laterally a little smaller but higher than in the MOVPE case. The wetting-layer appearance cannot be compared by the image contrast as it was not observable in the MBE case due to the image quality and sample polarity. But a comparison of the stoichiometry data shows that both wetting layers have a similar height and both consist of Ga(As,P)

without any indium. On the other hand the evaluation of the data for the quantum dots shows that the indium is only located within the quantum dots, with its maximum concentration in the quantum dot center. In both cases the quantum dots consist of (In,Ga)As where the total supplied indium is located. In conclusion, both methods, MOVPE and MBE with nominally the same material supply, lead to self-assembled growth of quantum dot layers with very similar structural properties.

4.3 $\text{In}_{0.5}\text{Ga}_{0.5}\text{As}$ Quantum Dots in GaP

In the following the $\text{In}_{0.5}\text{Ga}_{0.5}\text{As}$ layers grown without a GaAs interlayer will be investigated in detail, again with respect to the XSTM image contrast and their stoichiometry.

4.3.1 XSTM results: image contrast analysis

Layer 1: 2.0 ML $\text{In}_{0.5}\text{Ga}_{0.5}\text{As}$

As already mentioned above, all the grown $\text{In}_{0.5}\text{Ga}_{0.5}\text{As}$ layers appear much darker in the XSTM images as compared with the $\text{In}_{0.25}\text{Ga}_{0.75}\text{As}/\text{GaAs}$ layers. Figure 4.10 shows an overview image, in empty-state mode, of layer 1 containing the lowest amount (only 2.0 ML) of $\text{In}_{0.5}\text{Ga}_{0.5}\text{As}$. Among all the layers within this sample layer 1 shows the weakest contrast. Although the contrast is adjusted to the layer it is only slightly visible. A closer view can be found in Fig. 4.11, with the image again taken in empty-state mode. The atomic chains along the $[1\bar{1}0]$ direction are clearly visible. The area of the layer is highlighted by the dotted lines and appears inhomogeneous along both the $[1\bar{1}0]$ and the $[001]$ direction. Images with higher resolution, as shown in Fig. 4.12, reveal that the layer shows no clear borderline to the GaP matrix material underneath. Instead the (In,Ga)As material is distributed over several ML along growth direction. Regarding the expected quantum dot formation, from the image contrast one may only consider the presence of small material agglomerations within this layer.

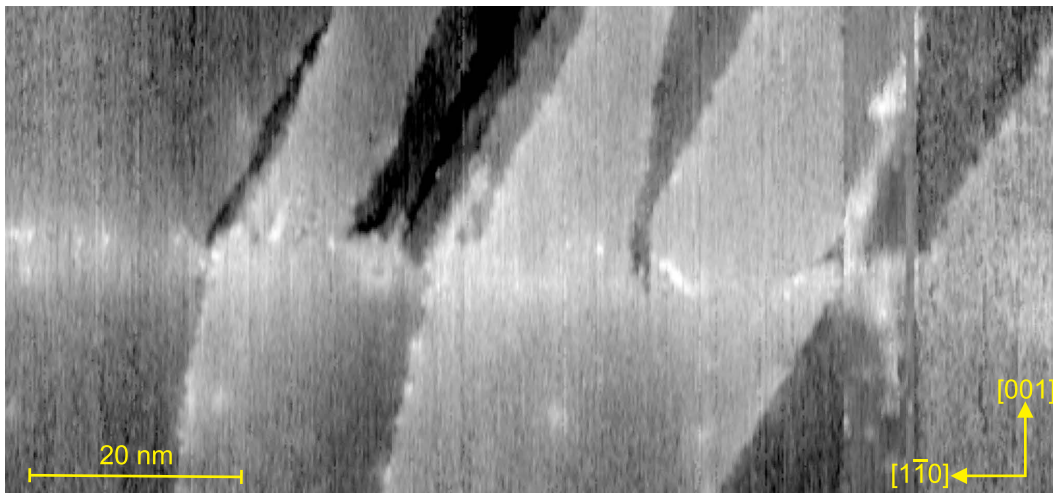


Figure 4.10: Empty-state XSTM image showing layer 1. The image was taken at a sample voltage $V_T = +2.9$ V and a tunneling current $I_T = 40$ pA.

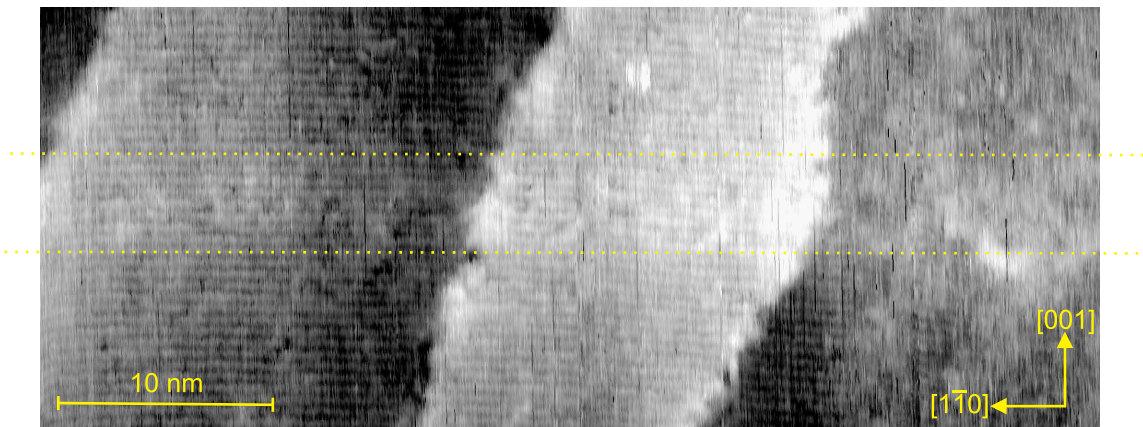


Figure 4.11: Empty-state XSTM images showing layer 1. The area of the layer is highlighted by the dotted lines. The image was taken at a sample voltage $V_T = +3.1$ V and at a tunneling current $I_T = 40$ pA.

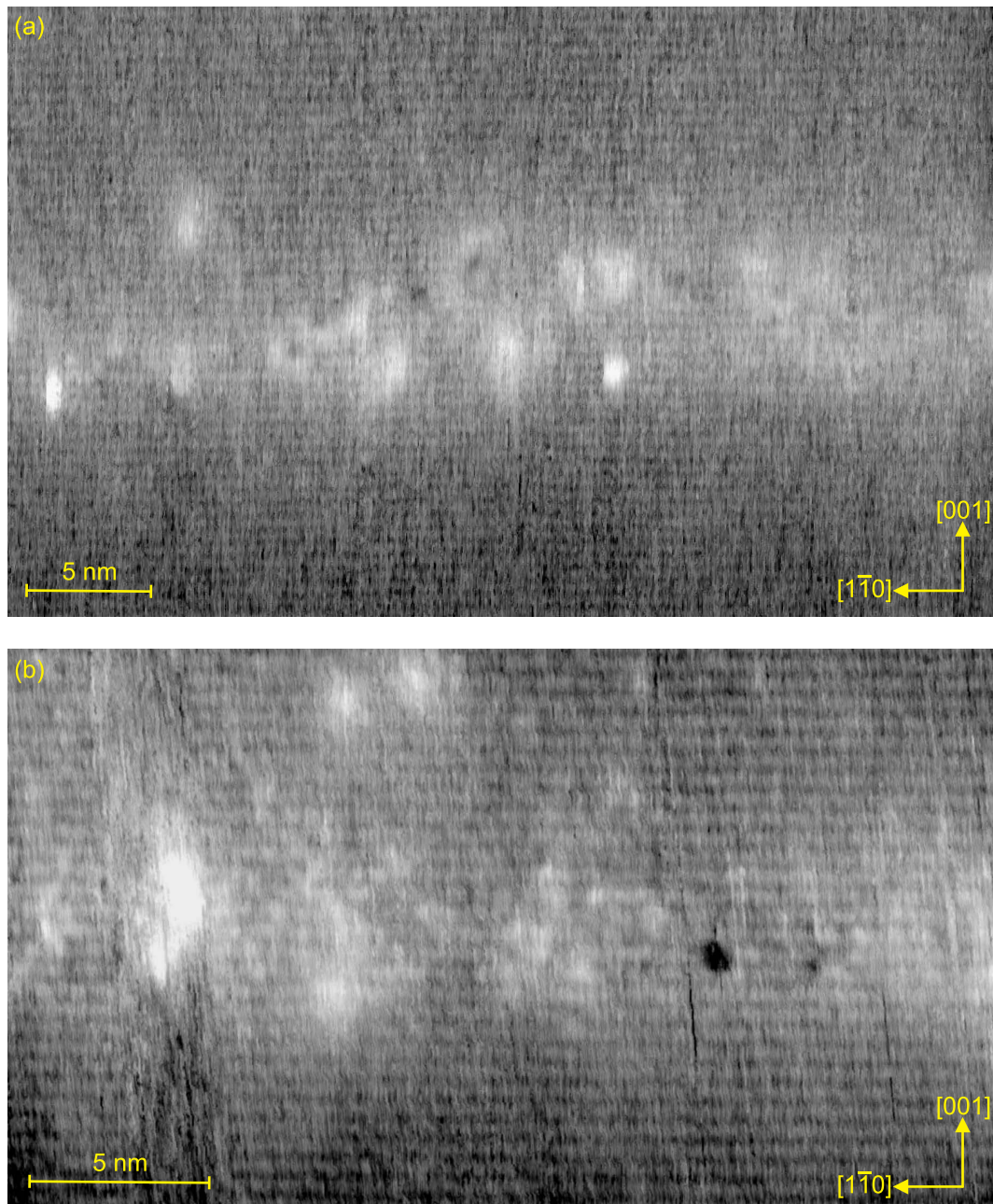


Figure 4.12: Empty-state XSTM images showing layer 1. The images were taken at a sample voltage (a) $V_T = +2.9$ V and (b) $V_T = +3.0$ V and both at a tunneling current $I_T = 40$ pA.

Layers 2 and 3: 3.0 ML $\text{In}_{0.5}\text{Ga}_{0.5}\text{As}$

Figures 4.13 and 4.14 show overview images of layers 2 and 3 taken in filled-state and empty-state imaging mode, respectively. Although both images are characterized by many scan-induced artifacts and adatoms/holes on the surface, the layers are clearly visible here. This can be attributed to the higher amount of deposited material, i.e. 3.0 ML $\text{In}_{0.5}\text{Ga}_{0.5}\text{As}$, in comparison with layer 1, so that layers 2 and 3 appear brighter and thicker. Furthermore, more pronounced agglomerations seem to be already observable. As expected, both layers show a similar appearance due to the identical growth parameters.

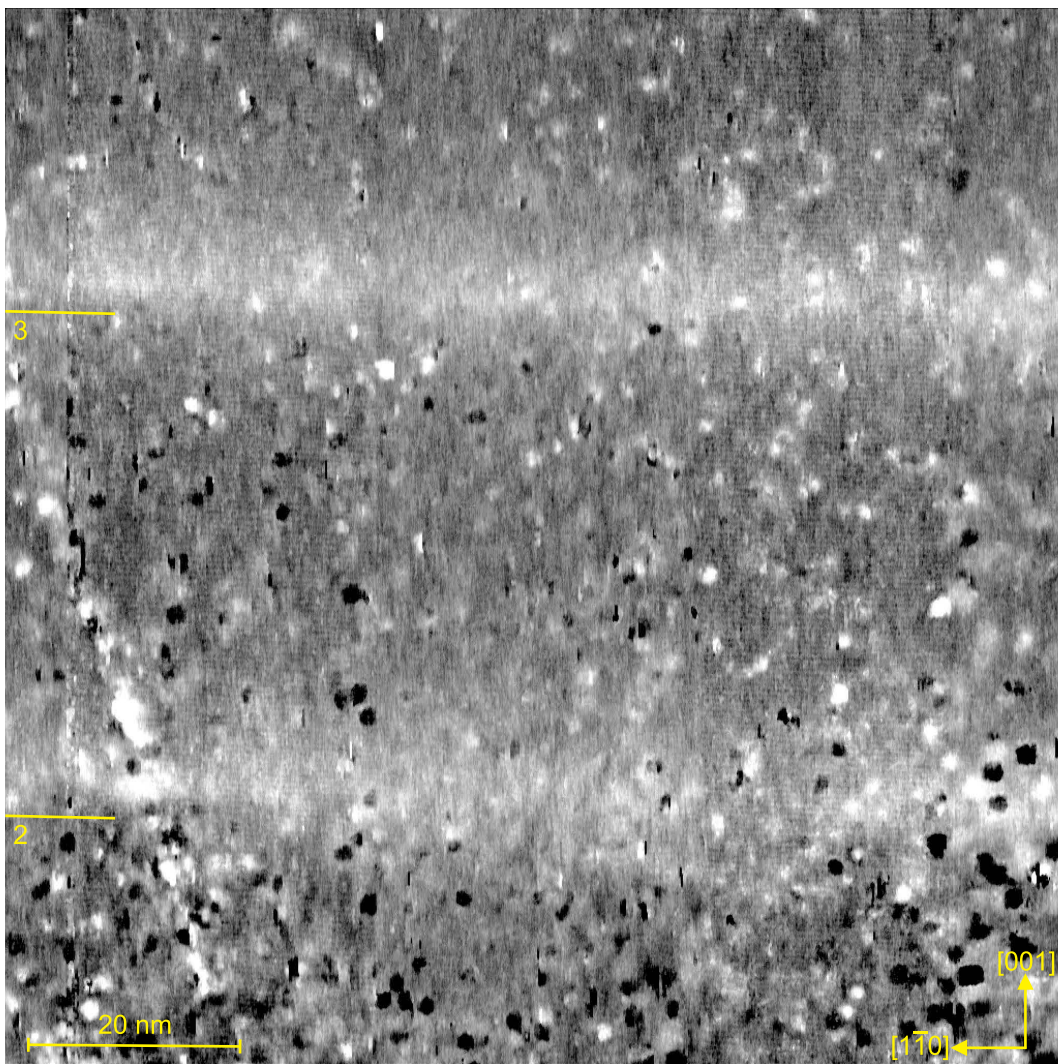


Figure 4.13: Filled-state XSTM overview image showing layers 2 and 3. The image was taken at a sample voltage $V_T = -3.7$ V and a tunneling current $I_T = 30$ pA.

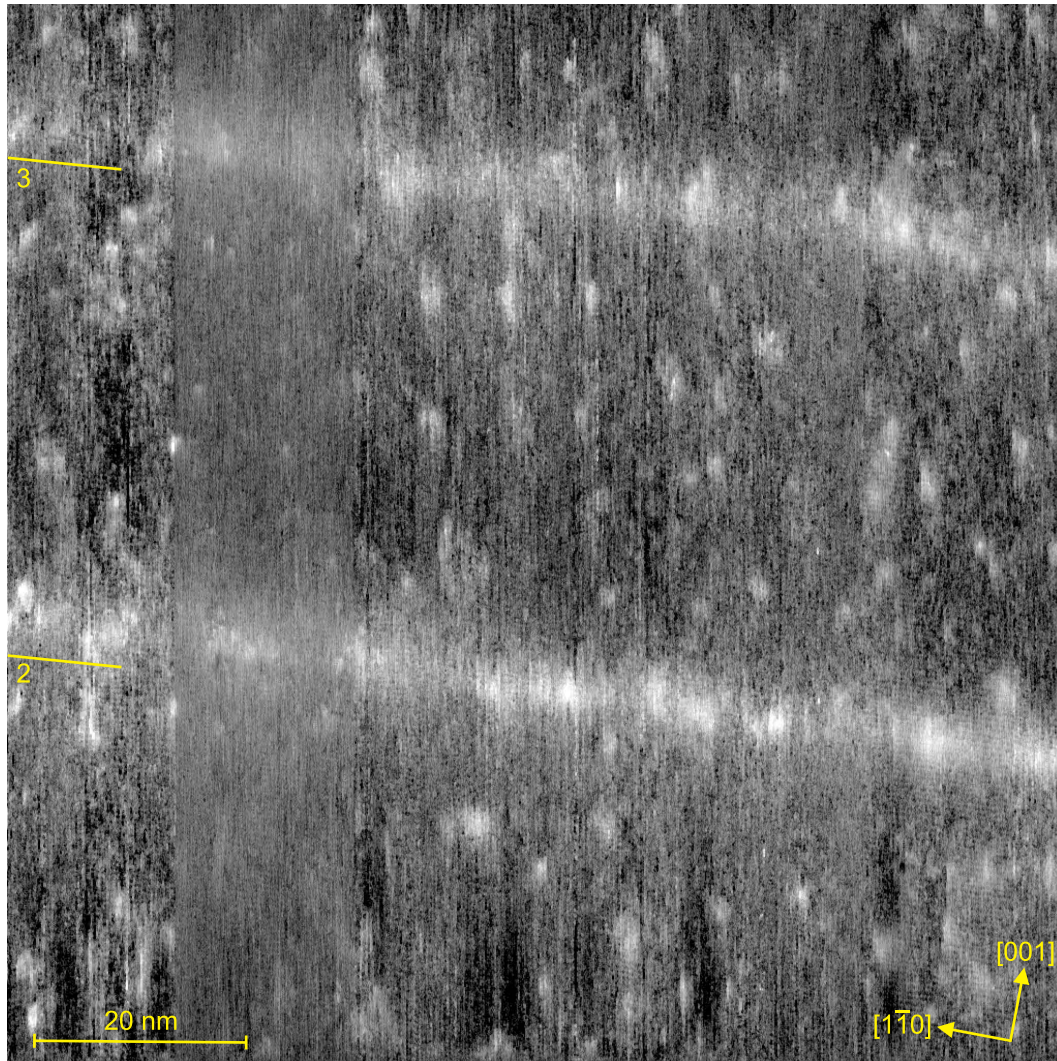


Figure 4.14: Empty-state XSTM overview image showing layers 2 and 3. The image was taken at a sample voltage $V_T = +4.3$ V and a tunneling current $I_T = 40$ pA.

A closer investigation of layer 2 can be found in Fig. 4.15. Again the surface quality makes a clear inspection of the layer difficult. Nevertheless, at the clean and hole-free parts of the surface the atomic chains are resolved and the images indicate the formation of agglomerations within the layer. One of the rarely observed more pronounced agglomerations is shown in Fig. 4.16. As highlighted by the dashed line in Fig. 4.16 (b) one could assume a trapezoidal cross-section of the agglomeration being typical for quantum dots. In this case it has a base length of about 12 nm and a height of 10 ML. Unfortunately, a statistical analysis on these quantum-dot like structures is not possible due to the lack of sufficient data, where these quantum dots were only rarely observed.

Figure 4.17 shows a filled-state image of layer 3 confirming, as expected, a similar appearance in comparison to layer 2, since both were grown identically.

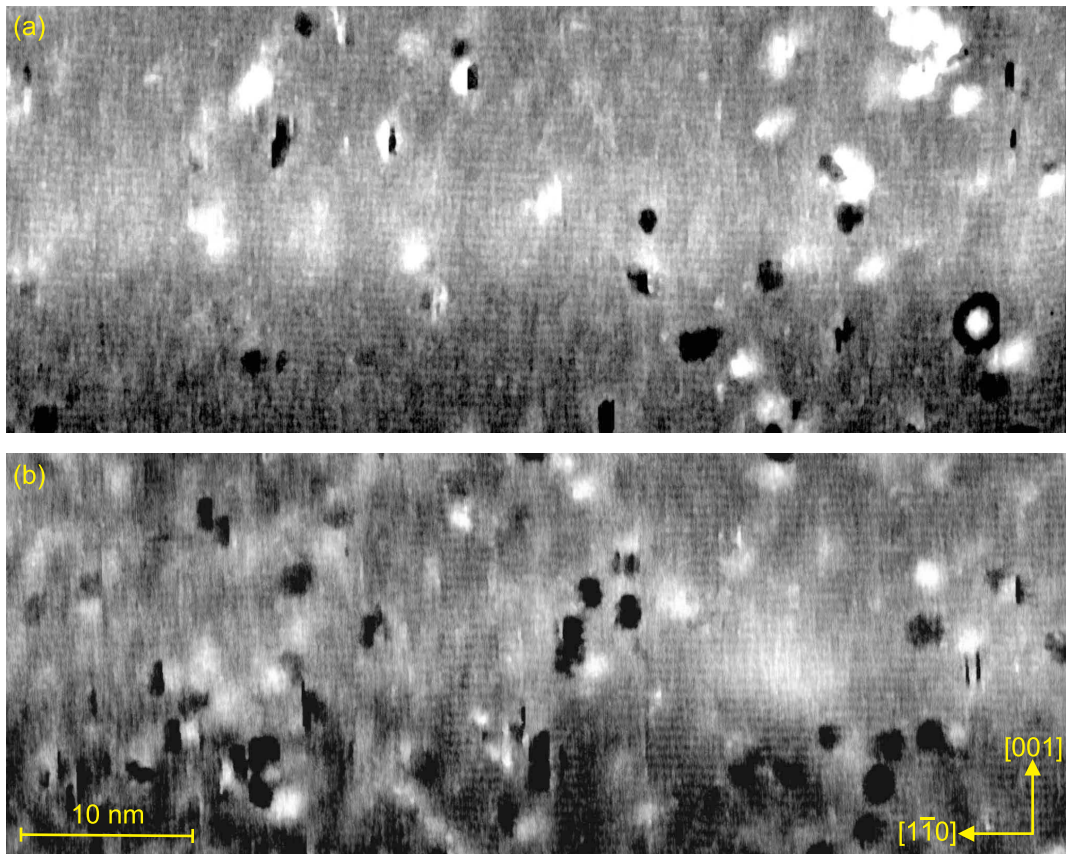


Figure 4.15: Filled-state XSTM images showing layer 2. The images were taken at a sample voltage (a) $V_T = -3.9$ V and (b) $V_T = -3.8$ V and both at a tunneling current $I_T = 30$ pA.

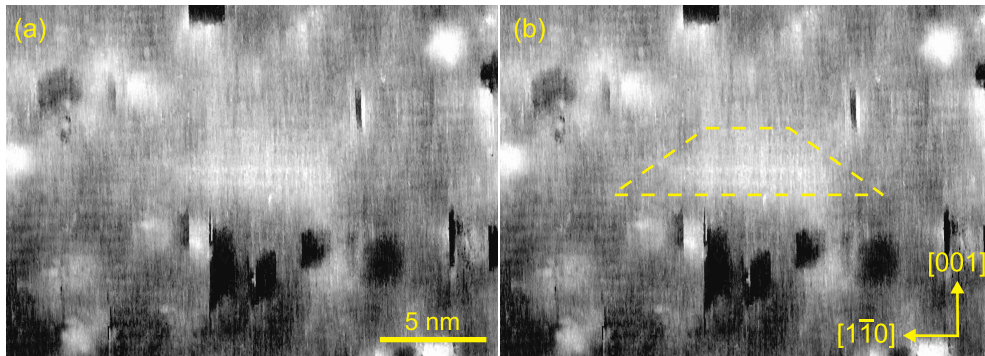


Figure 4.16: Filled-state XSTM image showing a quantum dot within layer 2. The contours of the quantum dot is marked by the dashed line in (b). The image was taken at a sample voltage $V_T = -3.7$ V and a tunneling current $I_T = 30$ pA.

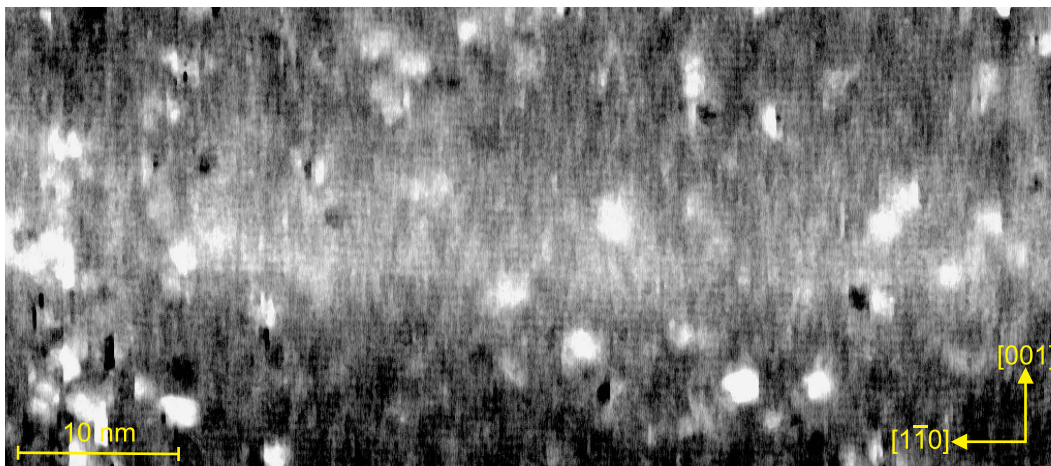


Figure 4.17: Filled-state XSTM image showing layer 3. The image was taken at a sample voltage $V_T = -3.7$ V and a tunneling current $I_T = 30$ pA.

Layer 4: 4.0 ML $\text{In}_{0.5}\text{Ga}_{0.5}\text{As}$

Figure 4.18 shows again an empty-state overview image of layers 3–5. The different appearances in contrast and brightness of the layers are clearly visible. Layer 4 is more pronounced than layer 3. But in comparison, layer 5 shows a much brighter appearance with a clear quantum-dot formation as already described before in Section 4.2.

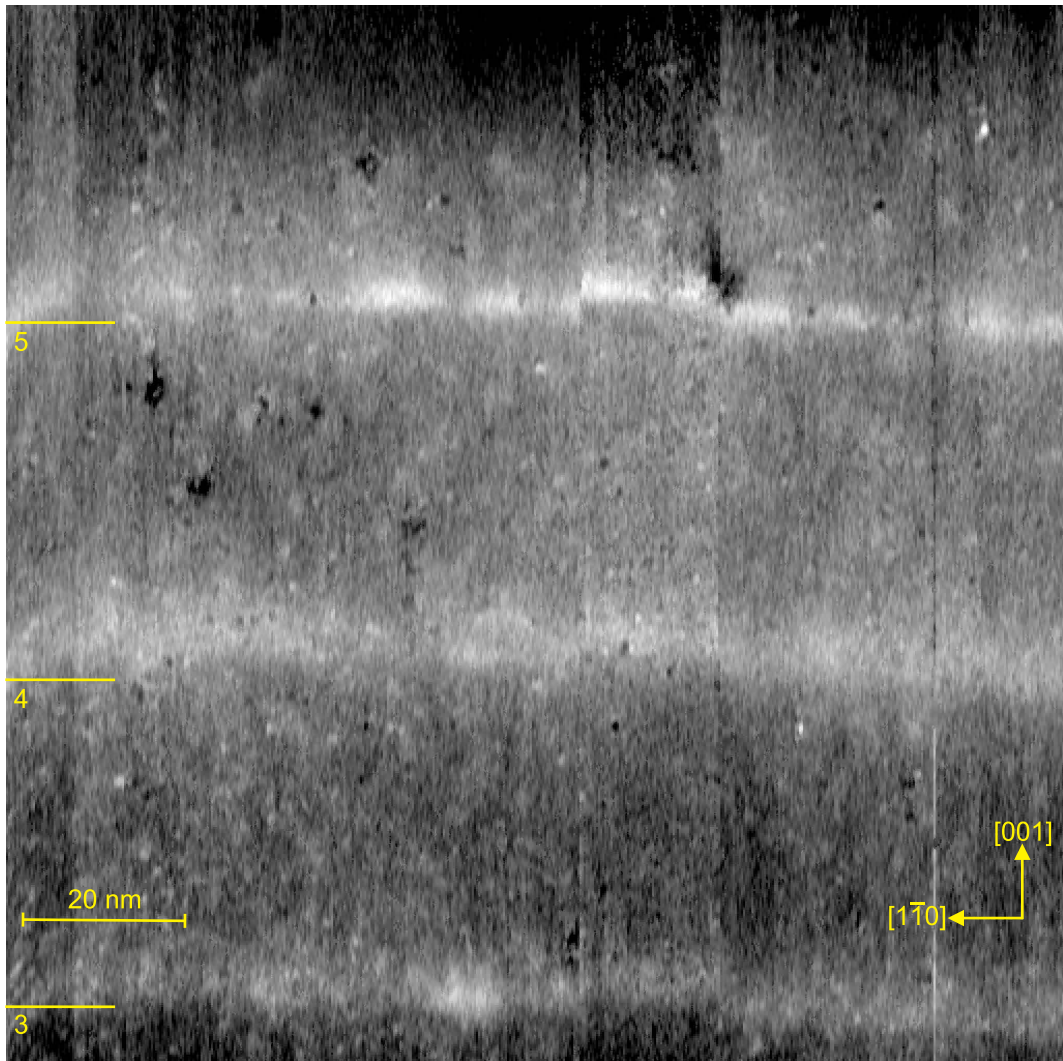


Figure 4.18: Empty-state XSTM overview image showing layers 3–5. The image was taken at a sample voltage $V_T = +4.3$ V and a tunneling current $I_T = 40$ pA.

The surface in overview images of layers 3 and 4 (Fig. 4.19), respectively layers 4 and 5 (Fig. 4.20), taken in filled-state mode, is again characterized by many adatoms and occasional atomic resolution underneath. Concerning layer 4, similar observations as in the image taken in empty-state mode can be made, i.e. that it appears more pronounced than layer 3 but not as bright as layer 5 which shows clear quantum-dot formation.

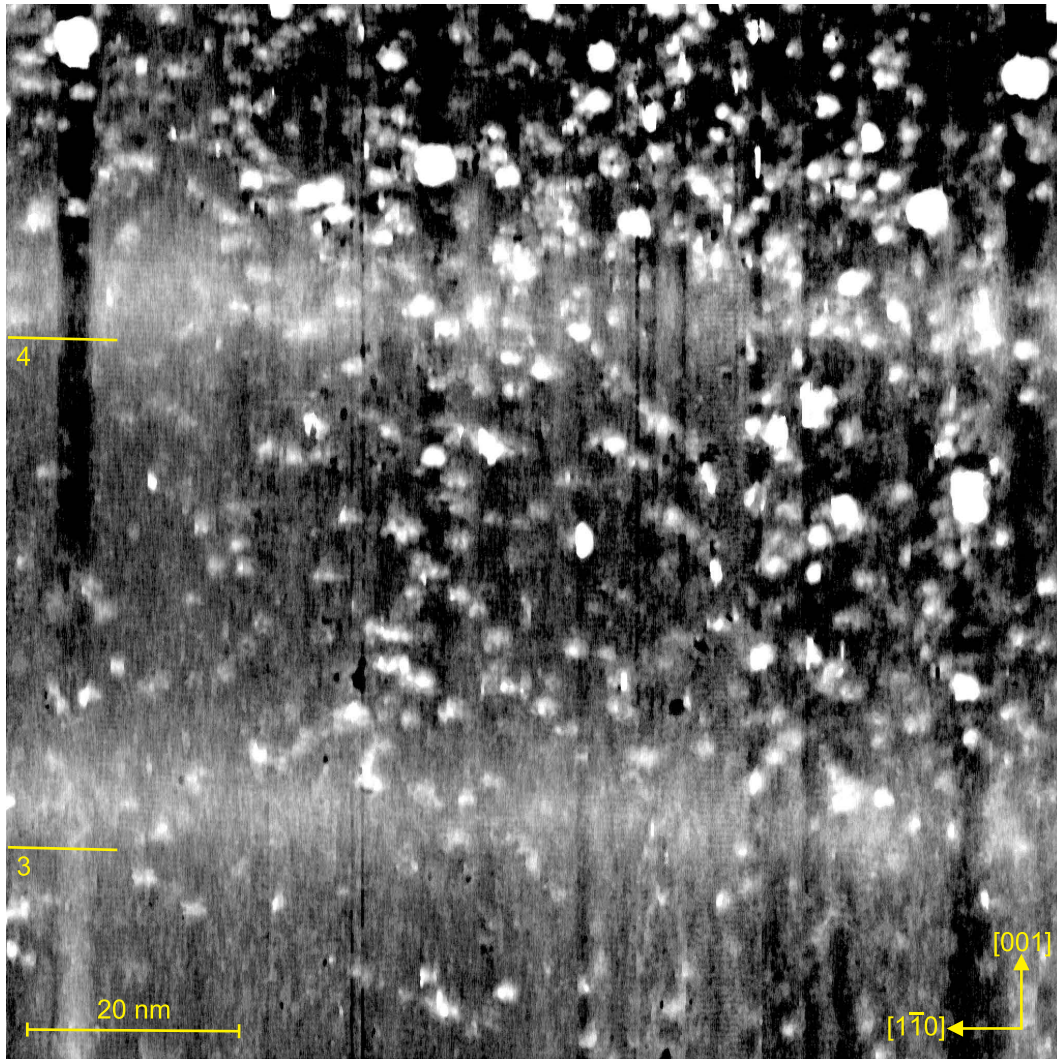


Figure 4.19: Filled-state XSTM overview image showing layers 3 and 4. The image was taken at a sample voltage $V_T = -4.0$ V and a tunneling current $I_T = 30$ pA.

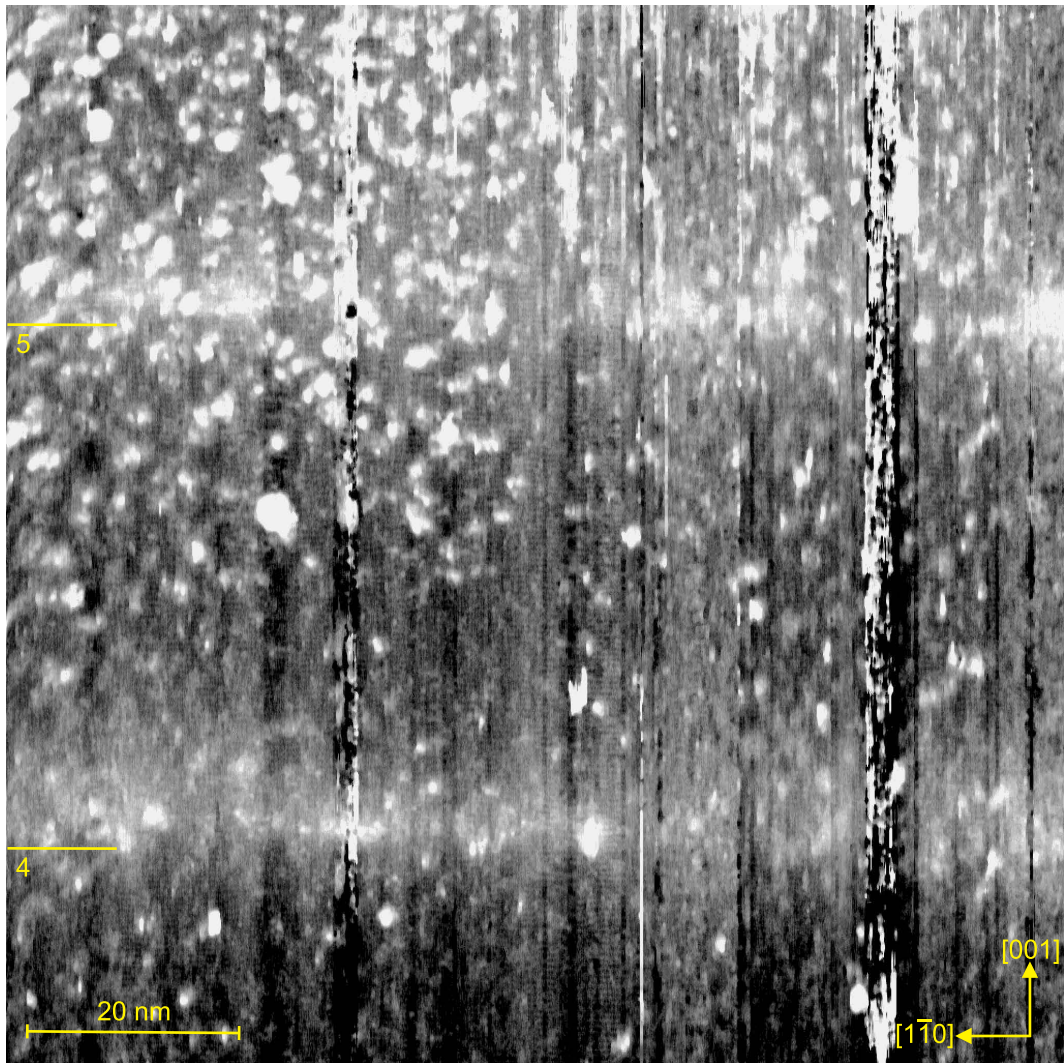


Figure 4.20: Filled-state XSTM overview image showing layers 4 and 5. The image was taken at a sample voltage $V_T = -4.1$ V and a tunneling current $I_T = 30$ pA.

A more detailed view of layer 4 can be found in Fig. 4.21, with the image again taken in filled-state mode. The image quality again makes general statements on layer 4 difficult, e.g. on the layer thickness. Nevertheless, layer 4 appears inhomogeneous and has no sharp borderline to the GaP substrate underneath. Even more, it seems at least from the highly-resolved image in Fig. 4.21 (b) that the layer consists of presumably InAs-rich agglomerations of bright contrast separated by parts of darker contrast attributed to more GaP-rich material. This observation is further supported by the few analyzable images taken in empty-state mode shown in Fig. 4.22.

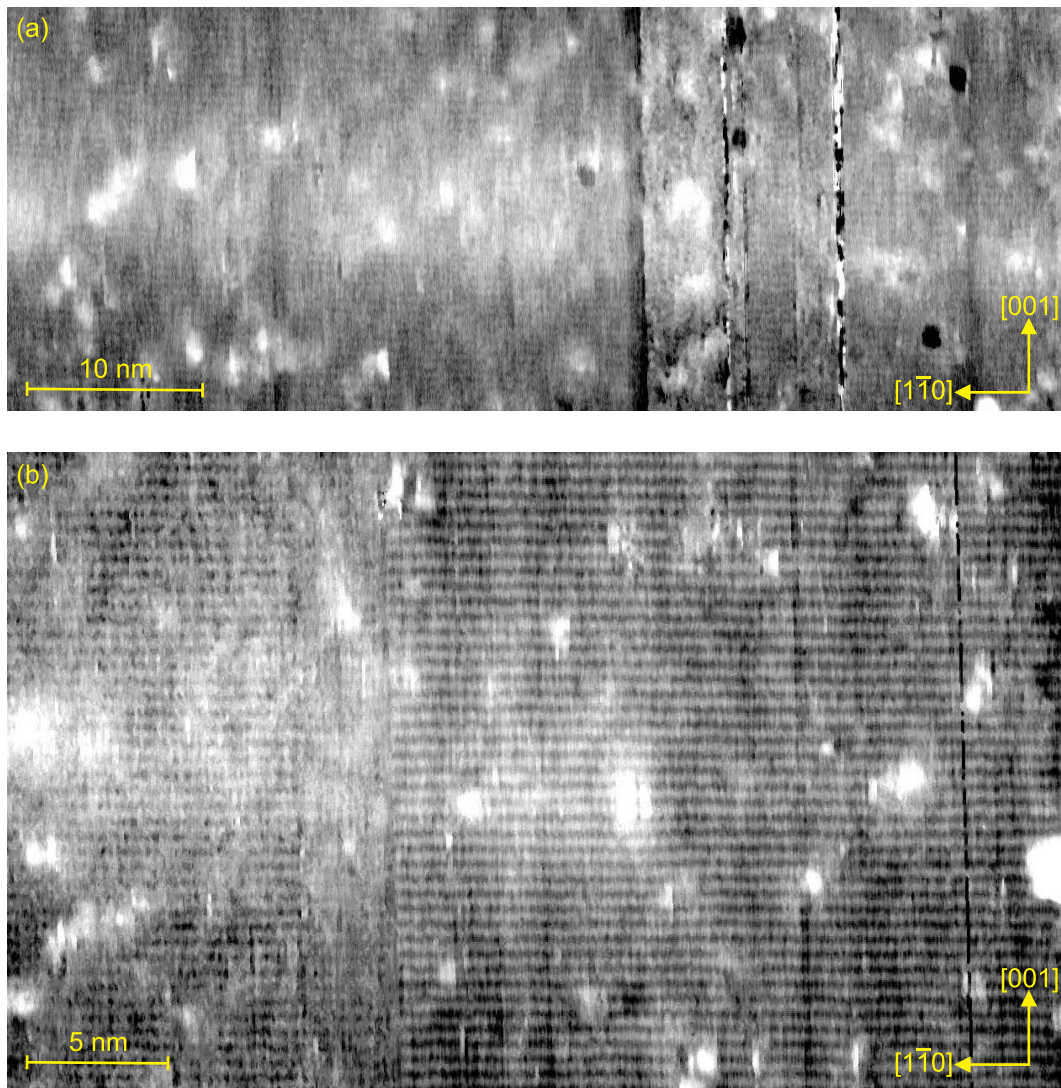


Figure 4.21: Filled-state XSTM images showing layer 4. The images were taken at a sample voltage $V_T = -3.7$ V and a tunneling current $I_T = 30$ pA.

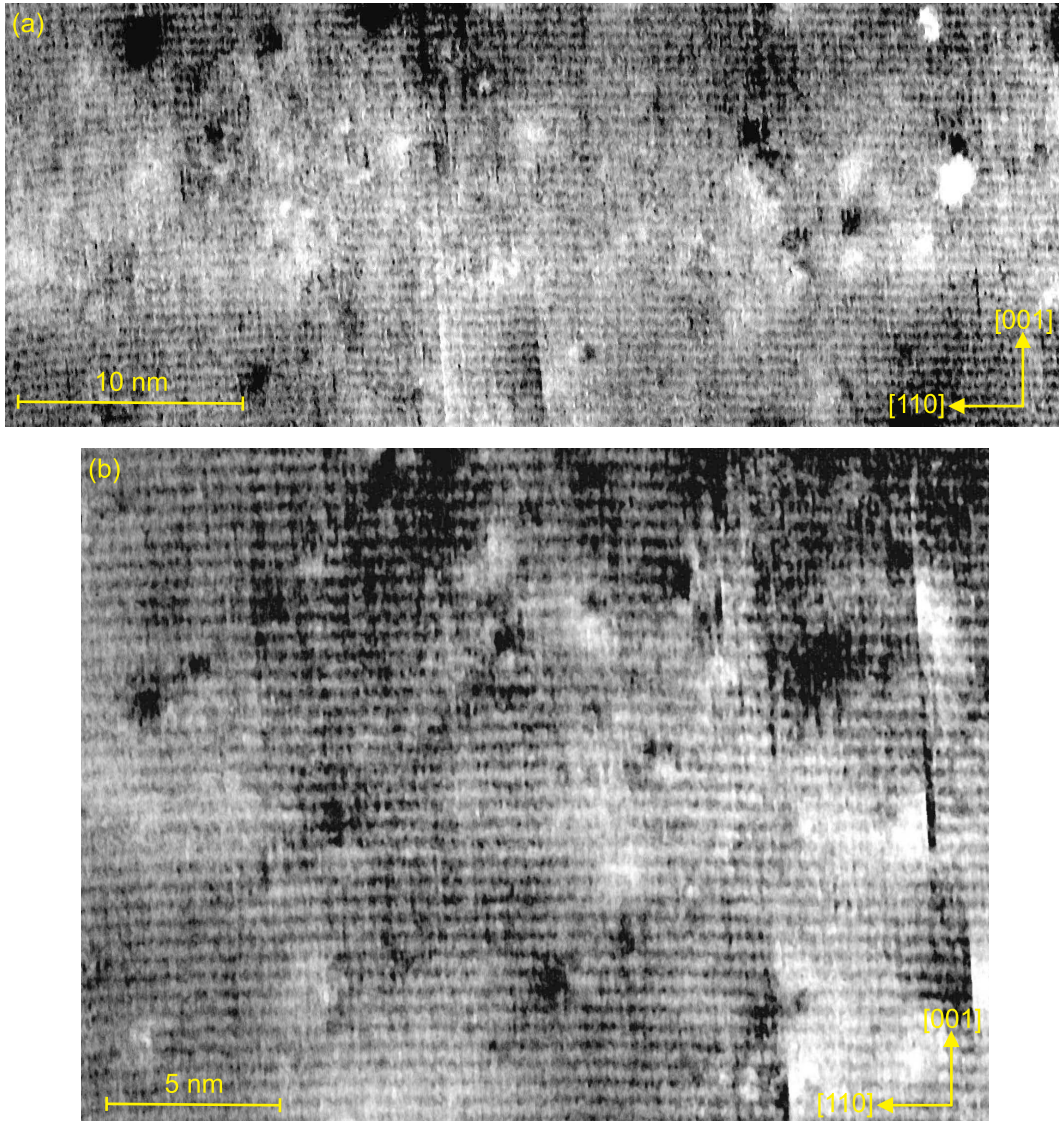


Figure 4.22: Empty-state XSTM images showing layer 4. The images were taken at a sample voltage (a) $V_T = -3.1$ V and (b) $V_T = -3.0$ V and both at a tunneling current $I_T = 40$ pA.

4.3.2 XSTM results: stoichiometry analysis

A further quantitative analysis of the different contrasted regions of the layers will be given in the following. However, the data quality here results in much higher noise levels, making a quantitative evaluation of the local stoichiometry more difficult than for the samples in the previous Sections 3.2.3, 3.3.3, and 4.2.2.

Layer 1: 2.0 ML $\text{In}_{0.5}\text{Ga}_{0.5}\text{As}$

Figure 4.23 shows the evaluation of the local lattice parameter for analyzable regions in layer 1. For these regions [as highlighted by the colored boxes in Fig. 4.23 (a)] the local lattice parameter shows a strong variation along growth direction.

For the more extended region 1 there is a significant rise of the local lattice parameter for about 6 ML at the position of the layer corresponding to the bright contrast in Fig. 4.23 (a). For one data point the local lattice parameter rises to a value being even a little higher than the one for pure GaAs in GaP which could indicate the presence of indium here. As already discussed in Section 3.3.3 such a behavior is not a strong evidence for local indium concentration within the layer, as it could also be due to a possible noise-related shift of the data point. Nevertheless, there is also only 1 ML of indium (and 2 ML of arsenic) deposited. In case of a more homogeneous distribution of the indium material, no significant signal in the local lattice parameter would be expected. In the smaller region 2 with a much cleaner surface there is not such an indium signal which would mean that for this local region there is a more indium-free intermixing of Ga(As,P) or a quaternary intermixing of an (In,Ga)(As,P) alloy.

Another evaluated area of layer 1 is shown in Fig. 4.24. Here, the curve for the local lattice parameter for the total region 1 is characterized by less noise. Only in the region where the layer is visible in the image of Fig. 4.24 (a) a significant rise compared to the GaP local lattice parameters occurs for a 6 ML wide region, but lying still below the value for 100% GaAs in GaP. For the center region 2 in Fig. 4.24 (a) containing the brighter part of the layer the curve is characterized by more noise but shows a rise of the local lattice parameter at the layer's position which could indicate the presence of indium. This may indicate the formation of a more local agglomeration of indium within a surrounding Ga(As,P) layer or quaternary (In,Ga)(As,P) layer.

However, a clear interpretation on basis of these few data cannot be easily made.

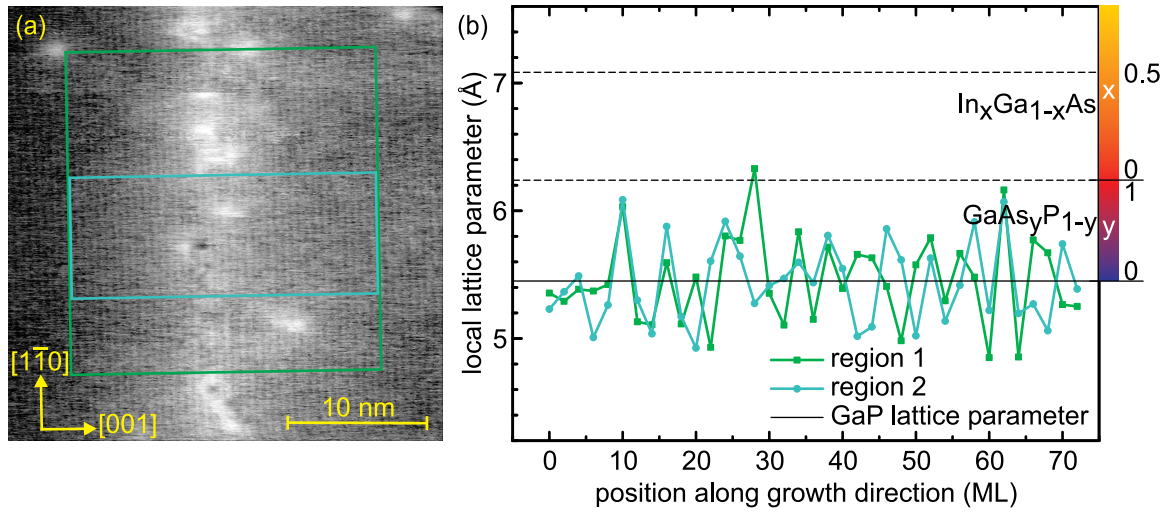


Figure 4.23: (a) Empty-state XSTM image of layer 1. The evaluated regions are highlighted by the colored boxes. The image was taken at $V_T = +2.7$ V and $I_T = 40$ pA. (b) Corresponding evaluation of the local lattice parameter and the related stoichiometric composition along growth direction. The graphs show the evaluated data for two regions in separated profiles for region 1 in green squares and for region 2 in light blue dots.

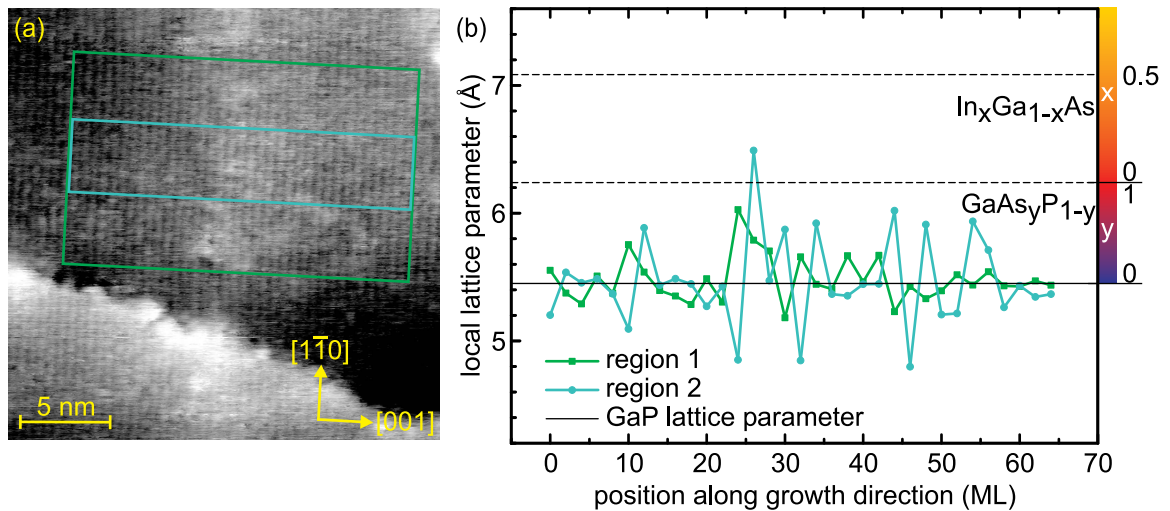


Figure 4.24: (a) Empty-state XSTM image of layer 1. The evaluated regions are highlighted by the colored boxes. The image was taken at $V_T = +3.1$ V and $I_T = 40$ pA. (b) Corresponding evaluation of the local lattice parameter and the related stoichiometric composition along growth direction. The graphs show the evaluated data for two regions in separated profiles for region 1 in green squares and for region 2 in light blue dots.

Layers 2 and 3: 3.0 ML $\text{In}_{0.5}\text{Ga}_{0.5}\text{As}$

Figure 4.25 shows rare data of layer 2, which can be used for stoichiometry analysis. In the image the surface is disturbed by scan-induced adatoms and holes, making the analysis difficult. For the analyzed region the local lattice parameter is again characterized by a noisy behavior, meaning there is a strong variation from the GaP lattice parameter along growth direction. At the expected position of the layer (bright contrast in Fig. 4.25 (a)) one could only guess that there is a slight rise of the local lattice parameter (at one data point) and a slight undershoot underneath the layer.

Analyzable data for layer 3, as shown in Fig. 4.26, make a clear interpretation even more difficult. The analyzed image in Fig. 4.26 (a) is characterized by an even higher surface contamination. Here, the noise is again higher especially in the right part of the curve representing the material at and on top of the expected position of the layer. Anyway, the local lattice parameter in the analyzed regions of both nominally identical layers stays below the value for pure GaAs in GaP.

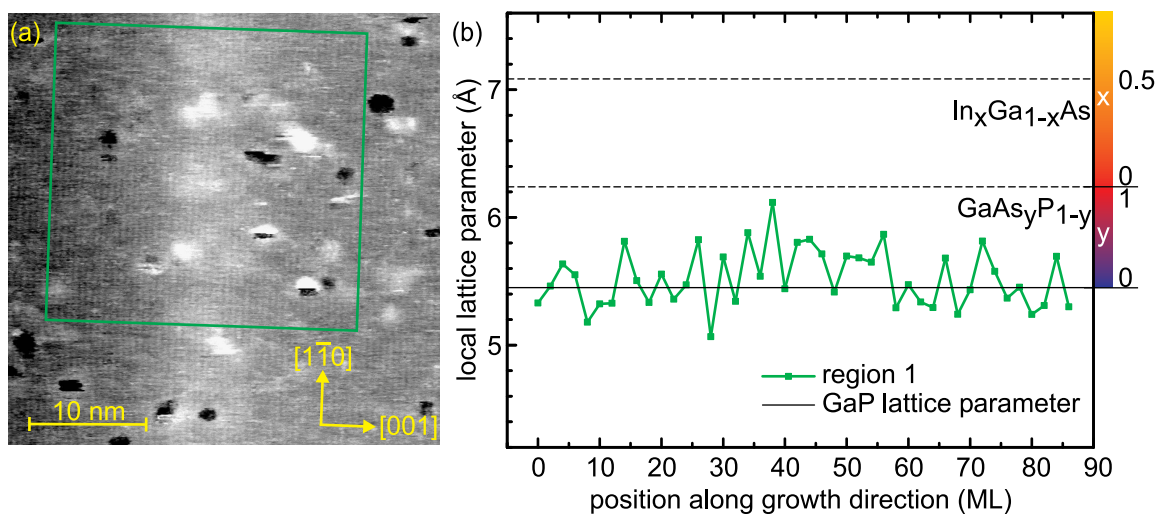


Figure 4.25: (a) Filled-state XSTM image of layer 2. The evaluated region is highlighted by the colored box. The image was taken at $V_T = -3.9$ V and $I_T = 30$ pA. (b) Corresponding evaluation of the local lattice parameter and the related stoichiometric composition along growth direction. The graph shows the evaluated data (region 1) in green squares.

From these findings one could only suggest that for the analyzable regions a Ga(As,P) layer or a quaternary (In,Ga)(As,P) layer has formed, where according to the image contrast the deposited InAs material (nominally 1.5 ML indium and 3 ML of arsenic) is located. Unfortunately, there is no analyzable data for the observed islands within the layer, as discussed in Section 4.3.1, to reveal whether there is a locally higher indium concentration within these quantum dots.

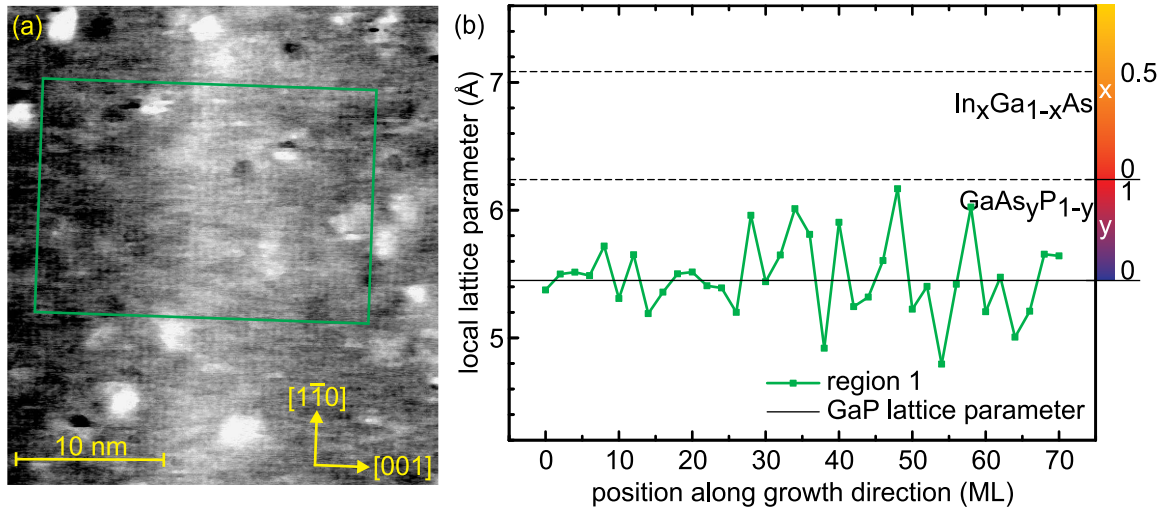


Figure 4.26: (a) Filled-state XSTM image of layer 3. The evaluated region is highlighted by the colored box. The image was taken at $V_T = -3.7$ V and $I_T = 30$ pA. (b) Corresponding evaluation of the local lattice parameter and the related stoichiometric composition along growth direction. The graph shows the evaluated data (region 1) in green squares.

Layer 4: 4.0 ML $\text{In}_{0.5}\text{Ga}_{0.5}\text{As}$

Figure 4.27 shows the evaluation of the local lattice parameter for layer 4, in this case for XSTM data with high resolution in filled-state mode. In Fig. 4.27 (b) the green graph represents the local lattice parameter for the whole evaluated area (region 1), as highlighted by the green box in (a). It is characterized by a very smooth progression around the value for the GaP lattice parameter. Only at the center of the curve, corresponding to the expected position of the layer in Fig. 4.27 (a), there is a small rise for 7 data points representing a layer thickness of about 14 ML. In Fig. 4.27 (c,d) the evaluated region has been separated into two parts. The red one (region 2) contains a bright contrasted agglomeration at the layer's position, while for the area highlighted in blue (region 3) the layer is hardly, respectively almost not, visible in the XSTM image. Both curves show a low noise level due to the high image and surface quality in the evaluated areas. For the area of the agglomeration (region 2) there is a significant rise of the local lattice parameter in an around 12 ML wide region reaching almost the value for pure GaAs in GaP. Concerning the material distribution, it again seems that these agglomerations consist of a quaternary $(\text{In,Ga})(\text{As,P})$ alloy or otherwise of $\text{Ga}(\text{As,P})$. For the latter case the location of the nominally deposited 2 ML indium within the layer would remain unclear.

For the darker region 3 there is also a significant but much smaller rise of the local lattice parameter at the same position along growth direction as for region 2. This indicates that though there is no bright contrast in the XSTM image at this position there indeed is a slight material change at least in the group-V (from phosphorus to arsenic) by forming a $\text{Ga}(\text{As,P})$ (wetting) layer.

Figure 4.28 shows evaluated data of layer 4 for an empty-state XSTM image. Here, the surface again is characterized by more adatoms and holes leading to a noisier behavior of the local lattice parameter, especially in the right part of the curve for material on top of the nominal position of the layer. At the position of the layer itself a significant rise is visible which proves again the formation of a $\text{Ga}(\text{As,P})$ or an $(\text{In,Ga})(\text{As,P})$ layer, in accordance with the evaluated filled-state image in Fig. 4.28. Nevertheless, for this graph a detailed analysis of the material amount and composition is difficult as the layer signal only slightly exceeds the noise level.

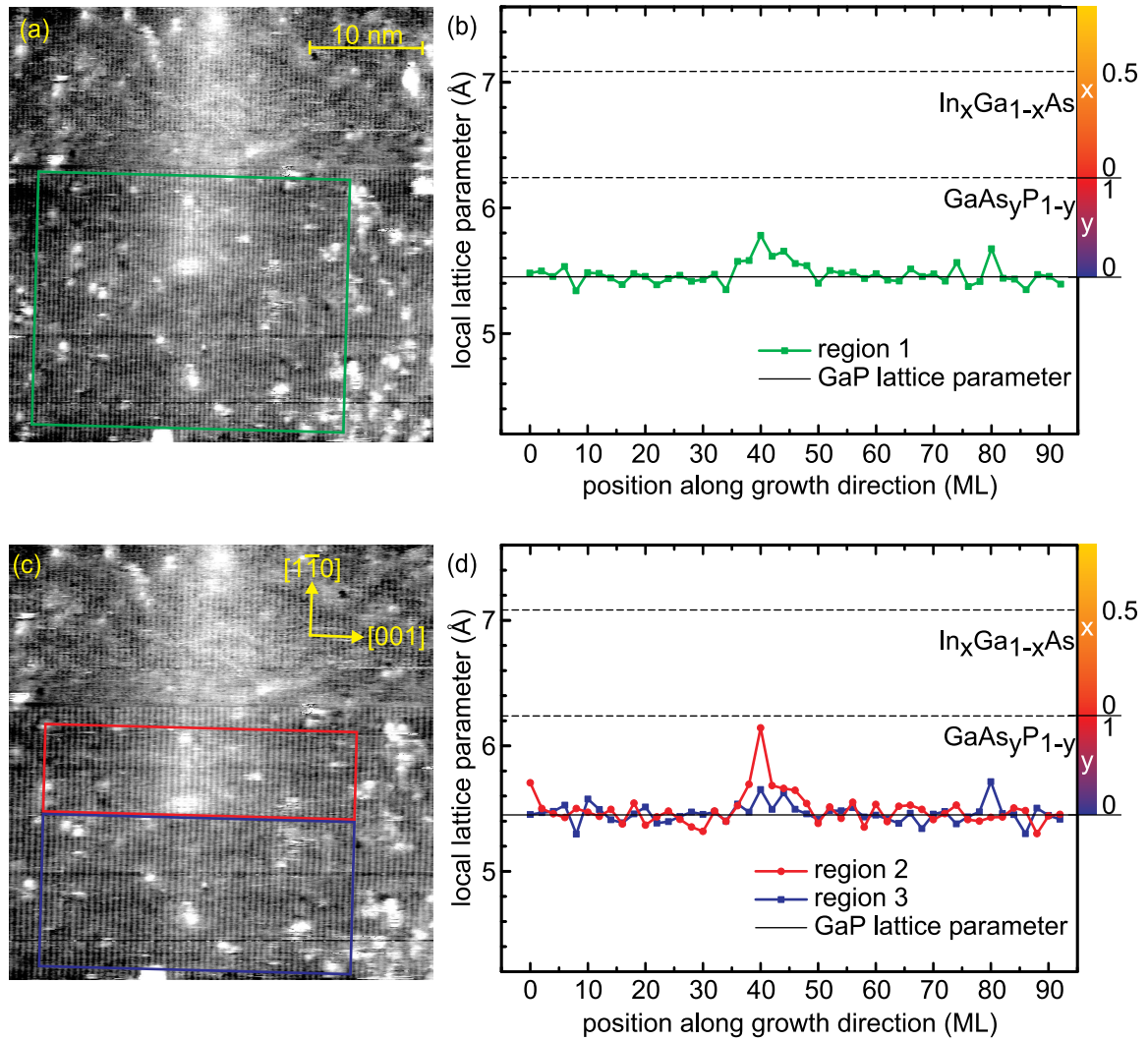


Figure 4.27: (a,c) Filled-state XSTM images of layer 4. The evaluated regions are highlighted by the colored boxes. The images were taken at $V_T = -3.7$ V and $I_T = 30$ pA. (b,d) Corresponding evaluation of the local lattice parameter and the related stoichiometric composition along growth direction. The graphs show the evaluated data (b) for the entire region 1 in green squares and (d) for separated profiles of the region 2 with brighter contrast in red dots and for the darker appearing region 3 in blue squares.

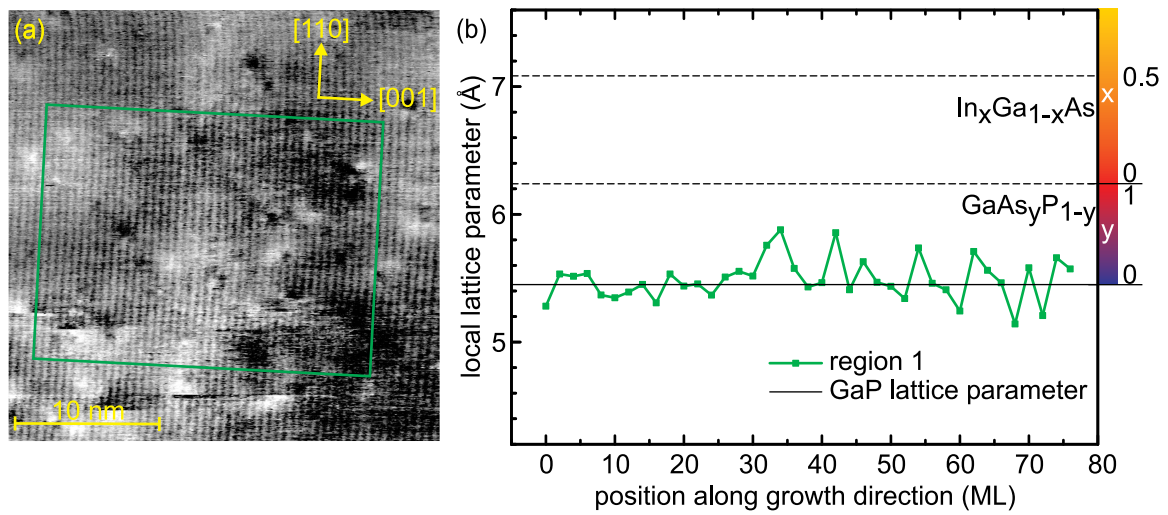


Figure 4.28: (a) Empty-state XSTM image of layer 4. The evaluated region is highlighted by the colored box. The image was taken at $V_T = +3.0$ V and $I_T = 40$ pA. (b) Corresponding evaluation of the local lattice parameter and the related stoichiometric composition along growth direction. The graph shows the evaluated data (region 1) in green squares.

4.3.3 Quantum Dot layer evolution with increasing material amount

An influence of the deposited $\text{In}_{0.5}\text{Ga}_{0.5}\text{As}$ material amount on the quantum dot layer evolution is ascertained, although the lack of data quality in the previous subsections prevents from a detailed quantitative analysis of the structural properties of the quantum dot layers. Concerning the XSTM image contrast, the $\text{In}_{0.5}\text{Ga}_{0.5}\text{As}$ layer gets more pronounced with increasing deposited material amount. During growth the $\text{In}_{0.5}\text{Ga}_{0.5}\text{As}$ material also redistributes into small agglomerations. This may already be considered from the image contrast for 2.0 ML, but is definitely indicated for 3.0 ML (with an assumed trapezoidal cross-section for the agglomerations), and also for 4.0 ML of deposited $\text{In}_{0.5}\text{Ga}_{0.5}\text{As}$ material. From the stoichiometry data in combination with the image contrast one can assume that the $\text{In}_{0.5}\text{Ga}_{0.5}\text{As}$ material intermixes with the GaP matrix to forming a more quaternary but inhomogeneous $(\text{In,Ga})(\text{As,P})$ layer. Thus, the formation of the agglomerations occurs, which is favored or at least getting more pronounced with increasing deposited $\text{In}_{0.5}\text{Ga}_{0.5}\text{As}$ amount. This is probably caused by a localization of indium-rich material. It indeed seems that the agglomerations contain more indium material in a quaternary $(\text{In,Ga})(\text{As,P})$ arrangement, compared to there surrounding parts where less indium seems to be present. For the higher material amount, definitely in the case of 4.0 ML, this redistribution effect is even more pronounced, indicating a material transformation, that leads to a presumably more ternary Ga(As,P) (wetting) layer surrounding the $(\text{In,Ga})(\text{As,P})$ agglomerations.

Chapter 5

Thin GaAs and (Al,Ga)P layers in GaP

In this chapter a closer look is taken on the thin GaAs and (Al,Ga)P layers that were included as marker layers in the samples discussed previously in Chapters 3 and 4.

5.1 GaAs/GaP layers grown by MOVPE

5.1.1 10-fold superlattices of GaAs/GaP

10x (2.0 ML GaAs and 10 nm GaP) (Sample TU9675)

The GaAs marker layer in the sample for first XSTM investigations on a GaP substrate (TU9675) consists of a 10-fold superlattice of 2.0 ML GaAs and 10 nm GaP grown at 600 °C (see also Fig. 3.1).

Figure 5.1 (a) shows again an overview image in filled-state mode of this marker layer confirming the equidistance of about 10 nm between the single GaAs layers. A closer view in Fig. 5.1 (b) reveals the structure of these layers due to the high resolution along the [001] direction identifying the atomic chains, as highlighted by the colored arrows. Regarding the contrast, each layer part of the 10-fold superlattice consists of an atomic chain with a more homogeneous brightness (indicated by the green arrows) and a second atomic chain with a more inhomogeneous brightness (indicated by the dashed green/yellow arrows) revealing a weak segregation of the nominally deposited GaAs material along growth direction. The distance between the bright contrasted GaAs layers can be determined to 18 atomic chains, which is 36 ML and equals 9.81 nm for pure GaP, being in accordance with the nominal distance or the deposited material amount of 10 nm GaP.

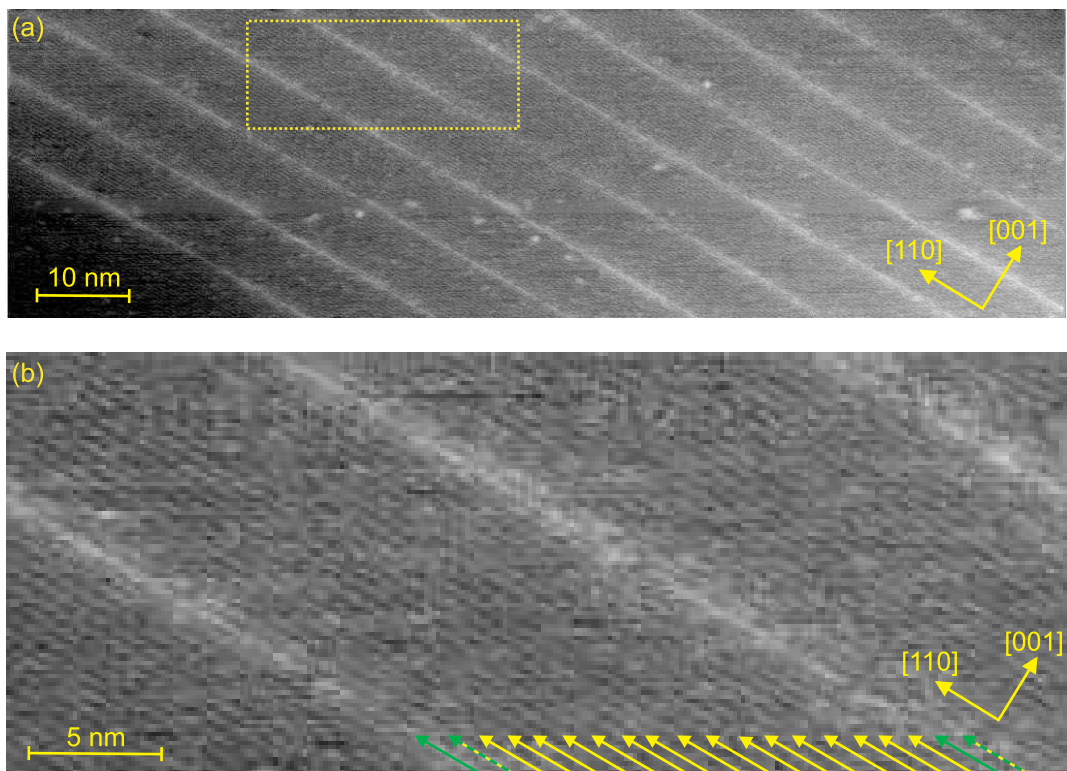


Figure 5.1: (a) Filled-state XSTM image of the GaAs marker layer (a 10-fold superlattice of 2.0 ML GaAs and 10 nm GaP). (b) Magnified section marked by the highlighted box in (a) where the atomic chains are marked by arrows (yellow for GaP, green for GaAs, dashed green/yellow for Ga(As,P)). The image was taken at a sample voltage $V_T = -3.2$ V and a tunneling current $I_T = 70$ pA.

Stoichiometry analysis

To evaluate the layer material content quantitatively, again the local lattice parameter was analyzed, as shown in Fig. 5.2. The analysis for one of the individual GaAs layer parts shows that the local lattice parameter notably rises for a 6 ML wide area, in correspondence to the bright contrast at this position with a local material amount of up to 50% per layer. The total material content could be determined to 1.8 ML GaAs which is again comparable to the nominally deposited material amount of 2 ML for an individual layer part.

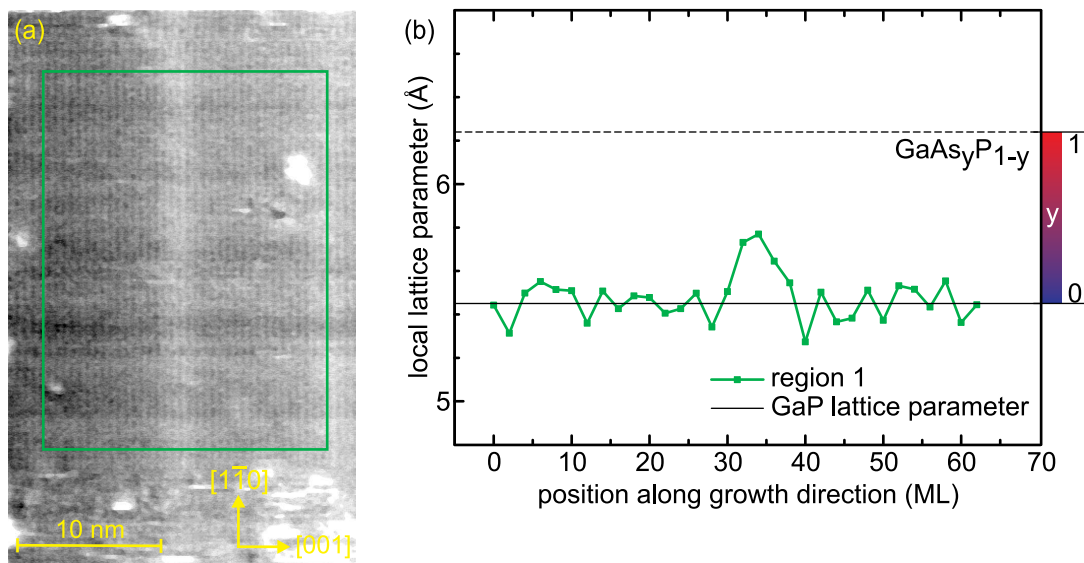


Figure 5.2: (a) Filled-state XSTM image of a layer part of the GaAs marker layer. The evaluated region is highlighted by the colored box. The image was taken at $V_T = -2.6$ V and $I_T = 40$ pA. (b) Corresponding evaluation of the local lattice parameter and the related stoichiometric composition along growth direction. The graph shows the evaluated data (region 1) in green squares.

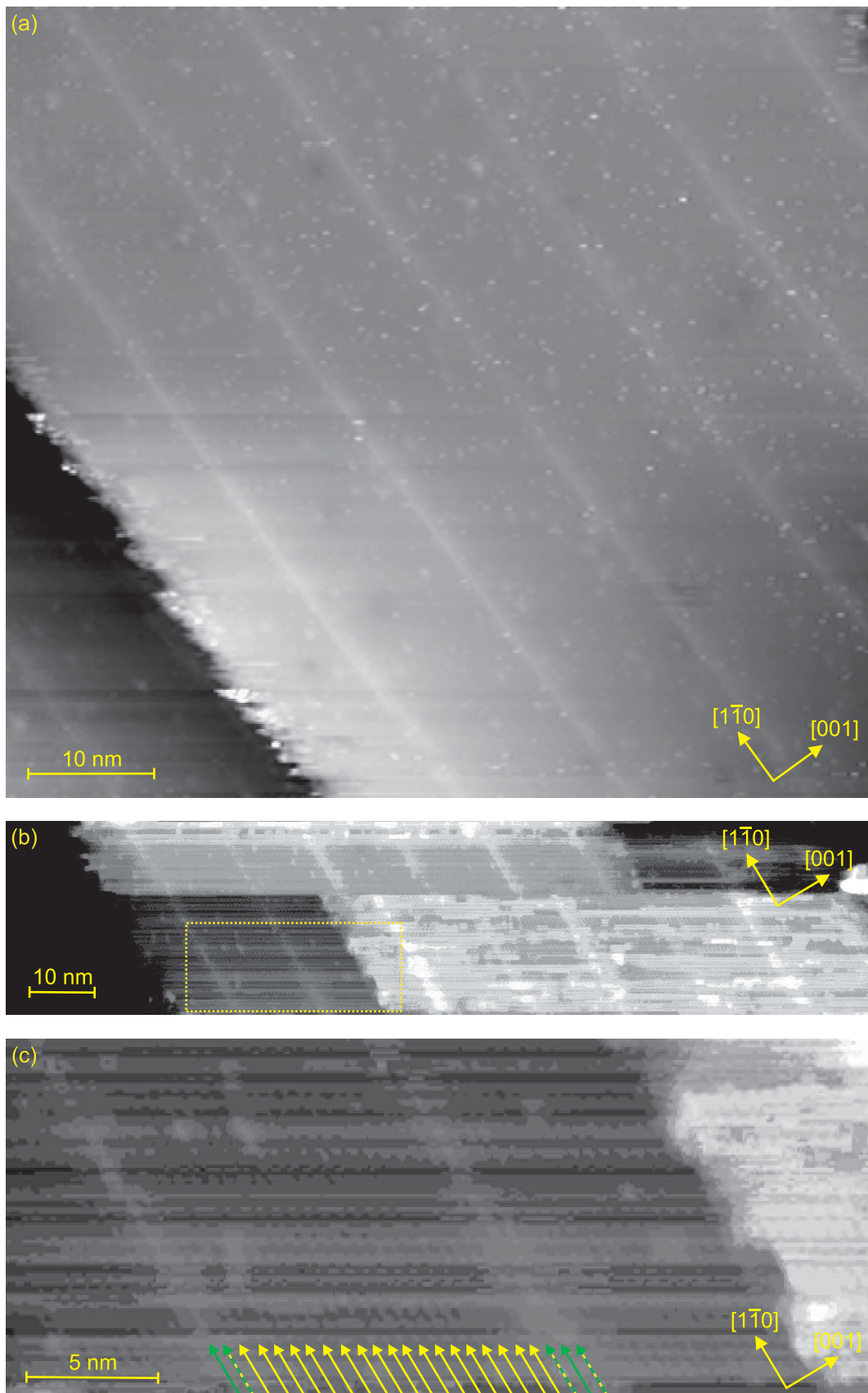


Figure 5.3: (a-b) Filled-state XSTM images of the GaAs marker layer (a 10-fold superlattice of 2.0 ML GaAs and 10 nm GaP). (c) Magnified section marked by the highlighted box in (b) where the atomic chains are marked by arrows (yellow for GaP, green for GaAs, dashed green/yellow for Ga(As,P)). The images were taken at a sample voltage $V_T = -2.5$ V and a tunneling current $I_T = 50$ pA.

10x (2.0 ML GaAs and 10 nm GaP) (Sample TU10350)

In the subsequent sample for XSTM investigations (TU10350) the GaAs marker layer consists again of a 10-fold superlattice of 2.0 ML GaAs and 10 nm GaP grown at 600 °C (see also Fig. 3.5).

Figures 5.3 (a-b) show some rare valuable XSTM data locating these layers which despite the lack of high resolution at least confirm the equidistance of 10 nm between the bright contrasted GaAs containing layer parts. The closer view in Fig. 5.3 (c) reveals a slight atomic resolution along the [001] direction. It shows in analogy to the previous sample that the GaAs material is only slightly distributed over a height of 2–6 ML indicated by the atomic chains highlighted by the green and dashed green/yellow arrows. The distance between the bright contrasted GaAs layers can be determined to 19–21 atomic chains which equals a layer height of about 10–11 nm which is again in accordance with the nominally deposited material amount of 10 nm GaP.

Stoichiometry analysis

The analysis of the local lattice parameter is shown in Fig. 5.4. The few analyzable data at least shows a significant rise of the local lattice parameter at the position of the two GaAs layer parts in the evaluated area in Fig. 5.4 (a). The rise exceeds the value for pure GaAs in GaP a little which may be caused by the noise of the data based on the lack of atomic high-resolution.

Therefore, the material content for the evaluated area can be approximated to about 3.7 ML GaAs which is in the range of the nominal deposited 2×2 ML GaAs material for the two layer parts.

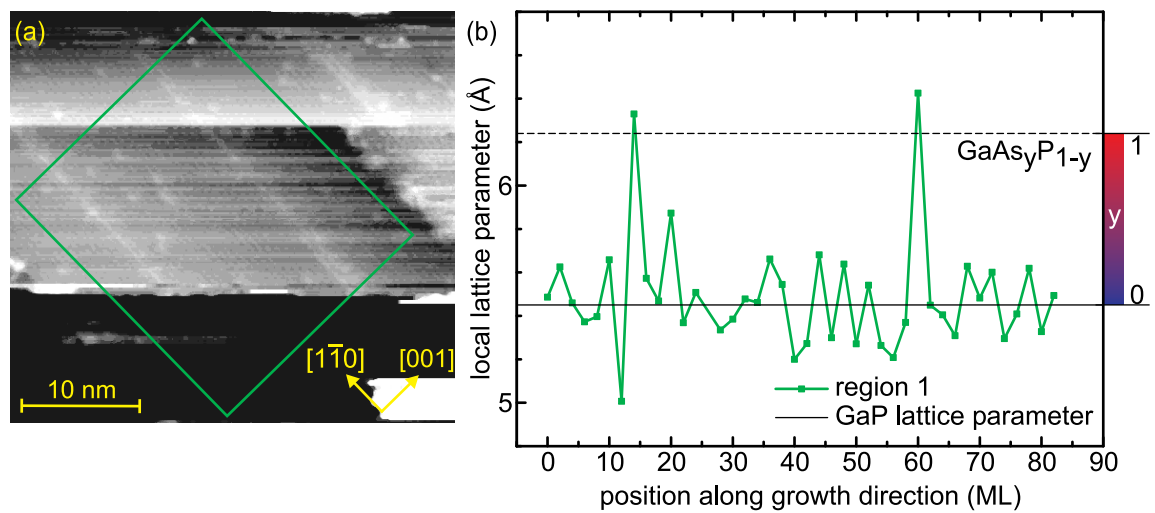


Figure 5.4: (a) Filled-state XSTM a layer part of the GaAs marker layer. The evaluated region is highlighted by the colored box. The image was taken at $V_T = -2.5$ V and $I_T = 50$ pA. (b) Corresponding evaluation of the local lattice parameter and the related stoichiometric composition along growth direction. The graph shows the evaluated data (region 1) in green squares.

5.1.2 3-fold layers of GaAs/GaP with varying material amount

In the following sample for XSTM investigations grown by MOVPE (Sample TU10815) GaAs layers with varying thickness were embedded, as shown in Fig. 3.17. The primary GaAs marker layer consists of a 3-fold superlattice of 1.0 ML GaAs and 6 nm undoped GaP grown at 500 °C while the secondary GaAs marker layer consists of a 3-fold superlattice of 2.0 ML GaAs and 6 nm undoped GaP followed by a 3-fold superlattice of 3.0 ML GaAs and 6 nm undoped GaP, also all grown at 500 °C.

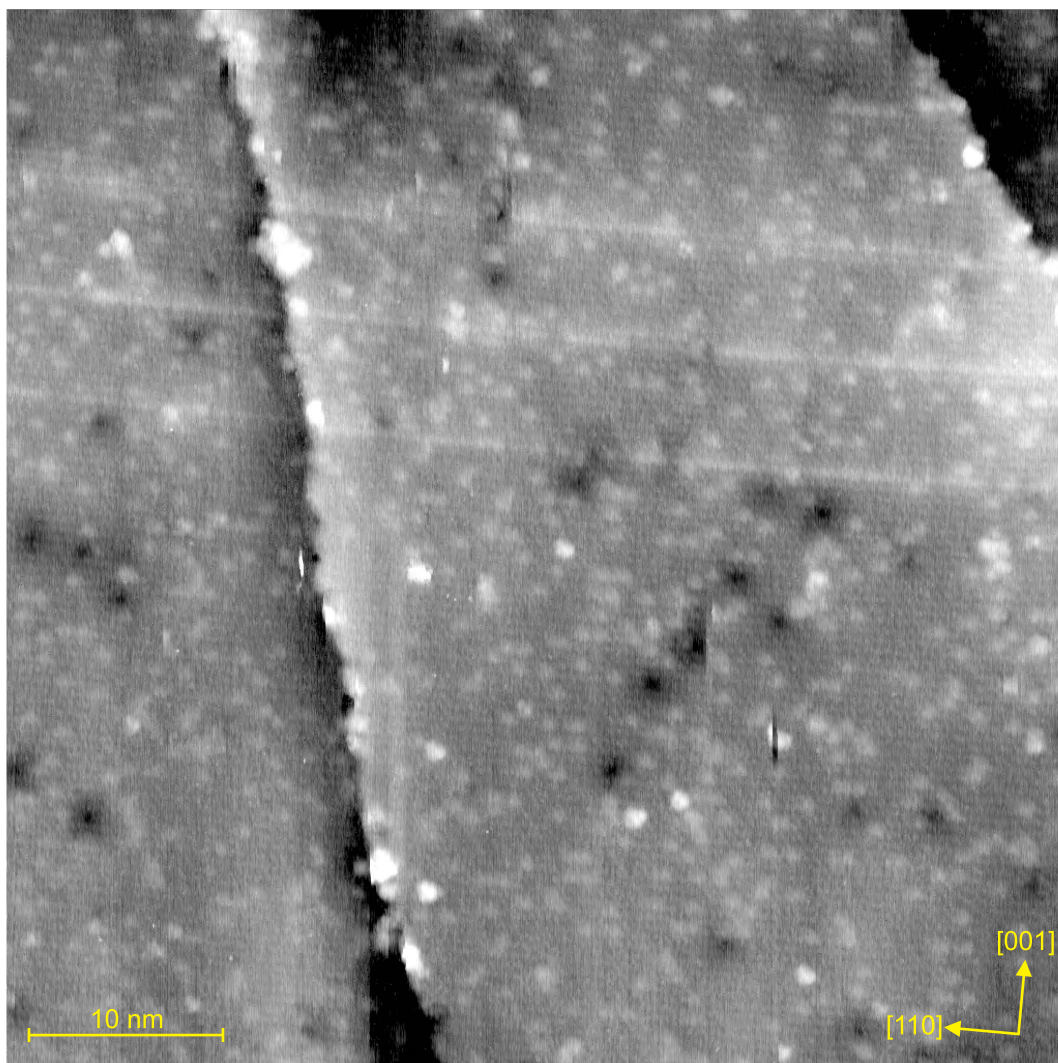


Figure 5.5: Filled-state XSTM image of the primary GaAs marker layer (a 3-fold superlattice of 1.0 ML GaAs and 6 nm GaP). The image was taken at a sample voltage $V_T = -5.8$ V and a tunneling current $I_T = 20$ pA.

3x (1.0 ML GaAs and 6 nm GaP) (Sample TU10815)

Figure 5.5 shows an overview image of the primary GaAs marker layer and the surrounding GaP matrix. As for the other investigated layers in this sample, described in Section 3.3, the image of the surface is well-resolved as the atomic chains parallel to the [110] direction are again clearly visible. Surface steps are also present as well as scan-induced adatoms and holes. The three GaAs containing layer parts of the primary marker layer can be clearly identified due to their bright contrast and their equidistance. A closer view is taken in Fig. 5.6 which shows that for each layer part of the 3-fold superlattice only one atomic chain appears with a bright contrast which is partly interrupted (indicated by the dashed green/yellow arrows). Hence, the nominally deposited GaAs material of 1 ML (per layer part) can be found here and it is located within a layer thickness (for each layer part) of 2 ML without any hint of further material segregation. The distance between the layer parts can be counted to 11 atomic chains or 22 ML which equals a distance of 6.0 nm for GaP which is exactly the nominal value, confirming a precise layer control in the MOVPE growth process.

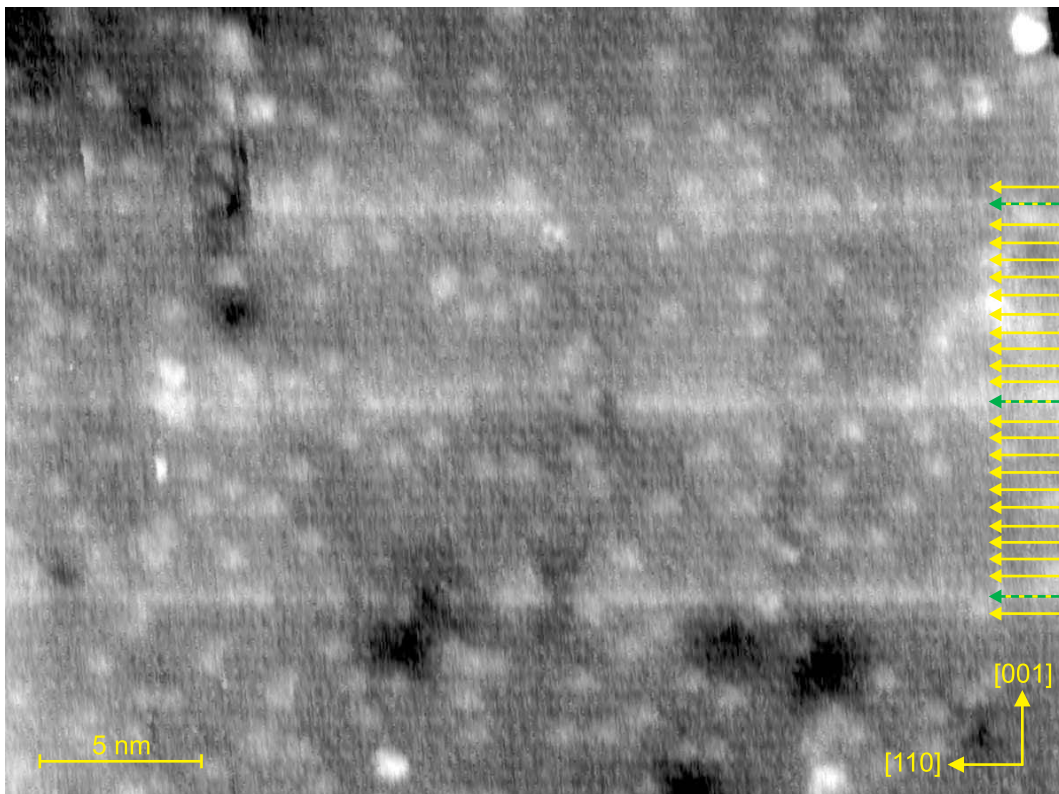


Figure 5.6: Filled-state XSTM image of the primary GaAs marker layer (a 3-fold superlattice of 1.0 ML GaAs and 6 nm GaP) where the atomic chains are marked by arrows (yellow for GaP, dashed green/yellow for Ga(As,P)). The image was taken at a sample voltage $V_T = -5.8$ V and a tunneling current $I_T = 20$ pA.

**3x (2.0 ML GaAs and 6 nm GaP) + 3x (3.0 ML GaAs and 6 nm GaP)
(Sample TU10815)**

An overview of the secondary GaAs marker layer can be found in Fig. 5.7, where again the surface is characterized by steps. Six bright lines with identical distances between each other and with a higher thickness compared with the primary GaAs marker layer parts can be seen. In Fig. 5.8 the expected difference in the GaAs material content of the six equidistant bright contrasted layer parts can be revealed as the lower three layer parts appear thinner than the upper three layer parts. The closer view in Fig. 5.9 even confirms these findings. The lower three layer parts show a homogeneous bright contrast for one atomic chain (indicated by the green arrows), while the upper three layer parts show a bright contrast for one complete and one non-complete or interrupted chain (the latter indicated by the dashed green/yellow arrows). For the material content in the bright contrasted GaAs layers this means that there is low segregation of the GaAs material and that material amounts of about 2 ML GaAs are located in each of the lower three layer parts and amounts of between 2 and 4 ML GaAs are located in each of the upper three layer parts. This again fits the nominal deposited material amount.

The distance between the layer parts can be counted here again to 11 atomic chains corresponding to a distance of 6.0 nm for GaP and therewith being in accordance with the nominal value.

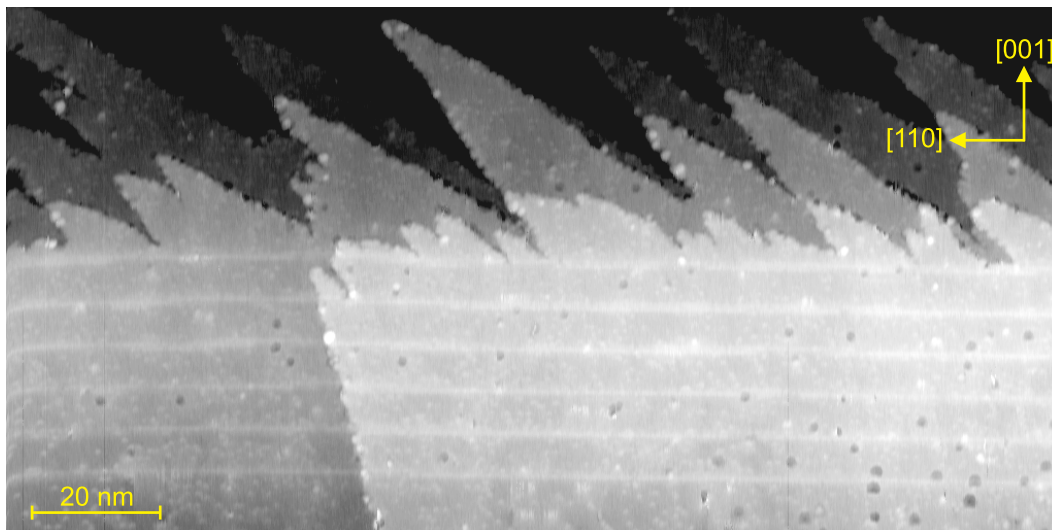


Figure 5.7: Filled-state XSTM overview image of the secondary GaAs marker layer (a 3-fold superlattice of 2.0 ML GaAs and 6 nm GaP followed by a 3-fold superlattice of 3.0 ML GaAs and 6 nm GaP). The image was taken at a sample voltage $V_T = -4.1$ V and a tunneling current $I_T = 20$ pA.

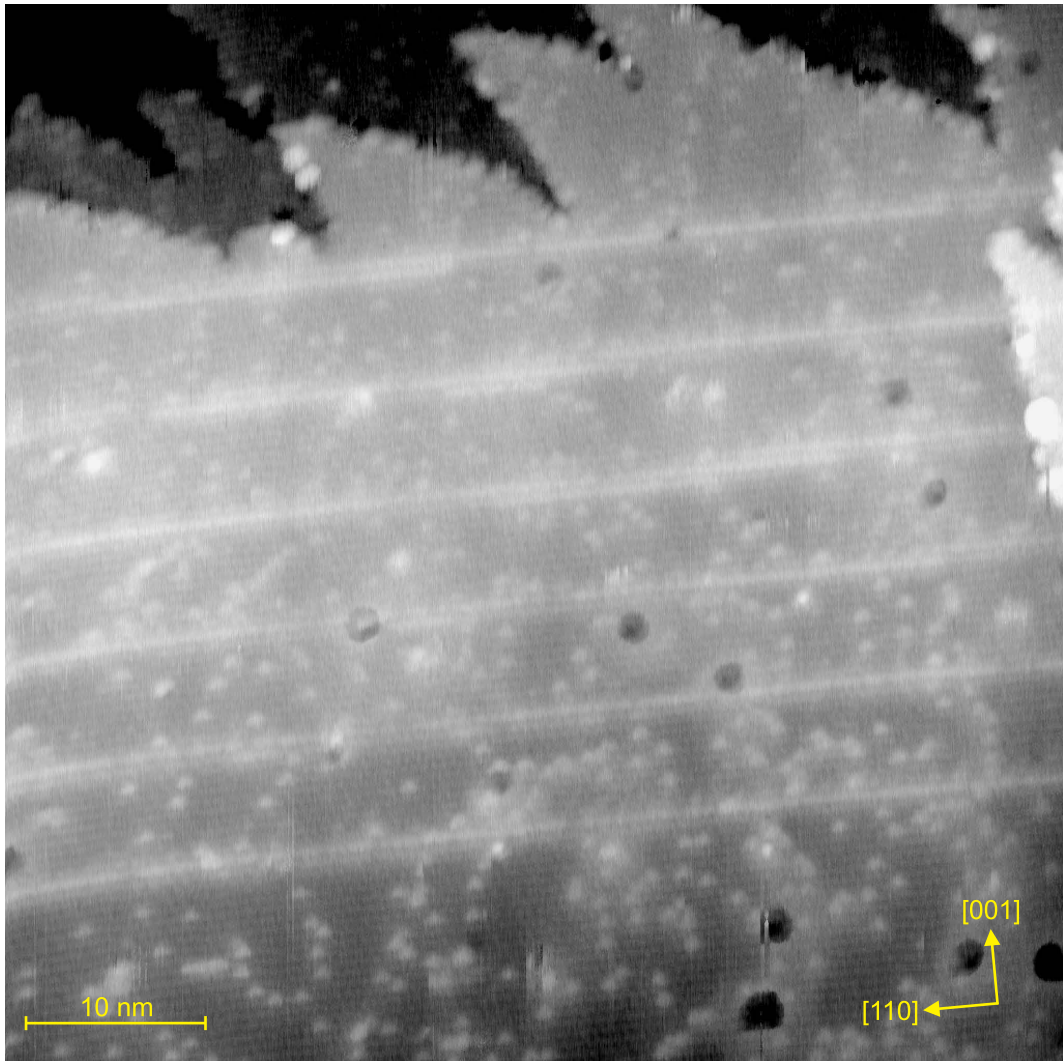


Figure 5.8: Filled-state XSTM image of the secondary GaAs marker layer (a 3-fold superlattice of 2.0 ML GaAs and 6 nm GaP followed by a 3-fold superlattice of 3.0 ML GaAs and 6 nm GaP). The image was taken at a sample voltage $V_T = -4.1$ V and a tunneling current $I_T = 20$ pA.

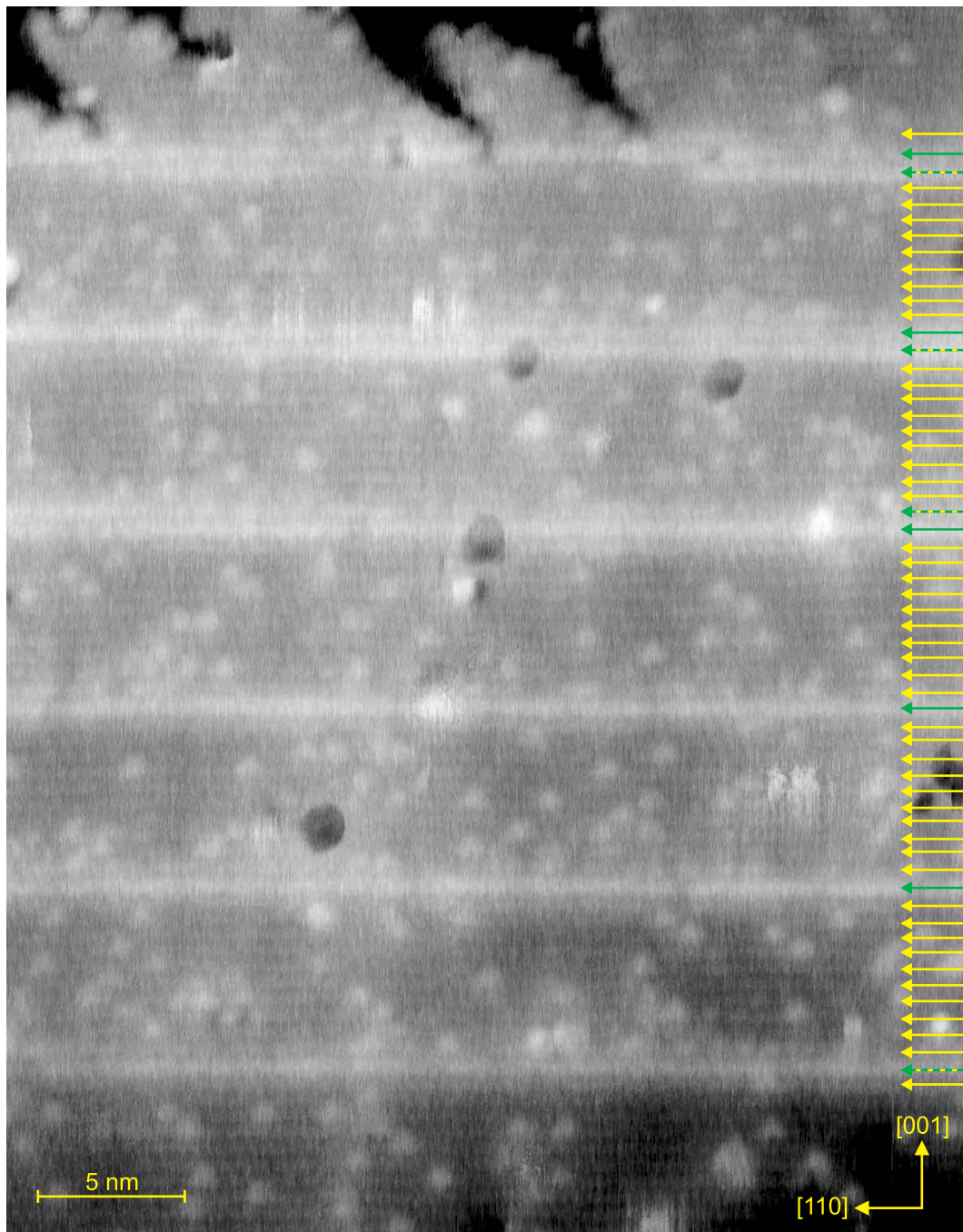


Figure 5.9: Filled-state XSTM image of the secondary GaAs marker layer (a 3-fold superlattice of 2.0 ML GaAs and 6 nm GaP followed by a 3-fold superlattice of 3.0 ML GaAs and 6 nm GaP) where the atomic chains are marked by arrows (yellow for GaP, green for GaAs, dashed green/yellow for Ga(As,P)). The image was taken at a sample voltage $V_T = -4.1$ V and a tunneling current $I_T = 20$ pA.

Stoichiometry analysis

In Fig. 5.10 the evaluation of the local lattice parameter for the primary GaAs marker layer is shown. As expected, the local lattice parameter in Fig. 5.10 (b) rises significantly at the positions of the corresponding three bright contrasted layer parts in Fig. 5.10 (a). These sharp rises exceed the value for pure GaAs, which is unexpected since no other material than GaAs should be present in the GaP matrix here. Even if data noise is taken into account, still the material amount would be approximated to about 2 ML per each of the three layer parts. This is in contradiction to the nominally deposited amount of 1 ML per layer part and also to the observed material contrast in the XSTM images discussed earlier, which indicates also a lower GaAs amount.

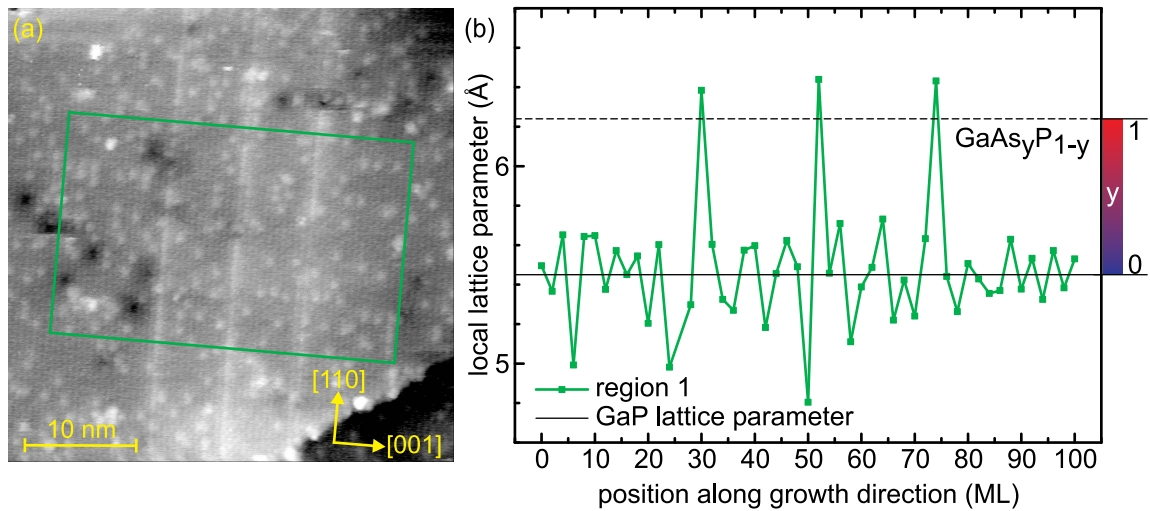


Figure 5.10: (a) Filled-state XSTM of the primary GaAs marker layer. The evaluated region is highlighted by the colored box. The image was taken at $V_T = -5.8$ V and $I_T = 20$ pA. (b) Corresponding evaluation of the local lattice parameter and the related stoichiometric composition along growth direction. The graph shows the evaluated data (region 1) in green squares.

The evaluated data for the secondary GaAs marker layer shown in Figs. 5.11 and 5.12 continues to show this behavior even more. In these cases there are extremely high rises of the local lattice parameter which again correspond to the positions of the GaAs layer parts of the marker layer in the XSTM images. For the lower three layer parts with nominally 2 ML GaAs each the local lattice parameter rises for a width of 2–4 ML with peak maxima up to 7.4 Å. For the upper three layer parts with nominal 3 ML GaAs per layer part the local lattice parameter rise for a higher width of 4 ML and peak maxima up to 7.9 Å. The difference of the local lattice parameters between lower and upper layer parts reflect the expected higher GaAs material amount in the upper layer parts. Nevertheless, the absolute values of the local lattice parameter here

cannot be explained that easily. These high values for the local lattice parameter definitely cannot be caused by noise, even not when regarding the fact of the present high resolution of the XSTM data here.

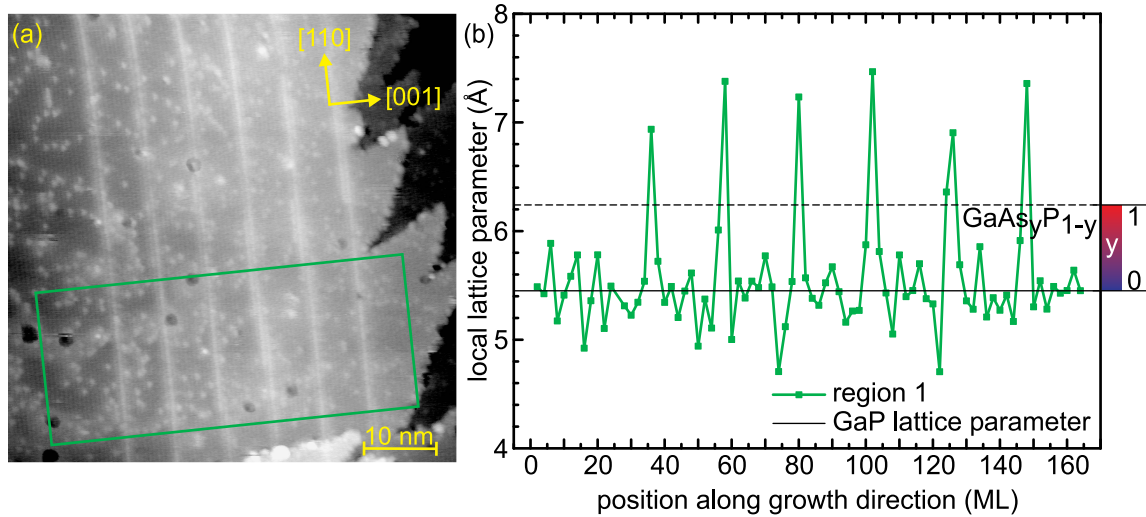


Figure 5.11: (a) Filled-state XSTM of the secondary GaAs marker layer. The evaluated region is highlighted by the colored box. The image was taken at $V_T = -4.1$ V and $I_T = 20$ pA. (b) Corresponding evaluation of the local lattice parameter and the related stoichiometric composition along growth direction. The graph shows the evaluated data (region 1) in green squares.

The here found behavior of a local overshoot of the local lattice parameter for both the primary and the secondary GaAs marker layer is guessed to be caused by some effect which is based on the specific structural properties of these marker layers. In comparison to the previously presented ones (Section 5.1.1) the GaAs layer parts of the marker layer have a lower distance of nominally 6 nm instead of 10 nm and show a high localization of the GaAs material, clearly visible in the XSTM image contrast. This strong localization of the GaAs material perhaps causes a strain effect leading to a strong extension of the GaAs layer parts or/and a strong compression of the GaP material in between influencing the local lattice parameter. To clarify this effect, some ideas will be discussed in the following.

Firstly, further reference values of the local lattice parameter for the GaAs/GaP system have been calculated by H. Eisele [118], taking the specific nominal structure of these layer stacks [(3x (1.0 ML GaAs and 6 nm GaP) and (3x (2.0 ML GaAs and 6 nm GaP) + 3x (3.0 ML GaAs and 6 nm GaP))] into account. The resulting values for these two specific cases unfortunately do not significantly differ from the previously calculated values discussed in Section 2.2.4. So this gives no explanation to the data in Figs. 5.10-5.12.

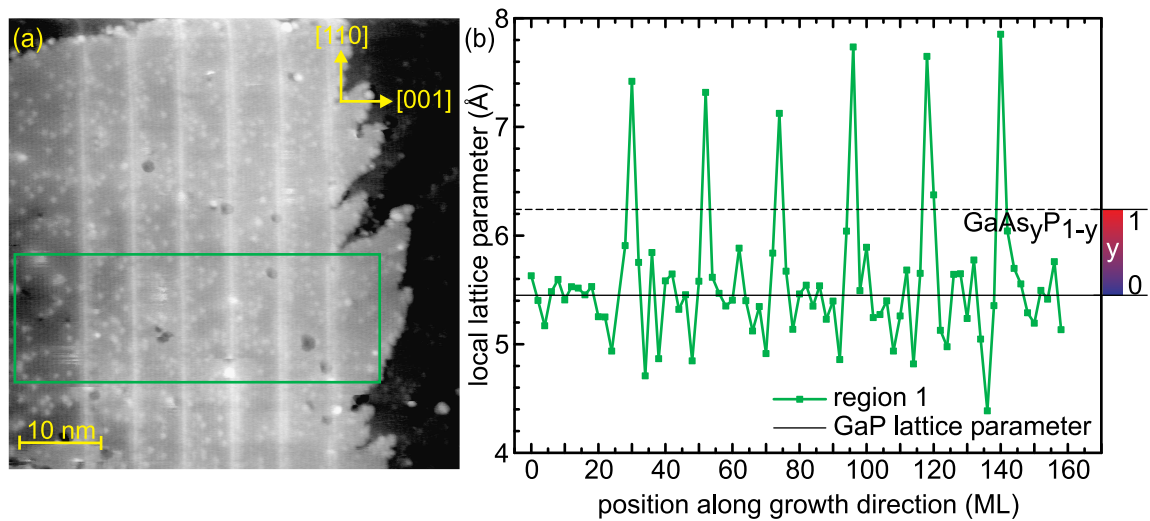


Figure 5.12: (a) Filled-state XSTM of the secondary GaAs marker layer. The evaluated region is highlighted by the colored box. The image was taken at $V_T = -4.1$ V and $I_T = 20$ pA. (b) Corresponding evaluation of the local lattice parameter and the related stoichiometric composition along growth direction. The graph shows the evaluated data (region 1) in green squares.

Secondly, for comparison high-resolution TEM data of the secondary GaAs marker layer in Sample TU10815 were taken [119]. The analysis is shown in Fig. 5.13. The high resolution, as shown in the inset of Fig. 5.13 (a), allows an analogous data evaluation as for the XSTM data. The only difference is that in the TEM image every atomic layer is visible compared to every second layer in the XSTM image so that instead of the local lattice parameter the local ML distance is evaluated here. (Therefore the reference values for the GaP lattice and the value for pure GaAs in GaP within the XSTM analysis need to be divided by a factor of two.) The data of the evaluated region in the TEM image in Fig. 5.13 (a) are shown in Fig. 5.13 (b). They reveal that at the positions of the individual marker layer parts, especially for the left two ones, a notable rise of the local ML distance is observable. Taking the noise in the data into account the local ML distance rises only (as compared to the XSTM data) to values equivalent to about and even less than 100% GaAs in GaP for the individual layer parts. For the marker layer parts at the position between 50 and 135 ML the material seems more segregated. But even when regarding the noise, the local ML distance still has values equivalent to material compositions of up to 30% GaAs in GaP. The total GaAs material amount then can be approximated to 14.9 ML which is in accordance to the nominal sum of deposited GaAs material in the total secondary GaAs marker layer of 15.0 ML, whereas for the comparable XSTM data in Figs. 5.11-5.12 a non-realistic average value of about 24 ML GaAs was calculated.

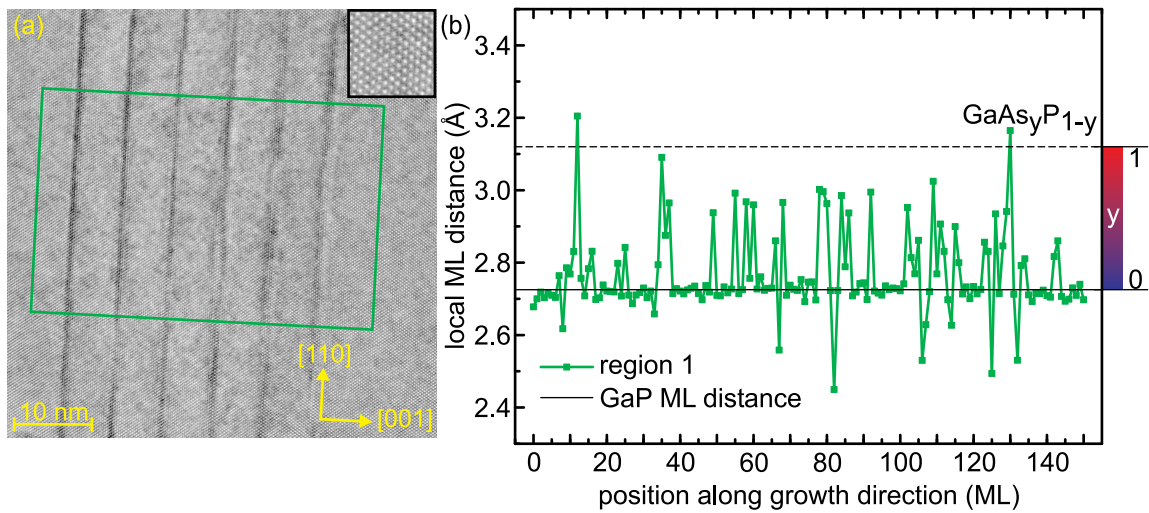


Figure 5.13: (a) High-resolution TEM image of the secondary GaAs marker layer. The image was taken with a FEI TITAN TEM instrument with an electron beam acceleration voltage of 300 kV [119]. The inset shows a magnification to highlight the high resolution. The evaluated region is highlighted by the colored box. (b) Corresponding evaluation of the local ML distance and the related stoichiometric composition along growth direction. The graph shows the evaluated data (region 1) in green squares.

The results of the local lattice parameter calculations for the specific marker layer structures and the TEM data evaluation give the hint that the observed effect might not be dominated by the bulk structure of the marker layers. Instead it may be some kind of surface effect that is observed in the XSTM measurements.

Thirdly, in Fig. 5.14 a schematic of the side view of the relaxed (110) zincblende surface is shown to indicate the shifts of the atomic positions Δ in the upper layers compared to the unrelaxed atomic (bulk) positions and the related tilt angle ω .

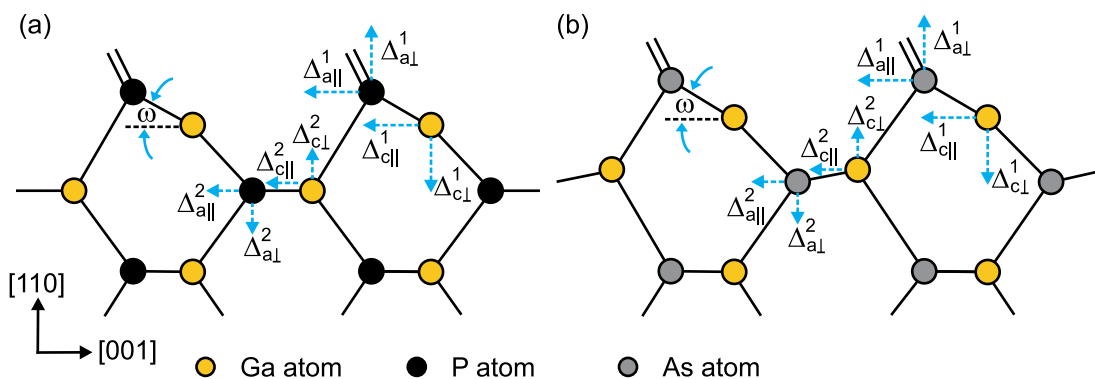


Figure 5.14: Schematics of the side view of the relaxed (110) zincblende surface showing the tilt angle ω and the atomic displacements Δ of anions and cations in the first and second atomic layer, adapted from [93, 94, 120]: (a) GaP, (b) GaAs.

Table 5.1: Structural parameters as defined in Fig. 5.14 [93,94,120].

		GaP	GaAs	difference values
ω	[$^{\circ}$]	27.5	27.3–31.1	-0.2–3.6
$\Delta_{a\perp}^1$	[\AA]	0.09	0.14–0.19	0.05–0.10
$\Delta_{a\parallel}^1$	[\AA]	0.32	0.18–0.33	0.01–0.14
$\Delta_{c\perp}^1$	[\AA]	0.54	0.51–0.53	0.01–0.03
$\Delta_{c\parallel}^1$	[\AA]	0.47	0.34–0.51	0.04–0.13
$\Delta_{a\perp}^2$	[\AA]	0	0.02–0.06	0.02–0.06
$\Delta_{a\parallel}^2$	[\AA]	0	0	0
$\Delta_{c\perp}^2$	[\AA]	0	0.02–0.06	0.02–0.06
$\Delta_{c\parallel}^2$	[\AA]	0	0	0

The literature values for these parameters for the GaP and GaAs (110) surfaces are listed in Table 5.1, taken from [93,94,120]. These values show that for the two materials there are only slight differences in the atomic displacements and the tilt angles. Definitely these values do not explain the measured high local lattice parameters in XSTM for the GaAs marker layers in GaP.

Thus, a final explanation of this singular behavior of the local lattice parameter in these specific cases of GaAs/GaP layer stacks then still has to be determined up to now, but a more detailed investigation is beyond the scope of this thesis.

5.2 GaAs/GaP layers grown by MBE

5x (2.0 ML GaAs and 6 nm GaP) (Sample Yale20130725)

The GaAs marker layer in the MBE-grown sample for XSTM investigations (Sample Yale20130725) consists of a 5-fold superlattice of 2.0 ML GaAs and 6 nm GaP grown at 480 °C, as shown in Fig. 4.1.

Figure 5.15 shows an overview image of the MBE-grown GaAs marker layer. The five individual GaAs layer parts of the marker layer can be again identified as bright contrasted and equidistant stripes. These stripes appear thicker along the [001] direction and with a more inhomogeneous contrast compared with the previously presented MOVPE-grown GaAs layers (see Section 5.1.1). The closer view shown in Fig. 5.16 reveals that the GaAs material for each layer part is distributed over a thickness of 4–5 atomic chains or 8–10 ML (as indicated by the dashed green/yellow arrows) which equals 2.2–2.7 nm for GaP. In between GaP material can be found with thicknesses of 6–8 atomic chains or 12–16 ML (as indicated by the yellow arrows) which equals 3.3–4.4 nm. Hence, the distance of the individual layer parts is 5.5–7.1 ML, which is in accordance with the nominal layer thickness. Together with the less pronounced contrast and the inhomogeneity of the GaAs layer parts along the $[1\bar{1}0]$ direction these findings indicate a segregation of the nominally deposited material of 2 ML GaAs per layer part along the [001] direction.

Stoichiometry analysis

The analysis of the local stoichiometry is shown in Figs. 5.17-5.18. Data of the local lattice parameter for two different regions are presented here, where those in Fig. 5.18 show less noise than those in Fig. 5.17. In both cases there is a significant rise of the local lattice parameter for each of the five layer parts of the GaAs layer in accordance to the position of the bright contrast in the corresponding XSTM-image. Furthermore, the local lattice parameter for each layer part rises in approx. 8 ML wide regions, which also fits the contrast analysis. Here, the local GaAs content rises to values of up to 70%. The material amount in each layer part can be evaluated to 1.9–2.5 ML, where the total GaAs material amount is summed up to 11.0 ML. Compared to the nominally deposited material amount of 5x 2.0 ML GaAs this shows that the total GaAs material is located here and is indeed slightly segregated, i.e. over the observed layer part thicknesses.

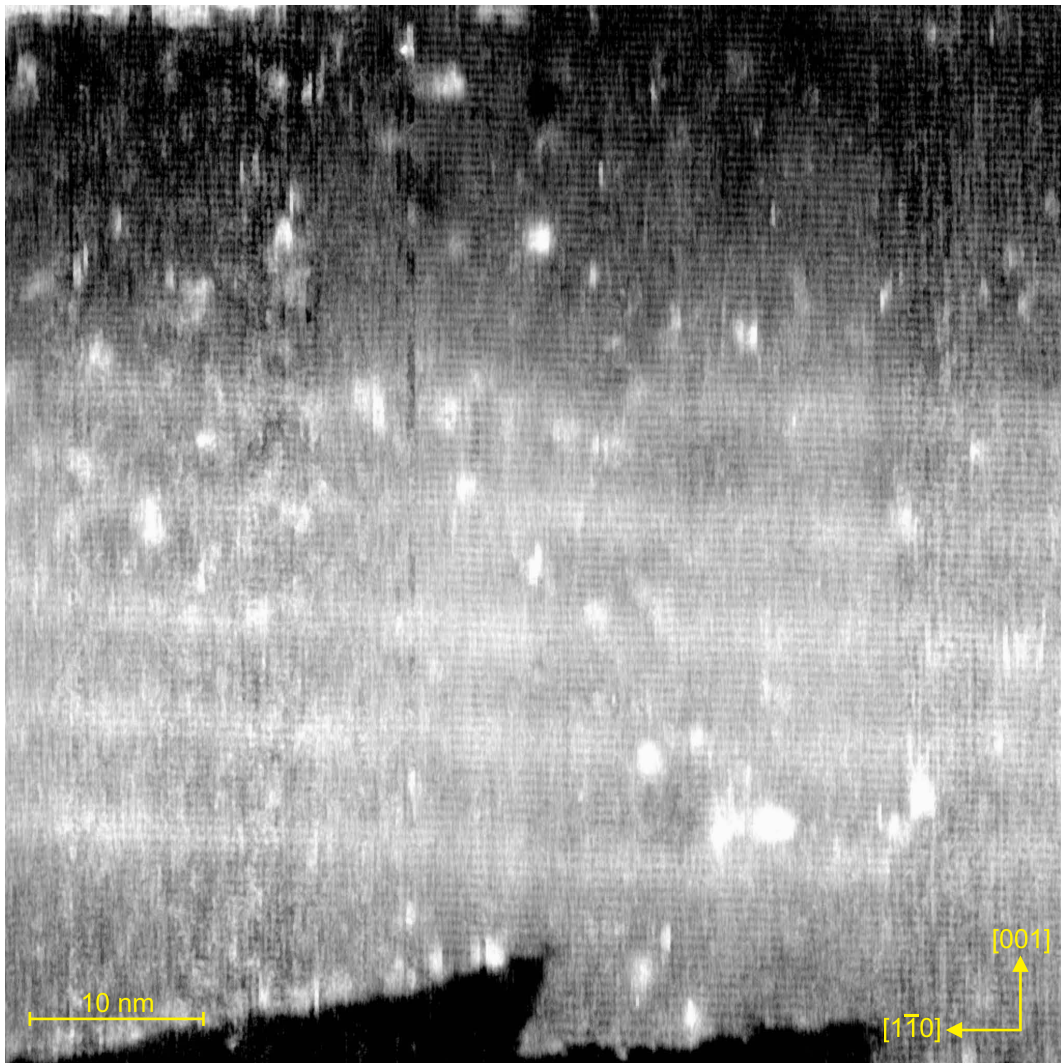


Figure 5.15: Filled-state XSTM image of the GaAs marker layer (a 5-fold superlattice of 2.0 ML GaAs and 6 nm GaP). The image was taken at a sample voltage $V_T = -2.8$ V and a tunneling current $I_T = 30$ pA.

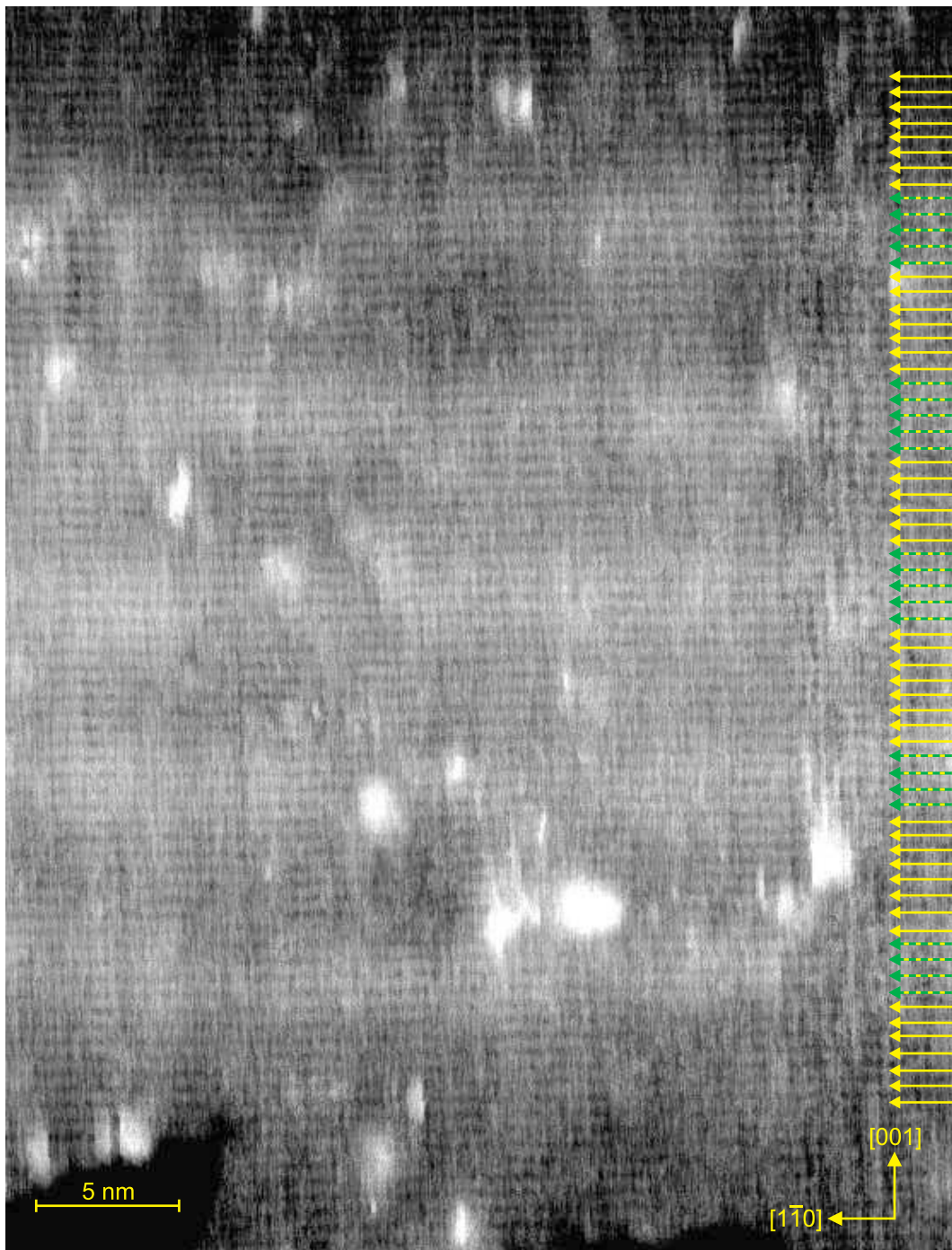


Figure 5.16: Filled-state XSTM image of the GaAs marker layer (a 5-fold superlattice of 2.0 ML GaAs and 6 nm GaP) where the atomic chains are marked by arrows (yellow for GaP, dashed green/yellow for Ga(As,P)). The image was taken at a sample voltage $V_T = -2.8$ V and a tunneling current $I_T = 30$ pA.

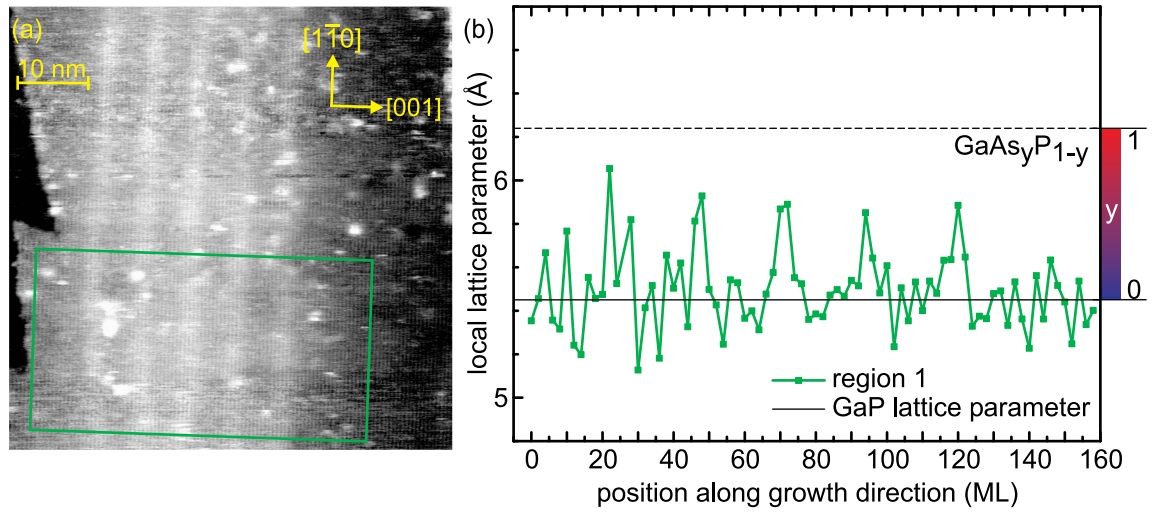


Figure 5.17: (a) Filled-state XSTM of the primary GaAs marker layer. The evaluated region is highlighted by the colored box. The image was taken at $V_T = -2.8$ V and $I_T = 30$ pA. (b) Corresponding evaluation of the local lattice parameter and the related stoichiometric composition along growth direction. The graph shows the evaluated data (region 1) in green squares.

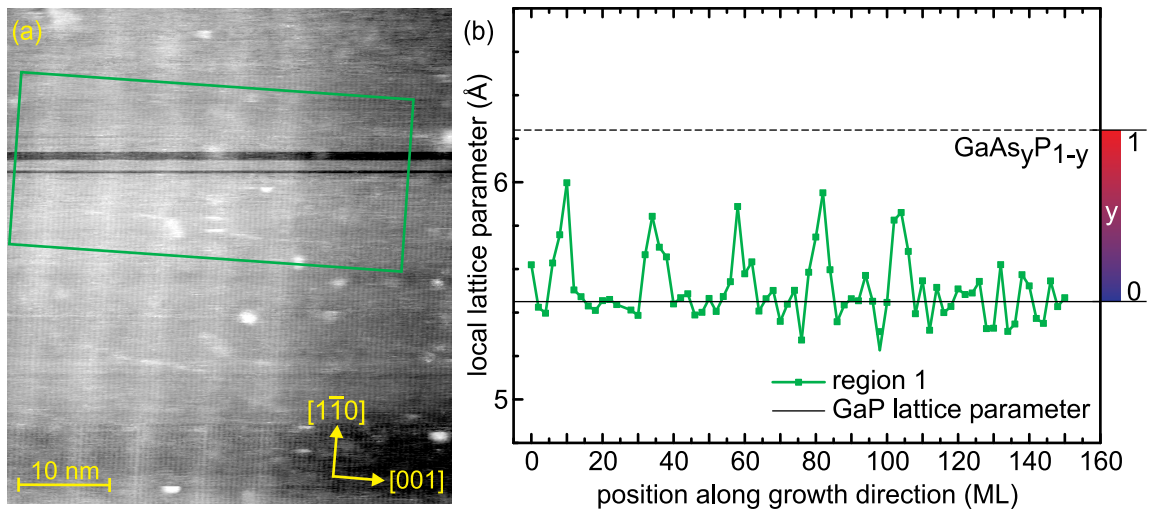


Figure 5.18: (a) Filled-state XSTM of the primary GaAs marker layer. The evaluated region is highlighted by the colored box. The image was taken at $V_T = -2.8$ V and $I_T = 30$ pA. (b) Corresponding evaluation of the local lattice parameter and the related stoichiometric composition along growth direction. The graph shows the evaluated data (region 1) in green squares.

5.3 (Al,Ga)P/GaP layers grown by MOVPE

3x (2 nm Al_{0.23}Ga_{0.77}P and 2 nm GaP) (Sample TU10815)

The additional (Al,Ga)P marker layer inserted in Sample TU10815 grown for XSTM investigations by MOVPE consists of a 3-fold superlattice of 2 nm Al_{0.23}Ga_{0.77}P and 2 nm undoped GaP, all grown at 620 °C, as shown in Fig. 3.17.

Figure 5.19 again shows an overview image of Sample TU10815. The surface here is characterized by many terraces divided by surface steps. The secondary GaAs marker layer with its 6-fold structure can again be clearly identified, whereas at a distance of 100 nm along the [001] direction a 3-fold layer structure that should be related to the (Al,Ga)P material can be guessed, as indicated by the yellow lines in Fig. 5.19.

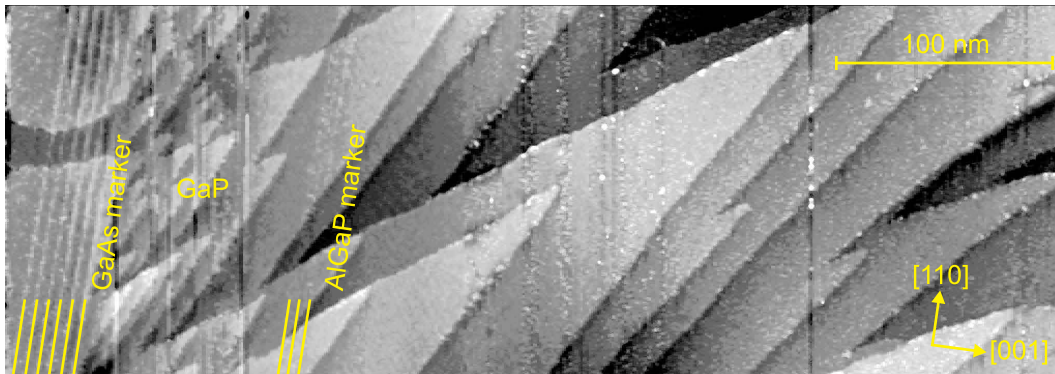


Figure 5.19: Filled-state XSTM overview image showing the secondary GaAs marker layer as well as the (Al,Ga)P marker layer (a 3-fold superlattice of 2 nm Al_{0.23}Ga_{0.77}P and 2 nm GaP). The image was taken at a sample voltage $V_T = -3.0$ V and a tunneling current $I_T = 20$ pA.

A closer view at this (Al,Ga)P marker layer is shown in Fig. 5.20. The three layer parts of the (Al,Ga)P marker layer cannot be identified by a difference of contrast compared to the surrounding GaP material. Instead the 3-fold structure as indicated by the yellow lines in Fig. 5.20 gets visible due to the location of the adatoms located on the surface. This behavior could be expected as aluminium-containing layers are known to attract adatoms on surfaces.

The image in Fig. 5.21 shows higher resolution slightly enabling to distinguish between atomic chains parallel to the [110] direction, as indicated by the yellow and orange arrows. The center positions of the three (Al,Ga)P layer parts of the (Al,Ga)P marker layer are approximated due to the adatom arrangement and are highlighted by the yellow lines/orange arrows. The distance between these atomic layers can be approximated to 8–9 atomic chains, which equals 16–18 ML or a distance of 4.4–4.9 nm for GaP, which is in accordance with the nominally expected value of 4 nm.

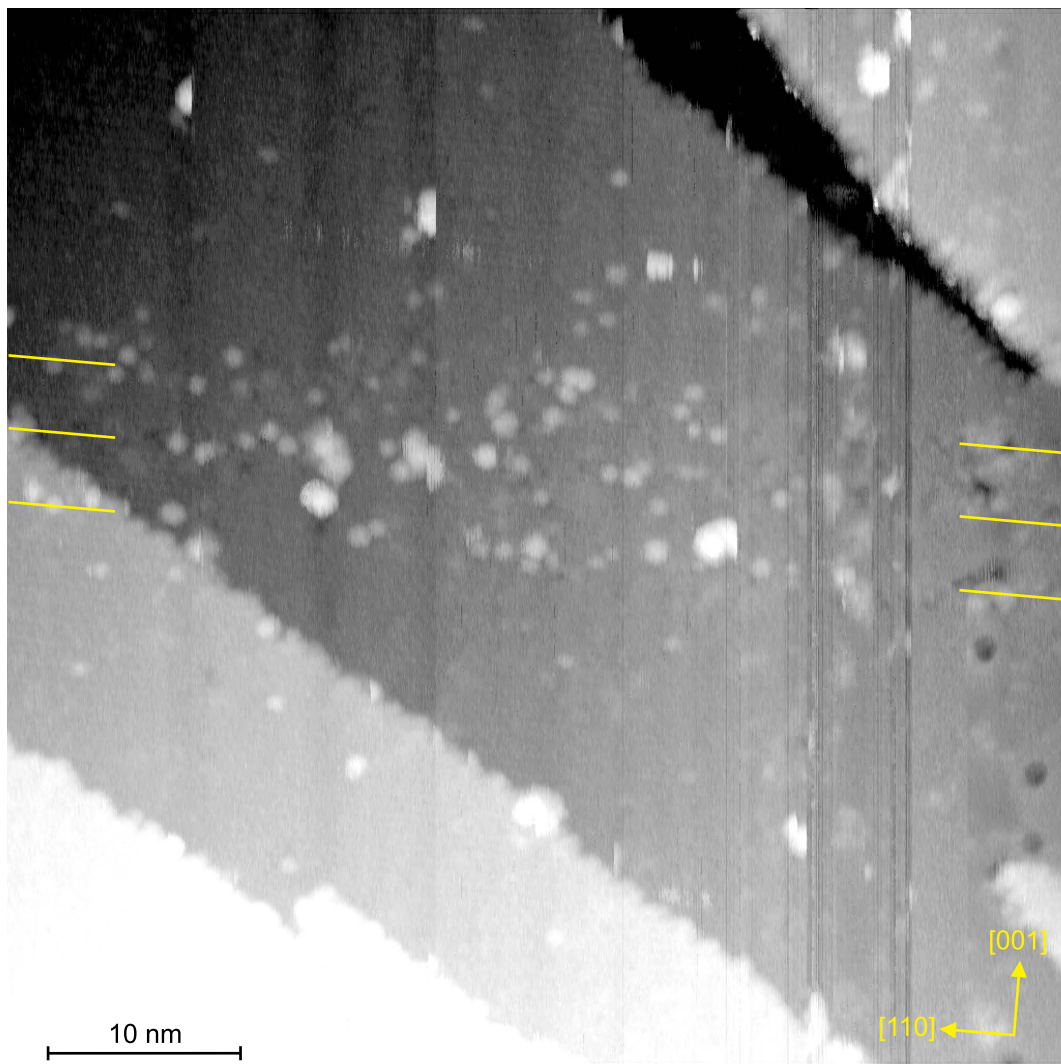


Figure 5.20: Filled-state XSTM image of the (Al,Ga)P marker layer (a 3-fold superlattice of 2 nm $\text{Al}_{0.23}\text{Ga}_{0.77}\text{P}$ and 2 nm GaP). The image was taken at a sample voltage $V_T = -4.3$ V and a tunneling current $I_T \approx 20$ pA.

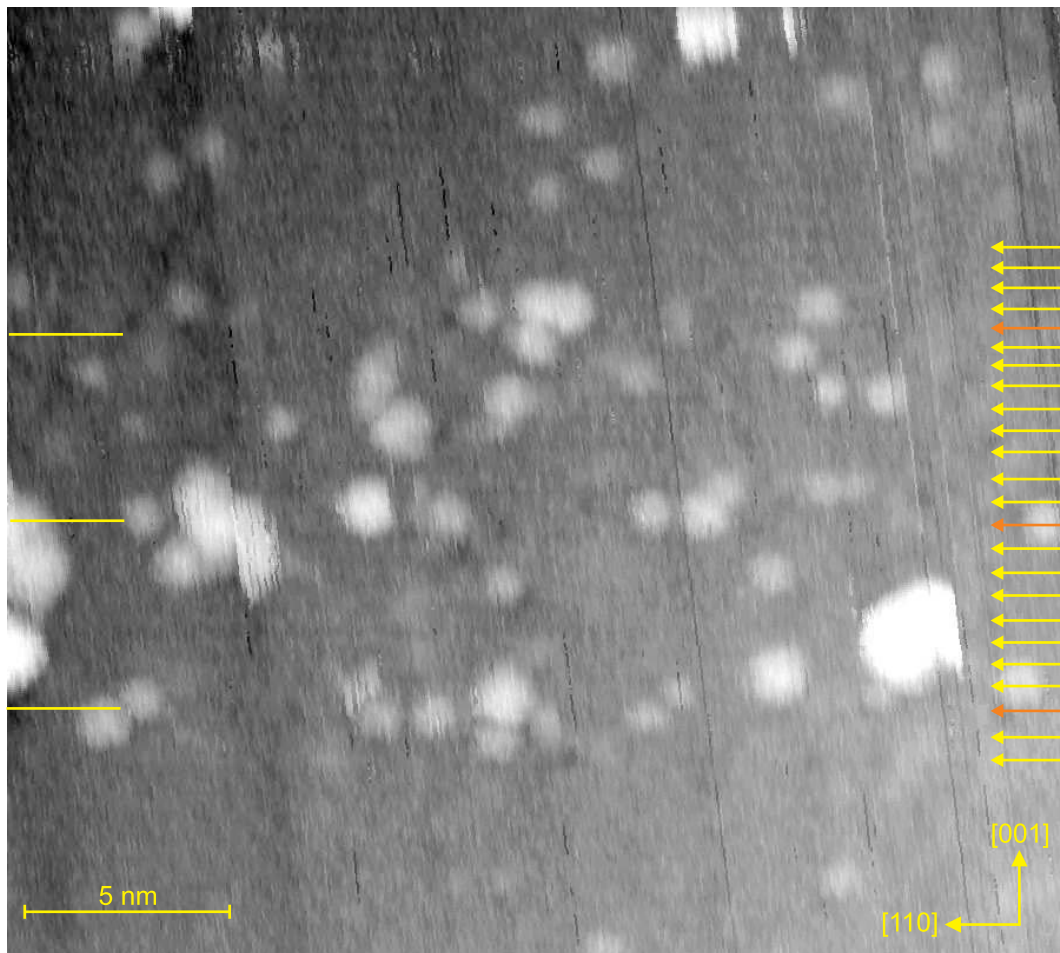


Figure 5.21: Filled-state XSTM image of the (Al,Ga)P marker layer (a 3-fold superlattice of 2 nm $\text{Al}_{0.23}\text{Ga}_{0.77}\text{P}$ and 2 nm GaP) where the atomic chains are marked by yellow arrows (orange for the approximated center position of the (Al,Ga)P layer parts). The image was taken at a sample voltage $V_T = -4.3$ V and a tunneling current $I_T \approx 20$ pA.

5.4 (Al,Ga)P/GaP layers grown by MBE

3x (2 nm $\text{Al}_{0.25}\text{Ga}_{0.75}\text{P}$ and 2 nm GaP) (Sample Yale20130725)

The (Al,Ga)P marker layer in the MBE-grown sample for XSTM investigations (Sample Yale20130725) consists of a 3-fold superlattice of 2 nm $\text{Al}_{0.25}\text{Ga}_{0.75}\text{P}$ and 2 nm undoped GaP, all grown at 580 °C, as shown in Fig. 4.1.

In the overview image shown in Fig. 4.3 (c) the expected 3-fold structure of the (Al,Ga)P marker layer was already visible and is further confirmed in the image in Fig. 5.22. In the empty-state images here, the marker layer parts are characterized not only by adatoms but also by holes in the surface.

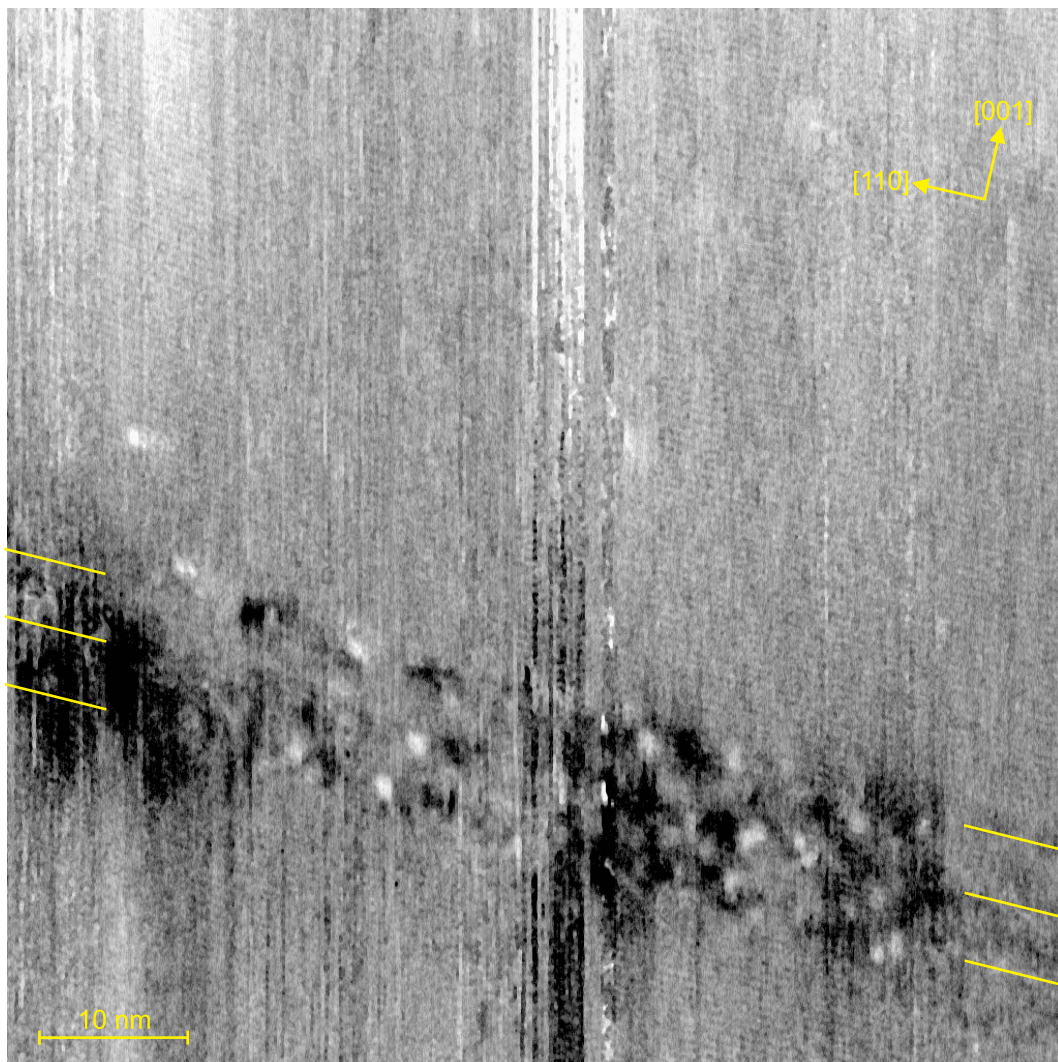


Figure 5.22: Empty-state XSTM image of the (Al,Ga)P marker layer (a 3-fold superlattice of 2 nm $\text{Al}_{0.25}\text{Ga}_{0.75}\text{P}$ and 2 nm GaP). The image was taken at a sample voltage $V_T = +5.2$ V and a tunneling current $I_T = 40$ pA.

The close view image in Fig. 5.23 indeed reveals the atomic chains on the surface. Although in these empty-state images one is sensitive to the group-III atoms a differentiation in contrast between Al-rich or Ga-rich regions is beyond the image or respectively the surface quality here also preventing a further investigation of the hole structures. Nevertheless, again the resolution enables to approximate the center positions of the (Al,Ga)P layer parts as indicated by the yellow lines/orange arrows and therewith to measure their distances. Here, values of 7 atomic chains which equals 14 ML or a distance of 3.8 nm for GaP, which is again in accordance with the nominal expected value of 4 nm.

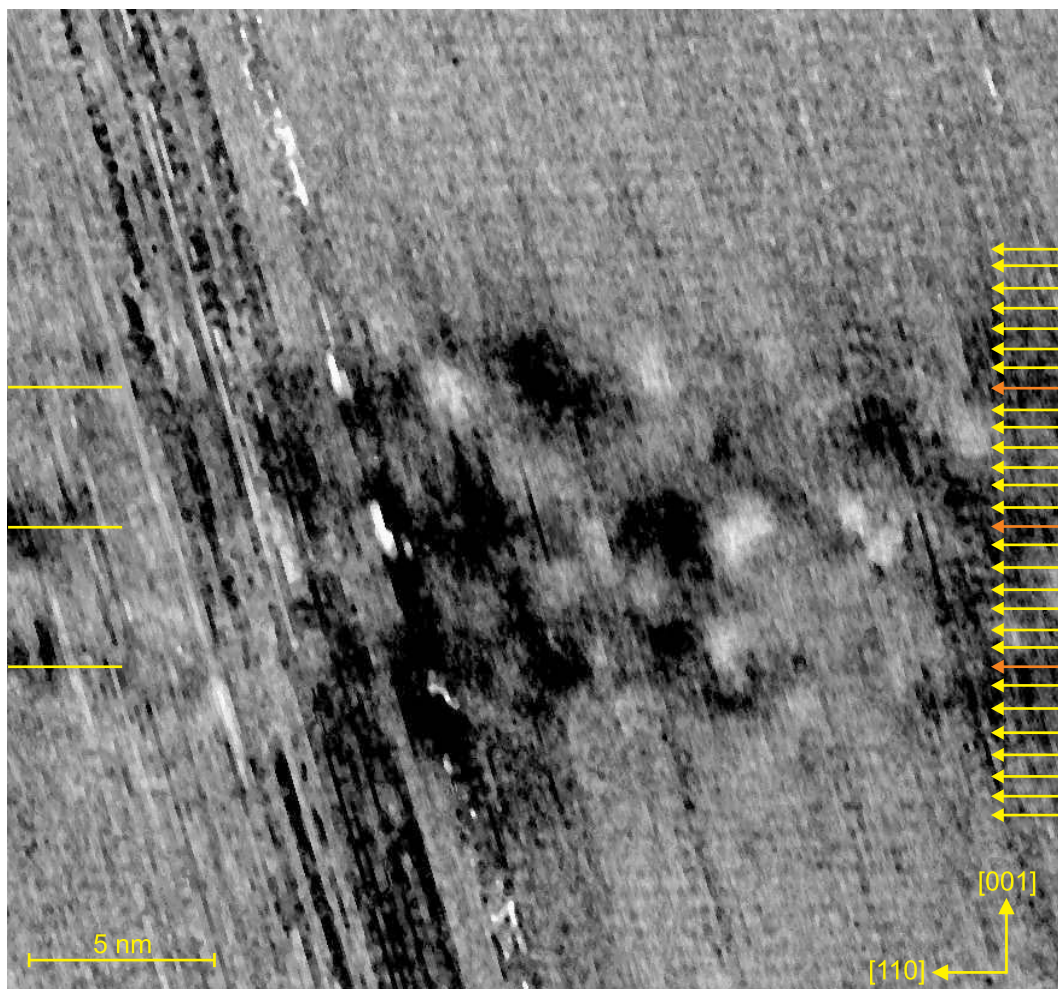


Figure 5.23: Empty-state XSTM image of the (Al,Ga)P marker layer (a 3-fold superlattice of 2 nm $\text{Al}_{0.25}\text{Ga}_{0.75}\text{P}$ and 2 nm GaP) where the atomic chains are marked by yellow arrows (orange for the approximated center position of the (Al,Ga)P layer parts). The image was taken at a sample voltage $V_T = +5.2$ V and a tunneling current $I_T = 40$ pA.

5.5 Growth behavior of thin GaAs and (Al,Ga)P layers in GaP

The presented XSTM investigations on thin GaAs and (Al,Ga)P layers in GaP show similarities in the growth behavior for MOVPE- and MBE-grown layers.

GaAs layers in GaP show only a slight segregation of the GaAs material along growth direction, which is a little stronger in MBE-grown samples than in the MOVPE-grown ones. Hence, in the MOVPE-growth a stronger localization of the deposited GaAs material occurs. For both growth methods, the total nominally deposited GaAs material amount is located inside the layers, which quantitatively supports the observations of low segregation effects in the GaAs/GaP system.

For thin (Al,Ga)P in GaP also no significant segregation effects of the (Al,Ga)P material along growth direction are indicated by the XSTM investigations. A difference between growth behavior in MOVPE compared to MBE cannot be observed. In both cases, the XSTM data reveals the nominal 3-fold structure of the grown layers. As the Al-containing layers attract adatoms on the cleavage surface in the XSTM, a more detailed analysis on the atomic scale is not possible here.

Chapter 6

Excursus: Calculations on the electronic structure

Using the presented experimental results on the structure of $\text{In}_{0.25}\text{Ga}_{0.75}\text{As}/\text{GaAs}/\text{GaP}$ quantum dots (Section 3.2) as input parameters for a quantum-dot model, a set of calculations was performed by Prof. Jacky Even at INSA Rennes/CNRS, France, in order to get a brief insight into the electronic and optoelectronic properties of these nanostructures.

6.1 The Quantum-Dot model

The experimental results on the quantum dots in Section 3.2 serve as a basis for the used model in the following calculations. The input parameters are the dimensions of the quantum dots with a height of 10 ML and a base length of 12 nm, and furthermore the determined material composition of an (In,Ga)As alloy without any phosphorus, but an indium-rich center with a reversed-cone stoichiometry profile and a total indium content of 2 ML inside a single quantum dot.

For the performed simulations, a cylindrical symmetry of the quantum dot is used for simplicity reasons. Following the dimension parameters above, the resulting quantum-dot model is shown in Fig. 6.1.

For comparison, five different configurations of the indium distribution within the quantum dot were taken into account, as shown in Fig. 6.2. All of them fulfill the required content of 2 ML indium. Cases A-C show a linear increase of the indium content from the quantum-dot base to its top, also including the reversed cone stoichiometry profile of the quantum-dot center. Case D assumes a homogeneous material distribution of 40 % indium, while case E again assumes a linear increase of the indium content but without an additional inner structure.

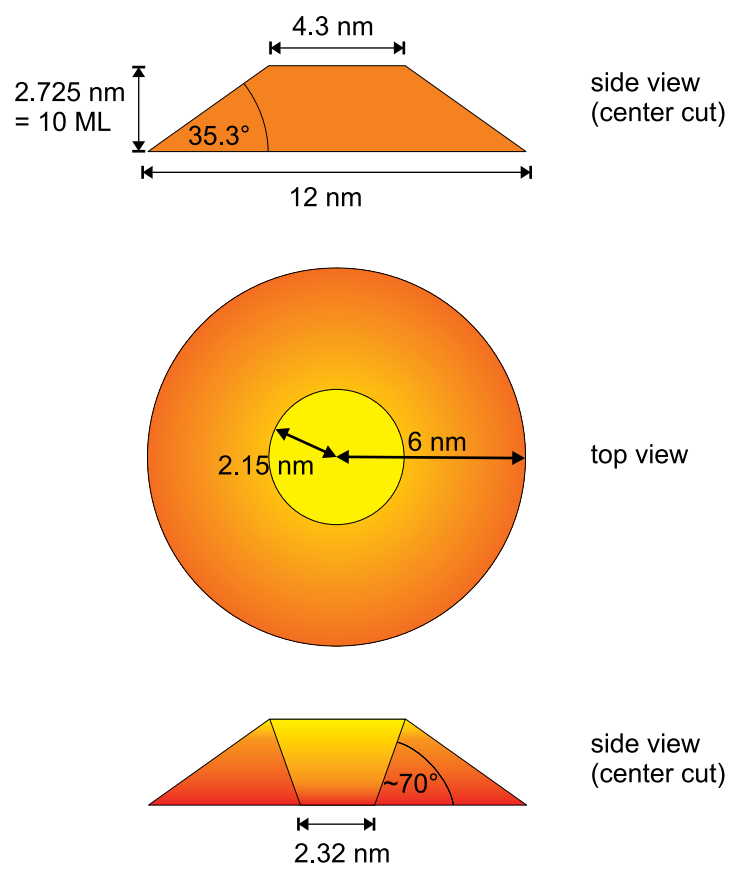


Figure 6.1: Schematics of the quantum dot model with cylindrical symmetry used for the simulations, which is based on the XSTM data.

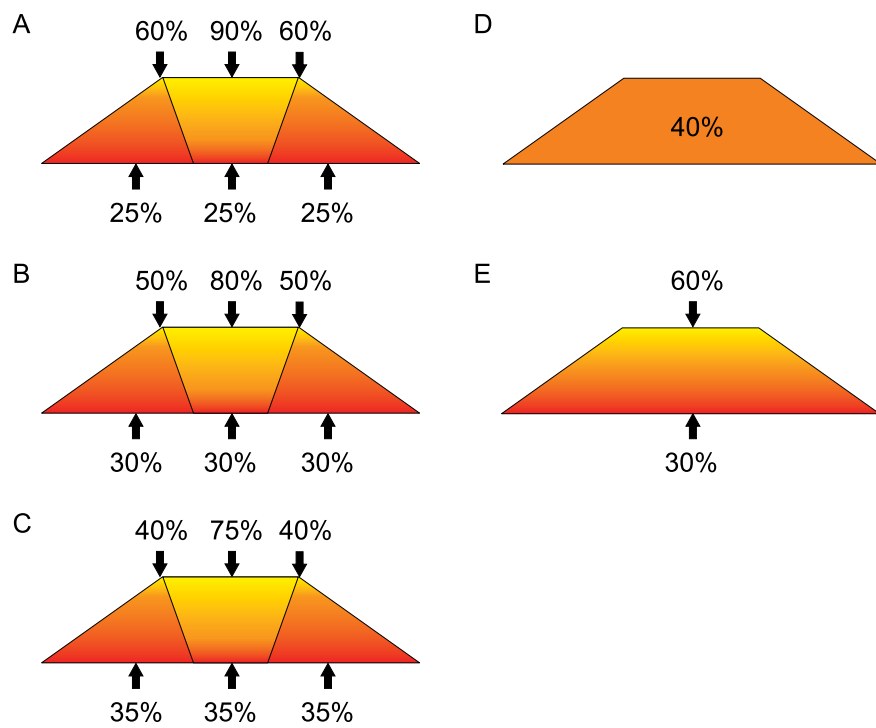


Figure 6.2: Schematics of the indium distribution within the quantum-dot model: (A-C) different profiles with increasing indium content from base to top including a reversed-cone center; (D) homogeneous material distribution, (E) profile with increasing indium content but without a reversed-cone center.

6.2 Performed calculations and results

The computational model used by J. Even is the eight-band $\mathbf{k}\cdot\mathbf{p}$ model with a cylindrical symmetry including the strain field. The numerical solution is obtained by the finite element method, and the Hamiltonian and elasticity equations are implemented in femlab/comsol. Details on the computational method can be found in Refs. [80,121].

Table 6.1 shows the energy parameters used for the different materials where $E_{V,av}$ is the average valence-band energy, δ is the spin-orbit splitting energy, and E_{gap} the direct electronic band-gap energy. The related equations are $E_V = E_{V,av} + \frac{\delta}{3}$ for the valence-band energy and $E_C = E_V + E_{gap}$ for the conduction-band energy.

The crystallographic meshes for the cylindrical symmetric quantum dots and its surrounding used in the calculations are shown in Fig. 6.3 for cases A-C and cases D-E respectively.

Table 6.1: Used parameters within the calculations [122].

		GaP	GaAs	InAs
$E_{V,av}$	[eV]	-1.27	-0.8	-0.59
δ	[eV]	0.08	0.34	0.39
E_{gap} ($T = 0K$)	[eV]	2.886	1.519	0.418

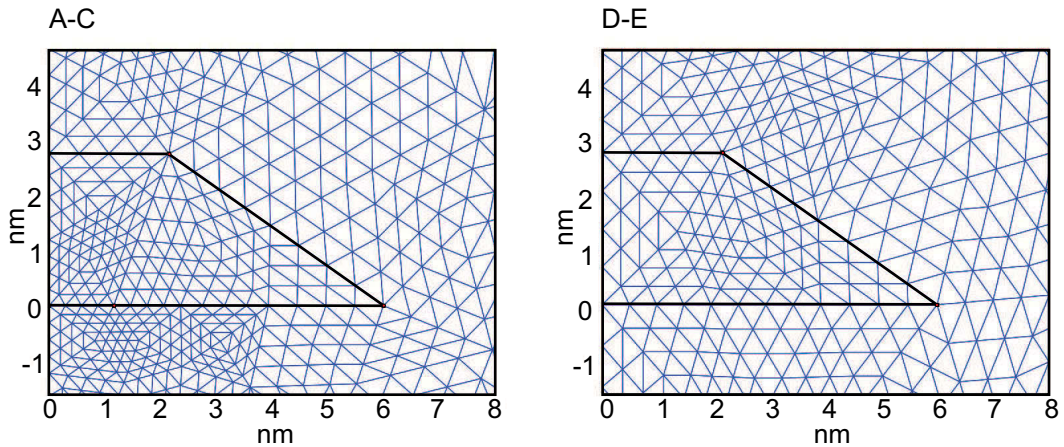


Figure 6.3: Schematic of the used meshes in the calculations.

6.3 Results and discussion about the electronic properties

Figure 6.4 shows a mapping of the norm of the wave function of the valence-band and conduction-band ground state in the different cases A-E. The images show that the probability density is at its maximum in the quantum-dot center in all cases and decreases almost radially to its minimum outside the quantum dot. In the conduction-band case the maximum region generally appears a little wider than the corresponding region for the valence-band ground state. The respective maps for the different cases look very similar, especially in cases A-C. For cases D-E the probability density decreases a little less from the center to the quantum-dot sides as compared with cases A-C, which could be expected for the lack of an indium-rich center.

The strain mapping in the homogeneous case D is shown in Fig. 6.5. In this case, the biaxial strain is tensile above and below the quantum dot, whereas the quantum-dot inside is compressively strained, as expected. The biaxial strain also has local extrema at the quantum-dot edges. The hydrostatic strain, on the other hand, is negligible almost everywhere outside the quantum dot but has a pronounced minimum at the inside with an almost homogeneous compression across the entire quantum dot. The shear strain component has a pronounced maximum within the quantum dot at its upper edge where quantum-dot top and side merge. Its minimum lies outside the quantum dot at its flanks.

The computational results for the ground-state and direct band-gap energies for the different cases A-E are listed in Table 6.2. The calculated values show only minor differences. They just show a variation of 19 meV for $E_{C,GS}$ and 8 meV for $E_{V,GS}$ and a variation of the direct band gap E_{gap} of only 24 meV. The homogeneous case D shows the highest shifts of the valence-band and conduction-band energies and also the largest band gap. Excluding case D the spread of the values gets even lower.

A schematic electronic band structure, deduced from the literature values for GaP (Table 6.1) and the averaged calculated values for the (In,Ga)As quantum dot (Table 6.2), is shown in Fig. 6.6. From this sketch it is clear that the conduction-band energy of the ground state at the Γ -Point in the quantum dot lies in between the corresponding values of the Γ -Point and X-Point of the GaP matrix. The position of X- and L-Point for the (In,Ga)As quantum dot however remains unclear. Regarding the electronic and optical properties it is of high interest whether for the (In,Ga)As quantum dot the X- and/or the L-Point is below the Γ -Point, as indicated (but not being a result) by the dashed orange lines in Fig. 6.6, or not. So from this data it is not clear whether the quantum dot has a direct or an indirect band gap and also

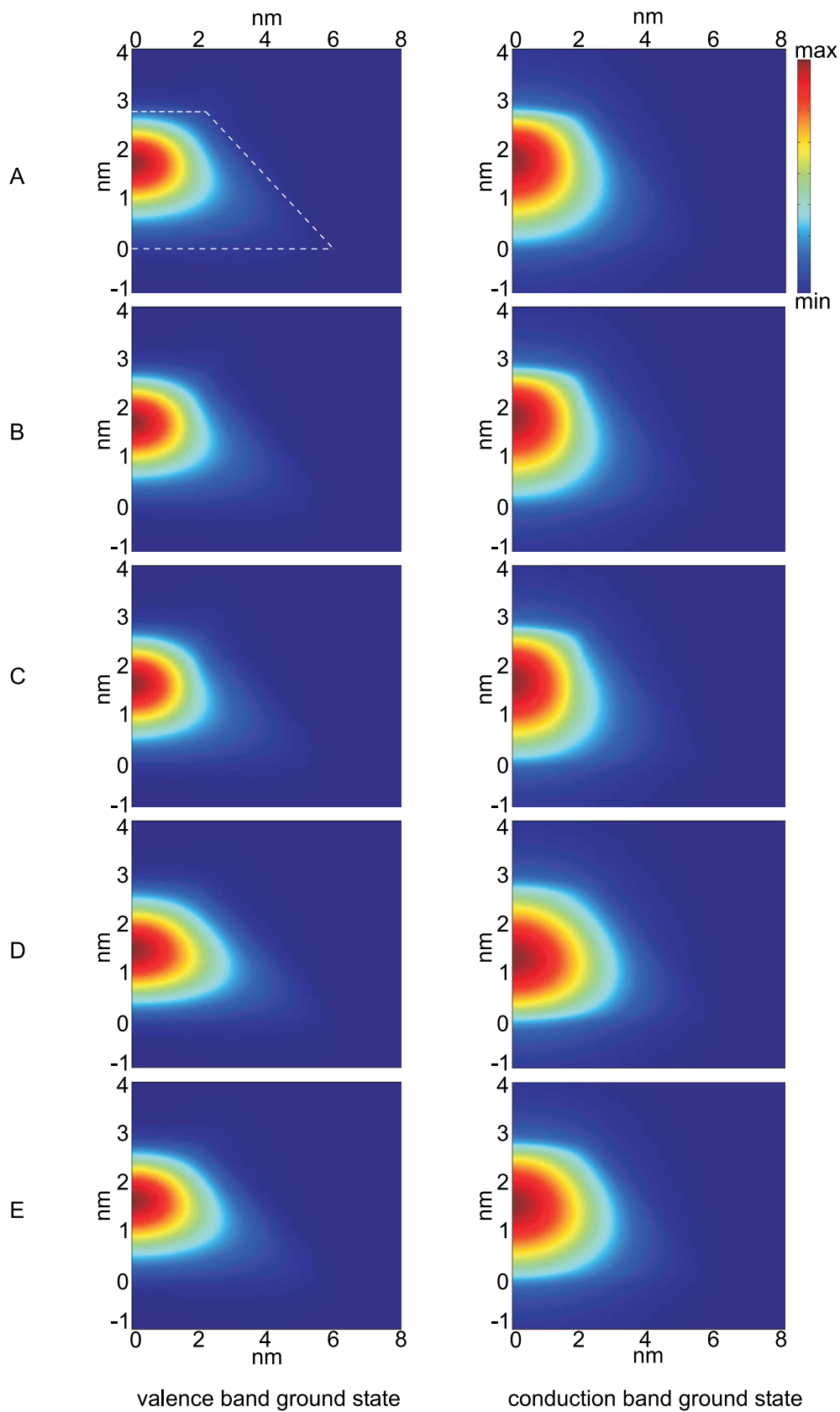


Figure 6.4: Mapping of the norm of the wave function for the valence band (left) and conduction band ground state (right) in cases A-E.

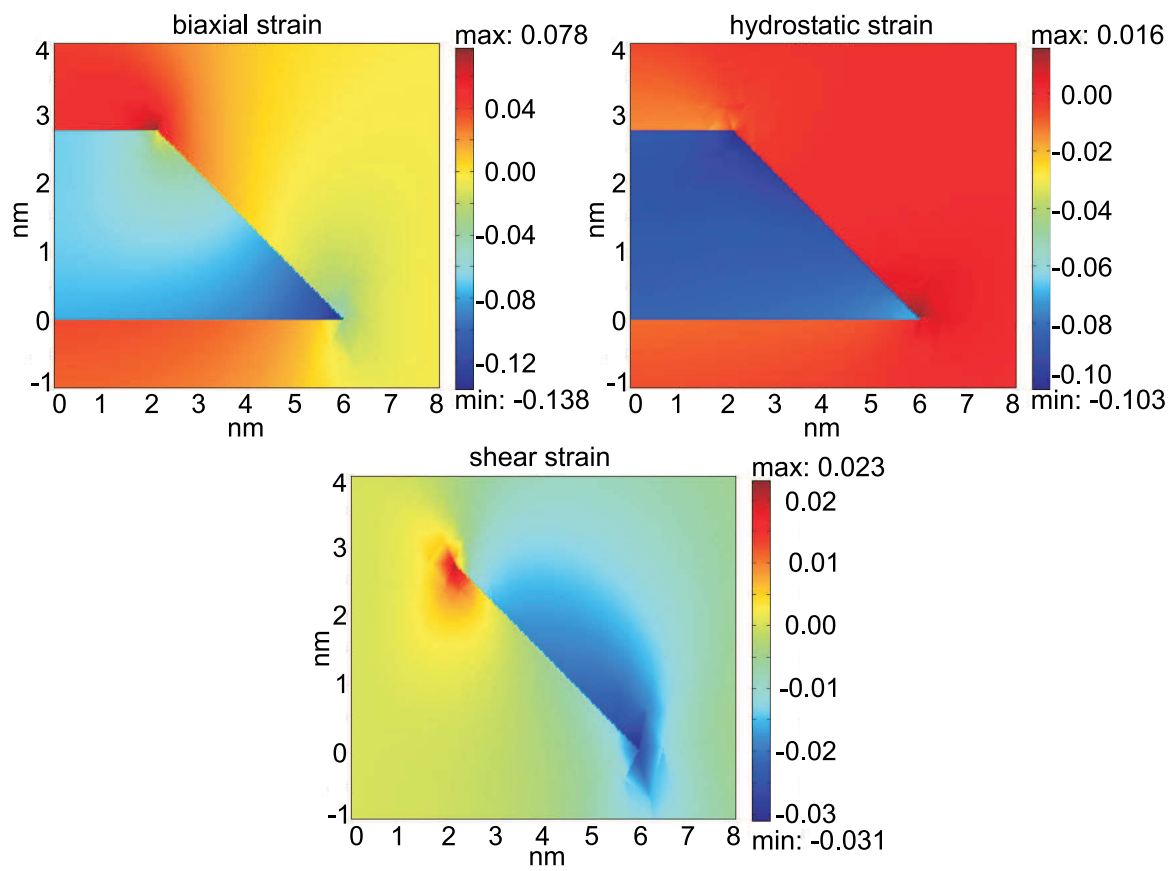


Figure 6.5: Mapping of the strain components for the homogeneous indium distribution (case D).

whether the band alignment is type I or type II. Another question that arises is the influence of a wetting layer which is definitely present since these quantum dots grow in the Stranski-Krastanow growth mode.

Table 6.2: Resulting ground-state and direct band-gap energies for the cases A-E and the average.

	A	B	C	D	E	average
$E_{C,GS}$ [eV]	1.3331	1.3285	1.3333	1.3478	1.3381	1.336
$E_{V,GS}$ [eV]	-0.6417	-0.6359	-0.6336	-0.6402	-0.6370	-0.638
E_{gap} [eV]	1.9748	1.9644	1.9669	1.9880	1.9751	1.974

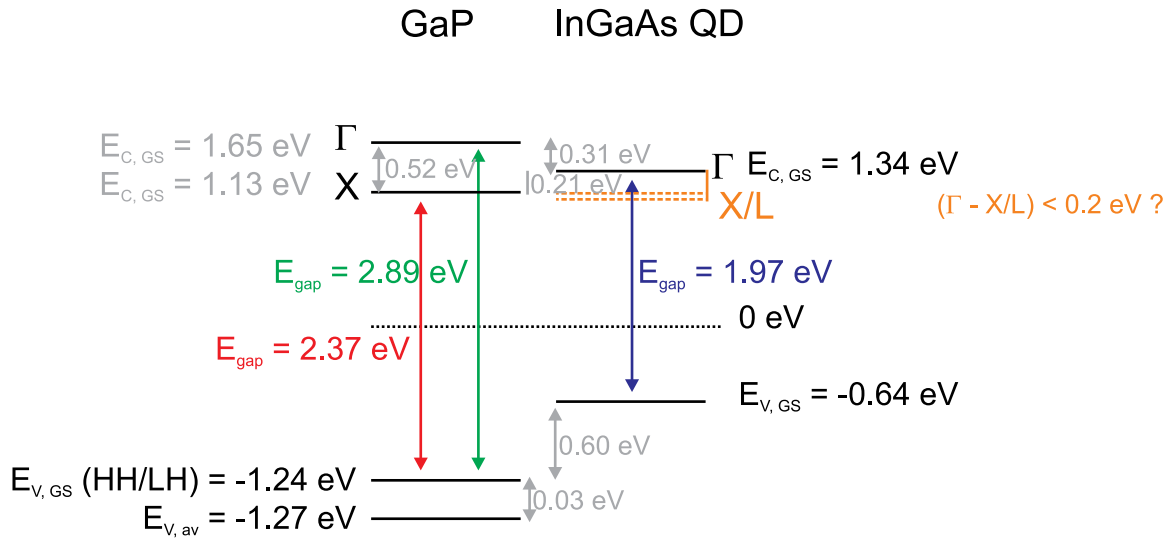


Figure 6.6: Schematic electronic band structure of GaP bulk material and the (In,Ga)As quantum dot deduced from the results in Tables 6.1-6.2 (average of cases A-E).

In order to solve these open questions, additional computations have been made by J. Even. The chosen approach here was to take the theoretical formula for a bulk material in a biaxially strained state, but using the relative volume variation and biaxial strain components resulting from the inhomogeneous strain tensor for a quantum dot with 40 % indium (Case D). This then results in an approximate mapping of the X_{xy} , X_z and L potentials inside and outside the quantum dot. Fig. 6.7 shows this mapping for the X_{xy} and X_z potentials. The average X_{xy} potential is not below the former calculated conduction-band ground state $E_{C,GS}$ (1.34 eV) but slightly above (1.4-1.45 eV). Moreover, the X_{xy} potential around the quantum dot is slightly higher (1.2-1.25 eV) than the value (1.13 eV) for bulk GaP, but still lower than the value

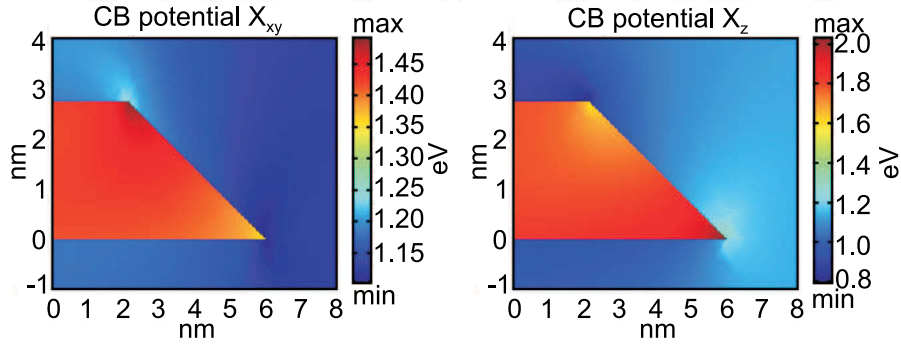


Figure 6.7: Mapping of the X_{xy} and X_z potentials for the (In,Ga)As quantum dot (case D).

Table 6.3: Resulting ground-state and band-gap energies for an (In,Ga)As quantum dot (case D), an (In,Ga)As quantum dot with a 3 ML GaAs wetting layer underneath and a separate quantum well of 3 ML GaAs.

	(In,Ga)As QD	(In,Ga)As QD + 3 ML WL	3 ML GaAs QW
$E_{C,GS}$ [eV]	1.3478	1.300	1.392
$E_{V,GS}$ [eV]	-0.6402	-0.609	-0.999
E_{gap} [eV]	1.9880	1.909	2.391

inside the quantum dot. The average X_z potential inside the quantum dot is even higher (about 1.8 eV) than the X_{xy} potential, and the X_z potential around the quantum dot has values (1.1-1.25 eV) which are around the value (1.13 eV) for bulk GaP. In conclusion, there are no X_{xy} - or X_z -like states confined inside the quantum dot, but there might be some confined X-like states in the barrier close to the quantum dot.

The results of calculations concerning the influence of an additional 3 ML GaAs wetting layer as well as results for a quantum well consisting of 3 ML thick GaAs are listed in Table 6.3 and are also included in an extended sketch for the band structure (Fig. 6.8). It shows that a wetting layer only leads to slight shifts of the valence- and conduction-band energies by about 40 meV, leading to a decrease of about 80 meV of the band gap. The separate GaAs quantum well in GaP has a much higher band gap of 2.39 eV and a valence-band energy, which is much closer to the valence-band energy of the GaP matrix than the valence-band energies of the (In,Ga)As quantum dot or the structure with quantum dot and wetting layer.

In conclusion, the results of the performed calculations show that a clear statement on the electronic properties, e.g. if the band gap is direct or indirect and if there

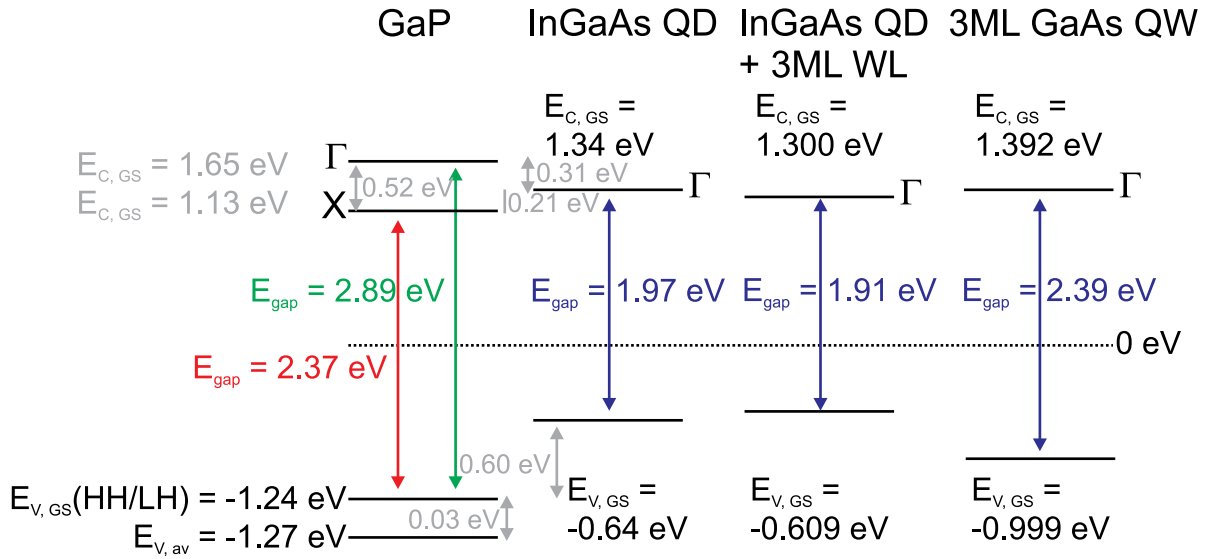


Figure 6.8: Schematic of the electronic bandstructure of GaP bulk material, an (In,Ga)As quantum dot (average of cases A-E), an (In,Ga)As quantum dot with a 3 ML GaAs wetting layer underneath and a quantum well of 3 ML GaAs. All values are deduced from the results in Tables 6.1-6.3.

is a type I or type II alignment, cannot be made easily. On the other hand, one could conclude that the material distribution inside an (In,Ga)As quantum dot with an indium content of 2 ML (cases A-E) only has a marginal effect on the energy level positions (for the ground state) and that also a GaAs wetting layer underneath has only a slight influence.

Chapter 7

Outlook: (In,Ga)Sb/GaAs Quantum Dots in GaP

Regarding possible applications of the investigated (In,Ga)As/GaP quantum dots, their use in QD-Flash memories already showed hole storage times of 3 μ s in experiments with $\text{In}_{0.25}\text{Ga}_{0.75}\text{As}/\text{GaAs}/\text{GaP}$ quantum dots [55] and 230 s for $\text{In}_{0.5}\text{Ga}_{0.5}\text{As}/\text{GaAs}/\text{GaP}$ quantum dots (with an additional AlP barrier) [123]. For a further increase of the storage times a change to antimony-containing quantum dot materials is a possible step, as larger hole localization energies and therewith larger storage times of up to years were predicted [58, 124], and already promising experiments for GaSb/GaAs quantum dots resulting in storage times of 3.9 days were reported [125].

Predictions for $\text{In}_{0.5}\text{Ga}_{0.5}\text{Sb}$ quantum dots in a GaP matrix yield storage times of more than 10 years [126], which make them a worthwhile material for fundamental investigations. Growth experiments on this material system using MOVPE have been performed by Elisa Sala in the workgroup of Prof. Dr. D. Bimberg at the TU Berlin [126]. It turned out that the introduction of a GaAs interlayer on the GaP substrate before the $\text{In}_{0.5}\text{Ga}_{0.5}\text{Sb}$ deposition again favors the quantum dot formation.

XSTM experiments on $\text{In}_{0.5}\text{Ga}_{0.5}\text{Sb}/\text{GaAs}$ Quantum Dots in GaP

Initial structural characterization experiments on these $\text{In}_{0.5}\text{Ga}_{0.5}\text{Sb}/\text{GaAs}/\text{GaP}$ quantum dot layers (performed under my guidance by Stavros Rybank [127]) using XSTM already gave a brief insight.

The designed XSTM sample (TU11263) grown by MOVPE is shown in Fig. 7.1 and contained four $\text{In}_{0.5}\text{Ga}_{0.5}\text{Sb}/\text{GaAs}/\text{GaP}$ layers, each consisting of 5.0 ML GaAs, followed by an antimony flush, 0.42 ML $\text{In}_{0.5}\text{Ga}_{0.5}\text{Sb}$ and a GRI of 1 s before the initial capping with 6 nm GaP, all grown at 500 °C. The duration of the Sb-flush was

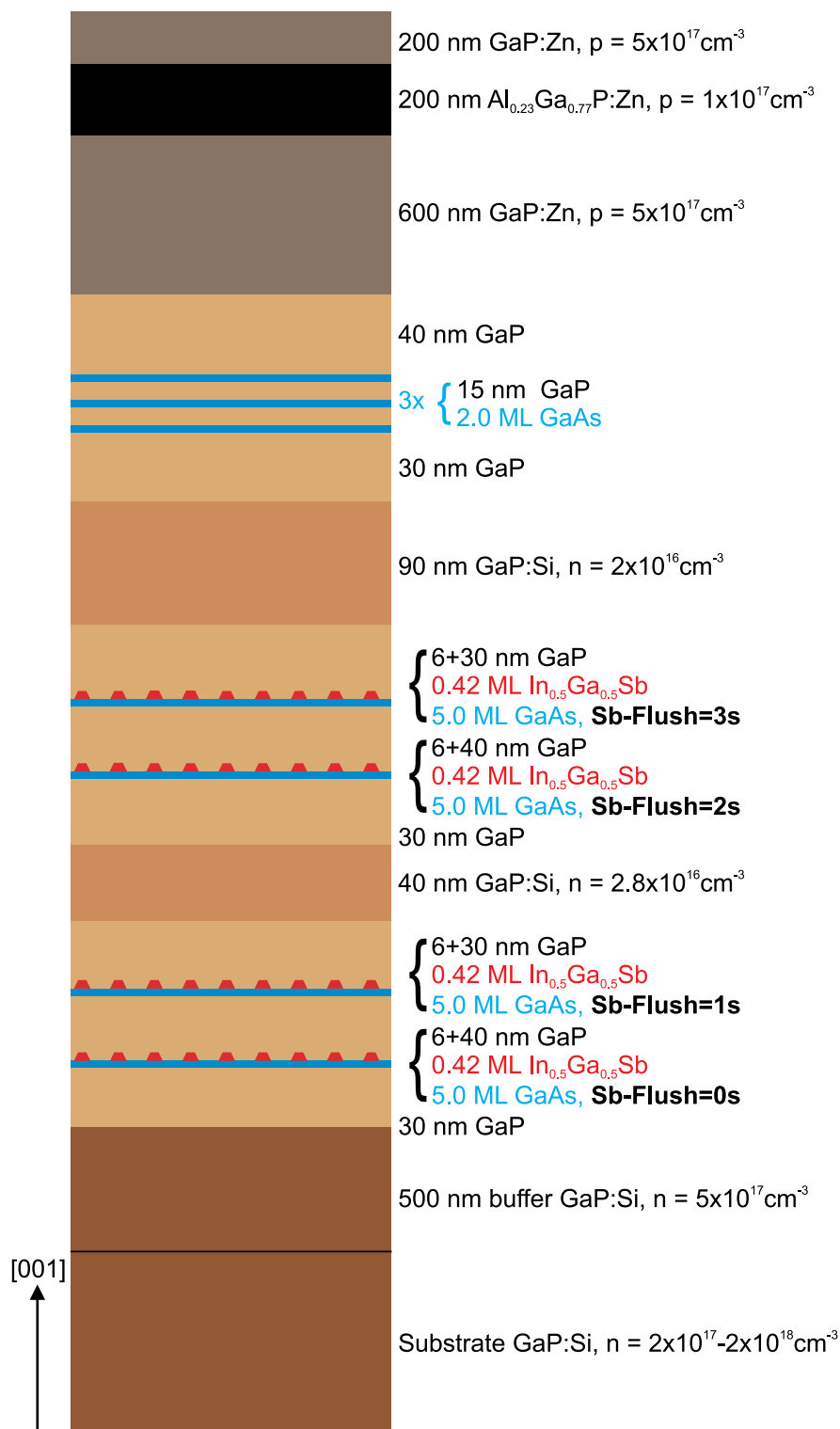


Figure 7.1: Schematic of the structure of sample TU11263.

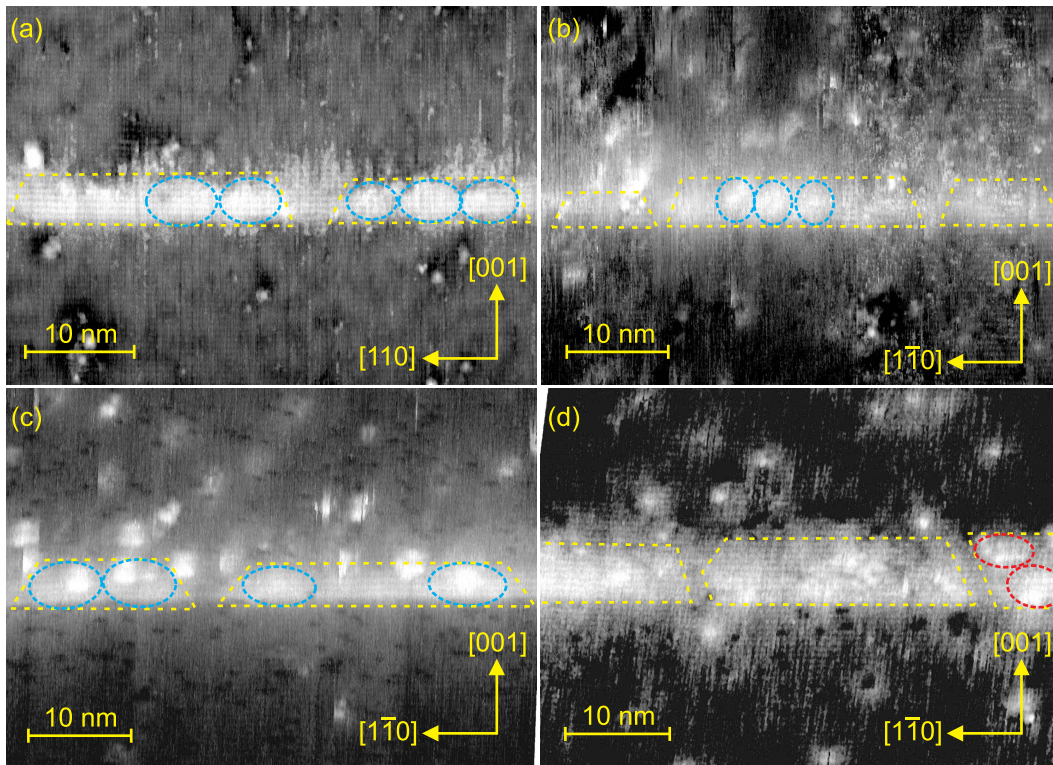


Figure 7.2: (a) Filled-state XSTM images of layer 1 (Sb-flush: 0 s) and (b-c) empty-state XSTM images of layers 2–4 (Sb-flush: 1 s, 2 s, 3 s), where the nanostructures are marked by the dashed yellow lines and the inner agglomerations are marked by dashed blue/red ovals. The images were taken at sample voltages $V_T = -3.5$ V (a), $V_T = +2.3/2.5$ V (b), and $V_T = +2.4$ V (c-d), and tunneling currents $I_T = 25$ pA (a) and $I_T = 30$ pA (b-d).

varied between the layers, as preliminary AFM experiments showed an influence on the growth of the layers [128], using values of 0 s, 1 s, 2 s, and 3 s. The sample design also included typical features for XSTM experiments which were already discussed in the previous chapters: a 500 nm thick buffer layer of n -doped GaP and 30 nm of undoped GaP on a n -doped GaP(001) substrate, both layers grown at 750 °C, a marker layer consisting of a 3-fold superlattice of 2.0 ML GaAs and 15 nm undoped GaP, grown at 500 °C, and a p -doped $\text{Al}_{0.23}\text{Ga}_{0.77}\text{P}$ barrier of 200 nm for attracting migrating surface adatoms, before the final capping of 200 nm of p -doped GaP, all grown at 620 °C. The GaP spacers in between the layers of interest were partly n -doped in order to increase the conductivity of the sample, with all GaP spacers grown at 620 °C.

Preliminary results of the structural properties

Initial XSTM images of the different $\text{In}_{0.5}\text{Ga}_{0.5}\text{Sb}/\text{GaAs}/\text{GaP}$ layers are shown in Fig. 7.2 (a-d). The XSTM contrast analysis showed that all of the layers consist

of bright contrasted nanostructures, which are separated by areas of darker contrast. These nanostructures are indicated by the dashed yellow lines in Fig. 7.2 (a-d) (which highlight the dimensions of the nanostructure but not their actual shape). For the layers with the Sb-flush of 0 s, 1 s, and 2 s, inside these nanostructures material agglomerations are proposed, which have an even brighter contrast, as indicated by the dashed blue ovals in Fig. 7.2 (a-c). For the longest Sb-flush of 3 s also agglomerations inside the nanostructures appear, which have a different arrangement, as indicated by the dashed red ovals in Fig. 7.2 (d). Concerning a quantitative evaluation of these nanostructures in all four layers, a preliminary statistics was made [127], which is based on only very few data but which provides already some average values of their base lengths (12–24 nm), heights (13.0–18.0 ML), and areal density $[(2.3–8.5) \times 10^{11} \text{ cm}^{-2}]$.

As a general observation from the XSTM contrast, all layers have a sharp borderline underneath but their top shows varying heights. Also the observed heights are much higher than the deposited amount of 5.0 ML GaAs and 0.42 ML $\text{In}_{0.5}\text{Ga}_{0.5}\text{Sb}$. These results already again indicate a material intermixing during growth and/or capping of the layer. From the different contrasts in the XSTM images in comparison with the deposited material amounts (nominal 5.0 ML arsenic but only 0.21 ML indium and 0.42 ML antimony + additional flush) one could guess that the nanostructures then probably mainly consist of Ga(As,P). The brighter contrast of the inner agglomerations could be related to Ga(As,P) with higher arsenic concentrations—and possibly also to the presence of indium and/or antimony. The results also show that the duration of the additional Sb-flush has an effect on the material distribution, leading to different nanostructures dimensions/densities, and for the longer investigated duration of 3 s even to a different material arrangement, shown by the non-uniform contrast along the [001]-direction in Fig. 7.2 (d).

First evaluation of the stoichiometry

An initial stoichiometry profile (exemplarily for a region in layer 4) is shown in Fig. 7.3 (b). The profile shows a significant rise of the local lattice parameter at the position of the bright contrast in the evaluated region in the XSTM image in Fig. 7.3 (a). A characteristic undershoot of the local lattice parameter shows that also in this material system there is a compression of the material underneath the layer. The primary peak consists of 5 data points, which equals an extension of 10 ML. Considering a layer mainly consisting of Ga(As,P) the local lattice parameter rises to the value of pure GaAs, with concentrations of 50–100%, and slightly also exceeds this value. The latter already gives the hint of additional incorporated material, which compared to the deposited material species can be indium and/or antimony.

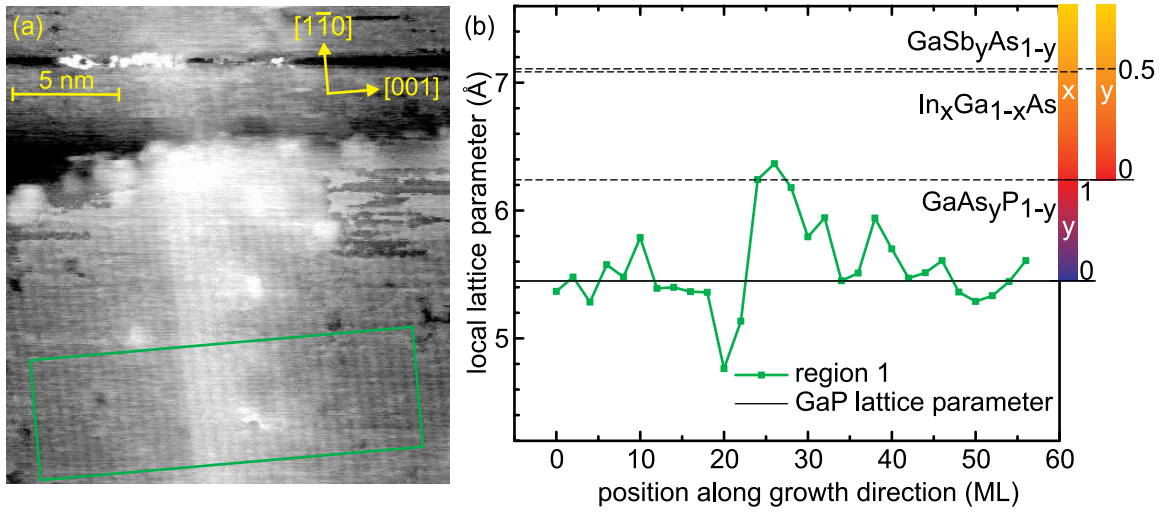


Figure 7.3: (a) Empty-state XSTM image of layer 4 (Sb-flush: 3 s). The evaluated region is highlighted by the colored box. The image was taken at $V_T = +2.7$ V and $I_T = 30$ pA. (b) Corresponding evaluation of the local lattice parameter and the related stoichiometric composition along growth direction. The graph shows the evaluated data (region 1) in green squares.

According to Fig. 2.15 now two scale bars have been included in Fig. 7.3 (b) representing a change in the group-III (from GaAs to $\text{In}_x\text{Ga}_{1-x}\text{As}$) but also in the group-V (from GaAs to $\text{GaSb}_y\text{As}_{1-y}$). In both cases, as the scales are similar, only a marginal amount of indium and/or antimony would be present according to the local lattice parameter. But, as the material inside the nanostructured layer is distributed over a height of at least 10 ML (due to the 5 data points of the peak), but only 5 ML of GaAs were deposited, additional indium and/or antimony material must be incorporated within the layer. This can be only realized by a further intermixing during growth and capping, leading to a quaternary arrangement of $(\text{In,Ga})(\text{As,P})$ or $\text{Ga}(\text{Sb,As,P})$, or even to a quinary material composition of $(\text{In,Ga})(\text{Sb,As,P})$.

A specialty of the shown profile which only appeared (according to the obtained data up to now) for layer 4 is that after a decline to the GaP lattice parameter a second rise of the local lattice parameter appears that can be attributed to the change in the contrast inside the nanostructure along the $[001]$ -direction, which is only characteristic for this layer having the longest Sb-flush (3 s).

For a detailed structural investigation of these highly interesting quinary $\text{In}_{0.5}\text{Ga}_{0.5}\text{Sb}/\text{GaAs}/\text{GaP}$ quantum dot layers, where a material redistribution during growth occurs leading to a nanostructured layer with quaternary or even quinary material agglomerations, further XSTM data are needed. High-resolution XSTM images of each layer in both polarities could help to distinguish between individual atoms of the

different material species [50]. The combination with a stoichiometry analysis of the different contrasted parts of the layers and the nanostructures (as presented in Chapters 3-4 for the $(\text{In,Ga})\text{As}/\text{GaP}$ quantum dot system) by evaluating the local lattice parameter would give a deeper insight of the indium and antimony incorporation and the effect of the duration of the additional Sb-flush. For comparison of the resulting local lattice parameters the table and map in Section 2.2.4 need to be extended to quaternary and quinary material combinations. With these requirements fulfilled XSTM will again be a powerful tool to reveal the special structural characteristics even of this challenging material system.

Chapter 8

Conclusions

The scientific work within the presented thesis reveals the structural characteristics of different (In,Ga)As quantum dot layers as well as of GaAs and (Al,Ga)P layers, all embedded within a GaP matrix, being investigated by using cross-sectional scanning tunneling microscopy.

Initial XSTM investigations on (In,Ga)As grown on a GaP(001) substrate with MOVPE showed that a GaAs interlayer before the $\text{In}_{0.25}\text{Ga}_{0.75}\text{As}$ deposition enables a Stranski-Krastanow growth mode. This leads to the formation of quantum-dot like islands with a supposed truncated pyramidal shape, with dimensions of 11–18 nm in base length, 8–10 ML in height, and an areal density of about $7\text{--}8 \times 10^{10} \text{ cm}^{-2}$.

Further XSTM experiments on MOVPE-grown $\text{In}_{0.25}\text{Ga}_{0.75}\text{As}/\text{GaAs}$ on GaP resulted in atomically resolved data revealing that intense material-redistribution effects occur during growth. The subsequently deposited GaAs and $\text{In}_{0.25}\text{Ga}_{0.75}\text{As}$ layers are not found to be incorporated separately, but they do intermix, which leads to a Stranski-Krastanow growth mode. The resulting quantum dots have a truncated pyramidal shape with an average base length of 12 nm and heights of up to 10 ML. An evaluation of both the XSTM image contrast and the local stoichiometry showed that the quantum dots consist of (In,Ga)As and contain the whole amount of deposited indium material, indicating a lateral indium material transfer into the forming quantum dots during the Stranski-Krastanow growth. Also a vertical back segregation of the indium material during capping of the quantum dots is probable, i.e. from the apex into the remaining quantum dot, as the entire indium material is found here. The capped quantum dots then exhibit a so-called reversed-cone stoichiometric profile of (In,Ga)As. The surrounding wetting layer consists of inhomogeneously distributed Ga(As,P) without any indium. This shows that, in contrast to observations for $\text{In}_{0.5}\text{Ga}_{0.5}\text{As}$ quantum dots in GaAs [91], there is no lateral back-segregation of indium material into the wetting layer during overgrowth. Nevertheless, here the wetting layer laterally decom-

poses into areas which are more GaAs-rich and more GaP-rich. The resulting larger quantum dots transform into quantum rings with average total base lengths of 21 nm and heights of up to 9 ML, and both quantum dots and quantum rings together have a relatively high density of $2.4 \times 10^{11} \text{ cm}^{-2}$.

Experiments on MOVPE-grown $\text{In}_{0.5}\text{Ga}_{0.5}\text{As}/\text{GaAs}$ on GaP showed that the duration of the growth interruption after the $\text{In}_{0.5}\text{Ga}_{0.5}\text{As}$ deposition has a significant influence on the photoluminescence emission of these layers, i.e. a rise of the PL intensity with increasing GRI up to a duration of 200 s and an intensity decrease for even longer GRI. Atomically resolved data from XSTM experiments on $\text{In}_{0.5}\text{Ga}_{0.5}\text{As}/\text{GaAs}$ layers with three different GRI revealed that this is caused by a change of the structural properties of the layers that occurs during the GRI.

For a low GRI duration (20 s) Stranski-Krastanow quantum dots form, which have again a truncated pyramidal shape with an average base length of 10.1 nm, an average quantum dot height of 8.0 ML, and maximum heights of 11 ML. In comparison to the formerly investigated $\text{In}_{0.25}\text{Ga}_{0.75}\text{As}/\text{GaAs}$ on GaP the quantum dots here show a similar appearance but a smaller size. The areal density of the quantum dots is slightly lower but in the same magnitude, amounting to about $1.5 \times 10^{11} \text{ cm}^{-2}$. This difference is also due to the lower nominally deposited material amount here of 0.4 ML InAs and 2.6 ML GaAs, in contrast to the nominal material amount of 0.5 ML InAs and 4.5 ML GaAs for the $\text{In}_{0.25}\text{Ga}_{0.75}\text{As}/\text{GaAs}$ quantum dots. Evaluating the image contrast and the local stoichiometry shows that material redistribution effects again occur during the Stranski-Krastanow growth. The quantum dots and the closely surrounding parts of the wetting layer consist of $(\text{In,Ga})\text{As}$, containing the total deposited amount of indium material. This again indicates a lateral indium material transfer during the quantum dot formation as well as a probable back segregation during capping from the former apex into the remaining truncated pyramidal shaped quantum dots and their surrounding. An inner structure of the quantum dots or a further transformation into quantum rings could not be observed here. The parts of the wetting layer away from the quantum dots are free of indium material, consisting of $\text{Ga}(\text{As,P})$, and in analogy to former observations decompose inhomogeneously into more GaAs-rich and more GaP-rich areas.

A longer GRI duration (200 s) results in a dissolution of the quantum dots into material agglomerations. A lateral back transfer of the indium material from the quantum dots into the former indium free areas of the wetting layer occurs but also a phosphorus transfer from the former $\text{Ga}(\text{As,P})$ wetting layer areas into the phosphorus free quantum dot areas. Both together lead to a material intermixing into a more quaternary $(\text{In,Ga})(\text{As,P})$ alloyed layer.

The even longer GRI duration (400 s) seems to reduce the number of agglomerations and a further lateral material transfer takes place. This intense material intermixing then leads to the formation of a more homogeneous quaternary (In,Ga)(As,P) layer.

Regarding the PL emission characteristics, the results of the structural analysis show that for the $\text{In}_{0.5}\text{Ga}_{0.5}\text{As}/\text{GaAs}/\text{GaP}$ quantum dot system investigated the following observations can be made: Quantum dots with a classical atomic structure consisting of (In,Ga)As have a weak emission intensity. In contrast the highest emission intensity is found for the phase, in which the quantum dots have transformed into agglomerations in a more quaternary environment. A decrease of the emission intensity is then related to the ongoing material intermixing with the longer GRI duration into a homogenous quaternary (In,Ga)(As,P) layer.

XSTM investigations on (In,Ga)As quantum dot layers in GaP grown with MBE confirmed the influence of the GaAs interlayer on the structural characteristics of those layers.

Layers with the same nominal amount of $\text{In}_{0.25}\text{Ga}_{0.75}\text{As}/\text{GaAs}$ material on GaP, as compared with previous MOVPE-grown layers, resulted in quantum dots with comparable structural properties. The MBE-grown $\text{In}_{0.25}\text{Ga}_{0.75}\text{As}/\text{GaAs}/\text{GaP}$ quantum dots also have a truncated pyramidal shape with an average base length of 9.2 nm, an average quantum dot height of 13.6 ML, and maximum heights of 20 ML, while the areal density of the quantum dots is $4.2 \times 10^{11} \text{ cm}^{-2}$. Compared to their MOVPE equivalents the quantum dots grown here are laterally a little smaller but higher with the areal density being in the same range. The evaluation of the image contrast and the local stoichiometry also reveals the similar material distribution inside these layers. The quantum dots consist of phosphorus-free (In,Ga)As containing the total deposited amount of indium, again with a high indium localization in the quantum-dot center, whereas the surrounding wetting layer consists of indium-free Ga(As,P).

Layers with a varying $\text{In}_{0.5}\text{Ga}_{0.5}\text{As}$ material amount grown directly on GaP, without a GaAs interlayer underneath, show an inhomogeneous distribution of the (In,Ga)As material within the layer. Small agglomerations are observed which get more pronounced in the image contrast when increasing the nominally deposited $\text{In}_{0.5}\text{Ga}_{0.5}\text{As}$ material amount (in the investigated regimes from 2.0–4.0 ML). Interpreting the few stoichiometry data in combination with the image contrast, it seems that these agglomerations contain indium but in a quaternary (In,Ga)(As,P) arrangement. Besides, the surrounding (wetting) layer parts have less indium embedded and may consist of (In,Ga)(As,P), where at least in the case of a nominally deposited amount of 4.0 ML $\text{In}_{0.5}\text{Ga}_{0.5}\text{As}$ the material redistribution during growth led to a presumably ternary Ga(As,P) arrangement.

In comparison, in the MBE-grown $\text{In}_{0.25}\text{Ga}_{0.75}\text{As}$ layers on GaP with a GaAs interlayer the quantum dots show a much brighter contrast than the agglomerations in the $\text{In}_{0.5}\text{Ga}_{0.5}\text{As}$ layers grown without a GaAs interlayer, which goes along with a higher and phosphorus-free indium material localization within the quantum dots. Hence also in MBE, again a GaAs interlayer can significantly affect the material arrangement inside (In,Ga)As layers grown on GaP.

Investigations by XSTM contrast on thin GaAs layers in GaP, which were grown by MOVPE, revealed that there is only a slight segregation of the GaAs material along growth direction. The stoichiometry analysis shows that the nominally deposited GaAs material amount is located inside the layers. In one case, where the contrast analysis shows a strong localization of the presumably total nominal deposited GaAs material, the local lattice parameter, which is a measure of the local material content, sharply rises to unexpectedly high values. The origin of this unusual behavior is still open though reasonable attempts for an explanation were performed by using further calculations and TEM data, which both favor an up-to-now unknown effect that occurs at the cleavage surface. Thin GaAs layers in GaP grown by MBE, here, show a little stronger segregation along growth direction compared to the MOVPE-grown layers. But also here the layers contain the total GaAs material which is only located at the observed position of the layers extracted from the XSTM image contrast.

Thin layers of (Al,Ga)P in GaP show a behavior that is independent from the performed growth method (MOVPE or MBE). In XSTM experiments, as expected, these Al-containing layers attract adatoms on the cleavage surface, what makes an analysis on the atomic scale almost impossible. The nominal structure of the grown layers, i.e. the 3-fold structure nevertheless could be identified and therewith the distance between the individual layer parts, which is in accordance with the nominal values, which then at least indicates indirectly that there is no significant segregation of the (Al,Ga)P material along growth direction.

Calculations on the electronic structure of $\text{In}_{0.25}\text{Ga}_{0.75}\text{As}/\text{GaAs}/\text{GaP}$ quantum dots show that for the model of a cylindrical symmetric quantum dot the distribution of the incorporated 2 ML of indium material within the quantum dot and also the existence of a wetting layer underneath have only a marginal effect on the electronic structure. The computational results for the energy level positions of the valence band and the conduction band ground states as well as the mapping of the X_{xy} and X_z potentials, the latter in the case of a homogeneous indium distribution within the quantum dot, give initial information on the electronic structure, but prevent from clear statements e.g. about the band alignment.

Initial XSTM experiments on $\text{In}_{0.5}\text{Ga}_{0.5}\text{Sb}/\text{GaAs}$ quantum dot layers on GaP grown by MOVPE, which are promising for future QD-Flash memories, show that again the deposited material intermixes and gets redistributed during growth, leading to the formation of nanostructures, which, according to the XSTM image contrast, also contain differing material agglomerations inside. The duration of an additional antimony flush after the GaAs and before the $\text{In}_{0.5}\text{Ga}_{0.5}\text{Sb}$ deposition has an influence on the dimensions and densities of the nanostructures, with the longest investigated duration of 3 s even leading to a different material distribution and therewith differing agglomerations inside the nanostructures. According to a first stoichiometry analysis, the nanostructures must consist mainly of a quaternary or even a quinary arrangement of the deposited $(\text{In,Ga})(\text{As,Sb,P})$ material with differing compositions. A detailed investigation of the specific material arrangement inside these $\text{In}_{0.5}\text{Ga}_{0.5}\text{Sb}/\text{GaAs}/\text{GaP}$ quantum dot layers as well as a better statistics on their dimensional properties is still open for future experiments.

In conclusion, the investigations presented within this thesis show that cross-sectional scanning tunneling microscopy is a powerful and worthwhile tool to reveal the structural characteristics of $(\text{In,Ga})\text{As}/\text{GaP}$ quantum dots and related materials on the atomic scale and to get a deeper insight into material redistribution effects occurring during growth of these material systems and many others, which are highly interesting for technological applications, but also in order to generally understand their fundamental properties. XSTM as the method of choice will continuously be a reliable ally for further structural investigations in the field of semiconductor nanostructures in the near future.

Bibliography

- [1] J. Bardeen and W. H. Brattain, *Physical Review* **74**, 230 (1948).
- [2] G. E. Moore, *Electronics* **38**, 114 (1965).
- [3] K. Hans Wedepohl, *Geochimica et Cosmochimica Acta* **59**, 1217 (1995).
- [4] J. Dąbrowski and H.-J. Müssig, *Silicon Surfaces and Formation of Interfaces: Basic Science in the Industrial World*, World Scientific Publishing, Singapore, 2000.
- [5] S. Adachi, *Properties of Group-IV, III-V and II-VI Semiconductors*, John Wiley & Sons, Ltd, 2005.
- [6] H. Welker, *Zeitschrift für Naturforschung A* **7**, 744 (1952).
- [7] O. Madelung (Ed.), *Semiconductors: Data Handbook*, Ed. 2., Springer, Berlin, Heidelberg, 2004.
- [8] I. Vurgaftman, J. R. Meyer and L. R. Ram-Mohan, *Journal of Applied Physics* **89**, 5815 (2001).
- [9] D. Bimberg (Ed.), *Semiconductor Nanostructures*, NanoScience and Technology, Springer, Berlin, Heidelberg, 2008.
- [10] D. Bimberg and U. W. Pohl, *Materials Today* **14**, 388 (2011).
- [11] Holger Eisele, *The Atomic Composition of Semiconductor Quantum Dots and Related Nanostructures*, Habilitation, Technische Universität Berlin, 2013.
- [12] P.M. Petroff and S.P. DenBaars, *Superlattices and Microstructures* **15**, 15 (1994).
- [13] J. M. Moison, F. Houzay, F. Barthe, L. Leprince, E. André and O. Vatel, *Applied Physics Letters* **64**, 196 (1994).
- [14] J. Oshinowo, M. Nishioka, S. Ishida and Y. Arakawa, *Applied Physics Letters* **65**, 1421 (1994).

- [15] D. Bimberg, M. Grundmann and N. N. Ledentsov, *Quantum Dot Heterostructures*, John Wiley & Sons Ltd., Chichester, 1999.
- [16] V. A. Shchukin, N. N. Ledentsov and D. Bimberg, *Epitaxy of Nanostructures*, NanoScience and Technology, Springer, Berlin, Heidelberg, 2004.
- [17] T. Ishikawa, S. Kohmoto and K. Asakawa, *Applied Physics Letters* **73**, 1712 (1998).
- [18] S. Kohmoto, H. Nakamura, T. Ishikawa and K. Asakawa, *Applied Physics Letters* **75**, 3488 (1999).
- [19] S. Birudavolu, N. Nuntawong, G. Balakrishnan, Y. C. Xin, S. Huang, S. C. Lee, S. R. J. Brueck, C. P. Hains and D. L. Huffaker, *Applied Physics Letters* **85**, 2337 (2004).
- [20] O. Schmidt (Ed.), *Lateral Alignment of Epitaxial Quantum Dots*, NanoScience and Technology, Springer, Berlin, Heidelberg, 2007.
- [21] P. Atkinson, O. G. Schmidt, S. P. Bremner and D. A. Ritchie, *Comptes Rendus Physique* **9**, 788 (2008), Recent advances in quantum dot physics / Nouveaux développements dans la physique des boîtes quantiques.
- [22] J. Y. Marzin, J. M. Gérard, A. Izraël, D. Barrier and G. Bastard, *Physical Review Letters* **73**, 716 (1994).
- [23] D. L. Huffaker and D. G. Deppe, *Applied Physics Letters* **73**, 520 (1998).
- [24] R. Heitz, I. Mukhametzhanov, A. Madhukar, A. Hoffmann and D. Bimberg, *Journal of Electronic Materials* **28**, 520 (1999).
- [25] L. Chu, M. Arzberger, G. Böhm and G. Abstreiter, *Journal of Applied Physics* **85**, 2355 (1999).
- [26] A. D. Yoffe, *Advances in Physics* **50**, 1 (2001).
- [27] G. S. Solomon, M. C. Larson and J. S. Harris Jr., *Applied Physics Letters* **69**, 1897 (1996).
- [28] A. Fiore, U. Oesterle, R. P. Stanley and M. Ilegems, *IEEE Photonics Technology Letters* **12**, 1601 (2000).

- [29] N. Kirstaedter, N. N. Ledentsov, M. Grundmann, D. Bimberg, V. M. Ustinov, S. S. Ruvimov, M. V. Maximov, P. S. Kop'ev, Z. I. Alferov, U. Richter, P. Werner, U. Gosele and J. Heydenreich, *Electronics Letters* **30**, 1416 (1994).
- [30] D. Bimberg, N. Kirstaedter, N. N. Ledentsov, Z. I. Alferov, P. S. Kop'ev and V. M. Ustinov, *IEEE Journal of Selected Topics in Quantum Electronics* **3**, 196 (1997).
- [31] D. L. Huffaker, G. Park, Z. Zou, O. B. Shchekin and D. G. Deppe, *Applied Physics Letters* **73**, 2564 (1998).
- [32] J. A. Lott, N. N. Ledentsov, V. M. Ustinov, N. A. Maleev, A. E. Zhukov, A. R. Kovsh, M. V. Maximov, B. V. Volovik, Z. I. Alferov and D. Bimberg, *Electronics Letters* **36**, 1384 (2000).
- [33] T. Vallaitis, C. Koos, R. Bonk, W. Freude, M. Laemmlin, C. Meuer, D. Bimberg and J. Leuthold, *Optics Express* **16**, 170 (2008).
- [34] H. Schmeckeber, C. Meuer, D. Bimberg, C. Schmidt-Langhorst, A. Galperin and C. Schubert, *Semiconductor Science and Technology* **26**, 014009 (2011).
- [35] Z. Yuan, B. E. Kardynal, R. M. Stevenson, A. J. Shields, C. J. Lobo, K. Cooper, N. S. Beattie, D. A. Ritchie and M. Pepper, *Science* **295**, 102 (2002).
- [36] C. Monat, B. Alloing, C. Zinoni, L. H. Li and A. Fiore, *Nano Letters* **6**, 1464 (2006).
- [37] A. Schlehahn, M. Gaafar, M. Vaupel, M. Gschrey, P. Schnauber, J.-H. Schulze, S. Rodt, A. Strittmatter, W. Stolz, A. Rahimi-Iman, T. Heindel, M. Koch and S. Reitzenstein, *Applied Physics Letters* **107**, 041105 (2015).
- [38] Christopher Prohl, *Strukturelle Eigenschaften von Submonolagen-Bedeckungen im InAs/GaAs-Quantenpunktsystem*, Diplomarbeit, Technische Universität Berlin, 2009.
- [39] C. Prohl, B. Höpfner, J. Grabowski, M. Dähne and H. Eisele, *Journal of Vacuum Science & Technology B* **28**, C5E13 (2010).
- [40] J. Grabowski, C. Prohl, B. Höpfner, M. Dähne and H. Eisele, *Applied Physics Letters* **95**, 233118 (2009).
- [41] H. Eisele, B. Höpfner, C. Prohl, J. Grabowski and M. Dähne, *Surface Science* **604**, 283 (2010).

- [42] J. Márquez, L. Geelhaar and K. Jacobi, *Applied Physics Letters* **78**, 2309 (2001).
- [43] H. Eisele and K. Jacobi, *Applied Physics Letters* **90**, 129902 (2007).
- [44] H. Eisele, O. Flebbe, T. Kalka, C. Preinesberger, F. Heinrichsdorff, A. Krost, D. Bimberg and M. Dähne-Prietsch, *Applied Physics Letters* **75**, 106 (1999).
- [45] A. Lenz, R. Timm, H. Eisele, Ch. Hennig, S. K. Becker, R. L. Sellin, U. W. Pohl, D. Bimberg and M. Dähne, *Applied Physics Letters* **81**, 5150 (2002).
- [46] A. Lenz, H. Eisele, R. Timm, L. Ivanova, H.-Y. Liu, M. Hopkinson, U.W. Pohl and M. Dähne, *Physica E: Low-dimensional Systems and Nanostructures* **40**, 1988 (2008), 13th International Conference on Modulated Semiconductor Structures.
- [47] H. Eisele, A. Lenz, R. Heitz, R. Timm, M. Dähne, Y. Temko, T. Suzuki and K. Jacobi, *Journal of Applied Physics* **104**, 124301 (2008).
- [48] A. Lenz, H. Eisele, J. Becker, L. Ivanova, E. Lenz, F. Luckert, K. Pötschke, A. Strittmatter, U. W. Pohl, D. Bimberg and M. Dähne, *Applied Physics Express* **3**, 105602 (2010).
- [49] A. Lenz, H. Eisele, J. Becker, J.-H. Schulze, T. D. Germann, F. Luckert, K. Pötschke, E. Lenz, L. Ivanova, A. Strittmatter, D. Bimberg, U. W. Pohl and M. Dähne, *Journal of Vacuum Science & Technology B* **29**, 04D104 (2011).
- [50] D. Quandt, J.-H. Schulze, A. Schliwa, Z. Diemer, C. Prohl, A. Lenz, H. Eisele, A. Strittmatter, U. W. Pohl, M. Gschrey, S. Rodt, S. Reitzenstein, D. Bimberg, M. Lehmann and M. Weyland, *Physical Review B* **91**, 235418 (2015).
- [51] R. Leon, C. Lobo, T. P. Chin, J. M. Woodall, S. Fafard, S. Ruvimov, Z. Liliental-Weber and M. A. Stevens Kalceff, *Applied Physics Letters* **72**, 1356 (1998).
- [52] S. Fuchi, Y. Nonogaki, H. Moriya, Y. Fujiwara and Y. Takeda, *Japanese Journal of Applied Physics* **39**, 3290 (2000).
- [53] Y. Song, P. J. Simmonds and M. L. Lee, *Applied Physics Letters* **97**, 223110 (2010).
- [54] T. Nguyen Thanh, C. Robert, C. Cornet, M. Perrin, J. M. Jancu, N. Bertru, J. Even, N. Chevalier, H. Folliot, O. Durand and A. Le Corre, *Applied Physics Letters* **99**, 143123 (2011).

- [55] G. Stracke, A. Glacki, T. Nowozin, L. Bonato, S. Rodt, C. Prohl, A. Lenz, H. Eisele, A. Schliwa, A. Strittmatter, U. W. Pohl and D. Bimberg, *Applied Physics Letters* **101**, 223110 (2012).
- [56] Yuncheng Song, *In_{0.5}Ga_{0.5}As self-assembled quantum dots on GaP/Si*, Dissertation, Yale University, 2014.
- [57] Gernot Stracke, *Wachstum und Charakterisierung von InGaAs Quantenpunkten auf GaP Substraten*, Dissertation, Technische Universität Berlin, 2014.
- [58] T. Nowozin, D. Bimberg, K. Daqrouq, M. N. Ajour and M. Awedh, *Journal of Nanomaterials* **2013**, 215613 (2013).
- [59] M. Geller, E. Stock, C. Kapteyn, R. L. Sellin and D. Bimberg, *Physical Review B* **73**, 205331 (2006).
- [60] L. Pedesseau, J. Even, A. Bondi, W. Guo, S. Richard, H. Folliot, C. Labbe, C. Cornet, O. Dehaese, A. Le Corre, O. Durand and S. Loualiche, *Journal of Physics D: Applied Physics* **41**, 165505 (2008).
- [61] K. Volz, A. Beyer, W. Witte, J. Ohlmann, I. Németh, B. Kunert and W. Stolz, *Journal of Crystal Growth* **315**, 37 (2011).
- [62] Y. Song and M. L. Lee, *Applied Physics Letters* **103** (2013).
- [63] C. Prohl, H. Döscher, P. Kleinschmidt, T. Hannappel and A. Lenz, *Journal of Vacuum Science & Technology A* **34** (2016).
- [64] H. Döscher, O. Supplie, S. Brückner, T. Hannappel, A. Beyer, J. Ohlmann and K. Volz, *Journal of Crystal Growth* **315**, 16 (2011).
- [65] A. Beyer, I. Németh, S. Liebich, J. Ohlmann, W. Stolz and K. Volz, *Journal of Applied Physics* **109**, 083529 (2011).
- [66] A. Beyer, J. Ohlmann, S. Liebich, H. Heim, G. Witte, W. Stolz and K. Volz, *Journal of Applied Physics* **111**, 083534 (2012).
- [67] A. Beyer, B. Haas, K. I. Gries, K. Werner, M. Luysberg, W. Stolz and K. Volz, *Applied Physics Letters* **103**, 032107 (2013).
- [68] A. Beyer, A. Stegmüller, J. O. Oelerich, K. Jandieri, K. Werner, G. Mette, W. Stolz, S. D. Baranovskii, R. Tonner and K. Volz, *Chemistry of Materials* **28**, 3265 (2016).

- [69] C. Prohl, A. Lenz, D. Roy, J. Schuppang, G. Stracke, A. Strittmatter, U. W. Pohl, D. Bimberg, H. Eisele and M. Dähne, *Applied Physics Letters* **102**, 123102 (2013).
- [70] U. W. Pohl, *Epitaxy of Semiconductors: Introduction to Physical Principles*, Graduate Texts in Physics, Springer, Berlin, Heidelberg, 2013.
- [71] M. A. Herman, W. Richter and H. Sitter, *Epitaxy: Physical Principles and Technical Implementation*, Materials Science, Springer, Berlin, Heidelberg, 2004.
- [72] E. Bauer, *Zeitschrift für Kristallographie* **110**, 372 (1958).
- [73] F. C. Frank and J. H. van der Merwe, *Proceedings of the Royal Society A* **198**, 205 (1949).
- [74] M. Volmer and A. Weber, *Zeitschrift für physikalische Chemie* **119**, 277 (1926).
- [75] I. N. Stranski and L. Krastanow, *SB Wiener Akademie der Wissenschaften, Klasse IIb* **146**, 797 (1938).
- [76] H. Lüth, *Surfaces and Interfaces of Solid Materials*, Ed. 3., Springer, Berlin, Heidelberg, 1995.
- [77] D. Leonard, K. Pond and P. M. Petroff, *Physical Review B* **50**, 11687 (1994).
- [78] R. Heitz, T. R. Ramachandran, A. Kalburge, Q. Xie, I. Mukhametzhanov, P. Chen and A. Madhukar, *Physical Review Letters* **78**, 4071 (1997).
- [79] B. Junno, T. Junno, M. S. Miller and L. Samuelson, *Applied Physics Letters* **72**, 954 (1998).
- [80] C. Robert, C. Cornet, P. Turban, T. Nguyen Thanh, M. O. Nestoklon, J. Even, J. M. Jancu, M. Perrin, H. Folliot, T. Rohel, S. Tricot, A. Balocchi, D. Lagarde, X. Marie, N. Bertru, O. Durand and A. Le Corre, *Physical Review B* **86**, 205316 (2012).
- [81] M. A. Herman und H. Sitter, *Molecular Beam Epitaxy: Fundamentals and Current Status*, Materials Science, Springer, Berlin, Heidelberg, 1989.
- [82] G. Binnig, H. Rohrer, Ch. Gerber and E. Weibel, *Physical Review Letters* **49**, 57 (1982).
- [83] G. Binnig and H. Rohrer, *Helvetica Physica Acta* **55**, 726 (1982).

- [84] G. Binnig, H. Rohrer, Ch. Gerber and E. Weibel, *Applied Physics Letters* **40**, 178 (1982).
- [85] G. Binnig and D. P. E. Smith, *Review of Scientific Instruments* **57**, 1688 (1986).
- [86] C. J. Chen, *Introduction to Scanning Tunneling Microscopy*, Oxford Series in Optical and Imaging Sciences, Ed. 1., Oxford University Press, 1993.
- [87] R. Wiesendanger, *Scanning Probe Microscopy and Spectroscopy: Methods and Applications*, Cambridge University Press, 1994.
- [88] R. Wiesendanger (Ed.), *Scanning Probe Microscopy: Analytical Methods*, NanoScience and Technology, Springer, Berlin, Heidelberg, 1998.
- [89] C. J. Chen, *Introduction to Scanning Tunneling Microscopy*, Monographs on the Physics and Chemistry of Materials, Ed. 2., Oxford University Press, 2007.
- [90] B. Voigtländer, *Scanning Probe Microscopy: Atomic Force Microscopy and Scanning Tunneling Microscopy*, NanoScience and Technology, Ed. 1., Springer, Berlin, 2015.
- [91] H. Eisele, Ph. Ebert, N. Liu, A. L. Holmes Jr. and C.-K. Shih, *Applied Physics Letters* **101**, 233107 (2012).
- [92] Andrea Lenz, *Atomic structure of capped In(Ga)As and GaAs quantum dots for optoelectronic devices*, Dissertation, Technische Universität Berlin, 2008.
- [93] C. B. Duke, A. Paton, W. K. Ford, A. Kahn and J. Carelli, *Phys. Rev. B* **24**, 562 (1981).
- [94] A. Kahn, *Surface Science Reports* **3**, 193 (1983).
- [95] Holger Eisele, *Cross-Sectional Scanning Tunneling Microscopy of InAs/GaAs Quantum Dots*, Dissertation, Technische Universität Berlin, 2001.
- [96] R. M. Feenstra, Joseph A. Stroscio, J. Tersoff and A. P. Fein, *Physical Review Letters* **58**, 1192 (1987).
- [97] Ph. Ebert, G. Cox, U. Poppe and K. Urban, *Surface Science* **271**, 587 (1992).
- [98] S. Adachi, *Properties of Semiconductor Alloys*, John Wiley & Sons, Ltd, 2009.
- [99] Alexandra Roth, *Aufbau eines Rastertunnelmikroskops für Untersuchungen an Querschnittsflächen*, Bachelorarbeit, Technische Universität Berlin, 2012.

- [100] J. P. Ibe, P. P. Bey, S. L. Brandow, R. A. Brizzolara, N. A. Burnham, D. P. DiLella, K. P. Lee, C. R. K. Marrian and R. J. Colton, *Journal of Vacuum Science & Technology A* **8**, 3570 (1990).
- [101] O. Flebbe, H. Eisele, T. Kalka, F. Heinrichsdorff, A. Krost, D. Bimberg and M. Dähne-Prietsch, *Journal of Vacuum Science & Technology B* **17**, 1639 (1999).
- [102] E. Lenz, In Berechnung, Version 160-182, TU Berlin, AG Dähne (2012-2017).
- [103] H. Eisele, private communication, TU Berlin (2012).
- [104] C. S. Schulze, X. Huang, C. Prohl, V. Füllert, S. Rybank, S. J. Maddox, S. D. March, S. R. Bank, M. L. Lee and A. Lenz, *Applied Physics Letters* **108** (2016).
- [105] R. Timm, H. Eisele, A. Lenz, S. K. Becker, J. Grabowski, T.-Y. Kim, L. Müller-Kirsch, K. Pötschke, U. W. Pohl, D. Bimberg and M. Dähne, *Applied Physics Letters* **85**, 5890 (2004).
- [106] R. Timm, J. Grabowski, H. Eisele, A. Lenz, S. K. Becker, L. Müller-Kirsch, K. Pötschke, U. W. Pohl, D. Bimberg and M. Dähne, *Physica E: Low-dimensional Systems and Nanostructures* **26**, 231 (2005).
- [107] R. Timm, H. Eisele, A. Lenz, L. Ivanova, G. Balakrishnan, D. L. Huffaker and M. Dähne, *Physical Review Letters* **101**, 256101 (2008).
- [108] R. Timm, A. Lenz, H. Eisele, L. Ivanova, M. Dähne, G. Balakrishnan, D. L. Huffaker, I. Farrer and D. A. Ritchie, *Journal of Vacuum Science & Technology B* **26**, 1492 (2008).
- [109] A. Lenz, E. Tournié, J. Schuppang, M. Dähne and H. Eisele, *Applied Physics Letters* **102**, 102105 (2013).
- [110] E. Lenz and H. Eisele, private communication, TU Berlin (2015).
- [111] L. Ivanova, H. Eisele, A. Lenz, R. Timm, M. Dähne, O. Schumann, L. Geelhaar and H. Riechert, *Applied Physics Letters* **92**, 203101 (2008).
- [112] Ph. Ebert and K. Urban, *Ultramicroscopy* **49**, 344 (1993).
- [113] N. Liu, J. Tersoff, O. Baklenov, A. L. Holmes and C. K. Shih, *Physical Review Letters* **84**, 334 (2000).
- [114] J. M. García, G. Medeiros-Ribeiro, K. Schmidt, T. Ngo, J. L. Feng, A. Lorke, J. Kotthaus and P. M. Petroff, *Applied Physics Letters* **71**, 2014 (1997).

- [115] L. Müller-Kirsch, R. Heitz, U. W. Pohl, D. Bimberg, I. Hausler, H. Kirmse and W. Neumann, *Applied Physics Letters* **79**, 1027 (2001).
- [116] G. Stracke, E. M. Sala, S. Selve, T. Niermann, A. Schliwa, A. Strittmatter and D. Bimberg, *Applied Physics Letters* **104**, (2014).
- [117] G. Stracke, private communication, TU Berlin (2013).
- [118] H. Eisele, private communication, TU Berlin (2018).
- [119] S. Selve, private communication, Zentraleinrichtung Elektronenmikroskopie, TU Berlin (2018).
- [120] A. Fasolino, A. Selloni and A. Shkrebtii, *Structure · Tables 11 - 18: Datasheet from Landolt-Börnstein - Group III Condensed Matter · Volume 24A: “Structure” in SpringerMaterials* (https://dx.doi.org/10.1007/10031427_32), Copyright 1993 Springer-Verlag Berlin Heidelberg.
- [121] J. Even, F. Doré, C. Cornet and L. Pedesseau, *Physical Review B* **77**, 085305 (2008).
- [122] J. Even, private communication, INSA Rennes/CNRS, France (2014).
- [123] L. Bonato, E. M. Sala, G. Stracke, T. Nowozin, A. Strittmatter, M. N. Ajour, Kh. Daqrouq and D. Bimberg, *Applied Physics Letters* **106**, 042102 (2015).
- [124] D. Bimberg, A. Marent, T. Nowozin and A. Schliwa, *Proceedings of SPIE* **7947**, 79470L (2011).
- [125] L. Bonato, I. F. Arikan, L. Desplanque, C. Coinon, X. Wallart, Y. Wang, P. Ruterana and D. Bimberg, *physica status solidi (b)* **253**, 1877 (2016).
- [126] E. M. Sala, G. Stracke, S. Selve, T. Niermann, M. Lehmann, S. Schlichting, F. Nippert, G. Callsen, A. Strittmatter and D. Bimberg, *Applied Physics Letters* **109**, 102102 (2016).
- [127] Stavros Rybank, *Cross-sectional scanning tunneling microscopy investigations of InGaSb/GaAs/GaP(001) nanostructures*, Master thesis, Royal Institute of Technology (KTH) / Technische Universität Berlin, 2015.
- [128] E. Sala, private communication, TU Berlin (2015).

Acknowledgments

I would like to thank Prof. Dr. Mario Dähne for the opportunity of studying, working, teaching, and writing my thesis in his group. Thank you for your infectious enthusiasm for physics, your patience, and also for the careful proofreading of my thesis.

I am very grateful to Prof. Dr. Holger Eisele. Thank you not only for your invaluable scientific support, many helpful ideas, simulations, and discussions, but also for introducing me into all aspects of the work of a scientist. Thank you for your continuous motivation and your trust in my abilities, for proofreading my thesis, and for being a true mentor.

PD Dr. Philipp Ebert is gratefully acknowledged for taking his time in refereeing this thesis and special thanks go to Prof. Dr. Kathy Lüdge for chairing the final defense.

I want to thank Prof. Dr. Udo W. Pohl, my co-advisor within the SFB 787, for his interest in my work, the fruitful scientific discussions, and for enabling the collaboration with Jacky Even.

My deepest thanks go to Dr. Andrea Lenz who taught me everything about XSTM, from sample preparation to handling the whole XSTM setup. Thank you for becoming such a great colleague and more through the last years, for the many conversations, and being someone who understands my passion in fencing.

I am also grateful to Dr. Ernst Lenz, who provided the very helpful Mathematica tools, which made the evaluation process of my data much easier. Thank you also for recommending me for the lecturer job.

Dr. Gernot Stracke is especially acknowledged for his preliminary epitaxy and PL work (supervised by Prof. Dr. André Strittmatter and Prof. Dr. Dieter Bimberg) and for providing the MOVPE-grown XSTM samples on (In,Ga)As/GaP QDs.

Special thanks go to Yuncheng Song, Ph. D. and Prof. Minjoo Larry Lee, Ph. D. for the nice collaboration and for providing the MBE-grown samples.

Prof. Dr. Jacky Even is gratefully acknowledged for the calculations on the electronic structure and the discussion of their results.

Sören Selve (ZELMI) is acknowledged for providing TEM data.

Thank you to Dr. Elisa Sala (AG Bimberg) for providing the MOVPE samples on (In,Ga)Sb/GaAs QDs in GaP.

I want to thank my students Dominik Roy and Stavros Rybank who performed the experiments for their Bachelor/Master theses under my guidance, whose results contributed to this thesis, and also to all other members of the great XSTM team for helping to fill some of the many necessary measuring shifts. Especially noticed are Andrea Lenz, Josephine Schuppang, Tim Amrhein, Thomas Brückmann, Zeno Diemer, Vivien Füllert, Celina Schulze and Holger Eisele.

Special thanks go to my fellow Ph.D. students in the group, Dr. Martin Franz and Dr. Stephan Appelfeller, for sharing the same path. Although both of you work on the "old STM", you were great colleagues all the time. I will remember the good times we had together in the lab, in the office, teaching undergraduate students, and beyond.

Thank you also to all former and current members of the AG Dähne and AG Eisele for their help and support during all the years and for creating a great atmosphere at work, at conference journeys, and at all the "Ostsee-Seminarfahrten". Also thank you to all other collaborators and members of the Institute of Solid State Physics and the SFB 787, who supported me during my doctorate.

My deepest thanks go to my fellows in the office for creating an awesome atmosphere, especially during the last weeks and month when writing and finishing this thesis: Stephan Appelfeller, Hendrik Janssen, Jonathan Karl Hoffmann, Gada Hweidi, Pascal Farin, Dorothee Eckert, Robert Zielinski, Lars Freter, Tim Amrhein, Christian Bruckmann and Mike Nehring. Thank You!

I want to thank my family and my friends for their support, distraction when needed, and for sometimes not asking about the status of my thesis.

This thesis is dedicated to my Mom and Dad, who always supported me and still do. Thank you for your trust in me finding my own way!

This work was supported by the Elsa-Neumann-Stipendium des Landes Berlin and by the Deutsche Forschungsgemeinschaft through SFB 787.